

---

# Design Strategies for Charge Reversal and Temporally Regulated Functionalities in Porous and Non-porous Systems

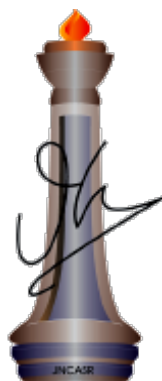
---

A Thesis Submitted for the Degree of

*Doctor of Philosophy*

By

K. P. Sonu



**Chemistry and Physics of Materials Unit**

**Jawaharlal Nehru Centre for Advanced Scientific Research**

**(A Deemed University)**

**Bangalore - 560064 (INDIA)**

**August 2019**



**Design Strategies for Charge Reversal and  
Temporally Regulated Functionalities in Porous  
and Non-porous Systems**

A Thesis Submitted for the Degree of

*Doctor of Philosophy*

By

**K. P. Sonu**

UNDER THE SUPERVISION OF

**Prof. M. Eswaramoorthy**

**Chemistry and Physics of Materials Unit**

**Jawaharlal Nehru Centre for Advanced Scientific Research**

**(A Deemed University)**

**Bangalore-560064 (INDIA)**

**August 2019**



“Great things are done by a series of small things brought together.”

-Vincent van Gogh

Dedicated to my mother



## DECLARATION

I hereby declare that the thesis entitled “*Design Strategies for Charge Reversal and Temporally Regulated Functionalities in Porous and Non-porous Systems*” is an authentic record of research work carried out by me at the Chemistry and Physics of Materials Unit, Jawaharlal Nehru Centre for Advanced Scientific Research, Bangalore, India under the supervision of **Prof. M. Eswaramoorthy** and that it has not been submitted elsewhere for the award of any degree or diploma.

In keeping with the general practice in reporting scientific observations, due acknowledgment has been made whenever the work described is based on the findings of other investigators. Any omission that might have occurred due to oversight or error in judgment is regretted.

**K. P. Sonu**







**Jawaharlal Nehru Centre for  
Advanced Scientific Research**

Prof. M. Eswaramoorthy  
Chemistry and Physics of Materials Unit  
Jawaharlal Nehru Centre for Advanced  
Scientific Research (JNCASR)  
Bangalore-560064, India  
Phone : +91 80 2208 2870  
Fax: + 91 80 22082766  
E-mail: eswar@jncasr.ac.in

Date: August 28, 2019

---

## CERTIFICATE

I hereby certify that the work described in this thesis titled “*Design Strategies for Charge Reversal and Temporally Regulated Functionalities in Porous and Non-porous Systems*” has been carried out by **K. P. Sonu** at the Chemistry and Physics of Materials Unit, Jawaharlal Nehru Centre for Advanced Scientific Research, Bangalore, India under my supervision and it has not been submitted elsewhere for the award of any degree or diploma.

**M. Eswaramoorthy**  
(Research Supervisor)



## ACKNOWLEDGEMENTS

During the course of my Ph.D., I have been helped by a large number of people, to whom I will always be grateful. Firstly, I would like to offer my most sincere thanks to one person who has stayed with me from the beginning to the end of my Ph.D., my research supervisor, **Prof. M. Eswaramoorthy**. I am thankful to him for introducing me to the field of mesoporous silica and other nanomaterials and for giving me the freedom to work on various problems. His ever-enthusiastic nature, constant encouragement and support has helped me in successful completion of this work.

I would like to express my gratitude to **Prof. C. N. R. Rao, FRS** for being a constant source of inspiration. I am also grateful to him for creating such a vibrant research atmosphere to carry out this work.

I thank the past and present chairmen of CPMU (*Prof. G. Kulkarni, Prof. S. Balasubramanian, Prof. C. Narayana and Prof. A. Sundaresan*) for allowing me to use various facilities of the centre.

I am thankful to *Prof. M. Eswaramoorthy, Prof. A. Sundaresan, Prof. S. Balasubramanian, Prof. S. M. Shiva Prasad, Prof. G. U. Kulkarni, Prof. C. Narayana, Prof. Subi J. George, Prof. Jayanta Halder, Prof. H. Illa, Prof. K. S. Narayan, Prof. Sridhar Rajaram, Prof. Rajesh Ganapathy, Prof. Ranjan Datta, Prof. Shobhana Narasimhan, Prof. Umesh V. Waghmare, Prof. Vidhyadhiraja N. S. and Prof. Aloknath Chakrabarti* for their excellent course works.

My special thanks to my labmates, the “NanoCat” group members: *Dr. K.K.R. Datta, Mrs. Josena, Dr. B.V.V.S. Pavan Kumar, Dr. Piyush Kumar Chadurbody, Dr. Amritroop Achari, Dr. Sisir Maity, Dr. Dheeraj Kumar, Ms. Suchi Smita Biswas, Ms. Soumita Chakraborty, Mr. Momin Ahamed, Mr. Arunava Saha, Ms. Divya Bhutani, Ms. Surishi Vashishth, Ms. Nijita Mathew, Mr. Abhishek, Dr. Krishnachary, Mrs. Reshma K R Kakunje, Mrs. Sahana Sheshachala, Mr. Subbu Devaraj, Dr. Mehraj Ud Din Sheikh, Dr. Monoj Kumar Barman, Mr. Toyin and Mr. Yusuf* for their cooperation, useful discussions and for creating a friendly atmosphere in the lab. Working with them was a real pleasure.

It is a great pleasure to thank my collaborators: *Prof. Subi J. George (JNCASR), Dr. Mohit Kumar (JNCASR), Dr. Ankit Kumar (JNCASR), Mr. Krishnendu Jalani*

(JNCASR), *Ms. Shikha Dhiman* (JNCASR), *Dr. Kesavan Subaharan* (ICAR-National Bureau of Agricultural Insect Resources), *Dr. Varma Rambaran* (The University of Trinidad and Tobago (UTT)), *Dr. R. Anbarasan* (Kamaraj College of Engineering and Technology) and *Dr. Saumya* (Bangalore University) for fruitful collaborations.

I am thankful to my friends *Mr. Arun Deepth*, *Mr. Sandeep*, *Mr. Jishnu*, *Mr. Vasudev*, *Mr. Krishnendu Jalani*, *Mr. A. Raaghes*, *Ms. Suseela*, *Mr. Mohini Mohan Konai*, *Dr. Uttam Gupta*, *Mr. Abhijith* and *Dr. Suchitra* for their encouragement at various occasions.

I am thankful to the following people for various technical assistance: *Mrs. Usha* (TEM); *Mrs. Selvi* (FESEM); *Mr. Mahesh* (NMR); *Mr. Vasu* (UV, PL, IR and TGA); *Dr. Mohit Kumar*, *Dr. Ankit Kumar* and *Mr. Krishnendu Jalani* (NMR); *Prof. K. S. Narayan* and *Mr. Raaghes* (Voltammetry); *Dr. Arpan* and *Mr. Subhajit Saha* (Vapor sorption); *Mr. Abhijith* (Magnetic measurements).

I am grateful to *Mr. Amit Bhattacharya* (SRF-2014), *Ms. Chetana Viswanatha* (POCE- 2015), *Mr. Jithu Raj* (SRF- 2015), *Mr. Rachit Saran* (SRF- 2015), *Ms. Savithri Vishwanathan* (POCE- 2016), *Ms. Sushmitha Vini* (visiting student 2017), *Mr. Jerin Tambi* (POCE-2017), *Mr. Sajan Chinnan* (visiting student 2017 and 2018) for working with me on various projects.

Besides the research life, I am thankful to *Prof. M. Eswaramoorthy* and his family members for their hospitality and affection.

I am thankful to academic and administrative staff of JNCASR for their assistance.

A deep sense of gratitude to my family for their support, love and affection throughout my life. A special thank you to my wife *Shanimol* for her constant encouragement and faith.

*Sonu*

## PREFACE

The thesis deals with novel strategies for the construction of charge reversal mesoporous silica and temporally regulated functional systems.

The thesis is consisting of seven chapters categorized into two parts.

**Chapter-1.1** briefly introduces mesoporous silica and provides an overview of important advances in the field of mesoporous silica pore engineering towards controlling molecular transport.

In **Chapter-1.2**, we introduce a simple noncovalent strategy to modulate the surface charge of the mesoporous silica by making use of the molecular assembly of ionic amphiphiles within the pores. The hexyl pendant groups covalently attached to the surface of the silica provided hydrophobic room for the facile assembly of charged amphiphiles. These charge-switchable surfaces were used for fast and charge selective adsorption of dyes from aqueous solutions.

**Chapter-1.3** deals with a logic gate-controlled release of cargo from mesoporous silica by utilizing the change in pH of the surrounding medium by multiple enzymatic reactions. By choosing appropriate enzymes and substrates, Boolean logic gate (OR and INH) controlled release of cargo was achieved.

Functional events occurring in the natural systems are temporally regulated via signaling, enzymatic regulatory networks, feedback loops, energy dissipation etc. In the recent years, there has been an urge to mimic these machineries (therefore to achieve precise temporal regulation of structural or functional feature of the system) into the man-made systems as an attempt to fabricate intelligent, autonomous and self-regulated functional systems. **Chapter-2.1** provides an overview of temporally regulated functional systems with an emphasis on various design principles.

In **Chapter-2.2**, we demonstrate a biochemical reaction driven temporal regulation of mass transport in mesoporous silica. The pH-responsive nanochannel was rationally

fabricated through a hetero functionalization approach utilizing propylamine and carboxylic acid moieties. At the basic pH, cationic small molecules can diffuse into the compartment which releases back to the solution at the acidic pH. The ‘molecule entrapped’ state is temporally controlled using a base as fuel along with esterase enzyme as the mediator. The slow enzymatic hydrolysis of a dormant deactivator (ethyl acetate) determines the transient lifetime of ‘molecules entrapped’ state, which is program easily by modulating the enzymatic activity of esterase. This system represents a unique approach to create autonomous artificial cellular models.

Recently, inorganic nanoparticles showing enzyme-like activity (nanozyme) have been emerged with several advantages compared to their natural counterparts. That triggered research for integrating them into certain biochemical reaction networks such as cascade networks. In **Chapter-2.3**, we report a successful construction of simple artificial biochemical reaction network consisting of a nanozyme and an enzyme. The peroxidase mimicking activity of the nanozyme is temporally regulated by urease mediated hydrolysis of urea in a fuel-driven manner. The system represents a close mimic of the fuel-driven temporally regulated enzymes networks in biology.

In **Chapter-2.4**, we have demonstrated temporally regulated switching of light transmittance and electrical conductance in polyaniline films by employing enzyme-catalyzed biochemical reaction. The enzymatic reaction produces feedback induced transient pH profile whose lifetime could be pre-programmed via enzyme concentration. This autonomous, temporally regulated polymer film represents an advancement to the existing switchable materials that operate at equilibrium.

# TABLE OF CONTENTS

Declaration	i
Certificate	iii
Acknowledgments	v
Preface	vii
Table of contents	ix

## PART - 1

### Chapter 1.1

#### *Introduction to Surface Engineering in Mesoporous Silica: Regulated Mass Transport through Mesochannels*

Summary	1
1.1.1 Introduction	3
1.1.2 Pore Gating	3
1.1.3 Incorporation of receptor molecules	8
1.1.4 Pore Philicity Modulation	9
1.1.5 Surface Charge Modulation	10
1.1.6 Covalent & Non-covalent Functionalization	15
1.1.7 Conclusions	16
1.1.8 References	16

### Chapter 1.2

#### *Simple Approach to Create Modular Charge Reversible Mesoporous Silica via Hydrophobic Anchoring of Ionic Amphiphiles*

Summary	27
1.2.1 Introduction	29
1.2.2 Scope of the present investigation	30
1.2.3 Experimental section	31

1.2.4	Characterization	35
1.2.5	Results and discussion	35
1.2.6	Conclusions	46
1.2.7	References	47

## **Chapter 1.3**

### **Molecular Logic Gate: Integrating Multi- Analyte Response in Mesoporous Silica for Logic Controlled Release**

Summary	51	
1.3.1	Introduction	53
1.3.2	Scope of the present investigation	54
1.3.3	Experimental section	56
1.3.4	Characterization	59
1.3.5	Results and discussion	59
1.3.6	Conclusions	68
1.3.7	References	69

## **PART - 2**

## **Chapter 2.1**

### **Introduction to Bio-inspired Temporally Regulated Functional Materials**

Summary	75	
2.1.1	Temporal Control in Stimuli-Responsive Switchable Systems	77
2.1.2	Conclusions	91
2.1.3	References	91

## **Chapter 2.2**

### **Bio-inspired Temporal Regulation of Ion-Transport in Nanochannels**

Summary	97	
2.2.1	Introduction	99
2.2.2	Scope of the present investigation	101
2.2.3	Experimental section	102



2.2.4	Characterization	105
2.2.5	Results and discussion	105
2.2.6	Conclusions	113
2.2.7	References	114

## **Chapter 2.3**

### **Bio-inspired Temporal Regulation of Catalytic Activity of a Nanozyme**

Summary		119
2.3.1	Introduction	121
2.3.2	Scope of the present investigation	123
2.3.3	Experimental section	124
2.3.4	Characterization	126
2.3.5	Results and discussion	126
2.3.6	Conclusions	134
2.3.7	References	134

## **Chapter 2.4**

### **Bio-inspired Temporally Programmed Switching in Dual Functional Polymer Film**

Summary		141
2.4.1	Introduction	143
2.4.2	Scope of the present investigation	145
2.4.3	Experimental section	146
2.4.4	Characterization	149
2.4.5	Results and discussion	149
2.4.6	Conclusions	161
2.4.7	References	161
	<b>Conclusions and Outlook</b>	169
	<b>Appendix</b>	171
	<b>List of Publications</b>	173
	<b>Curriculum vitae</b>	175



# **PART – 1**

**Chapter 1.1: Introduction to Surface Engineering in Mesoporous Silica: Regulated Mass Transport through Mesochannels**

**Chapter 1.2: Simple Approach to Create Modular Charge Reversible Mesoporous Silica via Hydrophobic Anchoring of Ionic Amphiphiles**

**Chapter 1.3: Molecular Logic Gate: Integrating Multi-Analyte Response in Mesoporous Silica for Logic Controlled Release**

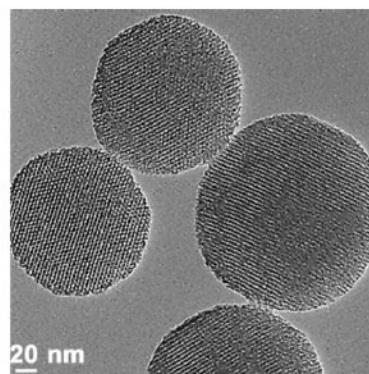


## Chapter-1.1

### ***Introduction to Surface Engineering in Mesoporous Silica: Regulated Mass Transport through Mesochannels***

#### **Summary:**

*Mesoporous materials have generated a lot of interest over the past few decades owing to their wide range of applications in catalysis, separation, drug delivery, sensors, adsorption, photonics, nanodevices etc. To realise such applications, it is necessary to regulate the transport of molecules through the mesochannels which resulted in a surge of interest to manipulate the pore size, surface charge and philicity. This chapter provides an overview of important advances made in mesoporous silica for controlling the molecular transport across the channel and their implications in drug delivery, bio-inspired membranes and catalysis.*





### **1.1.1. Introduction**

In the last few decades, tremendous advances have been made in synthesis of ordered porous solids with controlled pore size, shape and regularity of the pores.<sup>1-5</sup> Among them, ordered mesoporous silica stands out due to their high surface area, ease of synthesis and chemical modifications, high thermal stability and bio-compatibility.<sup>6-10</sup> Mesoporous silica is generally synthesized via organic-inorganic assembly of amphiphilic surfactants and silicate species (produced by base or acid catalysed hydrolysis of silane precursors, tetraalkoxysilane). The amphiphilic surfactants act as structure directing agents or templates. After the condensation of silicates species around the superstructures formed by surfactant molecules (template), the solid mesoporous silica can be obtained by removing the template (via calcination or ion exchange or simple washing).<sup>11-12</sup>

The term ‘surface engineering’ in the context of mesoporous silica is primarily associated with controlling the parameters like pore structure, pore philicity and surface charge. Since, these parameters define the mass transport through the mesopores, it is necessary to optimise them for their applications in drug delivery<sup>10, 13-16</sup>, sensing<sup>17</sup>, catalysis<sup>18-19</sup>, bio-mimetic channels<sup>20-21</sup> etc. This chapter highlights various strategies adopted such as gating, incorporation of receptor molecules, philicity and surface charge modifications to regulate the mass transport in mesoporous silica.

### **1.1.2. Pore Gating**

Pore gating is an important strategy to control the movement of cargo molecules from the pores of the mesoporous silica to the solution and vice versa, in response to pre-programmed stimulus (Figure 1).<sup>22</sup> In this approach, the entrapped cargo molecules are physically blocked from releasing via pore blocking agents (polymers<sup>23-25</sup>, cyclodextrins<sup>26-27</sup>, nanoparticles<sup>28-31</sup> etc.) attached at the entrance of the nanochannels. Once an appropriate stimulus is applied, the pore blocking agent is removed from the mesoporous silica to release the cargo molecules. The gated mesoporous silica nanodevices have demonstrated the potential of achieving pre-designed functions by means of mass transport regulation. The most studied applications of such systems are related to the drug delivery<sup>32</sup> and smart catalysis.<sup>33-34</sup>

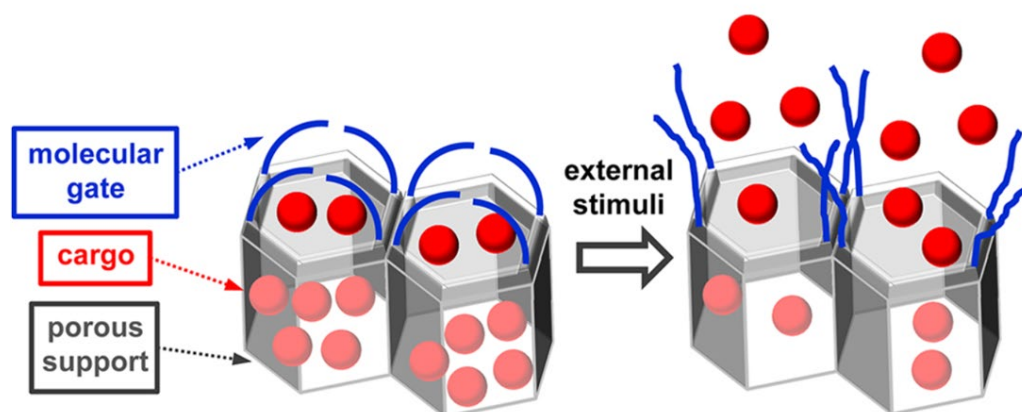


**Figure 1.** Schematic representation of a gated material for on-command controlled release. Reproduced with permission from reference 22. Copyright 2016, American Chemical Society

**1.1.2.1 Molecular Entities for Pore Gating.** Several molecular motifs such as (bio)-polymers<sup>24, 35,36</sup>, DNA aptamers<sup>37-38</sup>, lipids<sup>39-40</sup>, coumarin<sup>41</sup>, thymine<sup>42</sup> etc. have been successfully used as effective pore blocking agents at mesoporous silica surface. For instance, Kleitz et al. designed and synthesised a  $\beta$ -lactoglobulin functionalized mesoporous silica for pH dependent release of ibuprofen (Figure 2).<sup>25</sup> At pH < 5  $\beta$ -lactoglobulin on mesoporous silica surface undergoes a gelation process, leading to the-

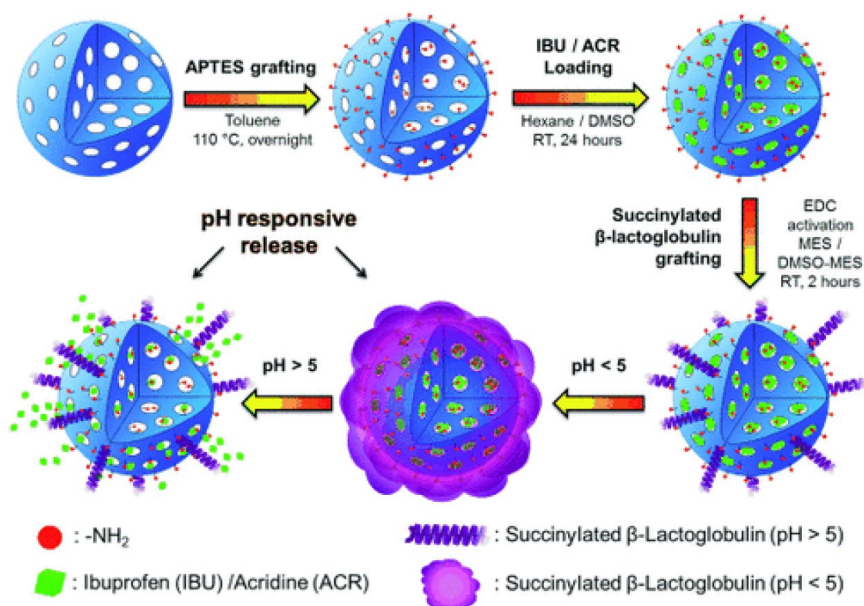


**Figure 2.** Schematic representation of the post-grafting, bio-functionalization, and pH-responsive release of drug or dye from basic pH sensitive MNPs. (Reproduced with permission from reference 25. Copyright 2013, Wiley-VCH (Germany)).



-formation of intermolecular hydrogen-bonded  $\beta$ -sheet. This conformational change is associated with lower solubility of the  $\beta$ -lactoglobulin in acidic media, resulting in a pH dependent “gel-shell” around the mesoporous silica. This gel will prevent the drug molecule release from the mesopores. At pH > 5,  $\beta$ -lactoglobulin becomes permeable, allowing the drug to get released. Recently, He and co-workers synthesised a controlled release system in which polymer containing coumarin moieties was used to gate the mesoporous silica (Figure 3).<sup>22,41</sup> Irradiation with 365 nm UV light leads to the formation of coumarin dimers which cross-link the polymer and effectively block the entrapped cargo molecules. However, when the hybrid was irradiated at 264 nm UV light, the coumarin moieties returned to the monomer form, therefore, open up the pores that leads to the release of entrapped cargo.

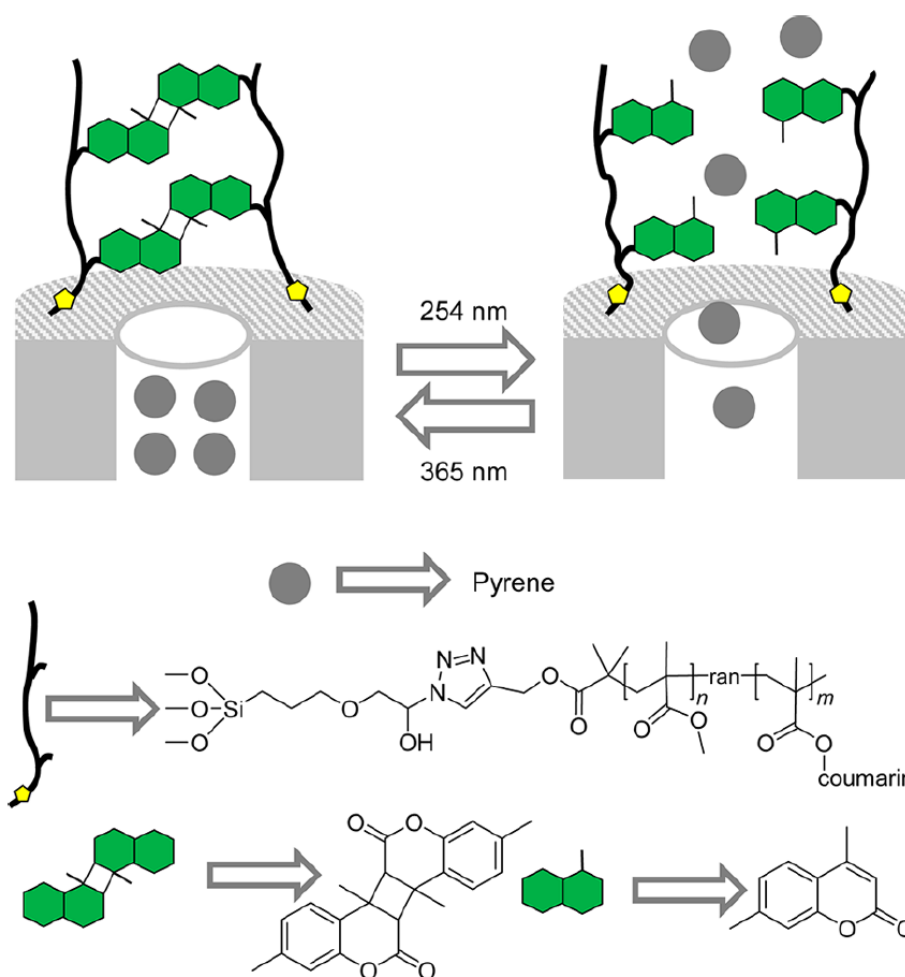


**Figure 3.** Gated MSNs loaded with pyrene and capped with a methyl methacrylate and 7-(2-methacryloyloxy)-4 methylcoumarin copolymer. Pyrene was released upon irradiation at 254 nm. Reproduced with permission from reference 22. Copyright 2016, American Chemical Society

**1.1.2.2 Supramolecular Entities for Pore Gating.** Supramolecular motifs like cyclodextrins<sup>43-45</sup>, cucurbitural<sup>26, 46</sup>, crown-ethers<sup>47-48</sup> and pillararenes<sup>49-50</sup> having molecular dimensions are of the order of pore size of mesoporous silica (2-3 nm) have also been utilized as pore gating agents. For example, azobenzene which is known to have a strong binding affinity with  $\beta$ -cyclodextrin in its *trans* form have been used widely on mesoporous silica surface as a light responsive supramolecular motif. Stoddart, Zink, and co-workers prepared mesoporous silica nanoparticles (MSNs) with outer surface modified with (E)-4-((4- (benzylcarbamoyl)phenyl)diazenyl)benzoic acid derivative.<sup>22, 43</sup> The azo-modified MSN were capped with  $\beta$ -cyclodextrins ( $\beta$ -CDs) via the formation of inclusion complexes with *trans* isomer of the grafted azobenzenes. Cargo delivery was triggered by irradiation with a laser light of 351 nm which switch the azobenzene from *trans* isomer to *cis* form as shown in Figure 4. The  $\beta$ -cyclodextrins are unable to thread to the stack (*cis*-form of azobenzene) as a consequence, the entrapped cargo (RhB) molecules were released.

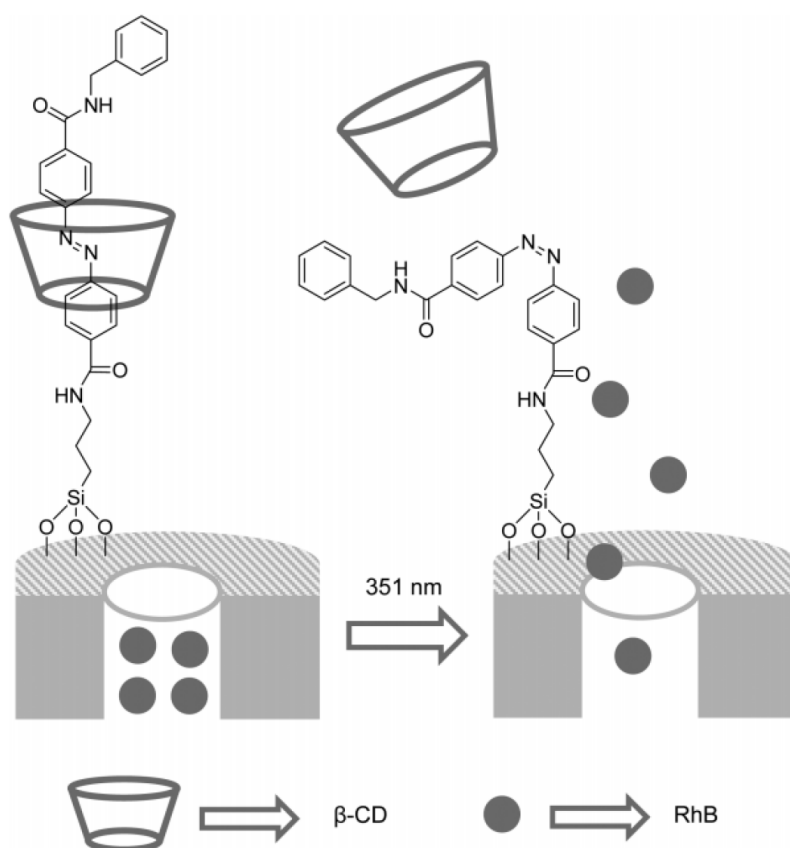


**Figure 4.** Azobenzene functionalized mesoporous silica loaded with Rh B and capped with  $\beta$ -CD. Rh B was released upon irradiation at 351 nm. Reproduced with permission from reference 22. Copyright 2016, American Chemical Society.

**1.1.2.3 Nanoparticles for Pore Gating.** Various nanoparticles of diameter around 3 nm have been utilized to effectively block the pores of mesoporous silica. These nanoparticles are generally attached to the external surface by stimuli responsive covalent linkages such as imide bonds, disulfide bonds, boronic ester bonds etc. Some of the nanoparticles utilized for this purpose are gold nanoparticles<sup>28, 51-52</sup>, CdS nanoparticles<sup>53</sup>, Fe<sub>3</sub>O<sub>4</sub> nanoparticles<sup>30-31</sup> etc. For instance, Lin and co-workers immobilized cadmium sulfide (CdS) nanoparticles on mesoporous silica surface using disulfide linkages (Figure 5)<sup>53</sup> which were then used to block the encapsulated drug molecules -vancomycin and ATP. When disulfide bond-reducing molecules like dithiothreitol was used as a trigger, encapsulated drug molecules were released from the mesopores.

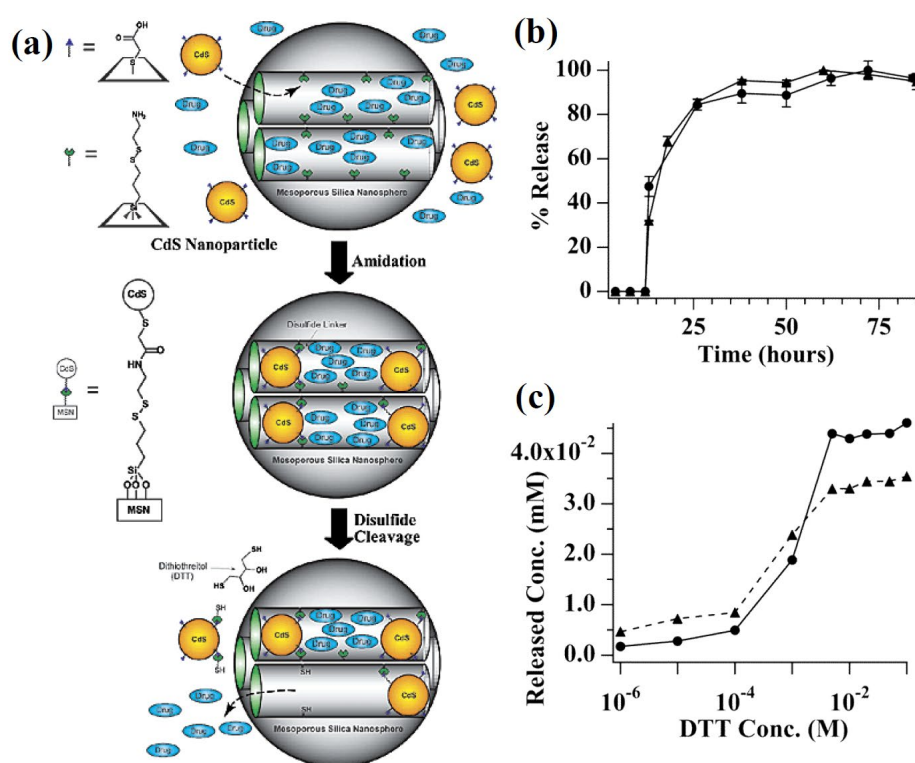


**Figure 5.** (a) Schematic representation of CdS nanoparticle-capped MSN-based drug delivery system. The controlled release mechanism of the system is based on chemical reduction of the disulfide linkage between the CdS caps and the MSN hosts. (b) The DTT-induced release profiles of Vancomycin (dotted) and ATP (triangle) from the CdS-capped MSN system. (DTT: dithiothreitol) over time. (c) The DTT concentration-dependent releases of Vancomycin (dotted) and ATP (triangle). Reproduced with permission from reference 53. Copyright 2016, American Chemical Society.

### 1.1.3. Incorporation of receptor molecules.

Incorporation of receptor motifs on to mesoporous silica is a well-accepted strategy to achieve specific uptake of molecules / ions from solution.<sup>54</sup> Owing to the facile silane chemistry on mesoporous silica surface, various receptor molecules with specific interactions to the adsorbate of interest could be immobilized on the silica surface to achieve controlled mass transport of specific molecules / ions. For example, mesoporous silica covalently functionalised with thiol, thiourea and thioether containing ligands (having soft electron donor atoms) showed high uptake for  $\text{Hg}^{2+}$  ions.<sup>55-56</sup> Further, by increasing the surface coverage of the thiol motifs, affinity for  $\text{Hg}^{2+}$  could be improved.<sup>57</sup> Similarly, mesoporous silica grafted with terminal amino-based (amine, urea, polyamidoamine, etc.) or carboxylic groups have shown efficient binding properties to many heavy metal ions (such as  $\text{Cu}^{2+}$ ,  $\text{Zn}^{2+}$ ,  $\text{Cr}^{3+}$ ,  $\text{Fe}^{3+}$ ,  $\text{Cd}^{2+}$  and  $\text{Ni}^{2+}$ ).<sup>58-61</sup> The uptake involves direct coordination of metal ions to these surface grafted motifs.

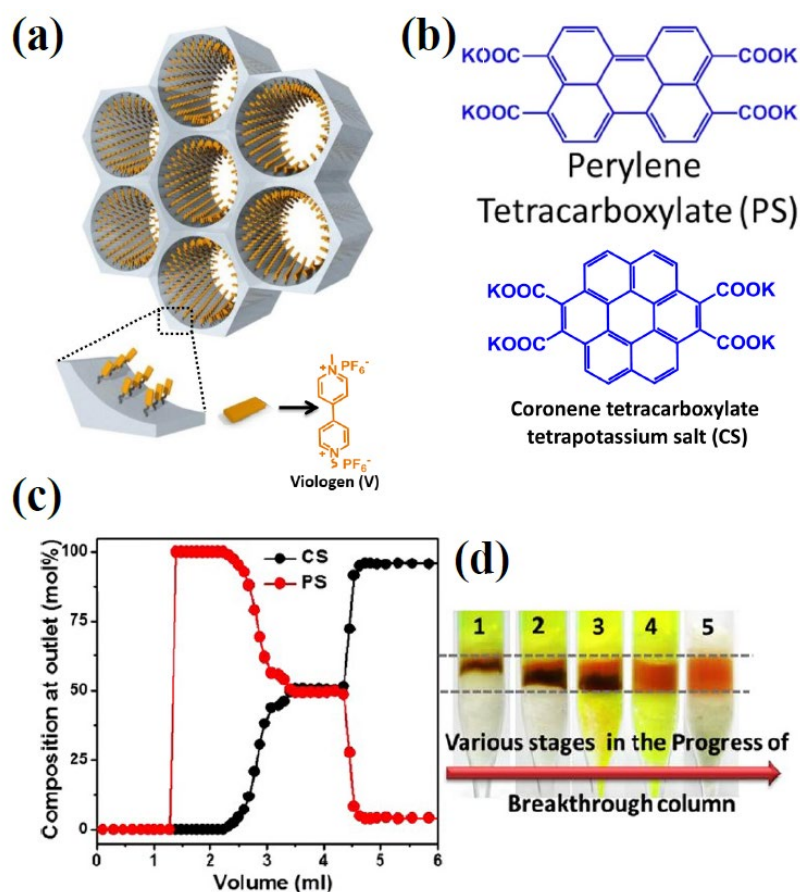


**Figure 6.** (a) Schematic representation of viologen modified mesoporous silica. (b) Chemical structures of donor molecules used in the study. (c) Experimental breakthrough curves for an equimolar mixture of CS and PS flowing through a bed of SBA-V, exhibiting clear separation and high selectivity. (d) Photographs of the bed of SBA-V (located

*between the dashed lines) at various stages of the breakthrough experiment. Reproduced with permission from reference 62. Copyright 2013, American Chemical Society.*

Recently, Pawan *et. al.* demonstrated viologen (electron acceptor) functionalized mesoporous silica (SBA-V) showing selective adsorption towards donor moieties, the anion components of pyranine, perylene (PS) and coronene (CS) salts (Figure 6).<sup>62</sup> SBA-V selectively bind to donors to form charge transfer complex (CT complex). The binding constant for the respective CT complex was found to increase within the nanochannels of the silica compared to the solution. The difference in the binding abilities for the respective CT complex was utilized for the separation of donors, CS and PS in a breakthrough column. The CS binds strongly to the SBA-V compared to PS therefore, was eluted first with respect to CS.

### **1.1.4. Pore Philicity Modulation.**

Pore philicity play vital role in defining the molecular transport through the mesochannels. A hydrophilic pore prefers hydrophilic molecules to accumulate within. On the other hand, hydrophobic pore prefers hydrophobic molecules. For example, a hydrophilic mesoporous silica (SBA-V) and its hydrophobic derivatives (SBA-V-PC<sub>6</sub> and SBA-V-PC<sub>12</sub>) tested for their selective uptake towards hydrophilic, FITC-labelled dextran and hydrophobic protein myoglobin, respectively. The molecular dimensions of myoglobin and 4 kDa dextran are similar (2.9×3.6×6.4 nm and 3 nm respectively). The SBA-V-PC<sub>12</sub> and SBA-V-PC<sub>6</sub> exhibited stronger uptake for myoglobin (hydrophobic) than dextran (hydrophilic) indicating hydrophobicity driven uptake. However, SBA-V shows a higher uptake for dextran than myoglobin implying hydrophilicity driven uptake.<sup>62</sup>

Similar philicity driven molecular transport have been recently utilised for advanced applications such as ‘smart catalysis’. For example, DK Singh *et. al.* reported a pH switchable catalyst based on functionalized mesoporous silica (Figure 7).<sup>63</sup> The smart catalyst consisted of propylamine functionalized mesoporous silica having gold nanoparticles immobilized inside the pores (Au-SBA-NH<sub>2</sub>). The catalytic activity of this system was tested using p-nitrophenol reduction in aqueous phase as a model reaction. The protonated amine groups make the pores hydrophilic in aqueous medium which in turn allows the reactant p-nitrophenol (and the reducing agent- borohydride) to get into

the pores and get reduced to aminophenol on the gold surface. However, when the pores were reversibly modified by alkyl chains through dynamic covalent bond between amine and aldehyde (imine chemistry), the pores became hydrophobic. The reductant dissolved in water now could not reach the gold nanoparticles through the hydrophobic channels and hence no reduction of *p*-nitrophenol occurred. The pore philicity can be switched between hydrophilic and hydrophobic in a pH responsive manner as the imine bonds are labile to acidic pH, demonstrating the pH responsive catalysis within the porous silica.

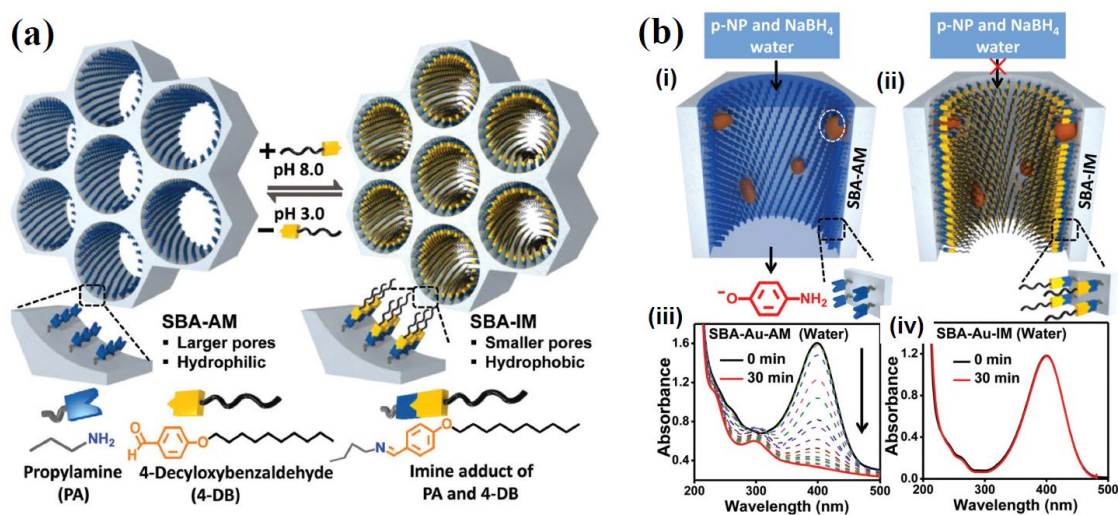


**Figure 7.** (a) Illustration depicting reversible engineering of the pore size and philicity of mesoporous SBA via dynamic covalent chemistry triggered by changes in pH. (b) Catalysis in water medium. (i) Schematic showing gold nanoparticles (encircled in white) immobilized in the pores of SBA-Au-AM, carrying out catalytic reduction of *p*-nitrophenol. (ii) UV-Vis spectra indicating complete reduction of *p*-nitrophenol to *p*-aminophenol within 30 min by SBA-Au-AM (arrow indicating the decrease in intensity with time). (iii) Illustration showing the absence of catalytic activity due to de-wetting of the pores caused by hydrophobicity of SBA-Au-IM. (iv) Corresponding UV-Vis spectra indicating no catalytic reduction. Reproduced with permission from reference 63. Copyright 2015, Royal Society of Chemistry.

### 1.1.5. Surface Charge Modulation

The transport of charged molecules through mesoporous silica is governed predominantly by surface charge on the pore surface due to the fact that size of these pores are comparable to the Debye length.<sup>64</sup> Therefore, the electrostatic potential does

not decay to the bulk values even at the centre of the pore.<sup>65-66</sup> This creates asymmetry of ion distribution inside the nanochannels/nanopores (counter-ion in nanochannels is enriched while the co-ion concentration decreased) due to the electrostatic interactions between ions and the charges of the nanopores (Figure 8). The asymmetric ion-distribution within nanopores makes them permselective with respect to ion transport by favouring the movement of counter ion.<sup>67</sup> This permselective nature of mesoporous silica nanochannels have been explored for various applications such as sensing<sup>68</sup>, fabrication of abiotic nanochannels<sup>69</sup>, charge mediated delivery<sup>70</sup>, electrochemical energy conversion<sup>71</sup> etc.

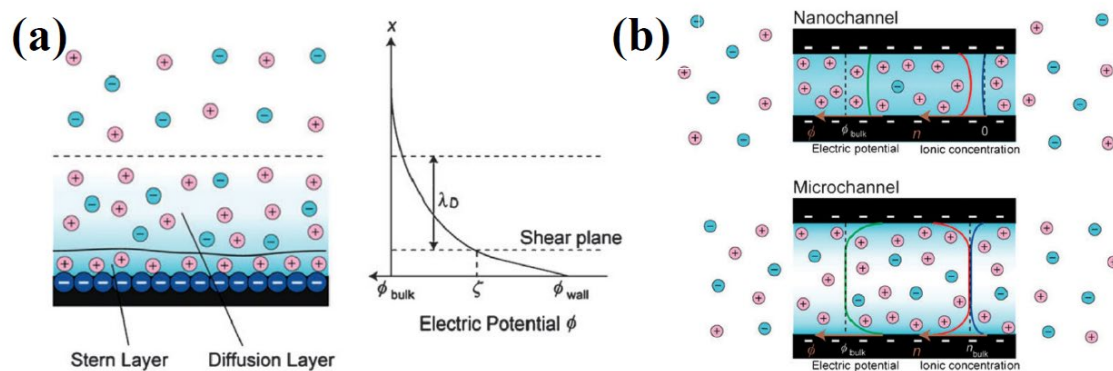


**Figure 8.** (a) Schematics showing the distribution of ions in a flat surface. Distribution of electric potential as a function of distance from the surface. The electric potential decays exponentially within Debye length. (b) The ion distribution in a nanochannel is almost unipolar in nature because its dimensions are smaller than the Debye length. In the case of nanochannels the electric potential even at the centre of the channel is influenced by the surface charge. Note that the concentration of the cations are higher in the nanochannels compared to anions. However, in the case of microchannels where the diameter is higher than that of Debye length, the electric potential rapidly drops to its bulk value and hence it shows similar concentrations of anions and cations within it. Reproduced with permission from reference 67. Copyright 2010, Royal Society of Chemistry.

**1.1.5.1 Surface Charge Modulation and Charge Reversal in Nanopores.** The surface charge in nanochannels have been typically modulated by attaching certain charge bearing group(s) such as quaternium ammonium<sup>70</sup>, viologen groups<sup>72</sup> etc. For instance, Omar Azzaroni *et al.* have used phosphate-bearing polymer brushes that shows pH

responsive charging to modulate the surface charge inside the pores of SBA-16 thin films and therefore modulate their perm selective properties (Figure 9).<sup>73</sup> The pKa of these phosphate groups are 7.7 and 4.5, therefore, below 4.5 the phosphate groups are unionized giving a non-selective ion transport. However, at pH 5 the surface becomes negatively charged owing to the ionization of phosphate groups and the channels show strong cation selective transport.

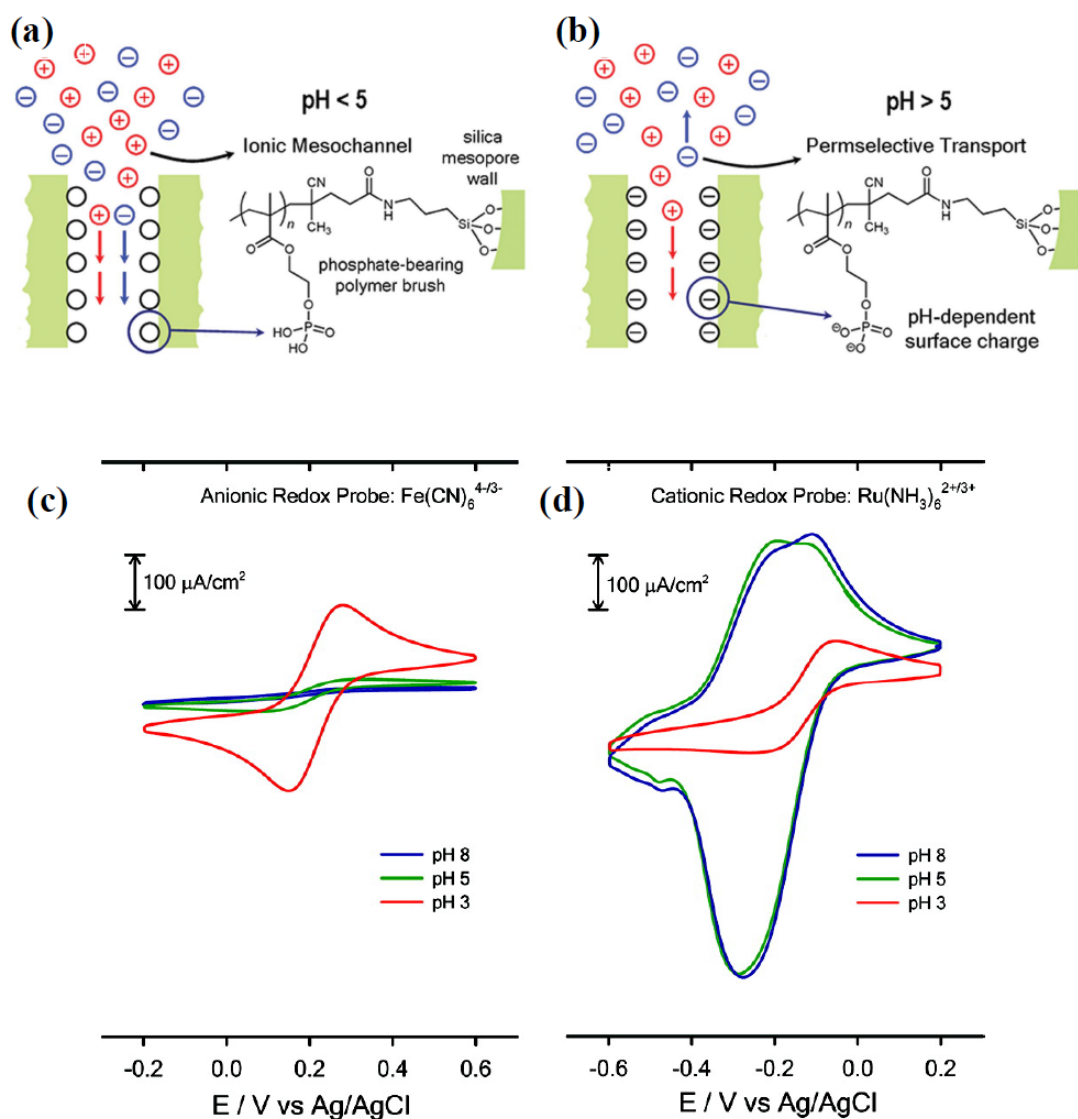


**Figure 9.** Schematic representation of the inner environment of the phosphate-bearing polymer brush attached mesoporous silica film. (a) In the case of pH < 5, the phosphate groups are protonated and the nanochannels show no perm selectivity. (b) For pH > 5, the ionization of phosphate groups give rise to negative surface charge inside the channels therefore they show strong cation selective transport. Comparative cyclic voltammograms displaying the molecular transport through PMEP-modified



mesoporous thin films as a function of pH using (c)  $\text{Fe}(\text{CN})_6^{3-}$  as an anionic redox probe and (d)  $\text{Ru}(\text{NH}_3)_6^{3+}$  as a cationic redox probe. Reproduced with permission from reference 73. Copyright 2012, American Chemical Society.

It is possible to switch the surface charge of nanochannels from one state to other by functionalizing them with molecules capable of switching the charge between positive and negative in response to various stimuli such as pH,<sup>74-77</sup> light,<sup>78-80</sup> redox<sup>81</sup> etc. (a stimuli responsive charge reversal). This in turn give rise to switchable ion transport which is important for various applications. Harry L. Anderson *et al.* demonstrated a pH responsive charge reversal surface by attaching aminodicarboxylic acid units to fused porous silica surfaces (Figure 10).<sup>82</sup> The anionic and cationic dye adsorption capabilities of these surface was studied to identify the charge reversal. At the acidic pH of around 1, the surface became positively charged owing to the protonation of tertiary amine groups. At this ionic state, the surface shows enhanced anionic dye adsorption through electrostatic attraction. On the other hand, the surface becomes negatively charged at pH 7 due to ionization of carboxylic acid groups. At this pH the surface shows enhanced adsorption for cationic dyes.

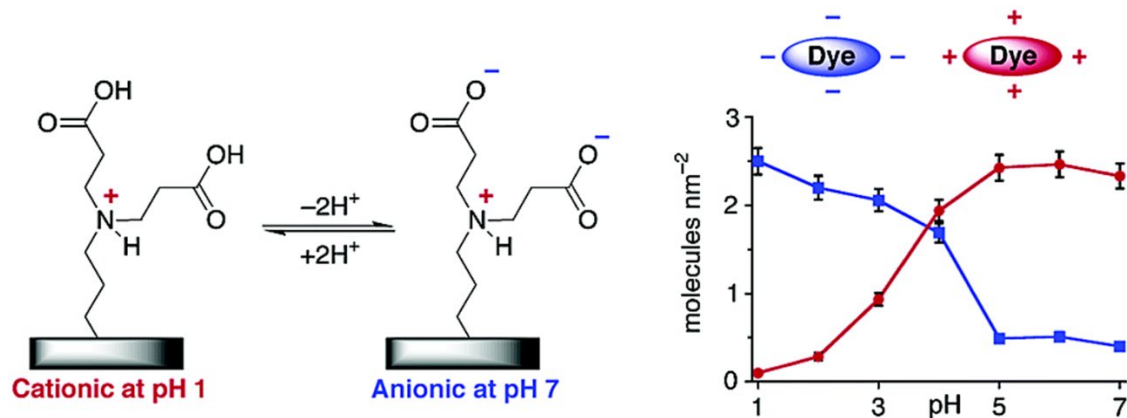


**Figure 10.** Schematic representation of fused porous silica surfaces designed for the pH responsive charge reversal. The pH dependent cationic and anionic dye adsorption to this surface. Reproduced with permission from reference 82. Copyright 2003, American Chemical Society.

It is also possible to achieve charge reversal through hetero-functionalization strategy. In this approach two or more types of molecules are anchored to the surface to synergistically achieve certain total surface charge.<sup>83-84</sup> The magnitude of the total charge can be easily modulated via controlling the ration of charge bearing molecules. For

example, Pavan *et al.* have demonstrated a hetero-functionalization approach to create a dual stimuli responsive (pH and glucose) charge reversal mesoporous surface.<sup>85</sup> This was achieved by functionalizing mesoporous silica with propylamine and phenylboronic acid groups in a 1:1 ratio (Figure 11). At pH 3, the surface is highly positive owing to the protonation of amine groups and it can be switched to negative upon increasing the pH to 9 where the phenylboronic acid groups start to ionize due to the binding of hydroxyl ions. Further, the surface ionization can be modulated via addition of glucose which binds to phenylboronic acid and lower the pKa of the ionization equilibrium. Therefore the negative surface could readily be obtained at much lower pH (ca. 7.4).

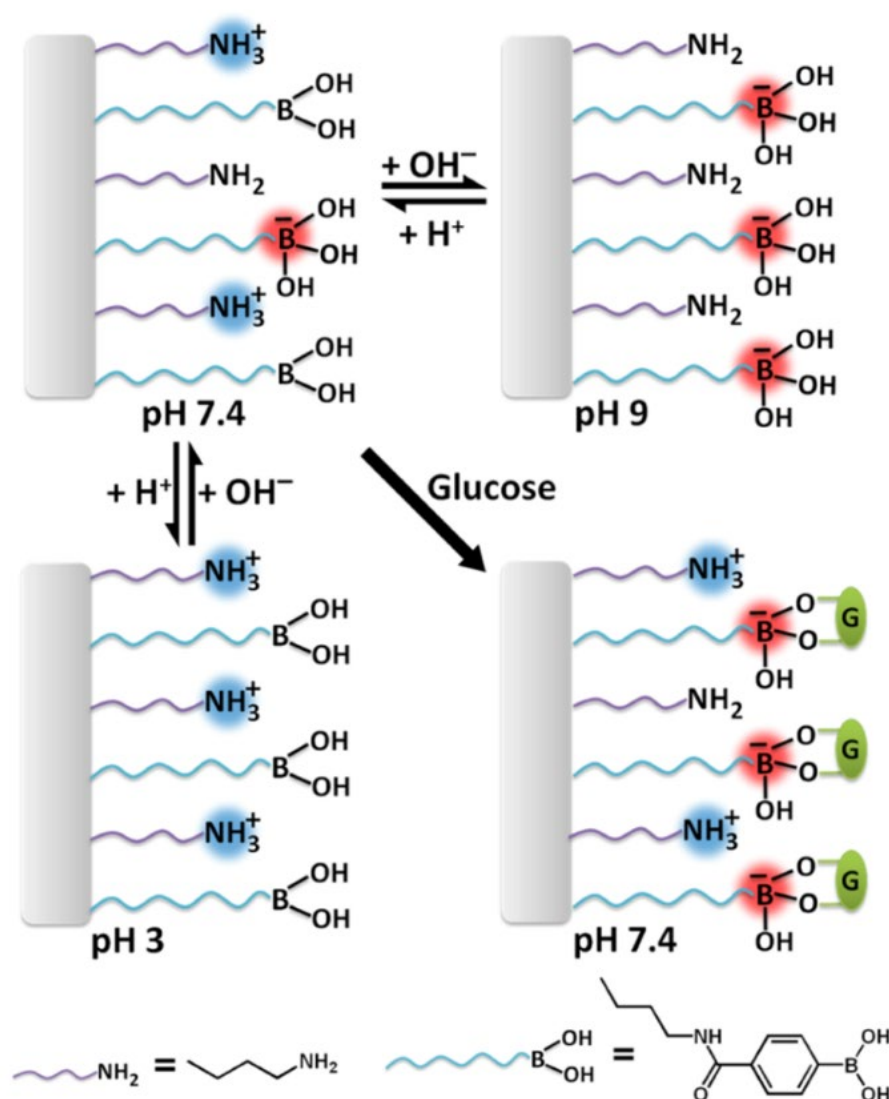


**Figure 11.** Schematic representation of dual mode charge reversal in a hetero-functionalized mesoporous silica. Reproduced with permission from reference 85. Copyright 2014, American Chemical Society.

### 1.1.6. Covalent and Non-covalent Approaches for Surface Functionalization.

Typically, post-synthetic surface modification in mesoporous silica have been carried out via covalent routes utilizing organically modified silanes to condense to the silica surface.<sup>86</sup> Desired surface charge can be achieved by wisely selecting silanes.<sup>70, 72</sup> Further, already attached organic functional groups on the surface of mesoporous silica can be used to perform regular organic modifications such as EDC coupling<sup>85</sup>, O-alkylation<sup>87</sup>, thiol-ene reaction<sup>88</sup> etc. to bring respective motifs on to the surface. Covalent modifications provide stable irreversible surface groups. However, this route provide no room for further manoeuvrability with custom designed functionalities.

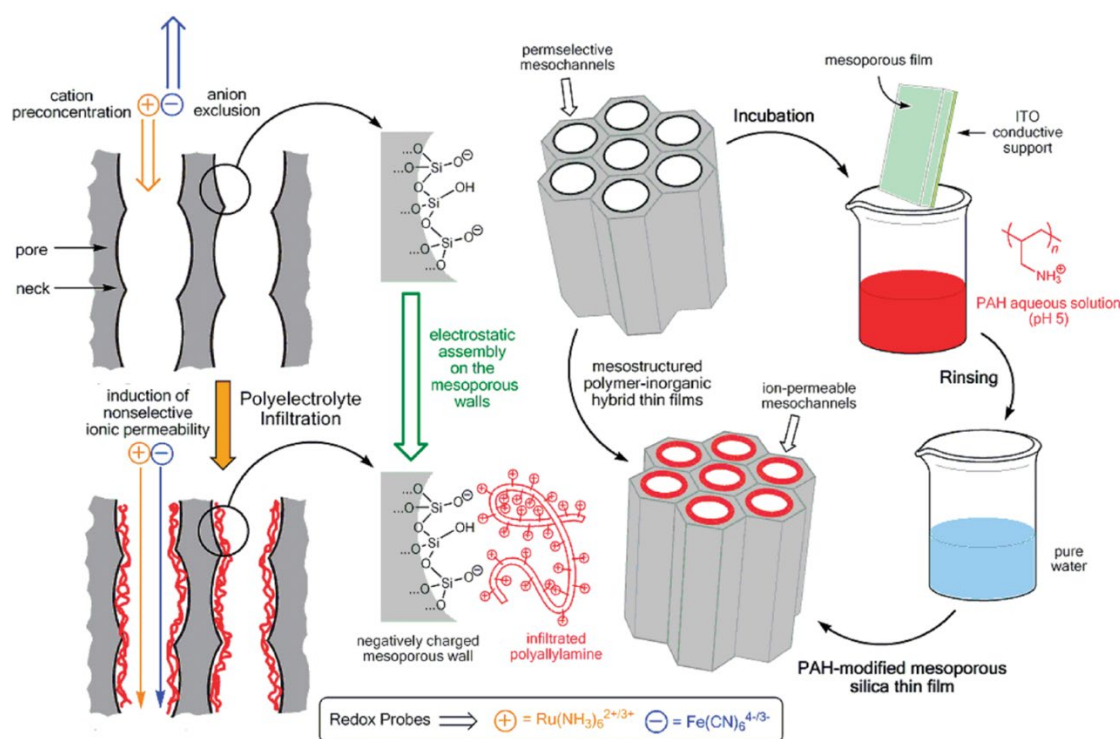


**Figure 12.** Schematic representation of infiltration of polyallylamine (PAH) inside the mesoporous silica nanochannels leading to the electrostatic assembly of the polyelectrolyte on the pore surface and subsequently the perm selectivity is influenced. Reproduced with permission from reference 90. Copyright 2011, American Chemical Society.

Recently, non-covalent approaches have been gaining increased attention towards reversible and dynamic surface functionalization.<sup>62, 89</sup> Omar Azzaroni *et al.* showed the use of electrostatic assembly of polyelectrolytes to manipulate the ion transport through mesoporous silica nanochannels (Figure 12).<sup>90</sup> The as-synthesized

mesoporous silica nanochannels are negatively charged due to the ionized silanol groups, thus showing a strong cation selective transport. However, the infiltration of cationic polyelectrolyte (poly(allylamine hydrochloride)) neutralizes the silica surface via electrostatic self-assembly which leads to the non-selective (allow both positive and negative ions) ion transport. Owing to the reversible nature of the assembly, this system could be switched between two ionic states through simple washing and re-assembly, hence, demonstrate high reversibility and post-synthetic flexibility.

### 1.1.7. Conclusions

In summary, surface engineering of mesoporous silica with suitable functionalities to precisely regulate the mass transport has broadened the scope of their applications in various fields such as adsorption, sensing, separation, photonics, drug delivery etc. The control of molecular transport through the mesopores can be achieved by physically blocking the pore and by manipulating parameters such as pore size, pore philicity and pore surface charge through surface functionalization. The traditional approaches towards surface functionalization of silica are based on covalent routes and utilize silane condensation strategy. Covalent routes render the pore surface with irreversible modifications. There are few reports on non-covalent approaches towards the reversible functionalization of mesoporous silica which is expected to elevate their application arena.

### 1.1.8. References

- (1) Valentin Valtchev, S. M., Michael Tsapatsis. *Ordered Porous Solids: Recent Advances and Prospects*, 1 ed.; Elsevier Science: 2008.
- (2) Occelli, M. L. *Synthesis of Porous Materials: Zeolites: Clays, and Nanostructures*, 1 ed.; CRC Press 1996.
- (3) Davis, M. E. Ordered porous materials for emerging applications. *Nature* **2002**, *417* (6891), 813-821.
- (4) Barton, T. J.; Bull, L. M.; Klemperer, W. G.; Loy, D. A.; McEnaney, B.; Misono, M.; Monson, P. A.; Pez, G.; Scherer, G. W.; Vartuli, J. C.; Yaghi, O. M. Tailored Porous Materials. *Chem. Mater.* **1999**, *11* (10), 2633-2656.
- (5) Slater, A. G.; Cooper, A. I. Function-led design of new porous materials. *Science* **2015**, *348* (6238), aaa8075.

- (6) Yang, P.; Gai, S.; Lin, J. Functionalized mesoporous silica materials for controlled drug delivery. *Chem. Soc. Rev.* **2012**, *41* (9), 3679-3698.
- (7) Rosenholm, J. M.; Sahlgren, C.; Lindén, M. Towards multifunctional, targeted drug delivery systems using mesoporous silica nanoparticles – opportunities & challenges. *Nanoscale* **2010**, *2* (10), 1870-1883.
- (8) Wu, S.-H.; Mou, C.-Y.; Lin, H.-P. Synthesis of mesoporous silica nanoparticles. *Chem. Soc. Rev.* **2013**, *42* (9), 3862-3875.
- (9) Lu, J.; Liong, M.; Li, Z.; Zink, J. I.; Tamanoi, F. Biocompatibility, Biodistribution, and Drug-Delivery Efficiency of Mesoporous Silica Nanoparticles for Cancer Therapy in Animals. *Small* **2010**, *6* (16), 1794-1805.
- (10) Li, Z.; Barnes, J. C.; Bosoy, A.; Stoddart, J. F.; Zink, J. I. Mesoporous silica nanoparticles in biomedical applications. *Chem. Soc. Rev.* **2012**, *41* (7), 2590-2605.
- (11) Chen, C.-Y.; Li, H.-X.; Davis, M. E. Studies on mesoporous materials: I. Synthesis and characterization of MCM-41. *Microporous Mat.* **1993**, *2* (1), 17-26.
- (12) Trewyn, B. G.; Slowing, I. I.; Giri, S.; Chen, H.-T.; Lin, V. S. Y. Synthesis and Functionalization of a Mesoporous Silica Nanoparticle Based on the Sol–Gel Process and Applications in Controlled Release. *Acc. Chem. Res.* **2007**, *40* (9), 846-853.
- (13) Vallet-Regí, M.; Balas, F.; Arcos, D. Mesoporous Materials for Drug Delivery. *Angew. Chem. Int. Ed.* **2007**, *46* (40), 7548-7558.
- (14) Slowing, I. I.; Vivero-Escoto, J. L.; Wu, C.-W.; Lin, V. S. Y. Mesoporous silica nanoparticles as controlled release drug delivery and gene transfection carriers. *Adv. Drug Deliv. Rev.* **2008**, *60* (11), 1278-1288.
- (15) Slowing, I. I.; Trewyn, B. G.; Giri, S.; Lin, V. S.-Y. Mesoporous Silica Nanoparticles for Drug Delivery and Biosensing Applications. *Adv. Funct. Mater.* **2007**, *17* (8), 1225-1236.
- (16) Tang, F.; Li, L.; Chen, D. Mesoporous Silica Nanoparticles: Synthesis, Biocompatibility and Drug Delivery. *Adv. Mater.* **2012**, *24* (12), 1504-1534.
- (17) Sancenón, F.; Pascual, L.; Oroval, M.; Aznar, E.; Martínez-Máñez, R. Gated Silica Mesoporous Materials in Sensing Applications. *ChemistryOpen* **2015**, *4* (4), 418-437.

- 
- 
- (18) Jiao, F.; Frei, H. Nanostructured Cobalt Oxide Clusters in Mesoporous Silica as Efficient Oxygen-Evolving Catalysts. *Angew. Chem. Int. Ed.* **2009**, *48* (10), 1841-1844.
- (19) Joo, S. H.; Park, J. Y.; Tsung, C.-K.; Yamada, Y.; Yang, P.; Somorjai, G. A. Thermally stable Pt/mesoporous silica core-shell nanocatalysts for high-temperature reactions. *Nat. Mater* **2008**, *8*, 126.
- (20) Liu, W.; Liu, J.; Yang, X.; Wang, K.; Wang, Q.; Yang, M.; Li, L.; Song, C. Phosphate modulated permeability of mesoporous silica spheres: a biomimetic ion channel decorated compartment model. *J. Mater. Chem. B* **2015**, *3* (2), 323-329.
- (21) Liu, W.; Yang, X.; He, D.; He, L.; Li, L.; Liu, Y.; Liu, J.; Wang, K. Dopamine modulated ionic permeability in mesoporous silica sphere based biomimetic compartment. *Colloids Surf. B* **2016**, *142*, 266-271.
- (22) Aznar, E.; Oroval, M.; Pascual, L.; Murguía, J. R.; Martínez-Máñez, R.; Sancenón, F. Gated Materials for On-Command Release of Guest Molecules. *Chem. Rev.* **2016**, *116* (2), 561-718.
- (23) Niedermayer, S.; Weiss, V.; Herrmann, A.; Schmidt, A.; Datz, S.; Müller, K.; Wagner, E.; Bein, T.; Bräuchle, C. Multifunctional polymer-capped mesoporous silica nanoparticles for pH-responsive targeted drug delivery. *Nanoscale* **2015**, *7* (17), 7953-7964.
- (24) Luo, Z.; Cai, K.; Hu, Y.; Zhao, L.; Liu, P.; Duan, L.; Yang, W. Mesoporous Silica Nanoparticles End-Capped with Collagen: Redox-Responsive Nanoreservoirs for Targeted Drug Delivery. *Angew. Chem. Int. Ed.* **2011**, *50* (3), 640-643.
- (25) Guillet-Nicolas, R.; Popat, A.; Bridot, J.-L.; Monteith, G.; Qiao, S. Z.; Kleitz, F. pH-Responsive Nutraceutical-Mesoporous Silica Nanoconjugates with Enhanced Colloidal Stability. *Angew. Chem. Int. Ed.* **2013**, *52* (8), 2318-2322.
- (26) Sun, Y.-L.; Yang, B.-J.; Zhang, S. X.-A.; Yang, Y.-W. Cucurbit[7]uril Pseudorotaxane-Based Photoresponsive Supramolecular Nanovalve. *Chem.: Eur. J* **2012**, *18* (30), 9212-9216.
- (27) Li, Q.-L.; Wang, L.; Qiu, X.-L.; Sun, Y.-L.; Wang, P.-X.; Liu, Y.; Li, F.; Qi, A.-D.; Gao, H.; Yang, Y.-W. Stimuli-responsive biocompatible nanovalves based on  $\beta$ -cyclodextrin modified poly(glycidyl methacrylate). *Chem.: Eur. J* **2014**, *5* (10), 3389-3395.

- (28) Vivero-Escoto, J. L.; Slowing, I. I.; Wu, C.-W.; Lin, V. S. Y. Photoinduced Intracellular Controlled Release Drug Delivery in Human Cells by Gold-Capped Mesoporous Silica Nanosphere. *J. Am. Chem. Soc.* **2009**, *131* (10), 3462-3463.
- (29) Muhammad, F.; Guo, M.; Qi, W.; Sun, F.; Wang, A.; Guo, Y.; Zhu, G. pH-Triggered Controlled Drug Release from Mesoporous Silica Nanoparticles via Intracellular Dissolution of ZnO Nanolids. *J. Am. Chem. Soc.* **2011**, *133* (23), 8778-8781.
- (30) Gan, Q.; Lu, X.; Yuan, Y.; Qian, J.; Zhou, H.; Lu, X.; Shi, J.; Liu, C. A magnetic, reversible pH-responsive nanogated ensemble based on Fe<sub>3</sub>O<sub>4</sub> nanoparticles-capped mesoporous silica. *Biomaterials* **2011**, *32* (7), 1932-1942.
- (31) Chen, P.-J.; Hu, S.-H.; Hsiao, C.-S.; Chen, Y.-Y.; Liu, D.-M.; Chen, S.-Y. Multifunctional magnetically removable nanogated lids of Fe<sub>3</sub>O<sub>4</sub>-capped mesoporous silica nanoparticles for intracellular controlled release and MR imaging. *J. Mater. Chem.* **2011**, *21* (8), 2535-2543.
- (32) Alberti, S.; Soler-Illia, G. J. A. A.; Azzaroni, O. Gated supramolecular chemistry in hybrid mesoporous silica nanoarchitectures: controlled delivery and molecular transport in response to chemical, physical and biological stimuli. *Chem. Commun.* **2015**, *51* (28), 6050-6075.
- (33) Chen, Z.; Cui, Z.-M.; Cao, C.-Y.; He, W.-D.; Jiang, L.; Song, W.-G. Temperature-Responsive Smart Nanoreactors: Poly(N-isopropylacrylamide)-Coated Au@Mesoporous-SiO<sub>2</sub> Hollow Nanospheres. *Langmuir* **2012**, *28* (37), 13452-13458.
- (34) Zhao, R.; Hu, J.; Niu, C.; Li, Y.; Hu, M.; Liu, R.; Li, S. A smart nanoreactor with photo-responsive molecular switches for controlling catalytic reactions. *J. Mater. Chem. C* **2016**, *4* (21), 4748-4755.
- (35) Zhang, Y.; Ang, C. Y.; Li, M.; Tan, S. Y.; Qu, Q.; Luo, Z.; Zhao, Y. Polymer-Coated Hollow Mesoporous Silica Nanoparticles for Triple-Responsive Drug Delivery. *ACS Appl. Mater. Interfaces* **2015**, *7* (32), 18179-18187.
- (36) Tian, B.; Liu, S.; Wu, S.; Lu, W.; Wang, D.; Jin, L.; Hu, B.; Li, K.; Wang, Z.; Quan, Z. pH-responsive poly (acrylic acid)-gated mesoporous silica and its application in oral colon targeted drug delivery for doxorubicin. *Colloids Surf. B* **2017**, *154*, 287-296.

- 
- 
- (37) Schlossbauer, A.; Warncke, S.; Gramlich, P. M. E.; Kecht, J.; Manetto, A.; Carell, T.; Bein, T. A Programmable DNA-Based Molecular Valve for Colloidal Mesoporous Silica. *Angew. Chem. Int. Ed.* **2010**, *49* (28), 4734-4737.
- (38) Zhang, P.; Cheng, F.; Zhou, R.; Cao, J.; Li, J.; Burda, C.; Min, Q.; Zhu, J.-J. DNA-Hybrid-Gated Multifunctional Mesoporous Silica Nanocarriers for Dual-Targeted and MicroRNA-Responsive Controlled Drug Delivery. *Angew. Chem. Int. Ed.* **2014**, *53* (9), 2371-2375.
- (39) Bringas, E.; Köysüren, Ö.; Quach, D. V.; Mahmoudi, M.; Aznar, E.; Roehling, J. D.; Marcos, M. D.; Martínez-Mañez, R.; Stroeve, P. Triggered release in lipid bilayer-capped mesoporous silica nanoparticles containing SPION using an alternating magnetic field. *Chem. Commun.* **2012**, *48* (45), 5647-5649.
- (40) Han, N.; Zhao, Q.; Wan, L.; Wang, Y.; Gao, Y.; Wang, P.; Wang, Z.; Zhang, J.; Jiang, T.; Wang, S. Hybrid Lipid-Capped Mesoporous Silica for Stimuli-Responsive Drug Release and Overcoming Multidrug Resistance. *ACS Appl. Mater. Interfaces* **2015**, *7* (5), 3342-3351.
- (41) Yang, J.; He, W.-D.; He, C.; Tao, J.; Chen, S.-Q.; Niu, S.-M.; Zhu, S.-L. Hollow mesoporous silica nanoparticles modified with coumarin-containing copolymer for photo-modulated loading and releasing guest molecule. *J. Polym. Sci., Part A: Polym. Chem.* **2013**, *51* (18), 3791-3799.
- (42) He, D.; He, X.; Wang, K.; Cao, J.; Zhao, Y. A Light-Responsive Reversible Molecule-Gated System Using Thymine-Modified Mesoporous Silica Nanoparticles. *Langmuir* **2012**, *28* (8), 4003-4008.
- (43) Ferris, D. P.; Zhao, Y.-L.; Khashab, N. M.; Khatib, H. A.; Stoddart, J. F.; Zink, J. I. Light-Operated Mechanized Nanoparticles. *J. Am. Chem. Soc.* **2009**, *131* (5), 1686-1688.
- (44) Mei, X.; Yang, S.; Chen, D.; Li, N.; Li, H.; Xu, Q.; Ge, J.; Lu, J. Light-triggered reversible assemblies of azobenzene-containing amphiphilic copolymer with  $\beta$ -cyclodextrin-modified hollow mesoporous silica nanoparticles for controlled drug release. *Chem. Commun.* **2012**, *48* (80), 10010-10012.
- (45) Yi, S.; Zheng, J.; Lv, P.; Zhang, D.; Zheng, X.; Zhang, Y.; Liao, R. Controlled Drug Release from Cyclodextrin-Gated Mesoporous Silica Nanoparticles Based on Switchable Host-Guest Interactions. *Bioconjugate Chem.* **2018**, *29* (9), 2884-2891.



- (46) Angelos, S.; Yang, Y.-W.; Patel, K.; Stoddart, J. F.; Zink, J. I. pH-Responsive Supramolecular Nanovalves Based on Cucurbit[6]uril Pseudorotaxanes. *Angew. Chem. Int. Ed.* **2008**, *47* (12), 2222-2226.
- (47) Lee, S.-F.; Zhu, X.-M.; Wang, Y.-X. J.; Xuan, S.-H.; You, Q.; Chan, W.-H.; Wong, C.-H.; Wang, F.; Yu, J. C.; Cheng, C. H. K.; Leung, K. C.-F. Ultrasound, pH, and Magnetically Responsive Crown-Ether-Coated Core/Shell Nanoparticles as Drug Encapsulation and Release Systems. *ACS Appl. Mater. Interfaces* **2013**, *5* (5), 1566-1574.
- (48) Nguyen, T. D.; Leung, K. C. F.; Liong, M.; Pentecost, C. D.; Stoddart, J. F.; Zink, J. I. Construction of a pH-Driven Supramolecular Nanovalve. *Org. Lett.* **2006**, *8* (15), 3363-3366.
- (49) Huang, X.; Du, X. Pillar[6]arene-Valved Mesoporous Silica Nanovehicles for Multiresponsive Controlled Release. *ACS Appl. Mater. Interfaces* **2014**, *6* (22), 20430-20436.
- (50) Sun, Y.-L.; Yang, Y.-W.; Chen, D.-X.; Wang, G.; Zhou, Y.; Wang, C.-Y.; Stoddart, J. F. Mechanized Silica Nanoparticles Based on Pillar[5]arenes for On-Command Cargo Release. *Small* **2013**, *9* (19), 3224-3229.
- (51) Liu, R.; Zhang, Y.; Zhao, X.; Agarwal, A.; Mueller, L. J.; Feng, P. pH-Responsive Nanogated Ensemble Based on Gold-Capped Mesoporous Silica through an Acid-Labile Acetal Linker. *J. Am. Chem. Soc.* **2010**, *132* (5), 1500-1501.
- (52) Yang, Y.; Lin, Y.; Di, D.; Zhang, X.; Wang, D.; Zhao, Q.; Wang, S. Gold nanoparticle-gated mesoporous silica as redox-triggered drug delivery for chemo-photothermal synergistic therapy. *J. Colloid Interface Sci.* **2017**, *508*, 323-331.
- (53) Lai, C.-Y.; Trewyn, B. G.; Jeftinija, D. M.; Jeftinija, K.; Xu, S.; Jeftinija, S.; Lin, V. S. Y. A Mesoporous Silica Nanosphere-Based Carrier System with Chemically Removable CdS Nanoparticle Caps for Stimuli-Responsive Controlled Release of Neurotransmitters and Drug Molecules. *J. Am. Chem. Soc.* **2003**, *125* (15), 4451-4459.
- (54) Wu, Z.; Zhao, D. Ordered mesoporous materials as adsorbents. *Chem. Commun.* **2011**, *47* (12), 3332-3338.

- 
- 
- (55) Antochshuk, V.; Olkhovyk, O.; Jaroniec, M.; Park, I.-S.; Ryoo, R. Benzoylthiourea-Modified Mesoporous Silica for Mercury(II) Removal. *Langmuir* **2003**, *19* (7), 3031-3034.
- (56) Zhang, L.; Zhang, W.; Shi, J.; Hua, Z.; Li, Y.; Yan, J. A new thioether functionalized organic–inorganic mesoporous composite as a highly selective and capacious Hg<sup>2+</sup> adsorbent. *Chem. Commun.* **2003**, (2), 210-211.
- (57) Feng, X.; Fryxell, G. E.; Wang, L.-Q.; Kim, A. Y.; Liu, J.; Kemner, K. M. Functionalized Monolayers on Ordered Mesoporous Supports. *Science* **1997**, *276* (5314), 923-926.
- (58) Algarra, M.; Jiménez, M. V.; Rodríguez-Castellón, E.; Jiménez-López, A.; Jiménez-Jiménez, J. Heavy metals removal from electroplating wastewater by aminopropyl-Si MCM-41. *Chemosphere* **2005**, *59* (6), 779-786.
- (59) Benitez, M.; Das, D.; Ferreira, R.; Pischel, U.; García, H. Urea-Containing Mesoporous Silica for the Adsorption of Fe(III) Cations. *Chem. Mater.* **2006**, *18* (23), 5597-5603.
- (60) Jiang, Y.; Gao, Q.; Yu, H.; Chen, Y.; Deng, F. Intensively competitive adsorption for heavy metal ions by PAMAM-SBA-15 and EDTA-PAMAM-SBA-15 inorganic–organic hybrid materials. *Microporous Mesoporous Mater.* **2007**, *103* (1), 316-324.
- (61) Heidari, A.; Younesi, H.; Mehraban, Z. Removal of Ni(II), Cd(II), and Pb(II) from a ternary aqueous solution by amino functionalized mesoporous and nano mesoporous silica. *Chem. Eng. J.* **2009**, *153* (1), 70-79.
- (62) Kumar, B. V. V. S. P.; Rao, K. V.; Soumya, T.; George, S. J.; Eswaramoorthy, M. Adaptive Pores: Charge Transfer Modules as Supramolecular Handles for Reversible Pore Engineering of Mesoporous Silica. *J. Am. Chem. Soc.* **2013**, *135* (30), 10902-10905.
- (63) Singh, D. K.; Pavan Kumar, B. V. V. S.; Eswaramoorthy, M. Reversible control of pore size and surface chemistry of mesoporous silica through dynamic covalent chemistry: philicity mediated catalysis. *Nanoscale* **2015**, *7* (32), 13358-13362.
- (64) Sparreboom, W.; van den Berg, A.; Eijkel, J. C. T. Principles and applications of nanofluidic transport. *Nat. Nanotechnol.* **2009**, *4*, 713.

- (65) Karnik, R.; Fan, R.; Yue, M.; Li, D.; Yang, P.; Majumdar, A. Electrostatic Control of Ions and Molecules in Nanofluidic Transistors. *Nano Lett.* **2005**, *5* (5), 943-948.
- (66) Stein, D.; Kruithof, M.; Dekker, C. Surface-Charge-Governed Ion Transport in Nanofluidic Channels. *Phys. Rev. Lett.* **2004**, *93* (3), 035901.
- (67) Daiguji, H. Ion transport in nanofluidic channels. *Chem. Soc. Rev.* **2010**, *39* (3), 901-911.
- (68) Pérez-Mitta, G.; Albesa, A. G.; Knoll, W.; Trautmann, C.; Toimil-Molares, M. E.; Azzaroni, O. Host-guest supramolecular chemistry in solid-state nanopores: potassium-driven modulation of ionic transport in nanofluidic diodes. *Nanoscale* **2015**, *7* (38), 15594-15598.
- (69) Li, M.; Harbron, R. L.; Weaver, J. V. M.; Binks, B. P.; Mann, S. Electrostatically gated membrane permeability in inorganic protocells. *Nat. Chem.* **2013**, *5*, 529.
- (70) Lee, C.-H.; Lo, L.-W.; Mou, C.-Y.; Yang, C.-S. Synthesis and Characterization of Positive-Charge Functionalized Mesoporous Silica Nanoparticles for Oral Drug Delivery of an Anti-Inflammatory Drug. *Adv. Funct. Mater.* **2008**, *18* (20), 3283-3292.
- (71) Daiguji, H.; Yang, P.; Szeri, A. J.; Majumdar, A. Electrochemomechanical Energy Conversion in Nanofluidic Channels. *Nano Lett.* **2004**, *4* (12), 2315-2321.
- (72) Kumar, B. V. V. S. P.; Sonu, K. P.; Rao, K. V.; Sampath, S.; George, S. J.; Eswaramoorthy, M. Supramolecular Switching of Ion-Transport in Nanochannels. *ACS Appl. Mater. Interfaces* **2018**, *10* (28), 23458-23465.
- (73) Brunsen, A.; Díaz, C.; Pietrasanta, L. I.; Yameen, B.; Ceolín, M.; Soler-Illia, G. J. A. A.; Azzaroni, O. Proton and Calcium-Gated Ionic Mesochannels: Phosphate-Bearing Polymer Brushes Hosted in Mesoporous Thin Films As Biomimetic Interfacial Architectures. *Langmuir* **2012**, *28* (7), 3583-3592.
- (74) Yameen, B.; Ali, M.; Neumann, R.; Ensinger, W.; Knoll, W.; Azzaroni, O. Single Conical Nanopores Displaying pH-Tunable Rectifying Characteristics. Manipulating Ionic Transport With Zwitterionic Polymer Brushes. *J. Am. Chem. Soc.* **2009**, *131* (6), 2070-2071.
- (75) Lee, S. B.; Martin, C. R. pH-Switchable, Ion-Permeable Gold Nanotubule Membrane Based on Chemisorbed Cysteine. *Anal. Chem.* **2001**, *73* (4), 768-775.

- 
- 
- (76) Ali, M.; Ramirez, P.; Mafé, S.; Neumann, R.; Ensinger, W. A pH-Tunable Nanofluidic Diode with a Broad Range of Rectifying Properties. *ACS Nano* **2009**, *3* (3), 603-608.
- (77) Yameen, B.; Ali, M.; Neumann, R.; Ensinger, W.; Knoll, W.; Azzaroni, O. Synthetic Proton-Gated Ion Channels via Single Solid-State Nanochannels Modified with Responsive Polymer Brushes. *Nano Lett.* **2009**, *9* (7), 2788-2793.
- (78) Brunsen, A.; Cui, J.; Ceolín, M.; Campo, A. d.; Soler-Illia, G. J. A. A.; Azzaroni, O. Light-activated gating and permselectivity in interfacial architectures combining “caged” polymer brushes and mesoporous thin films. *Chem. Commun.* **2012**, *48* (10), 1422-1424.
- (79) Wen, L.; Liu, Q.; Ma, J.; Tian, Y.; Li, C.; Bo, Z.; Jiang, L. Malachite Green Derivative-Functionalized Single Nanochannel: Light-and-pH Dual-Driven Ionic Gating. *Adv. Mater.* **2012**, *24* (46), 6193-6198.
- (80) Wang, G.; Bohaty, A. K.; Zharov, I.; White, H. S. Photon Gated Transport at the Glass Nanopore Electrode. *J. Am. Chem. Soc.* **2006**, *128* (41), 13553-13558.
- (81) Elbert, J.; Krohm, F.; Rüttiger, C.; Kienle, S.; Didzoleit, H.; Balzer, B. N.; Hugel, T.; Stühn, B.; Gallei, M.; Brunsen, A. Polymer-Modified Mesoporous Silica Thin Films for Redox-Mediated Selective Membrane Gating. *Adv. Funct. Mater.* **2014**, *24* (11), 1591-1601.
- (82) Matthews, J. R.; Tuncel, D.; Jacobs, R. M. J.; Bain, C. D.; Anderson, H. L. Surfaces Designed for Charge Reversal. *J. Am. Chem. Soc.* **2003**, *125* (21), 6428-6433.
- (83) Wang, Y.; Sun, Y.; Wang, J.; Yang, Y.; Li, Y.; Yuan, Y.; Liu, C. Charge-Reversal APTES-Modified Mesoporous Silica Nanoparticles with High Drug Loading and Release Controllability. *ACS Appl. Mater. Interfaces* **2016**, *8* (27), 17166-17175.
- (84) Fattakhova-Rohlfing, D.; Wark, M.; Rathouský, J. Ion-Permselective pH-Switchable Mesoporous Silica Thin Layers. *Chem. Mater.* **2007**, *19* (7), 1640-1647.
- (85) Kumar, B. V. V. S. P.; Salikolimi, K.; Eswaramoorthy, M. Glucose- and pH-Responsive Charge-Reversal Surfaces. *Langmuir* **2014**, *30* (16), 4540-4544.
- (86) Brühwiler, D. Postsynthetic functionalization of mesoporous silica. *Nanoscale* **2010**, *2* (6), 887-892.

- (87) Alauzun, J.; Mehdi, A.; Rey , C.; Corriu, R. Direct synthesis of ordered mesoporous silica containing iodopropyl groups. A useful function for chemical modifications. *New J. Chem.* **2007**, *31* (6), 911-915.
- (88) Shen, A.; Guo, Z.; Yu, L.; Cao, L.; Liang, X. A novel zwitterionic HILIC stationary phase based on “thiol-ene” click chemistry between cysteine and vinyl silica. *Chem. Commun.* **2011**, *47* (15), 4550-4552.
- (89) Carter, T. G.; Yantasee, W.; Sangvanich, T.; Fryxell, G. E.; Johnson, D. W.; Addleman, R. S. New functional materials for heavy metal sorption: “Supramolecular” attachment of thiols to mesoporous silica substrates. *Chem. Commun.* **2008**, (43), 5583-5585.
- (90) Brunsen, A.; Calvo, A.; Williams, F. J.; Soler-Illia, G. J. A. A.; Azzaroni, O. Manipulation of Molecular Transport into Mesoporous Silica Thin Films by the Infiltration of Polyelectrolytes. *Langmuir* **2011**, *27* (8), 4328-4333.

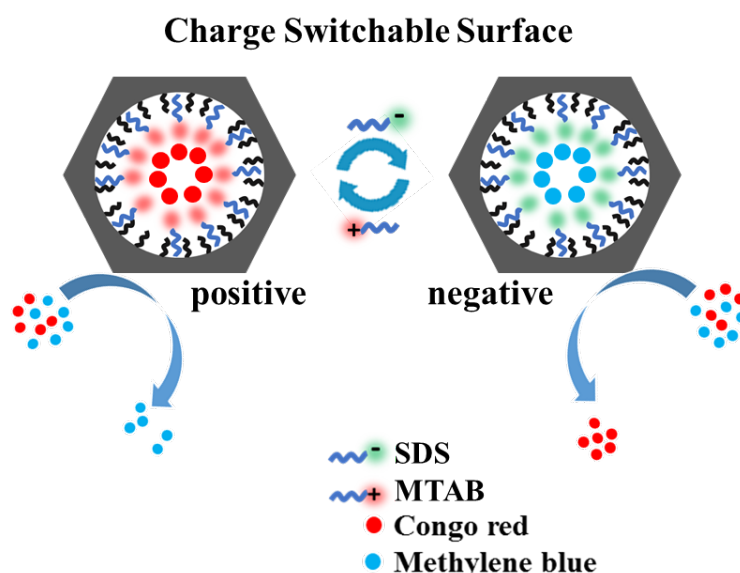


## Chapter-1.2

### *Simple Approach to Create Modular Charge Reversible Mesoporous Silica via Hydrophobic Anchoring of Ionic Amphiphiles*

#### **Summary:**

Charge reversible mesoporous silica surfaces have gained a great deal of interest in recent years due to their variety of applications. Conventional approach to create such charge reversal systems involves covalent attachment of charge bearing motifs on to the silica surface. However, the covalent chemistry often leads to irreversible pore modification limiting their wider applicability. Herein, we introduce a simple non-covalent strategy to modulate the surface charge of the mesoporous silica by making use of molecular assembly of ionic amphiphiles within the pores. The hexyl pendant groups covalently attached to the silica surface provides hydrophobic room for the facile assembly of charged amphiphiles. These charge-switchable surfaces were used for fast and selective adsorption of dyes from aqueous solutions.



Publication based on this work has appeared in *ACS Appl. Mater. Interfaces* **2017**, *9*, 9136-9142





### **1.2.1. Introduction**

Electrostatic modulation of molecular transport through charged pores finds a lot of interest in the field of environmental remediation<sup>1-3</sup>, sensing<sup>4</sup>, interface engineering<sup>5-6</sup> and drug delivery.<sup>7-9</sup> In recent years, mesoporous silica has emerged as an important class of charged scaffolds with the capability of modulating their surface charge.<sup>10-13</sup> This leads to the realization of various advanced applications compared to their conventional uses in adsorption and catalysis. The fabrication of mesoporous silica based charge reversal surface typically involves chemically attaching one or more charge bearing groups via post-synthetic grafting<sup>14</sup> or co-condensation approach.<sup>15</sup> In grafting, silanes of desired functionalities are used to modify the silica surface post synthesis. On the other hand, in co-condensation, the silane is used along with the silica precursor during the synthesis. The usual charge bearing functional groups are quaternary ammonium (for cationic surface)<sup>16</sup>, sulphonyl groups (anionic surface)<sup>17</sup> etc. In addition, stimuli responsive charging of surface could be achieved by using moieties such as amino acids,<sup>18</sup> viologen,<sup>19-20</sup> spiropyran<sup>21</sup> etc. Further, by choosing appropriate functional groups (or a combination of functional groups),<sup>22-24</sup> it is possible to achieve charge switchable surfaces. Nevertheless, these covalent approaches often modify the surface irreversibly and hence leave no room for the modulation after functionalization.

To overcome the inherent limitation associated with covalent functionalization, a few strategies have emerged in the recent past utilizing supramolecular interactions.<sup>25-27</sup> Recently, Pavan et al introduced a non-covalent design strategy based on redox responsive charge transfer (C-T) modules (viologen and pyranine derivatives).<sup>28</sup> Viologen, an electron acceptor was covalently attached to the mesoporous silica surface which gave rise to a cationic surface. By employing pyranine (an electron donor), they were able to show surface charge switching from cationic to anionic as a consequence of which, the ion transport properties also switched from anionic transport to cationic transport. The C-T interaction between donor and acceptor motifs could be broken by reducing the viologen using a mild reducing agent. Further, the C-T interactions could be re-established by oxidizing the viologen back to its electron deficient state. In addition, pH responsive ion transport was achieved in this system by supramolecularly attaching a pH responsive electron donor (coronene tetracarboxylic acid). This example demonstrates the significance of supramolecular approaches in achieving modular, flexible mesoporous silica. However, continuous redox cycles to switch the pore

characteristics could cause acceptor moieties to degrade over time, limiting its potential for recyclability over a large number of cycles. Thus, there exists a need for robust noncovalent strategies to enable the fabrication of highly reversible charge-convertible systems that can withstand a considerable number of cycles.

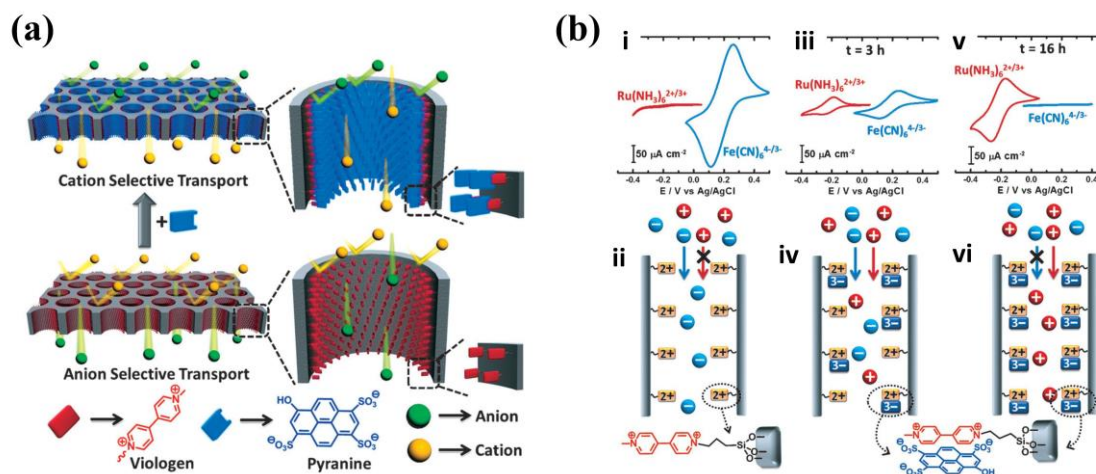
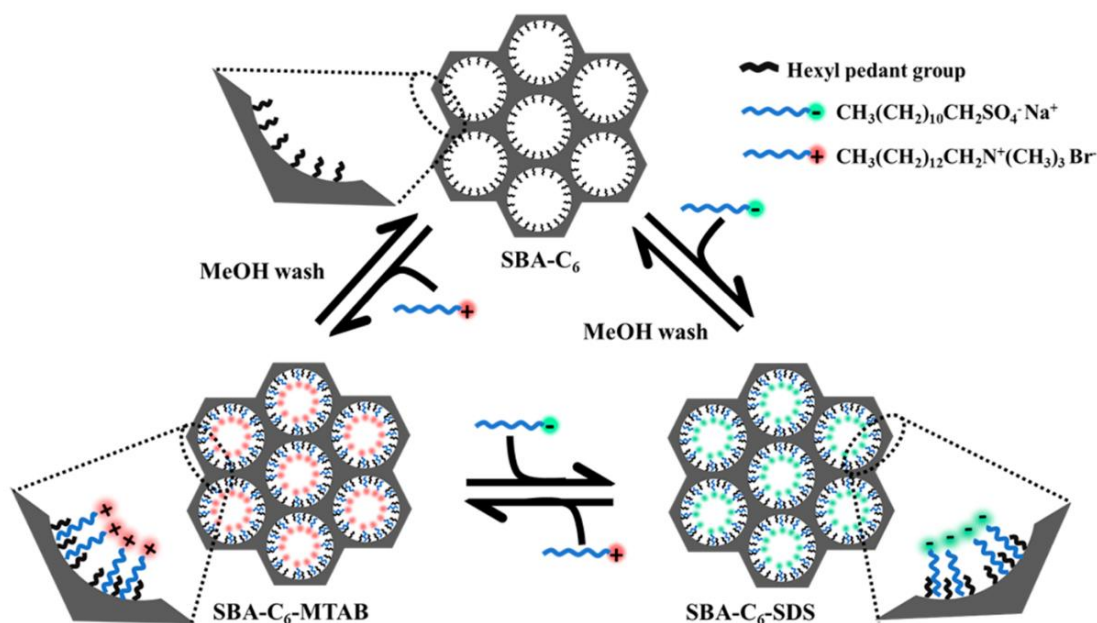


**Figure 1.** (a) Scheme showing the supramolecular functionalization of viologen modified nanopores with anionic donor- pyranine (coronene tetracarboxylic acid) to switch the ion-transport properties of mesopores from anion selective to cation selective. (b) Cyclic voltammograms of anionic and cationic electrochemical probes obtained using viologen functionalized mesoporous silica coated ITO as working electrode and corresponding schematics. Viologen modified mesoporous silica films before (i and ii) and after soaking in pyranine solution for 3 hours (iii and iv) and 16 hours (v and vi). Reproduced with permission from reference 28. Copyright 2013, Wiley-VCH (Germany).

### 1.2.2. Scope of the present investigation

In this chapter, we introduce a noncovalent approach utilizing hydrophobic interactions and charged amphiphiles (surfactants) to reversibly manipulate surface charge of mesoporous silica (Scheme 1). The silica surface modified with hexyl groups can noncovalently anchor the charged amphiphiles to the pore surface, by hydrophobic coassembly, to modulate the surface charge of the mesopores. Further, the surface charge of these materials can be reversibly modified by regeneration of the parent material by washing with a suitable solvent followed by reloading with an appropriate charged amphiphile. Due to the soft nature of the interactions and regenerative treatment, the system could demonstrate remarkable reversibility in switching the surface charge.



**Scheme 1.** (a) Non covalent functionalization of hexyl modified mesoporous silica. The charged amphiphiles (SDS or MTAB) self-assembled within the hydrophobic mesoporous channels. Reversible manipulation of surface charges is achieved by breaking the assembly in an appropriate solvent, which allows the pore form a new assembly. Conversion from one charge state to other is also possible through competitive amphiphile replacement.

### 1.2.3. Experimental section

**Synthesis of SBA- 15.** Monodispersed SBA- 15 rods were synthesized following a previously reported procedure.<sup>29</sup> In a typical synthesis procedure, a mixture containing 4.0 g of Pluronic P123, 30 g of water and 120 g of 2 M HCl aqueous solution in a Teflon-lined container was stirred at 35 °C overnight. To this mixture, 8.50 g of TEOS was added under vigorous stirring. After 5 min of stirring, the mixture was kept under static conditions at 35 °C for 20 h, after which the temperature was raised to 100 °C and maintained for 24 h. The solid product was collected via suction filtration and washed with copious amount of water. The white solid powder was dried at 60 °C over night before subjecting to calcination at 550 °C.

**Synthesis of SBA- C<sub>6</sub>.** 1 g of calcined mesoporous silica rod was degassed for 5 h under vacuum and dispersed in dry toluene (100 mL) under ultra-sonication. To this dispersion, 2 mL of trichloro(hexyl)silane (10 mmol) was added under N<sub>2</sub> bed and stirred overnight at room temperature. The obtained SBA- C<sub>6</sub> was washed with toluene (1 x 40 mL), and

ethanol (1 x 40 mL) and subjected to soxhlet extraction in ethanol for overnight. The product was dried at 60 °C for overnight under vacuum.

**Molecular assemblies of surfactant within mesoporous channel.** 50 mg of SBA- C<sub>6</sub> was dispersed in 300 μL of ethanol under sonication. To this dispersion, a 5 mL of aqueous solution of surfactant (10 mM, SDS or MTAB) was added. The mixture was stirred for 3 h at room temperature for surfactant self-assembly. The surfactant assembled SBA- C<sub>6</sub> was collected through centrifugation. The solid was washed with water (2 x 10 mL) and dried at 60 °C overnight.

**Disassembly of surfactant molecules from mesopores.** 50 mg of surfactant assembled SBA- C<sub>6</sub> (SBA-C<sub>6</sub>-SDS or SBA-C<sub>6</sub>-MTAB) was dispersed in 5 mL of methanol under sonication. The dispersion was heated at 60 °C under vigorous stirring for 30 min. The surfactant removed SBA- C<sub>6</sub> was collected via centrifugation. The solid was washed with water (2 x 10 mL) and dried at 60 °C overnight.

**Zeta potential measurements.** 10 mg of surfactant assembled SBA-C<sub>6</sub> (SBA-C<sub>6</sub>-MTAB or SBA-C<sub>6</sub>-SDS) was dispersed in 0.1 mL of ethanol under sonication for 2 min. This dispersion was diluted by adding 3 mL of water. The pH of the dispersion was measured using a pH meter before the zeta potential analysis. The temperature was always kept at 25 °C with the help of inbuilt thermostat in Zetasizer Nano ZS.

**Dye adsorption studies.** 10 mg of surfactant assembled SBA-C<sub>6</sub> (SBA-C<sub>6</sub>-MTAB or SBA-C<sub>6</sub>-SDS) was dispersed in 50 μL of ethanol. To this dispersion, a 950 μL of aqueous solutions containing known amount of the respective dye was added. The mixture was stirred at room temperature for 1 h. The dispersion was centrifuged to collect the solid product and washed extensively with a known volume of water. The supernatant solution was collected to quantify the amount of dye loading using UV-Vis spectroscopy.

**Calculation of hexyl pedant groups in SBA-C<sub>6</sub> and surfactant loading.** The weight of organic functionalization determined by TGA was utilized to calculate amount of hexyl pendant groups and surfactant loading.

Overall organic functionalization in SBA-C<sub>6</sub> is **13.65 wt %** (with respect to SBA-15)

Thus 1 g of SBA-C<sub>6</sub> contain 0.1365 g of organic functionalization.

Molecular weight of hexyl groups = **85.18 g/mol**.

## *Hydrophobic Anchoring of Ionic Amphiphiles*

---

Hexyl functionalization in terms of mmol per gram of SBA-15 = 0.1365/85.18

$$= \mathbf{1.6 \text{ mmol/g}}$$

Overall organic functionalization in SBA-C<sub>6</sub>-SDS is 18.52 %

Weight corresponding to SDS loading = 18.52 - 13.65

$$= \mathbf{4.87 \text{ wt \%}} \text{ (with respect to SBA-15)}$$

Thus 1 g of SBA-C<sub>6</sub>-SDS contain 0.0487 g of SDS.

Molecular weight of SDS = 288.37 g/mol.

Thus amount of SDS loading terms of mmol per gram of SBA-15 = 0.0338/288.37

$$= \mathbf{0.168 \text{ mmol/g}}$$

Similarly,

Overall organic functionalization in SBA-C<sub>6</sub>-MTAB is 25.44 %

Weight corresponding to MTAB loading = 25.44 - 13.65

$$= \mathbf{11.79 \text{ wt \%}} \text{ (with respect to SBA-15)}$$

Thus 1 g of SBA-C<sub>6</sub>-MTAB contain 0.1179 g of MTAB.

Molecular weight of MTAB = 336.39 g/mol.

Thus amount of MTAB loading terms of mmol per gram of SBA-15 = 0.1196/336.39

$$= \mathbf{0.350 \text{ mmol/g}}$$

### **Calculation of quantitative coverage of surfactants.**

In the case of SBA-C<sub>6</sub>:

Amount of hexyl groups = 1.6 mmol/g (From TGA measurements)

Number of molecules of hexyl groups = 1.6 mmol x N<sub>A</sub> /g

$$= 9.63 \times 10^{20} \text{ molecules/g}$$

Surface area of SBA-15 = 500 m<sup>2</sup>/g

$$= 500 \times 10^{18} \text{ nm}^2/\text{g}$$

Number of hexyl groups per nm<sup>2</sup> = 9.63 x 10<sup>20</sup> molecules / 500 x 10<sup>18</sup> nm<sup>2</sup>

$$= \mathbf{1.92 \text{ molecules/nm}^2}$$

In the case of SBA-C<sub>6</sub>-MTAB:

Amount of MTAB assembled to SBA-C<sub>6</sub> = 0.35 mmol/g (From TGA measurements)

Number of molecules of MTAB assembled to SBA-C<sub>6</sub> = 0.35 mmol x N<sub>A</sub> /g = 2.107 x 10<sup>20</sup> molecules/g

Number of MTAB molecules per nm<sup>2</sup> = 2.107 x 10<sup>20</sup> molecules / 500 x 10<sup>18</sup> nm<sup>2</sup>

= **0.421 molecules/nm<sup>2</sup>**

Quantitative coverage of MTAB assembly on SBA-C<sub>6</sub> = **22 %**

For SBA-C<sub>6</sub>-SDS:

Amount of SDS assembled to SBA-C<sub>6</sub> = 0.168 mmol/g (From TGA measurements)

Number of molecules of SDS assembled to SBA-C<sub>6</sub> = 0.168 mmol x N<sub>A</sub> /g

= 1.01 x 10<sup>20</sup> molecules/g

Number of SDS molecules per nm<sup>2</sup> = 1.01 x 10<sup>20</sup> molecules / 500 x 10<sup>18</sup> nm<sup>2</sup>

= **0.202 molecules/nm<sup>2</sup>**

Quantitative coverage of SDS assembly on SBA-C<sub>6</sub> = **11 %**

**Langmuir model for calculating binding constant.** The binding constant for the interaction of charged dye molecules with amphiphile assembled SBA-C<sub>6</sub> was calculated using Langmuir model of adsorption.<sup>30-32</sup> The Langmuir model is a good approximation for this case because of the following reasons:

1. The adsorption of charged dye molecules onto the oppositely charged scaffold follows surface neutralisation and hence a monolayer adsorption model (that consider the strong binding interactions between the adsorbent and adsorbate) would be ideal.
2. The adsorption sites are non-uniform in the case of functionalized mesoporous silica due to clustering of silane functionalization. Nevertheless, it could still be a reasonable model to obtain a rough estimate of the binding constant.

The Langmuir binding constant is determined by using the following mathematical expression.<sup>33-34</sup>

$$\frac{1}{x} = \frac{1}{Kcx_m} + \frac{1}{x_m}$$

$x$  — moles of dye adsorbed per gram of adsorbent

$x_m$  — moles of dye adsorbed to form a monolayer per gram of adsorbent

$K$  — binding constant

$c$  — concentration of the adsorbate (dye) in equilibrium.

The binding constant calculated by plotting the inverse of moles of dye adsorbed per gram of adsorbate against the inverse of equilibrium concentration of adsorbate in solution. The intercept of this plot divided by the slope gives the Langmuir binding constant ( $K$ ).

### **1.2.4. Characterization**

Please see the appendix for the details of the instrumentation of UV-Visible spectroscopy, X-ray diffraction, Transmission electron microscopy (TEM), Field emission scanning electron microscopy (FESEM), nitrogen sorption analysis, thermogravimetric analysis, infra-red spectroscopy, zeta potential measurements.

### **1.2.5. Results and discussion**

Mesoporous silica, SBA-15 short rods of 1- 2  $\mu\text{m}$  length have been synthesised using a non-ionic block copolymer, P123 as template following a reported sol-gel method (Figure 2). The as prepared SBA-15 rods were subjected to high temperature calcination at 550  $^{\circ}\text{C}$  to remove the organic template. The pores were functionalized with hexyltrichlorosilane to obtain covalently attached hexyl groups on the silica surfaces (SBA-C<sub>6</sub>) (Figure 3). The successful covalent functionalization was confirmed using Fourier transformed infrared spectra (FT-IR) of SBA-C<sub>6</sub> which showed intense C-H stretching vibrations between 2850 and 3000  $\text{cm}^{-1}$  (Figure 4a). The X-ray diffraction patterns of SBA-15 and SBA-C<sub>6</sub> showed a small angle corresponding to the (100) plane

associated with hexagonal pore periodicity, revealing the retention of mesostructure (Figure 4b). The transmission electron micrographs (TEM) of SBA-15 and SBA-C<sub>6</sub> also suggest retention of mesoporous periodicity upon hexyl functionalization (Figure 2c and 2d).

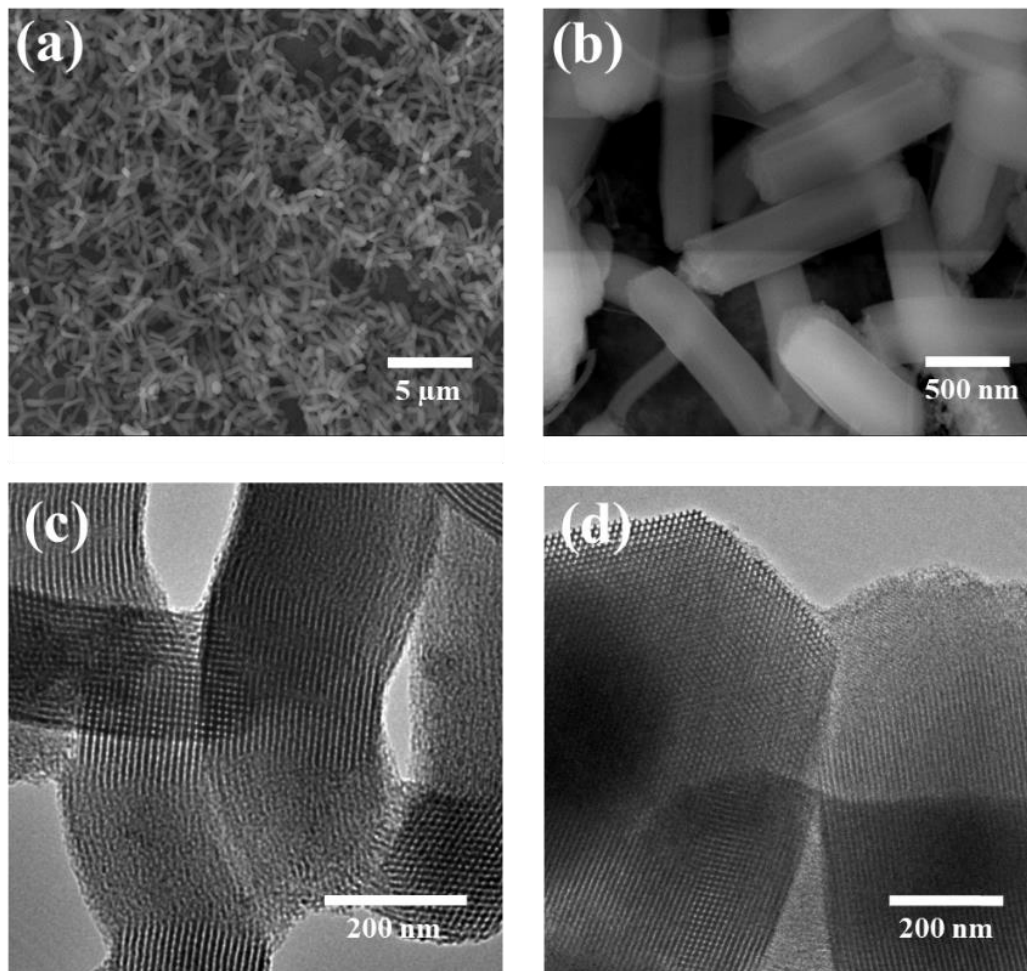


**Figure 2.** (a-b) FESEM images of SBA-15 at different magnifications showing monodispersed short rods like morphology. TEM image of (c) SBA-15 and (d) SBA-C<sub>6</sub> showing hexagonally arranged channels.

The amount of hexyl groups attached to the silica surface was found to be 1.6 mmol/g (13.6% w/w) by thermogravimetric analysis (TGA) (Figure 5a). The nitrogen physisorption isotherms for SBA-15 and SBA-C<sub>6</sub> obtained at 77 K were type IV isotherms typical of mesoporous materials with narrow pore size distribution (Figure 5b). The Barrett–Joyner–Halenda (BJH) pore size distribution showed a shift of the average pore size ( $\sim 1.7$  nm) from 10.3 nm for SBA-15 to 8.6 nm for SBA-C<sub>6</sub> (Figure 5b, inset). Further, the number of hexyl groups on SBA-C<sub>6</sub> was calculated to be 1.9 molecules per nm<sup>2</sup> area using TGA and nitrogen physisorption measurements.



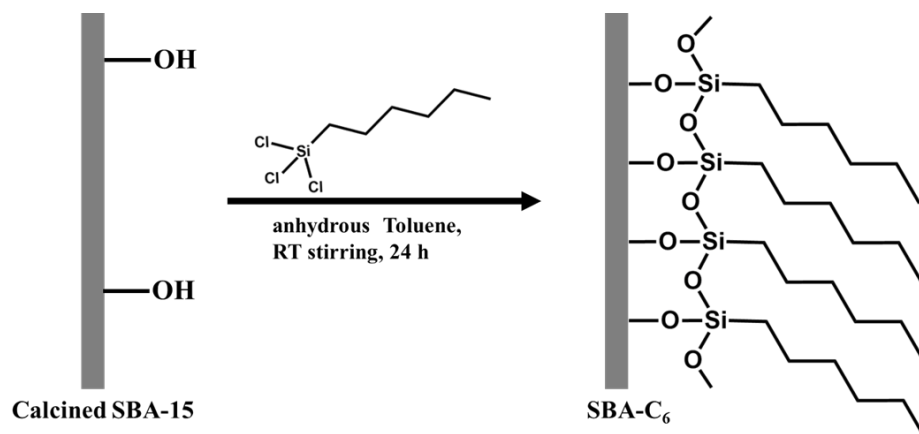


Figure 3. Schematic showing the synthetic strategy for SBA-C<sub>6</sub>.

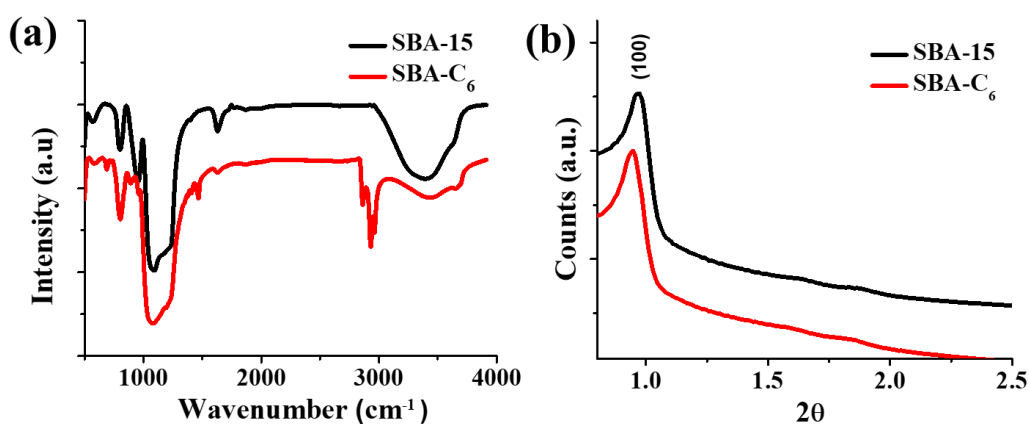


Figure 4. (a) FT-IR spectra of SBA-15 and SBA-C<sub>6</sub>. (b) Powder X-ray diffraction patterns of SBA-15 and SBA-C<sub>6</sub> showing retention of mesostructural ordering with the functionalization.

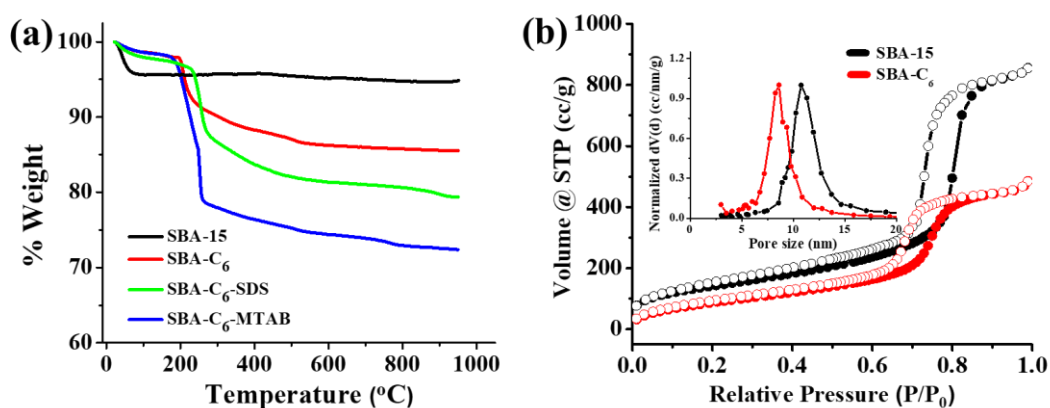
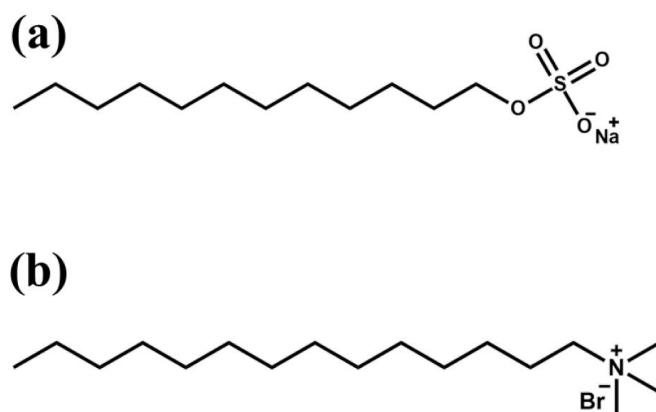


Figure 5. (a) Thermogravimetric analysis curves of SBA-15, SBA-C<sub>6</sub>, SBA-C<sub>6</sub>-MTAB, and SBA-C<sub>6</sub>-SDS. (b) Nitrogen sorption isotherms of SBA-15 and SBA-C<sub>6</sub> at 77 K. (Inset) Corresponding normalized BJH pore size distribution.

Covalent functionalization of silica with hexyl groups rendered the pore surface of SBA-C<sub>6</sub> hydrophobic in contrast to pristine SBA-15 which is polar in nature. To enable the coassembly, an aqueous solution of charged amphiphiles/surfactants was mixed with SBA-C<sub>6</sub>. For instance, myristyltrimethylammonium bromide (MTAB, CH<sub>3</sub>(CH<sub>2</sub>)<sub>12</sub>CH<sub>2</sub>N<sup>+</sup>(CH<sub>3</sub>)<sub>3</sub>Br<sup>-</sup>), a positively charged surfactant with 14-carbon alkyl chain (Figure 6b), was noncovalently assembled in the mesopores of SBA-C<sub>6</sub> to form SBA-C<sub>6</sub>-MTAB by soaking SBA-C<sub>6</sub> in MTAB solution for 3 h. (the textural parameters of SBA-15 and all its derivatives are given in Table 1).



**Figure 6.** Molecular structures of surfactants used in this study: (a) sodium dodecyl sulphate (SDS), (b) myristyltrimethylammonium bromide (MTAB).

The amount of MTAB assembled into the pores of SBA-C<sub>6</sub> was found to be 0.35 mmol/g (11.8% (w/w)) (determined by TGA). The assembly of MTAB within the pores was followed through nitrogen physisorption isotherms, which showed a reduction in the average pore size from 8.6 to 7.4 nm (Figure 7a-b). This reduction of pore size didn't commensurate with the molecular length of the MTAB (~2.1 nm). This difference suggests that the assembled MTAB molecules are arranged in a slanted orientation within the mesopores. The pore size distributions of SBA-C<sub>6</sub> and SBA-C<sub>6</sub>-MTAB exhibited more or less similar full width half-maximum (FWHM), suggesting uniform assembly of MTAB within the mesochannels. The density of MTAB molecules covering the SBA-C<sub>6</sub> pore surface was calculated (see the experimental section for details) to be 0.421 molecules/nm<sup>2</sup> area. This corresponds to 22% coverage with respect to hexyl groups, which is significant enough to influence the pore characteristics. Regeneration to parent material (SBA-C<sub>6</sub>) was achieved by washing SBA-C<sub>6</sub>-MTAB with hot methanol, which weakened the hydrophobic interactions between the hexyl groups and MTAB (Figure

7a-c). As the assembly of surfactant is based on the hydrophobic interactions, one would expect its organization inside the pores would be favoured with all types of surfactants irrespective of their charge in the head groups. Indeed, a negatively charged surfactant, sodium dodecyl sulfate (SDS,  $\text{CH}_3(\text{CH}_2)_{10}\text{CH}_2\text{SO}_4^- \text{Na}^+$ , Figure 6a) within SBA- $\text{C}_6$  pores (SBA- $\text{C}_6$ -SDS) also resulted in a concomitant reduction of pore size by 0.7 nm as shown by the pore size distributions (PSDs) calculated from the nitrogen sorption isotherms (Figure 7d). Similar to MTAB assembly, SDS assembly also caused a reduction in pore size that is not in commensuration with the molecular length of SDS ( $\sim 1.9$  nm), which suggests that SDS molecules are also arranged in a slanted orientation inside the mesopores. The amount of SDS assembled into the pores was found to be 0.168 mmol/g (4.9% (w/w)), nearly two times lower than that of the MTAB. This value corresponds to 0.202 molecules of SDS per  $\text{nm}^2$  (11% quantitative coverage with respect to hexyl groups).

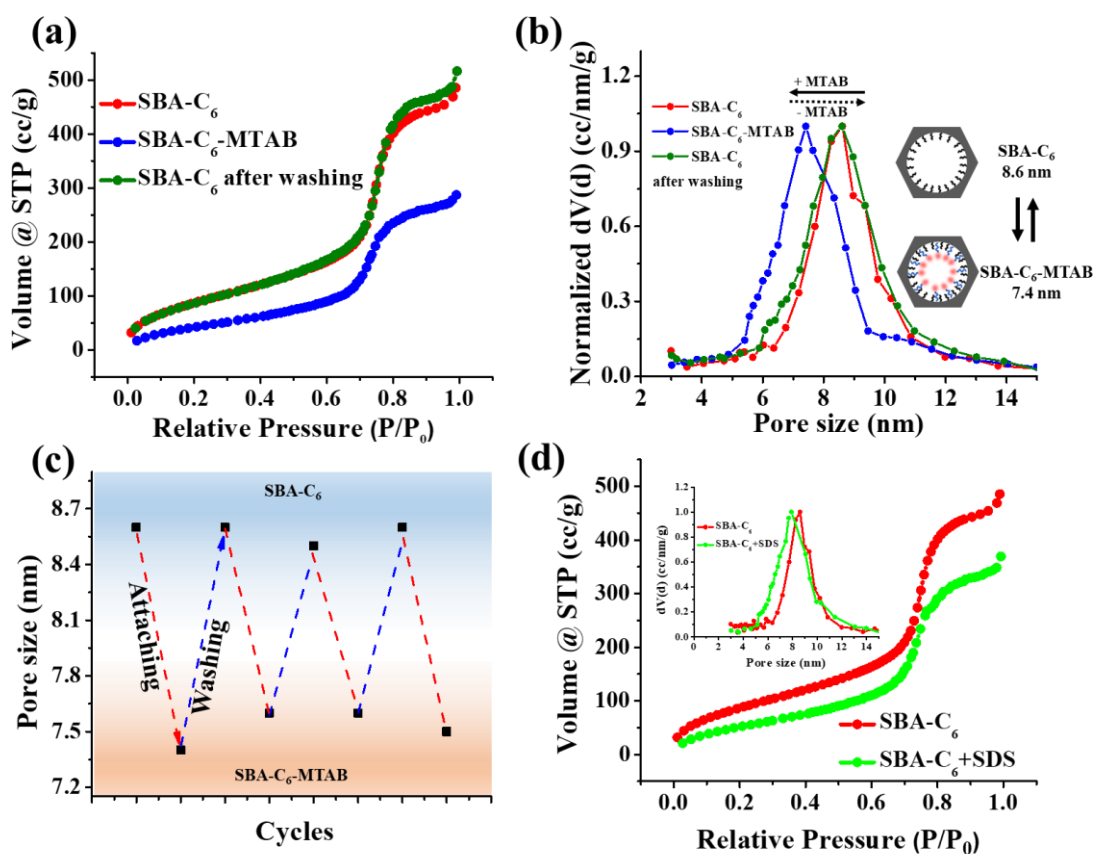


**Figure 7.** (a) Nitrogen adsorption isotherms of SBA- $\text{C}_6$ , SBA- $\text{C}_6$ -MTAB, and SBA- $\text{C}_6$  after washing off the MTAB assembly showing the reversibility of the assembly. (b) BJH pore size distributions (normalized) of SBA- $\text{C}_6$  and SBA- $\text{C}_6$ -MTAB showing the decrease

in pore size upon MTAB attachment. Recovery of pore size upon removal of MTAB is indicated by the dotted arrow. Schematic illustrates the reversibility of pore size on addition or removal of MTAB. (c) Variation of pore size (monitored through nitrogen sorption isotherms) on addition and removal of MTAB to SBA-C<sub>6</sub> (with initial pore diameter of 8.6 nm). (d) Nitrogen sorption isotherms of SBA-C<sub>6</sub> and SBA-C<sub>6</sub>-SDS at 77 K (inset showing corresponding BJH pore size distribution).

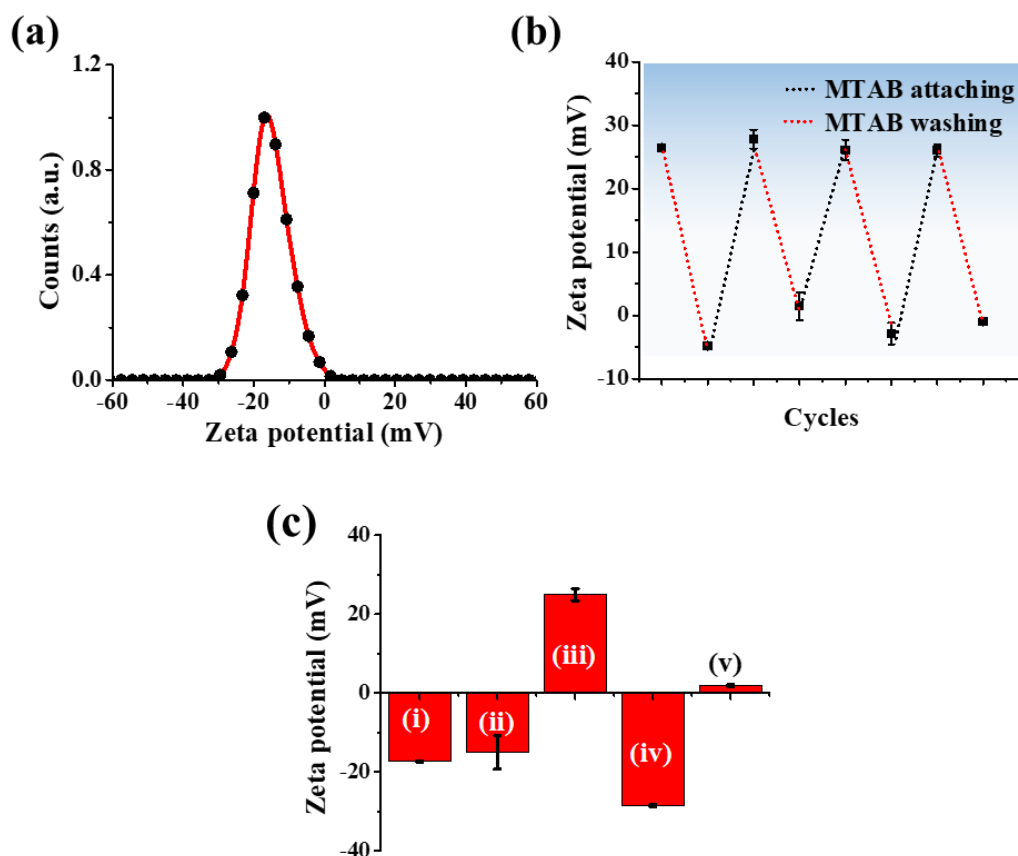


**Figure 8.** (a) Zeta potential distribution of SBA-C<sub>6</sub> at pH 5.5. (b) Variation of zeta potential up on successive immobilization and washing of MTAB to the SBA-C<sub>6</sub> surface. (c) Zeta potential of SBA-15 (i), SBA-C<sub>6</sub> (ii), SBA-C<sub>6</sub>-MTAB (iii) and SBA-C<sub>6</sub>- SDS (iv) and SBA-15-MTAB (v).

The switchable assembly of charged amphiphiles into SBA-C<sub>6</sub> was further confirmed through zeta potential measurements. SBA-C<sub>6</sub> dispersed in water/ethanol mixture was negatively charged ca.  $-15.0 \pm 4$  mV at pH 5.5 due to ionized silanol groups (Figure 8a). Upon addition of MTAB to SBA-C<sub>6</sub> the zeta potential increased to  $+26 \pm 0.5$  mV, owing to the binding of MTAB to SBA-C<sub>6</sub> surfaces (Figure 8b). Washing with hot methanol removed MTAB from the SBA-C<sub>6</sub> surface, and consequently, the zeta

potential dropped to  $-3.7 \pm 2$  mV (nearly neutral). It is worth noting that the surface charge is not turning negative (as that of SBA-C<sub>6</sub>) probably due to neutralization of the silica surface by the remaining electrostatically bound MTAB molecules. In order to check the recyclability of this noncovalent approach, MTAB was reattached to SBA-C<sub>6</sub> by soaking it again in MTAB solution, upon which the zeta potential increased to  $+27.7 \pm 2$  mV, which can be repeated for more than 4 cycles. However, when MTAB was mixed with unfunctionalized SBA-15, the surface charge varied from negative to near zero value due to charge neutralization. This suggests that hexyl pendant groups are important in charge reversal inside mesopores by self-assembly of more than excess MTAB surfactant molecules required for neutralization of negative surface charge (Figure 8c). The positive surface of SBA-C<sub>6</sub> bound with MTAB (SBA-C<sub>6</sub>-MTAB) showed a charge reversal to ca.  $-28.2 \pm 0.5$  mV on addition of SDS after the removal of MTAB by washing with hot methanol (Figure 9a). This charge conversion was highly reversible (shown in Figure 9a) signifying the modularity of the strategy. It is worth noting that the charge reversal can happen even without having an intermediate washing step. For example, positively charged SBA-C<sub>6</sub>-MTAB (zeta potential  $+31 \pm 2$  mV) becomes negative (zeta potential =  $-30 \pm 2$  mV) upon soaking with SDS solution of higher concentration (10 mM), suggesting replacement of MTAB with SDS. Similar competitive binding (replacement of SDS with MTAB) was observed in the case of SBA-C<sub>6</sub>-SDS upon soaking with MTAB solution (Figure 9b).

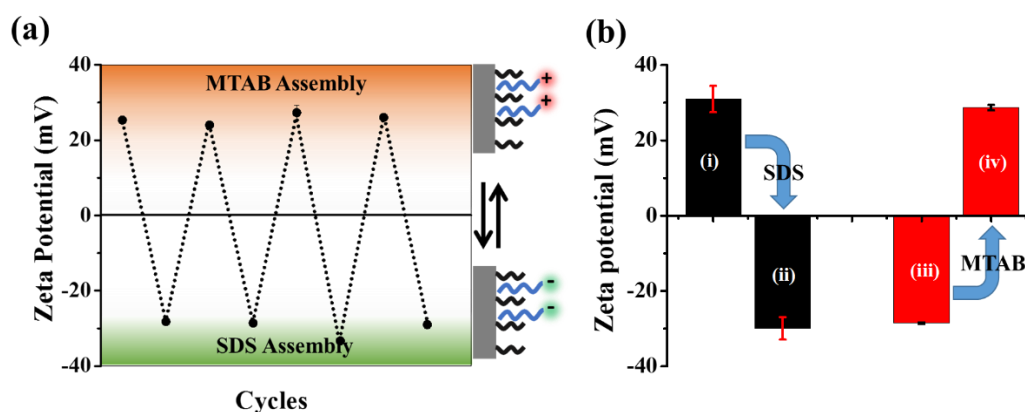


**Figure 9:** (a) Charge conversion of SBA-C<sub>6</sub> upon MTAB and SDS assembly. MTAB assembly on SBA-C<sub>6</sub> showed a positive zeta potential which changed to negative when MTAB was removed followed by SDS assembly. (b) **Dynamism of Assembly:** Zeta potential of (i) SBA-C<sub>6</sub>-MTAB, (ii) after soaking in SDS solution, (iii) SBA-C<sub>6</sub>-SDS, (iv) after soaking in MTAB solution.

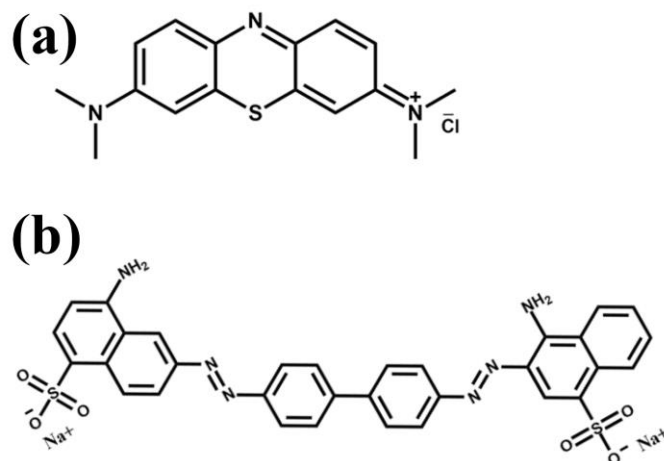


**Figure 10.** Molecular structures of charged dye molecules used in this study: (a) methylene blue (MB) and (b) congo red (CR).

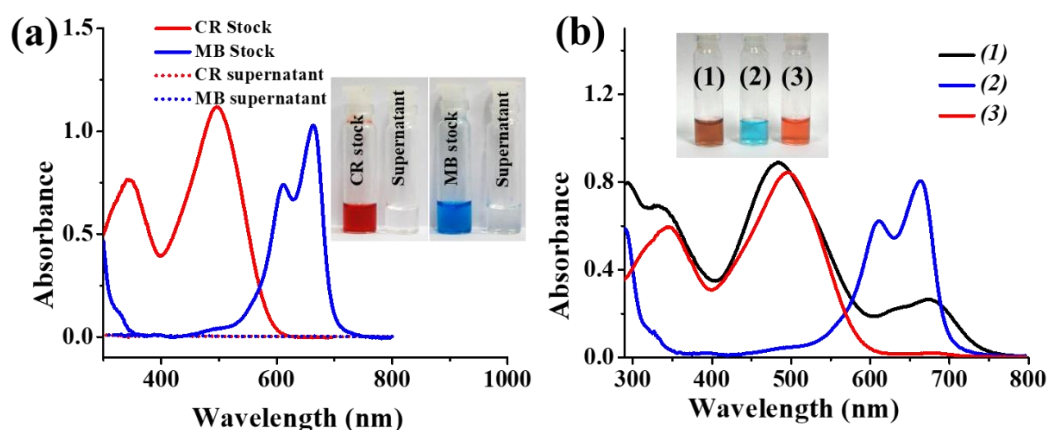


**Figure 11.** (a) Complete uptake of dye from the individual solution by respective surfactant bound SBA-C<sub>6</sub>: UV-Vis spectra of individual dye solutions before and after the dye uptake. (b) UV-vis spectrum of equimolar mixture of MB and CR (1). (2 and 3) UV-vis spectra of MB and CR recovered from the mixture using SBA-C<sub>6</sub>-MTAB and SBA-C<sub>6</sub>-SDS, respectively (inset shows corresponding photographs).

In order to further understand the charge reversal achieved in our system/strategy, adsorption studies were conducted with charged chromophores to evaluate the extent of the surface charge reversal as the adsorption proceeds by charge neutralization primarily. Methylene blue (MB; cationic dye) and Congo red (CR; anionic dye) were used as model dyes in this study (Figure 10a, b). When ethanol wetted SBA-C<sub>6</sub>-MTAB and SBA-C<sub>6</sub>-SDS were mixed with aqueous solutions of CR and MB, respectively, complete uptake of dye from solution was observed (Figure 11a). Photographs show the stock solution of

respective dyes and the clear supernatant after complete uptake (Figure 11a *inset*). Charge selective adsorption/separation of charged chromophores from a mixture using MTAB- or SDS-bound SBA-C<sub>6</sub> was also studied. When SBA-C<sub>6</sub>-MTAB mixed with an aqueous solution containing an equimolar mixture of dyes, CR (negatively charged) was selectively adsorbed leaving MB in the supernatant. Similarly, when SBA-C<sub>6</sub>-SDS was used, MB was selectively adsorbed leaving CR in the supernatant (Figure 11b).

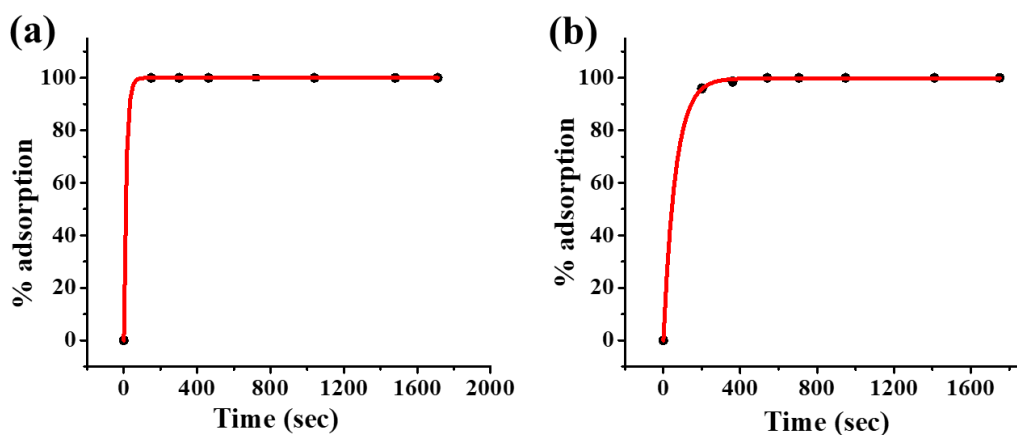


**Figure 12.** Kinetics of adsorption of (a) congo red to SBA-C<sub>6</sub>-MTAB and (b) methylene blue to SBA-C<sub>6</sub>-SDS.

The kinetics of this uptake was found to be very fast (complete uptake within ~2 min for both dyes) (Figure 12). The binding titration curves of MTAB/SDS-assembled SBA-C<sub>6</sub> with respective dyes were constructed to study the adsorption in greater detail (Figure 13a). The adsorption of MB to the SBA-C<sub>6</sub>-SDS showed a saturated uptake of around 0.4 mmol/g, whereas the adsorption for CR onto SBA-C<sub>6</sub>-MTAB was around 0.2 mmol/g, nearly one-half that of MB. The intercepts of MB and CR in linear Langmuir adsorption isotherm showed that the monolayer capacity of CR is about half of that of MB (Figure 14). However, Langmuir binding constants for both dyes were the same ( $\sim 1.3 \times 10^5 \text{ M}^{-1}$ ), suggesting a similar interaction strength operational in both cases. CR is having two negative charges which can form a neutralizing monolayer on the surface with one-half of the number of molecules as compared to MB (which is having one positive charge) (see the inset schematics in Figure 13a). This suggests that both anionic and cationic surfactant assemblies give rise to a similar magnitude of charge inside the mesopores. In order to de-convolute the extent of silanol participation in the adsorption of MB on to SBA-C<sub>6</sub>-SDS, a control study was carried out in which

the saturation uptake of MB on to SBA-C<sub>6</sub> was found to be 0.15 mmol/g (Figure 15a) lower than that for SBA-C<sub>6</sub>-SDS. It clearly suggests that the SDS assembly provides additional charge on the SBA-C<sub>6</sub> surface to achieve higher uptake of positive chromophores.

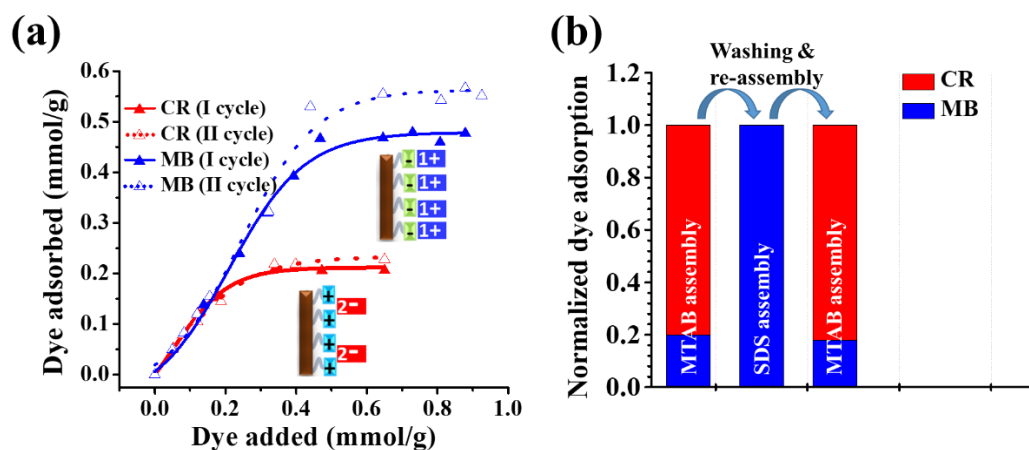


**Figure 13.** (a) *Charged dye adsorption to the surface:* Binding curves for MB (blue) and CR (red) on to SBA-C<sub>6</sub>-SDS and SBA-C<sub>6</sub>-MTAB respectively. (b) *Reversal of dye adsorption:* SBA-C<sub>6</sub>-MTAB showed a high loading of CR which reversed to MB up on washing followed by SDS assembly. Further, when same scaffold subjected to MTAB assembly, a high loading of CR was restored.

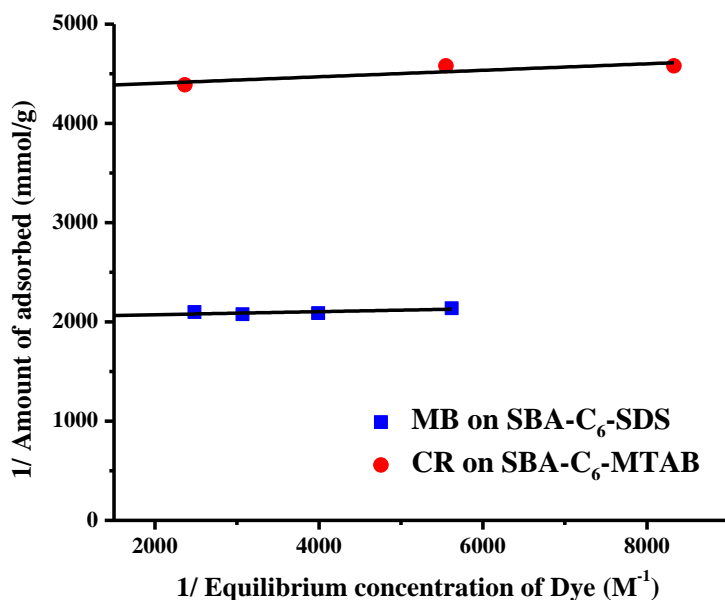


**Figure 14.** *Linear Langmuir plots for the adsorption of MB (blue) and CR (red) onto SBA-C<sub>6</sub>-SDS and SBA-C<sub>6</sub>-MTAB respectively.*



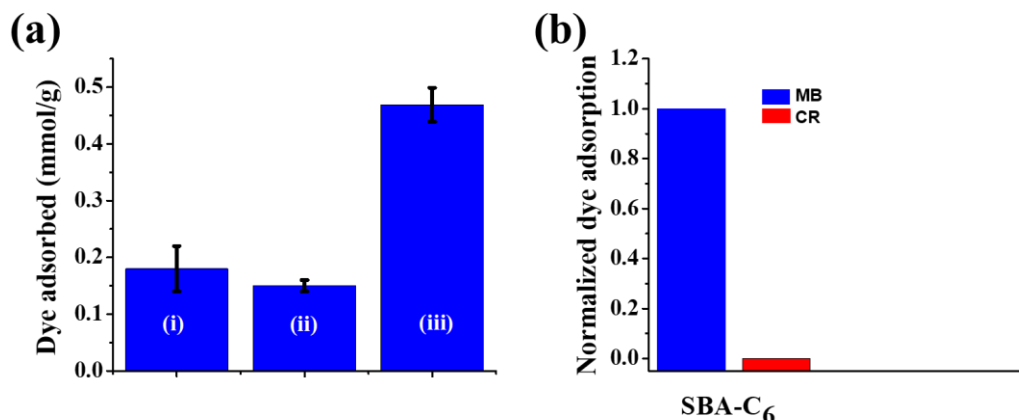


**Figure 15.** (a) Saturation uptake of MB on to SBA-15 (i), SBA-C<sub>6</sub> (ii), and SBA-C<sub>6</sub>-SDS (iii). Soaking concentration of MB was 0.8 mmol/g for all. (b) Normalized uptake of MB and CR on to SBA-C<sub>6</sub>.

To evaluate the effects of salt concentration on the dye adsorption process, we carried out adsorption of dyes at higher ionic strength (Figure 16). In principle, one would expect relatively low adsorption of dye at higher ionic strength due to electrostatic screening of charges. However, the adsorption of MB on SBA-C<sub>6</sub>-SDS (and CR on SBA-C<sub>6</sub>-MTAB as well) at higher ionic strength was found to be similar to that in water. In the case of CR on SBA-C<sub>6</sub>-SDS (MB on SBA-C<sub>6</sub>-MTAB as well) the effect of electrostatic repulsion was clearly observed in water evident by negligible adsorption. However, once the electrostatic interactions are screened at higher ionic strength the adsorption got enhanced. The enhanced adsorption under high ionic strength was previously observed and attributed to the reduced repulsion between the adsorbing dyes facilitating multilayer adsorption.<sup>35</sup> These results clearly indicate that the electrostatic interactions dominate over hydrophobic interactions in our system. However, once the electrostatic interactions are screened the hydrophobic interactions become pronounced in governing adsorption process.

The recyclability of these materials for dye adsorption was demonstrated by washing the dye-loaded MTAB/SDS assembly. The same binding titration curve was observed when an existing assembly was removed, and subsequently, fresh surfactant was assembled (Figure 13a). Furthermore, dye adsorption behaviour of surfactant-bound SBA-C<sub>6</sub> could be completely reversed by simply changing the surfactant, clearly demonstrating the modularity of these materials. SBA-C<sub>6</sub> was first bound with MTAB, which showed maximum adsorption for CR, which when washed off and subjected to

SDS assembly resulted in a maximum adsorption for MB (Figure 13b). The same scaffold was washed off and further put through MTAB assembly to obtain the maximum sorption to CR.

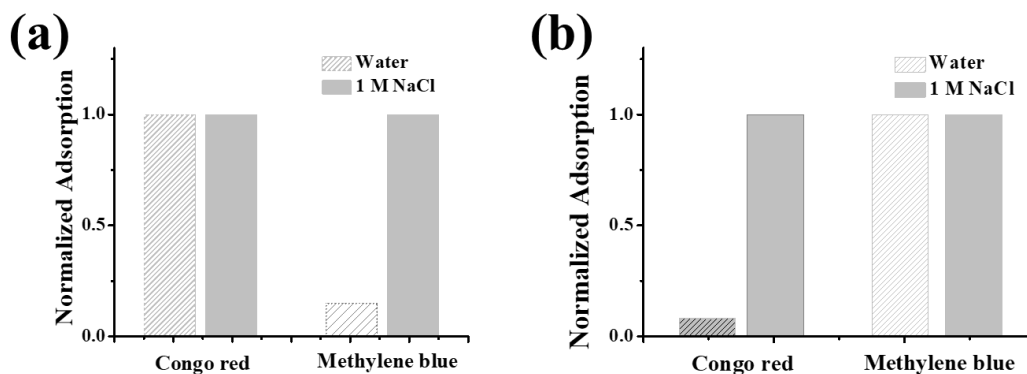


**Figure 16.** Relative amount of dyes adsorbed on to (a) SBA-C<sub>6</sub>-MTAB and (b) SBA-C<sub>6</sub>-SDS in water and 1 M NaCl solution (Dye added= 0.1 mmol/g. Normalized with respect to the uptake of individual dye).

	SSA <sub>(BET)</sub> <sup>a</sup> (m <sup>2</sup> /g)	BJH pore size <sup>b</sup> (nm)	Vp <sup>c</sup> (cc/g)	BET 'C' constant <sup>d</sup>
<b>SBA-15</b>	500	10.3	1.32	150.3
<b>SBA-C<sub>6</sub></b>	340	8.6	0.72	31.3
<b>SBA-C<sub>6</sub>-MTAB</b>	190	7.4	0.46	19.6
<b>SBA-C<sub>6</sub> after removal of MTAB</b>	330	8.6	0.73	30.8
<b>SBA-C<sub>6</sub>-SDS</b>	230	7.9	0.57	20.6

**Table 01:** Textural parameters of SBA-15 and its derivatives used in this study.

### 1.2.6. Conclusions

In this chapter, we demonstrated a highly reversible and modular approach to fabricate mesoporous silica-based charge-convertible surfaces. The strategy is based on hydrophobic interactions between hexyl pendant groups and surfactant molecules of the desired charge. The reversible nature of the assembly was confirmed by N<sub>2</sub> sorption, zeta potential measurements, and dye sorption experiments. The modularity of this approach

was utilized for engineering highly recyclable materials for charge-based adsorption and selective separation of dye molecules.

### **1.2.7. References**

- (1) Sayari, A.; Hamoudi, S.; Yang, Y. Applications of Pore-Expanded Mesoporous Silica. 1. Removal of Heavy Metal Cations and Organic Pollutants from Wastewater. *Chem. Mater.* **2005**, *17* (1), 212-216.
- (2) Mohammadi, N.; Khani, H.; Gupta, V. K.; Amereh, E.; Agarwal, S. Adsorption process of methyl orange dye onto mesoporous carbon material—kinetic and thermodynamic studies. *J. Colloid Interface Sci.* **2011**, *362* (2), 457-462.
- (3) Anbia, M.; Hariri, S. A.; Ashrafizadeh, S. N. Adsorptive removal of anionic dyes by modified nanoporous silica SBA-3. *Appl. Surf. Sci.* **2010**, *256* (10), 3228-3233.
- (4) Wu, S.; Li, Z.; Han, J.; Han, S. Dual colored mesoporous silica nanoparticles with pH activable rhodamine-lactam for ratiometric sensing of lysosomal acidity. *Chem. Commun.* **2011**, *47* (40), 11276-11278.
- (5) Ng, C. C. A.; Magenau, A.; Ngalim, S. H.; Ciampi, S.; Chockalingham, M.; Harper, J. B.; Gaus, K.; Gooding, J. J. Using an Electrical Potential to Reversibly Switch Surfaces between Two States for Dynamically Controlling Cell Adhesion. *Angew. Chem. Int. Ed.* **2012**, *51* (31), 7706-7710.
- (6) Radovic-Moreno, A. F.; Lu, T. K.; Puscasu, V. A.; Yoon, C. J.; Langer, R.; Farokhzad, O. C. Surface Charge-Switching Polymeric Nanoparticles for Bacterial Cell Wall-Targeted Delivery of Antibiotics. *ACS Nano* **2012**, *6* (5), 4279-4287.
- (7) Lee, C.-H.; Lo, L.-W.; Mou, C.-Y.; Yang, C.-S. Synthesis and Characterization of Positive-Charge Functionalized Mesoporous Silica Nanoparticles for Oral Drug Delivery of an Anti-Inflammatory Drug. *Adv. Funct. Mater.* **2008**, *18* (20), 3283-3292.
- (8) Zhou, Z.; Shen, Y.; Tang, J.; Fan, M.; Van Kirk, E. A.; Murdoch, W. J.; Radosz, M. Charge-Reversal Drug Conjugate for Targeted Cancer Cell Nuclear Drug Delivery. *Adv. Funct. Mater.* **2009**, *19* (22), 3580-3589.
- (9) Feng, T.; Ai, X.; An, G.; Yang, P.; Zhao, Y. Charge-Convertible Carbon Dots for Imaging-Guided Drug Delivery with Enhanced in Vivo Cancer Therapeutic Efficiency. *ACS Nano* **2016**, *10* (4), 4410-4420.

- 
- 
- (10) Wang, Y.; Sun, Y.; Wang, J.; Yang, Y.; Li, Y.; Yuan, Y.; Liu, C. Charge-Reversal APTES-Modified Mesoporous Silica Nanoparticles with High Drug Loading and Release Controllability. *ACS Appl. Mater. Interfaces* **2016**, *8* (27), 17166-17175.
  - (11) Liu, W.; Liu, J.; Yang, X.; Wang, K.; Wang, Q.; Yang, M.; Li, L.; Song, C. Phosphate modulated permeability of mesoporous silica spheres: a biomimetic ion channel decorated compartment model. *J. Mater. Chem. B* **2015**, *3* (2), 323-329.
  - (12) Liu, W.; Yang, X.; He, D.; He, L.; Li, L.; Liu, Y.; Liu, J.; Wang, K. Dopamine modulated ionic permeability in mesoporous silica sphere based biomimetic compartment. *Colloids Surf. B* **2016**, *142*, 266-271.
  - (13) Yamamoto, E.; Kuroda, K. Colloidal Mesoporous Silica Nanoparticles. *Bull. Chem. Soc. Jpn.* **2016**, *89* (5), 501-539.
  - (14) Brühwiler, D. Postsynthetic functionalization of mesoporous silica. *Nanoscale* **2010**, *2* (6), 887-892.
  - (15) Hoffmann, F.; Cornelius, M.; Morell, J.; Fröba, M. Silica-Based Mesoporous Organic–Inorganic Hybrid Materials. *Angew. Chem. Int. Ed.* **2006**, *45* (20), 3216-3251.
  - (16) Wong, E. M.; Markowitz, M. A.; Qadri, S. B.; Golledge, S. L.; Castner, D. G.; Gaber, B. P. Preparation of Quaternary Ammonium Organosilane Functionalized Mesoporous Thin Films. *Langmuir* **2002**, *18* (4), 972-974.
  - (17) Lee, E. C.; Nguyen, C. T. H.; Strounina, E.; Davis-Poynter, N.; Ross, B. P. Structure–Activity Relationships of GAG Mimetic-Functionalized Mesoporous Silica Nanoparticles and Evaluation of Acyclovir-Loaded Antiviral Nanoparticles with Dual Mechanisms of Action. *ACS Omega* **2018**, *3* (2), 1689-1699.
  - (18) Shen, A.; Guo, Z.; Yu, L.; Cao, L.; Liang, X. A novel zwitterionic HILIC stationary phase based on “thiol-ene” click chemistry between cysteine and vinyl silica. *Chem. Commun.* **2011**, *47* (15), 4550-4552.
  - (19) Fattori, N.; Maroneze, C. M.; Costa, L. P. D.; Strauss, M.; Mazali, I. O.; Gushikem, Y. Chemical and photochemical formation of gold nanoparticles supported on viologen-functionalized SBA-15. *Colloids Surf. A* **2013**, *437*, 120-126.

- (20) Liu, A.; Han, S.; Che, H.; Hua, L. Fluorescent Hybrid with Electron Acceptor Methylene Viologen Units inside the Pore Walls of Mesoporous MCM-48 Silica. *Langmuir* **2010**, *26* (5), 3555-3561.
- (21) Mühlstein, L. A.; Sauer, J.; Bein, T. Tuning the Thermal Relaxation of a Photochromic Dye in Functionalized Mesoporous Silica. *Adv. Funct. Mater.* **2009**, *19* (13), 2027-2037.
- (22) Brunelli, N. A.; Venkatasubbaiah, K.; Jones, C. W. Cooperative Catalysis with Acid–Base Bifunctional Mesoporous Silica: Impact of Grafting and Co-condensation Synthesis Methods on Material Structure and Catalytic Properties. *Chem. Mater.* **2012**, *24* (13), 2433-2442.
- (23) Kumar, B. V. V. S. P.; Salikolimi, K.; Eswaramoorthy, M. Glucose- and pH-Responsive Charge-Reversal Surfaces. *Langmuir* **2014**, *30* (16), 4540-4544.
- (24) Han, L.; Ruan, J.; Li, Y.; Terasaki, O.; Che, S. Synthesis and Characterization of the Amphoteric Amino Acid Bifunctional Mesoporous Silica. *Chem. Mater.* **2007**, *19* (11), 2860-2867.
- (25) Kumar, B. V. V. S. P.; Rao, K. V.; Soumya, T.; George, S. J.; Eswaramoorthy, M. Adaptive Pores: Charge Transfer Modules as Supramolecular Handles for Reversible Pore Engineering of Mesoporous Silica. *J. Am. Chem. Soc.* **2013**, *135* (30), 10902-10905.
- (26) Pérez-Mitta, G.; Albesa, A.; Gilles, F. M.; Toimil-Molares, M. E.; Trautmann, C.; Azzaroni, O. Noncovalent Approach toward the Construction of Nanofluidic Diodes with pH-Reversible Rectifying Properties: Insights from Theory and Experiment. *J. Phys. Chem. C* **2017**, *121* (16), 9070-9076.
- (27) Pérez-Mitta, G.; Burr, L.; Tuninetti, J. S.; Trautmann, C.; Toimil-Molares, M. E.; Azzaroni, O. Noncovalent functionalization of solid-state nanopores via self-assembly of amphipols. *Nanoscale* **2016**, *8* (3), 1470-1478.
- (28) Kumar, B. V. V. S. P.; Rao, K. V.; Sampath, S.; George, S. J.; Eswaramoorthy, M. Supramolecular Gating of Ion Transport in Nanochannels. *Angew. Chem.* **2014**, *126* (48), 13289-13293.
- (29) Sayari, A.; Han, B.-H.; Yang, Y. Simple Synthesis Route to Monodispersed SBA-15 Silica Rods. *J. Am. Chem. Soc.* **2004**, *126* (44), 14348-14349.
- (30) Mittal, A.; Kurup, L.; Mittal, J. Freundlich and Langmuir adsorption isotherms and kinetics for the removal of Tartrazine from aqueous solutions using hen feathers. *J. Hazard. Mater.* **2007**, *146* (1), 243-248.

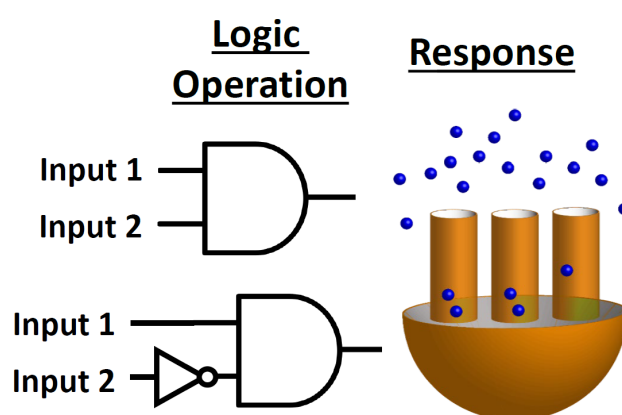
- (31) Everett, D. H. Thermodynamics of adsorption from solution. Part 1.—Perfect systems. *Trans. Faraday Soc.* **1964**, *60* (0), 1803-1813.
- (32) Gast, A. P.; Adamson, A. W. *Physical Chemistry of Surfaces*, 6th ed.; A Wiley-Interscience Publication, John Wiley & Sons, Inc. : 1960.
- (33) Wu, Y.; Zhang, M.; Zhao, H.; Yang, S.; Arkin, A. Functionalized mesoporous silica material and anionic dye adsorption: MCM-41 incorporated with amine groups for competitive adsorption of Acid Fuchsin and Acid Orange II. *RSC Adv.* **2014**, *4* (106), 61256-61267.
- (34) Almeida, C. A. P.; Debacher, N. A.; Downs, A. J.; Cottet, L.; Mello, C. A. D. Removal of methylene blue from colored effluents by adsorption on montmorillonite clay. *J. Colloid Interface Sci.* **2009**, *332* (1), 46-53.
- (35) Gómez, J. M.; Galán, J.; Rodríguez, A.; Walker, G. M. Dye adsorption onto mesoporous materials: pH influence, kinetics and equilibrium in buffered and saline media. *J. Environ. Manage.* **2014**, *146*, 355-361.

## Chapter- 1.3

### ***Molecular Logic Gate: Integrating Multi-Analyte Response in Mesoporous Silica for Logic Controlled Release***

#### **Summary:**

*Stimuli-responsive release of cargo from mesoporous silica-based systems have gained significant attention by virtue of their applications in drug delivery, sensing, bioassay etc. Recently, these systems are being explored as logically programmable devices utilizing the molecular logic gate principles. A molecular logic gate performs a logic operation based on one or more physical or chemical inputs and a single output. However, they rely on functionalized responsive motifs which limit the number of logic operations obtained. In this chapter, we report a generic approach to integrate multi-analytes responsive release of cargo from pH-responsive mesoporous silica nanoparticles. We utilized a pH switchable medium consisting of different enzymes which selectively act on respective substrates (analytes) to trigger the release of cargo from mesoporous silica, thereby, achieving multi-analytes responsive release. Further, by choosing appropriate enzymes and substrates, Boolean logic gate (OR and INH) controlled release of cargo was obtained.*



Manuscript based on this work is under preparation.





### **1.3.1. Introduction**

Since the pioneering works of Aviram and de Silvia on application of Boolean algebra to chemical systems, stimuli-responsive systems are currently being envisioned as computational devices that process chemical or physical inputs to generate outputs based on simple logic operations.<sup>1-21</sup> Till date, a plethora of molecular<sup>22-27</sup>, supramolecular<sup>28-31</sup> and hybrids systems<sup>32-35</sup> that respond to temperature<sup>36-37</sup>, light<sup>38-39</sup>, pH<sup>40-42</sup>, redox potential<sup>43</sup>, small molecules<sup>33</sup>, metal ions<sup>34, 44-46</sup> etc. have been employed as processing units for various Boolean logic functions. These processing units report “YES” or “NO” outputs depending on the input combinations and the in-built logic functions and therefore potential candidates for a wide variety of applications such as data security<sup>24</sup>, intelligent sensing<sup>47</sup>, disease diagnosis<sup>48</sup>, automatic therapy processing<sup>27</sup>, data and signal processing<sup>49-50</sup> etc.

Recently, mesoporous silica have been utilized for the logic operations in which the release of cargo from the channels is interpreted as “YES” output.<sup>51-57</sup> The standard strategy for fabricating such units often rely on the functionalization of silica surface with responsive molecules.<sup>58</sup> For instance, Jeffrey I. Zink and co-workers recently demonstrated “AND” gate-controlled release of cargo molecules from dual responsive mesoporous silica. They utilized surface-functionalized azobenzene motifs as nanoimpellers and the pore opening was blocked with a pH-responsive nanovalve.<sup>53</sup> The release of guest molecules was obtained only in presence of both base and 448 nm light (inputs) and therefore showed an AND gate-controlled release. Further, Yanlin Song and co-workers demonstrated a DNA functionalized mesoporous silica showing dual logic operations (OR gate & AND gate).<sup>52</sup> The DNA strand was grafted into mesoporous silica and the pores were gated using gold nanoparticles capped with complementary DNA (Figure 1). The OR gate was executed by choosing heat and K<sup>+</sup> ion as inputs. In presence of any of these inputs, the gated DNA unbind from the grafted DNA which leads to the release of cargo (Figure 1a). In case of AND gate, they have used a different complementary DNA strand with certain unhybridized portion which has specific interaction with adenosine (target 2). The presence of adenosine (target 2) destabilizes the DNA hybridization but not to the extent of complete breakage, therefore, cargo would be still within the pores. However, the presence of both adenosine (target 2) and cocaine (target 3) breaks the DNA binding completely, thereby cargo gets released which indicates an AND gate-controlled release (Figure 1b). Whilst, these examples

demonstrate the utility of mesoporous silica as the logical processing units, the complex functionalization steps remain as a bottleneck for further developments. Hence, there is a demand for a generic strategy to install more number of logic functions into the mesoporous silica (without rigorous functionalization steps) to obtain high performing systems.

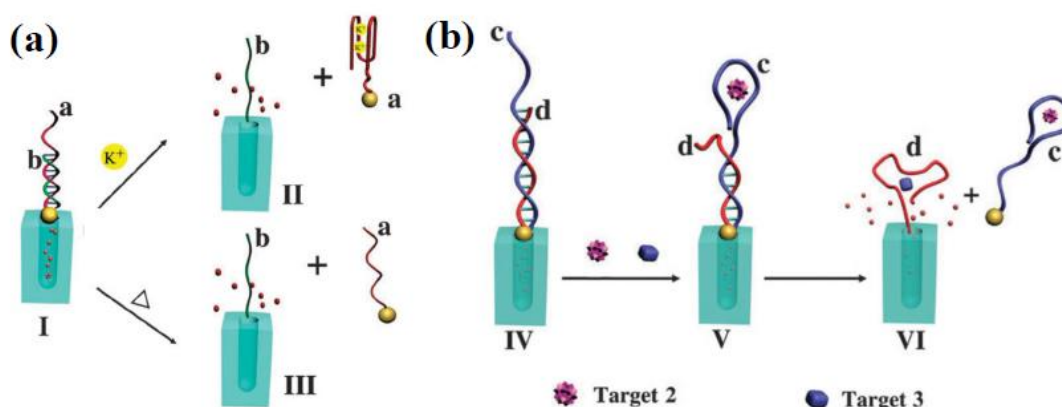
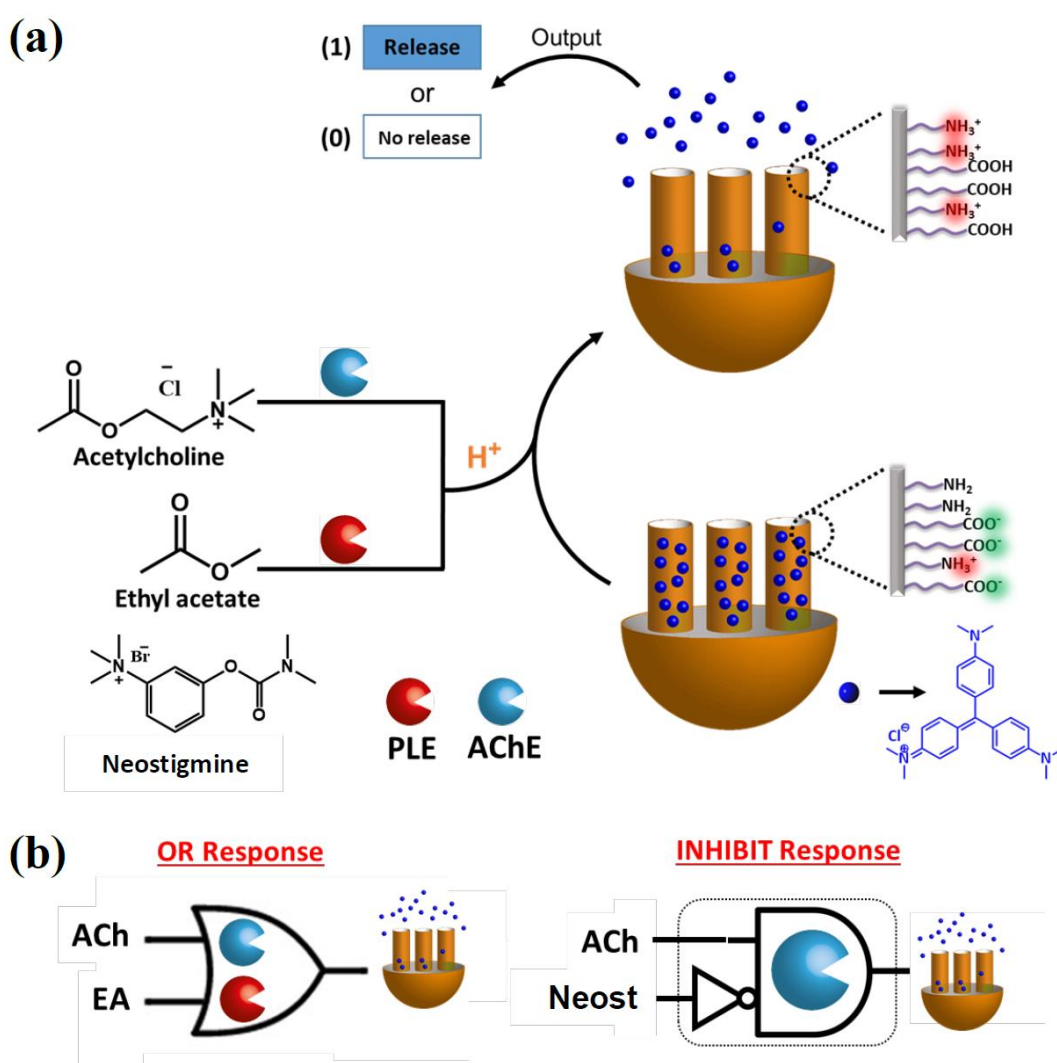


**Figure 1.** DNA functionalized mesoporous silica for logic gate-controlled release of cargo (a) Schematic showing the OR gated release. The mesoporous silica system is functionalized with DNA strand and a complementary DNA attached gold nanoparticles were used as gatekeepers. (b) Schematic representation of AND gate-controlled release. Here, the complementary strand DNA is having certain un-hybridized portion which specifically interacts with target 2 (adenosine). In presence of target 2, the double-strand get destabilized. Further, addition of target 3 (cocaine) induces complete de-binding of double-strand and the cargo gets released. Reproduced with permission from reference 52. Copyright 2012, Royal Society of Chemistry.

### 1.3.2. Scope of the present investigation

In this chapter, we demonstrated a new methodology to achieve Boolean logic gate-controlled release of cargo from mesoporous silica by integrating them with enzyme driven biochemical reactions. The generic strategy used a pH-dependent charge reversal mesoporous silica having the capability to control the release of charged cargos from the channels, in response to pH change. This mesoporous silica was integrated into a pH switchable solution containing enzymes and respective substrates (analytes) (Scheme-1) to demonstrate some of the fundamental logic gate functions. The hetero-functionalized mesoporous silica consisting of carboxylic acid and propylamine functional groups in

certain proportion give rise to pH-dependent charge reversal surface (*i.e.* cationic surface at acidic pH due to protonation of amine groups and anionic surface at basic pH due to deprotonation of carboxylic acid groups). The cationic dye (cargo) was loaded into the mesoporous silica at basic pH utilizing the electrostatic attractions between dye molecules and anionic surfaces. The loaded cargo could be quantitatively released by decreasing the pH to the acidic range. Further, by employing the enzyme or combination of enzymes (to install respective biochemical reactions that change the solution pH), multi-analytes responsive release from mesoporous silica (regulated by respective logic gate functions- OR and INH) was demonstrated.



*Scheme 1. Multi-stimuli responsive, logic gate-controlled release of cargo from mesoporous silica. (a)  $CV^+$  loaded MCM-Z was taken at pH 8.0. Switching the pH of the dispersion to an acidic value triggers the release of  $CV^+$  from the mesochannels. The*

*pH of the dispersion could be switched via different biochemical reactions. (b) By appropriately selecting the enzymes and substrates (analytes), two elementary logic gates (OR and INHIBIT) were demonstrated.*

### 1.3.3. Experimental section

**Synthesis of MCM-41.** Mesoporous silica nanoparticles (MCM-41) were synthesized by following a previously reported procedure.<sup>59</sup> In a typical synthesis, 1.0 g (2.74 mmol) of hexadecyltrimethyl-ammonium bromide (CTAB) and 0.28 g of NaOH were dissolved in 480 mL of water under stirring and the temperature was raised to 80°C. 5 ml (22.4 mmol) of tetraethyl orthosilicate (TEOS) was added dropwise to the reaction mixture and stirred for 2 h at 80 °C. The white solid product was centrifuged, washed thoroughly with water followed by ethanol, and dried in an oven for overnight. The surfactant (CTAB) was removed by refluxing it for 6 h in acidic ethanol solution (50 mL EtOH containing 0.5 mL concentrated HCl (37 %)). The precipitate was thoroughly washed with water and ethanol.

**Synthesis of MCM-N.** 1.0 g of surfactant-free MCM-41 (1.0 g) and 1.0 mL (5.67 mmol) of (3-aminopropyl)triethoxysilane (APTES) were added to 80 mL anhydrous toluene and ultra-sonicated to get a homogenous dispersion. The mixture was refluxed along with stirring under N<sub>2</sub> atmosphere for 24 h. The reaction mixture was centrifuged and the precipitate was washed thoroughly with toluene, hexane followed by ethanol, finally dried under high vacuum at 353 K for 6 h.

**Synthesis of MCM-Z.** 0.5 g of MCM-N was dispersed in 25 mL 1,4-dioxane and ultra-sonicated for 5 minutes. To this dispersion, a solution of 60 mg of succinic anhydride (0.6 mmol) in 12.5 mL of 1,4-dioxane was added under stirring. This mixture was heated at 80 °C for 1 h. The resultant product was centrifuged, and washed thoroughly with water followed by ethanol, and dried in an oven for overnight.

**Ninhydrin test for the estimation of amine groups.** The ninhydrin solution was prepared as follows: 0.266 g (1.49 mmol) of ninhydrin was dissolved in 10 mL dimethyl sulfoxide (DMSO) and 0.04 g hydrindantin was added. The mixture was sonicated for 10 min to form a clear solution and 3.3 mL of lithium hydroxide/acetic acid buffer (4 N) was added to form ninhydrin stock solution. The solution was purged with N<sub>2</sub> gas for 10 min before use.

To construct a calibration plot, 1 mL of ninhydrin solution was added to 1 mL of n-propylamine standard solutions (concentration range: 0.2 mM to 0.8 mM) and thoroughly mixed. All of these solutions were placed in closed containers and heated at 80 °C for 30 min. After 30 min the reaction mixture was immediately placed in an ice-bath. The mixture was diluted by adding 20 mL of 1:1 ethanol-water mixture. This mixture was further diluted three times before being subjected to UV-Vis spectroscopy. The absorbance at 572 nm was used for all calculations.

For determining the amount of the amine groups in MCM-N and **MCM-Z**: 1 mL of ninhydrin solution was added to the dispersions of 5 mg MCM-N in 1 mL of water and 5 mg **MCM-Z** in 1 mL water each. The resultant mixtures were placed in closed containers and heated at 80 °C for 30 min. After 30 min, the reaction mixture was immediately placed in the ice-bath. The precipitate was removed through centrifugation and the supernatants were diluted by adding 20 mL of 1:1 ethanol-water mixture. This mixture was further diluted three times before subjected to UV-Vis spectroscopy.

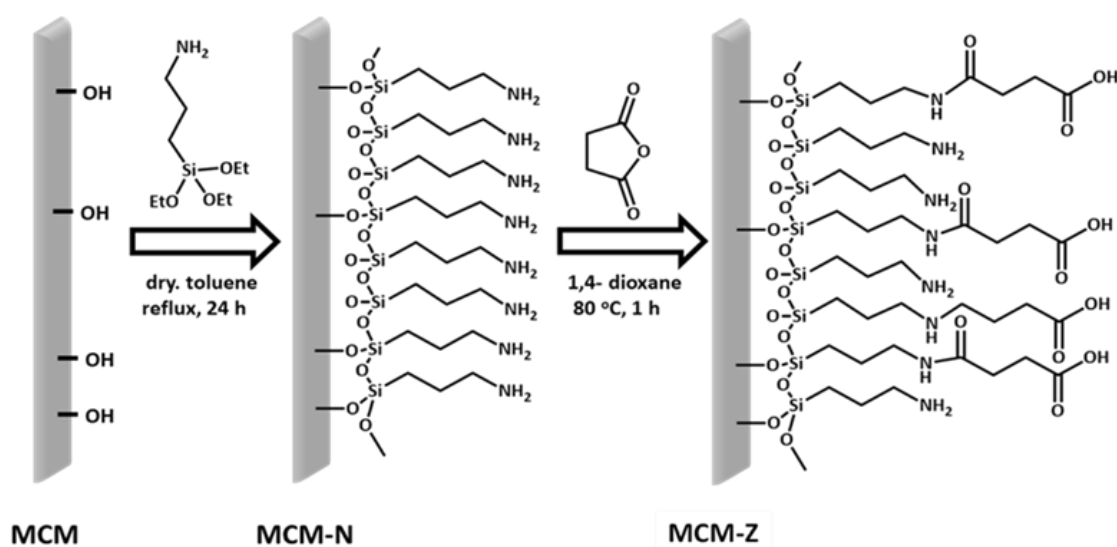


**Figure 2.** Schematic showing the synthetic strategy for functionalization of MCM nanochannels to create pH-responsive heterofunctionalized **MCM-Z** nanochannels.

#### Calculation of quantitative coverage of functionalization.

For MCM-N:

Amount of propylamine groups present in MCM-N = 2.0 mmol/g (From TGA measurements).

$$\begin{aligned}\text{Number of molecules of propylamine} &= 2.0 \text{ mmol} \times N_A / \text{g} \\ &= 1.204 \times 10^{21} \text{ molecules/g}\end{aligned}$$

$$\begin{aligned}\text{Surface area of MCM-41} &= 965 \text{ m}^2/\text{g} \\ &= 965 \times 10^{18} \text{ nm}^2/\text{g}\end{aligned}$$

$$\begin{aligned}\text{Number of propylamine groups per nm}^2 &= 1.204 \times 10^{21} \text{ molecules} / 965 \times 10^{18} \text{ nm}^2 \\ &= \mathbf{1.25 \text{ molecules} / \text{nm}^2}\end{aligned}$$

**For MCM-Z:**

Amount of carboxylic acid groups present in MCM-Z = 1.13 mmol/g

$$\begin{aligned}\text{Number of molecules of carboxylic acid moieties} &= 1.13 \text{ mmol} \times N_A / \text{g} \\ &= 6.804 \times 10^{20} \text{ molecules/g}\end{aligned}$$

$$\begin{aligned}\text{Number of carboxylic acid groups per nm}^2 &= 6.804 \times 10^{20} \text{ molecules} / 965 \times 10^{18} \text{ nm}^2 \\ &= \mathbf{0.71 \text{ molecules} / \text{nm}^2}\end{aligned}$$

**Zeta potential measurements.** A dispersion of MCM-N or **MCM-Z** having a concentration of 0.5 mg/mL in respective buffers was used for the zeta potential measurements. The measurements were carried out in a Zetasizer Nano ZS (Malvern, UK) employing a 532 nm laser at a backscattering angle of 173°. The temperature was always kept at 25 °C with the help of inbuilt thermostat in Zetasizer Nano ZS.

**CV<sup>+</sup> dye loading to MCM-Z.** Loading of CV<sup>+</sup> into the mesoporous channels of **MCM-Z** was achieved as follows. 5 mg of **MCM-Z** was dispersed in 1.95 mL pH 8.0 Tris-HCl buffer (10 mM). To this, a 0.05 mL of CV<sup>+</sup> solution (stock concentration of 0.5 mM) was added and the resultant dispersion was mixed well. After 15 min of gentle shaking, the dispersion was centrifuged to collect the CV<sup>+</sup> loaded **MCM-Z** and the supernatant was subjected to UV-Vis spectroscopy to calculate the loading amount.

**The pH-dependent CV<sup>+</sup> release from MCM-Z.** The CV<sup>+</sup>-loaded **MCM-Z** (5 mg) was dispersed in 3 mL buffer (10 mM) of respective pH. The aliquots (0.2 mL) were taken at regular intervals of 5 minutes to monitor the CV<sup>+</sup> release and the volume of the sample was adjusted with respective buffer. The amount of CV<sup>+</sup> released was monitored by UV-visible absorption spectroscopy.

**Stepwise release of CV<sup>+</sup> from MCM-Z.** CV<sup>+</sup> loaded **MCM-Z** (5 mg) was dispersed in 3 mL buffer (pH 8.5, 10 mM Tris-HCl buffer). The release was monitored every 5 minutes by collecting the supernatant by centrifugation. The pH of the dispersion was gradually decreased in small steps to pH 3.8 by sequentially replacing the supernatant with the same volume of the buffer solution of lower pH (pH 8.5, 7.0, 6.4, 5.0 and 3.8) at pre-determined time intervals.

**OR gate regulated release.** 5 mg of CV<sup>+</sup> loaded **MCM-Z** was dispersed in 2.5 mL buffer (pH 8.5, 10 mM) consisting of 5 U/mL of acetylcholinesterase (AChE) and 10 U/mL porcine liver esterase (PLE). A 0.5 mL buffer (pH 8.5, 10 mM) consisting of analytes (EA and acetylcholine as determined by the truth table) was prepared and the amount of analytes was taken in such a way that the final concentration of each analyte was 20 mM. The analytes solution was added to the above dispersion to trigger the release of cargo. The release was monitored via UV-Vis spectroscopy every 5 minutes by collecting the supernatant by centrifugation.

**INHIBIT gate regulated release.** 5 mg of CV<sup>+</sup> loaded **MCM-Z** was dispersed in 2.5 mL buffer (pH 8.5, 10 mM) consisting of 5 U/mL of acetylcholinesterase (AChE). A 0.5 mL buffer (pH 8.5, 10 mM) consisting of analytes (acetylcholine and neostigmine as determined by the truth table) was prepared and the amount of analytes was taken in such a way that the final concentration of acetylcholine was 20 mM and same for neostigmine was 30  $\mu$ M. The analytes solution was added to the above dispersion to trigger the release of cargo. The release was monitored via UV-Vis spectroscopy every 5 minutes by collecting the supernatant by centrifugation.

#### **1.3.4. Characterization**

Please see the appendix for the details of the instrumentation of UV-Visible spectroscopy, X-ray diffraction, FT-IR spectroscopy, Transmission electron microscopy, Field emission scanning electron microscopy (FESEM), nitrogen sorption analysis, thermogravimetric analysis (TGA), zeta potential measurements and pH measurements.

#### **1.3.5. Results and discussion**

Mesoporous silica spheres (MCM) (Figure 3a-c) were synthesized following a well-known sol-gel procedure and the surface was covalently modified with (3-

aminopropyl)triethoxysilane to obtain MCM-N with amine-functionalized surface. A portion of amine groups was then reacted with succinic anhydride to form **MCM-Z** with zwitterionic nature having carboxyl and amine groups on the nanochannel surface (Figure 2).

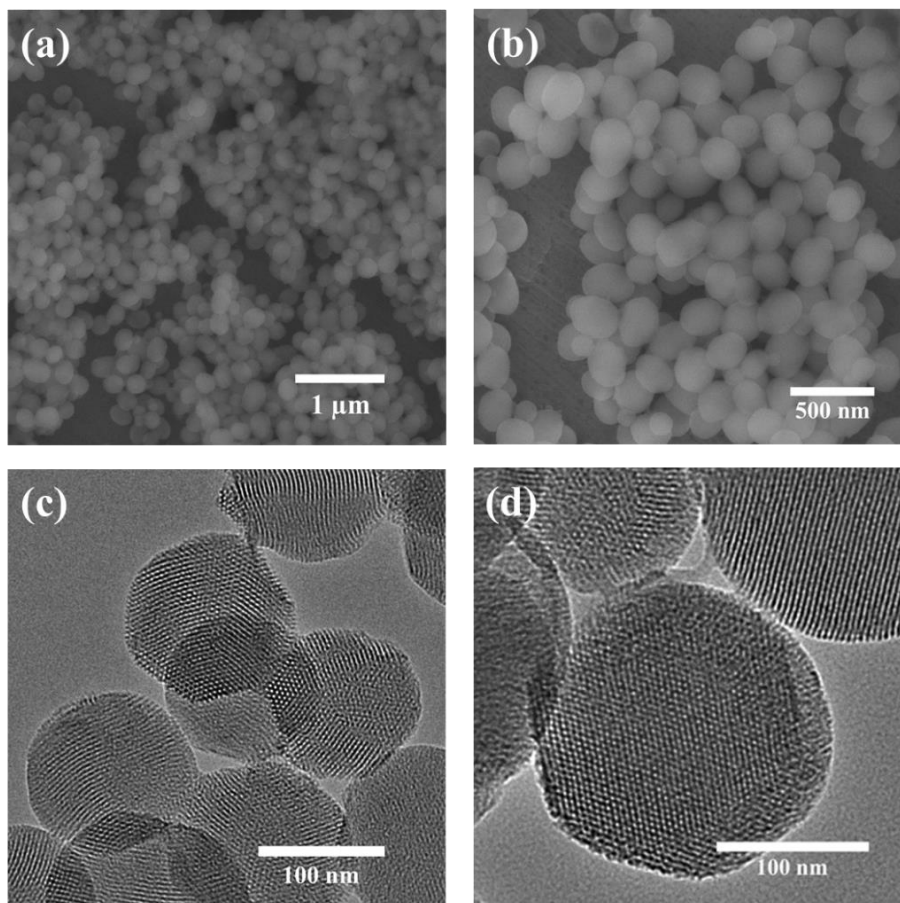


**Figure 3.** FE-SEM images of (a-b) MCM-41 at different magnifications. TEM images of (c) MCM and (d) **MCM-Z**.

The observation of low angle peak (at  $2\theta \approx 2.2$ ) in the XRD patterns of MCM, MCM-N and **MCM-Z** suggests that the hexagonal mesostructure was retained during functionalization (Figure 4b). Retention of mesostructure was also confirmed via transmission electron microscopy (Figure 3d). Thermogravimetric analysis (TGA) suggested propylamine functionalization in MCM-N was around ca.  $2.0 \text{ mmol g}^{-1}$  (Figure. 4a). The carboxylic acid groups ( $-\text{COOH}$ ) in **MCM-Z** was determined to be around ca.  $1.1 \text{ mmol g}^{-1}$  using TGA (Figure. 4a) and ninhydrin test (Figure. 5), which suggest that approximately 56% of amine groups were covalently connected (via amide linkage) to carboxylic acid groups in **MCM-Z**.



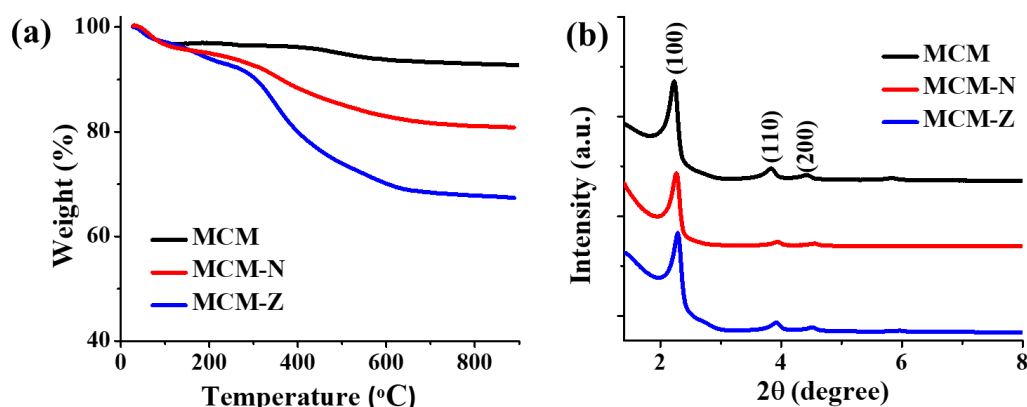


**Figure 4.** (a) Thermogravimetric analysis (TGA) curves of MCM, MCM-N and MCM-Z. (b) PXRD patterns of MCM, MCM-N and MCM-Z.

Nitrogen adsorption-desorption analyses were carried out at 77 K to evaluate the progress of functionalization inside the nanochannels (Figure 6a). The Barrett–Joyner–Halenda (BJH) pore size distributions showed a gradual reduction in average pore size from ca. 2.9 nm for MCM to 2.5 nm for MCM-N which further decreased to 2.2 nm for MCM-Z suggesting the progress of functionalization inside the nanochannels (Figure 6b). Furthermore, the number of propylamine groups on MCM-N was calculated to be 1.25 molecules per nm<sup>2</sup> area from N<sub>2</sub> sorption studies and TGA (see the experimental section for details). Similarly, in the case of MCM-Z, the number of carboxylic acid groups present was around 0.71 molecule per nm<sup>2</sup>.

The successful formation of MCM-Z was also confirmed via zeta potential measurements (Figure 7a). The zeta potential of MCM-N at pH 8 was found to be around + 30 ± 2 mV which changed to - 41 ± 1 mV for MCM-Z owing to the deprotonated carboxylic acid groups on the surface of the silica. The charge reversal of mesoporous silica (MCM-Z) was characterized through zeta potential measurements at different pH. When the pH was ca. 4.0, the surface showed a zeta potential about + 38 ± 1 mV due to protonation of amine groups. Upon increasing the pH, the zeta potential decreased to zero at a pH of about 6.0 (isoelectric point) and further decreased to - 40 ± 0.5 mV at pH 8.0 due to the formation of carboxylate groups (Figure 7b).

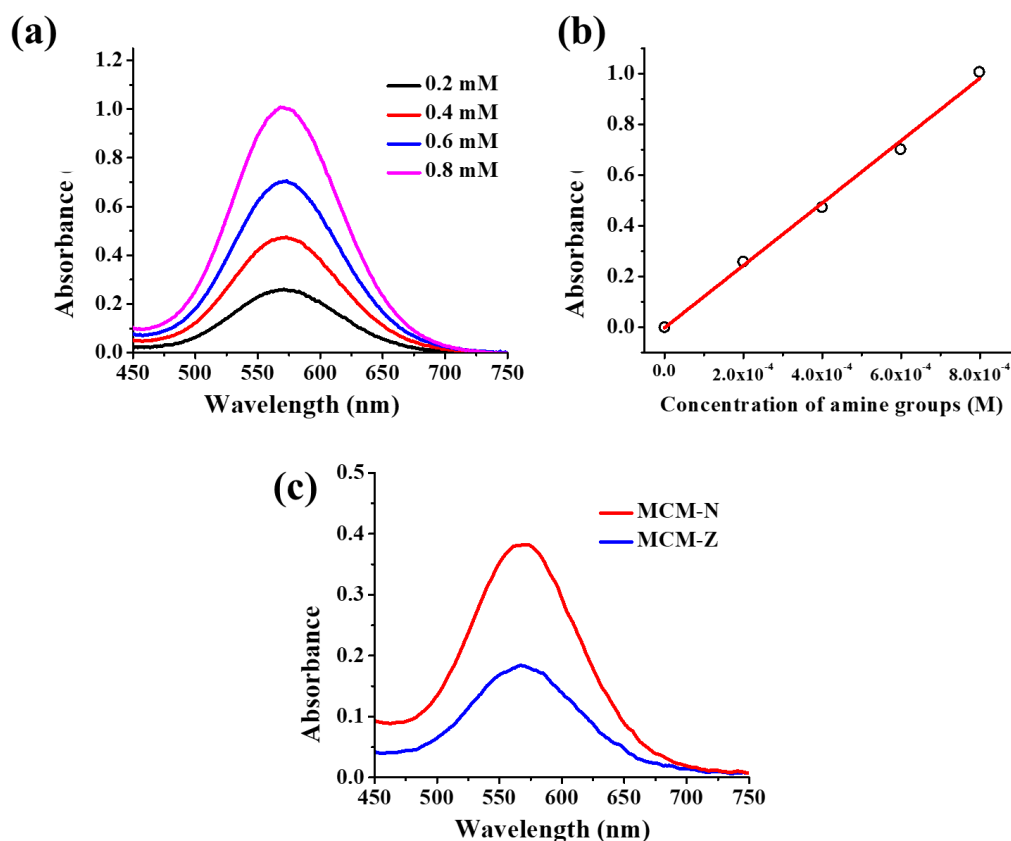


**Figure 5.** (a) UV-visible spectra of the ninhydrin complex in the propylamine solutions used for calibration. (b) Linear calibration plot showing an increase in absorbance with increase in propylamine used in the standard solution. This calibration plot was used to determine the concentration of amine groups in MCM-N and MCM-Z. (c) UV-visible spectra of the ninhydrin test to quantify the amount of amine groups in MCM-N and MCM-Z. The propylamine functionalization in MCM-Z is half of that in MCM-N.

The nanochannels with charged surfaces are known to display charge selective transport properties associated with the surface charge-dependent gating phenomena.<sup>60</sup> The pH-responsive charge reversal in MCM-Z was further demonstrated via charge based adsorption and desorption of a positively charged dye, crystal violet (CV<sup>+</sup>), which maintain a positive charge in the pH range 3.0 to 10 (Figure 8a).<sup>61-62</sup> The CV<sup>+</sup> was first loaded into the MCM-Z at pH 8.5 (about 5  $\mu\text{mol/g}$  loading) where the negatively charged silica surface and positively charged dye molecule attract each other via electrostatic interactions. The loaded CV<sup>+</sup> could be quantitatively released by carefully adjusting the surrounding pH. The pH dependent release of CV<sup>+</sup> from MCM-Z studied at different pH (Figure 8b), showed no significant release of dye at pH 8.5 owing to the strong

electrostatic attraction between the silica surface and dye molecules. However, a substantial release of CV<sup>+</sup> was observed at pH 3.8 owing to the electrostatic repulsion-

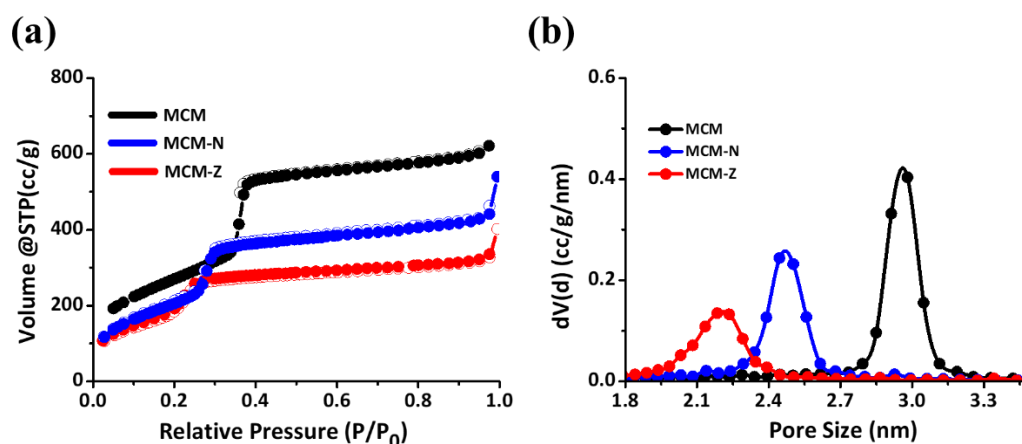


**Figure 6.** (a) Nitrogen adsorption-desorption isotherms and (b) Barrett-Joyner-Halenda pore size distribution curves of MCM, MCM-N and MCM-Z.

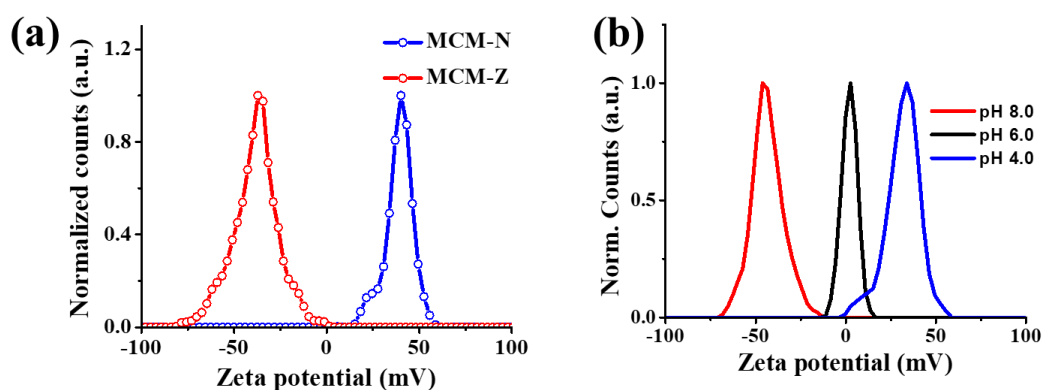


**Figure 7.** (a) Normalized zeta potential distribution curves of MCM-N and MCM-Z (in 10 mM tris buffer, pH 8.0). (b) Normalized zeta potential distribution of MCM-Z at different pH.

- (see the schematics in Figure 8b). It is interesting to note that the pH-dependent release of CV<sup>+</sup> from MCM-Z is highly quantitative in nature (Figure 8c). The desorption response was 8 % and 10 % at pH 8.5 and 7.0 respectively. However, the CV<sup>+</sup> desorption from MCM-Z was significantly increased to 28 % and 67 % at pH 5.0 and 3.8 respectively. It should be noted that CV<sup>+</sup> is not completely desorbed at pH 3.8, even though zeta potential measurements suggest positive surface charge at all pH less than 6.0. This can be explained by the fact that MCM-Z is a heterogeneously functionalized

system and the zeta potential provides only an overall charge of the system but not its spatial distribution.<sup>63</sup>

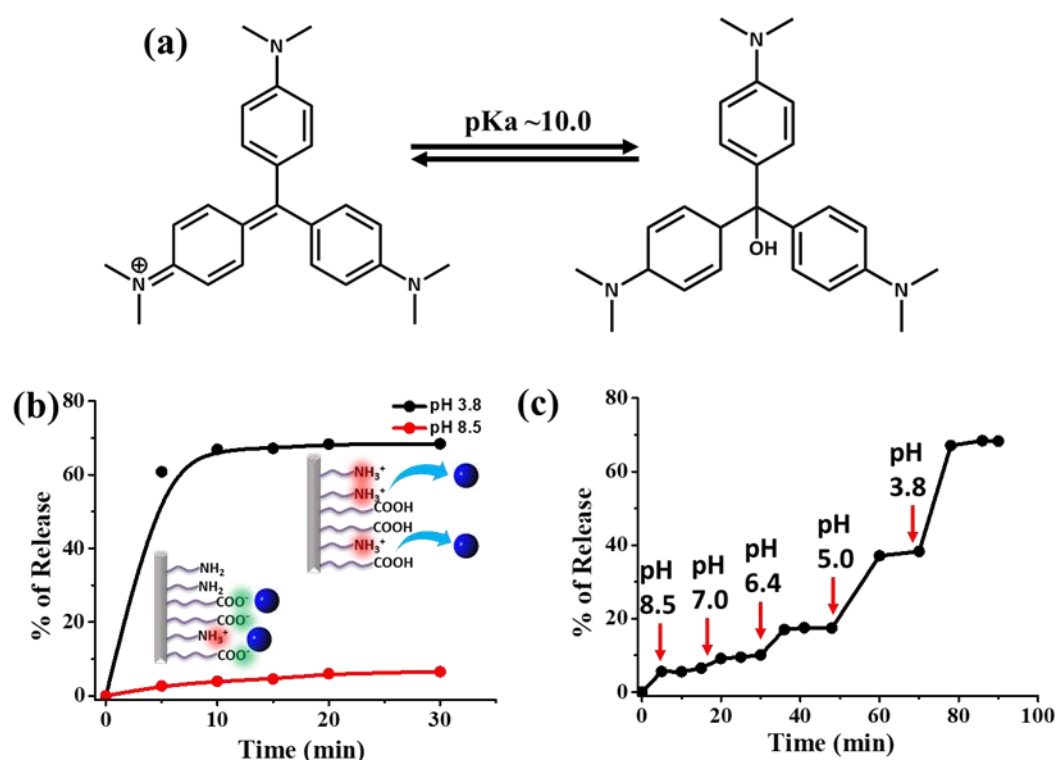


**Figure 8.** (a) The pH-dependent equilibrium existing in the case of CV<sup>+</sup>. During all our studies, the cationic state of CV<sup>+</sup> was utilized. (b) The release profile of CV<sup>+</sup> from the MCM-Z at pH 3.8 and pH 8.6. Schematics representing electrostatic attraction and repulsion between the CV<sup>+</sup> and the MCM-Z surface at respective pH. (c) Stepwise release profiles of CV<sup>+</sup> with increasing pH from MCM-Z.

Having established the release characteristics of CV<sup>+</sup> from MCM-Z, we went ahead with integrating the multi-analyte response in this MCM-Z. For this purpose, two enzymes were chosen- acetylcholinesterase (AChE) and porcine liver esterase (PLE). The substrates (analytes) were ethylacetate (EA), acetylcholine (Ach, which is the neurotransmitter used at the neuromuscular junction)<sup>64</sup> and neostigmine (a pharmaceutical drug used in the treatment of myasthenia gravis).<sup>65</sup> These enzymes and analytes were employed to change the pH of the solution in which CV<sup>+</sup> loaded MCM-Z was dispersed so that the release of CV<sup>+</sup> could be obtained in response to the analytes. Further, a combination of enzymes and analytes were used to construct a logic gate controlled release system. Before such a construction, it is necessary to make sure that the given enzyme only acts on the respective analyte. For this purpose, pH of the solution

was measured for AChE and PLE in presence of EA or ACh substrates (Figure. 9). Clearly, a pH change was observed only when the right enzyme-substrate combination was used. This high selectivity of enzymes for their respective substrates was illustrated using a  $2 \times 2$  identity matrix where the value 1 represents the enzyme reaction leading to pH fall whereas the value 0 represents no reaction (Figure. 9a). Further, the release of CV<sup>+</sup> from MCM-Z at pH 8.5 was also studied to confirm the substrates (in the absence of enzymes) used are not inducing any significant release (Figure. 10).

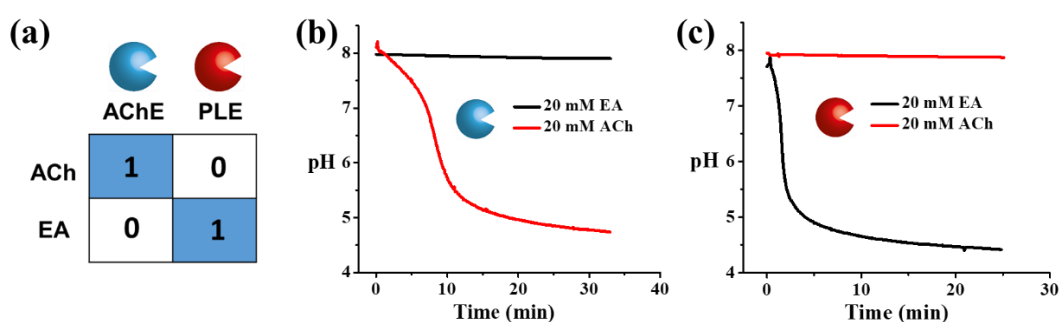


**Figure 9.** Control studies demonstrating the selectivity of the substrates towards the respective enzymes. (a) Identity matrix showing the high selectivity of enzymes to the respective substrates. Variation of the pH as a function of time for solution containing (b) 5 U/mL of acetylcholinesterase and (c) 10 U/mL porcine liver esterase with different substrates (acetylcholine and ethylacetate)

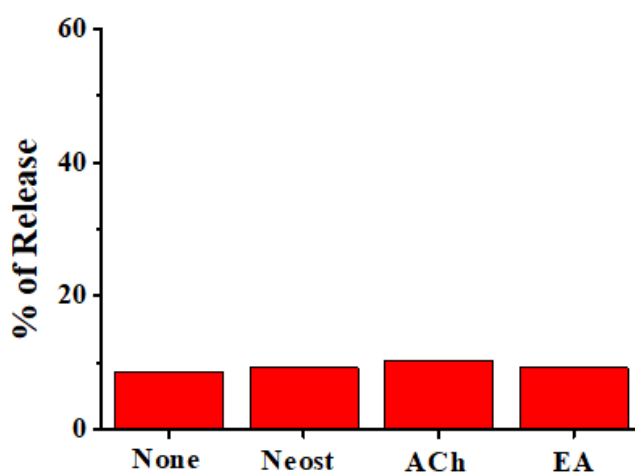


**Figure 10.** Effect of substrates (Neostigmine (Neost), Acetylcholine (ACh) and Ethylacetate (EA)) on the release of CV<sup>+</sup> from MCM-Z at pH 8.0.

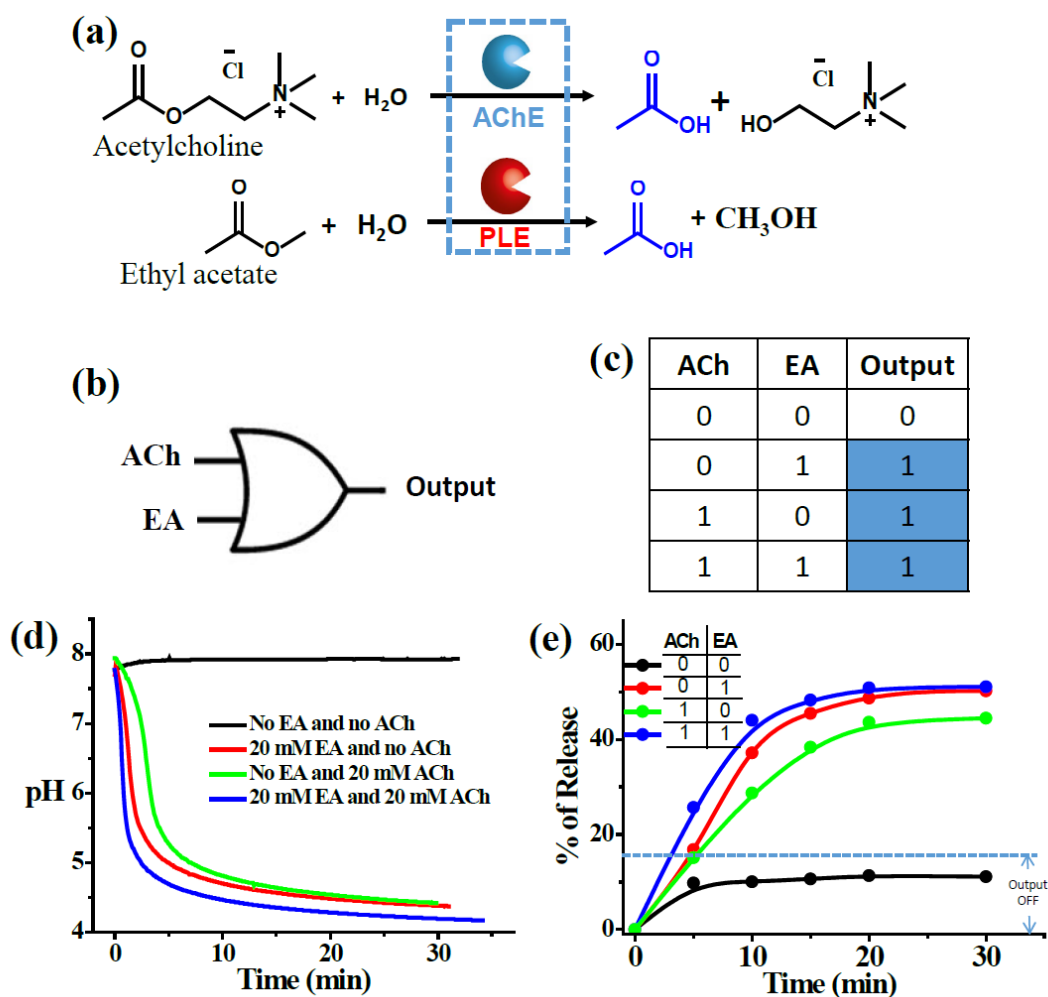


**Figure 11. OR Logic gate-controlled release of CV<sup>+</sup> from MCM-Z:** (a-b) Construction of OR gate using acetylcholine esterase and porcine liver esterase together. Presence of any one of the substrates or both together (ethylacetate or (and) acetylcholine) produces acetic acid and therefore triggers the release of CV<sup>+</sup> from MCM-Z. (c) The truth table corresponding to the OR logic gate. (d) The pH profiles of the solution consisting of both acetylcholine esterase and porcine liver esterase with different combinations of substrates. (e) Release profiles of CV<sup>+</sup> from MCM-Z in presences of different combinations of substrates showing an OR gated release.

After establishing the pH-responsive release properties of MCM-Z and high selectivity of enzymes, we devised a general strategy to obtain logic gate-controlled release by suitably programming the surrounding solution. Firstly we opted to demonstrate an OR gate (Figure. 11b-c). For this purpose, we have taken AChE and PLE in the solution (5.4 U/mL and 10 U/mL respectively) along with CV<sup>+</sup>-loaded MCM-Z (Figure. 11a) at pH 8.5. This system was expected to reduce the pH of the solution in

presence of either of the substrates or both. In presence of acetylcholine, AChE acts on this substrate to produce acetic acid and choline (Figure. 11a). The acetic acid formed reduces the pH close to the pKa of the acetic acid (Figure. 11d). Similarly, in presence of ethylacetate (EA), PLE acting on it to produce acetic acid which again brings down the pH to about 4.5. If both the substrates were present, a similar reduction of pH was again observed. This pH reduction triggers the release of CV<sup>+</sup> from **MCM-Z** owing to the pH-dependent charge reversal in the nanochannels (Figure. 11e). In absence of any of the substrates, only a marginal release of CV<sup>+</sup> was observed. However, in presence of both EA and ACh or either of EA or ACh, CV<sup>+</sup> loaded **MCM-Z** showed significant release of more than 40 %. It represents a typical OR logic gate with corresponding truth table (Figure 11c). These release profiles in response to various combinations of analytes mark a successful attempt to develop **MCM-Z** and enzymes based processing unit with OR gate operation.

The strategy was further extended to construct an INH gate (Figure. 12b). For this we have utilized AChE enzyme and its inhibitor – neostigmine (Figure. 12a). Neostigmine binds to the esteric and anionic sites of AChE effectively inhibiting the activity of the enzyme. The pH profile of this INHBIT logic system shows a pH response (from ca. 8.0 to ca. 4.5) in presence of acetylcholine (ACh) alone (Figure. 12d). When both ACh and neostigmine were present, the pH did not change initially. However, after some time, pH slowly started to decrease because of the competitive nature of AChE inhibition by neostigmine. Nevertheless, the pH didn't decrease below ca. 7.0 which is still in the regime where **MCM-Z** shows negative surface charge and therefore only marginal release was observed. The release profile of CV<sup>+</sup> from **MCM-Z** clearly showed a significant release only in the presence of acetylcholine (ACh) alone (corresponding to an input of (0, 1)) (Figure 12 c, e). In the case of both ACh and neostigmine, the inhibition of AChE caused a low release of CV<sup>+</sup> from **MCM-Z**. Similar marginal release was observed when no inputs or only neostigmine was used (Figure 12 c, e). These release profiles in response to various combinations of analytes demonstrate a successful effort to obtain **MCM-Z** and enzymes based processing unit with INHBIT gate operation.

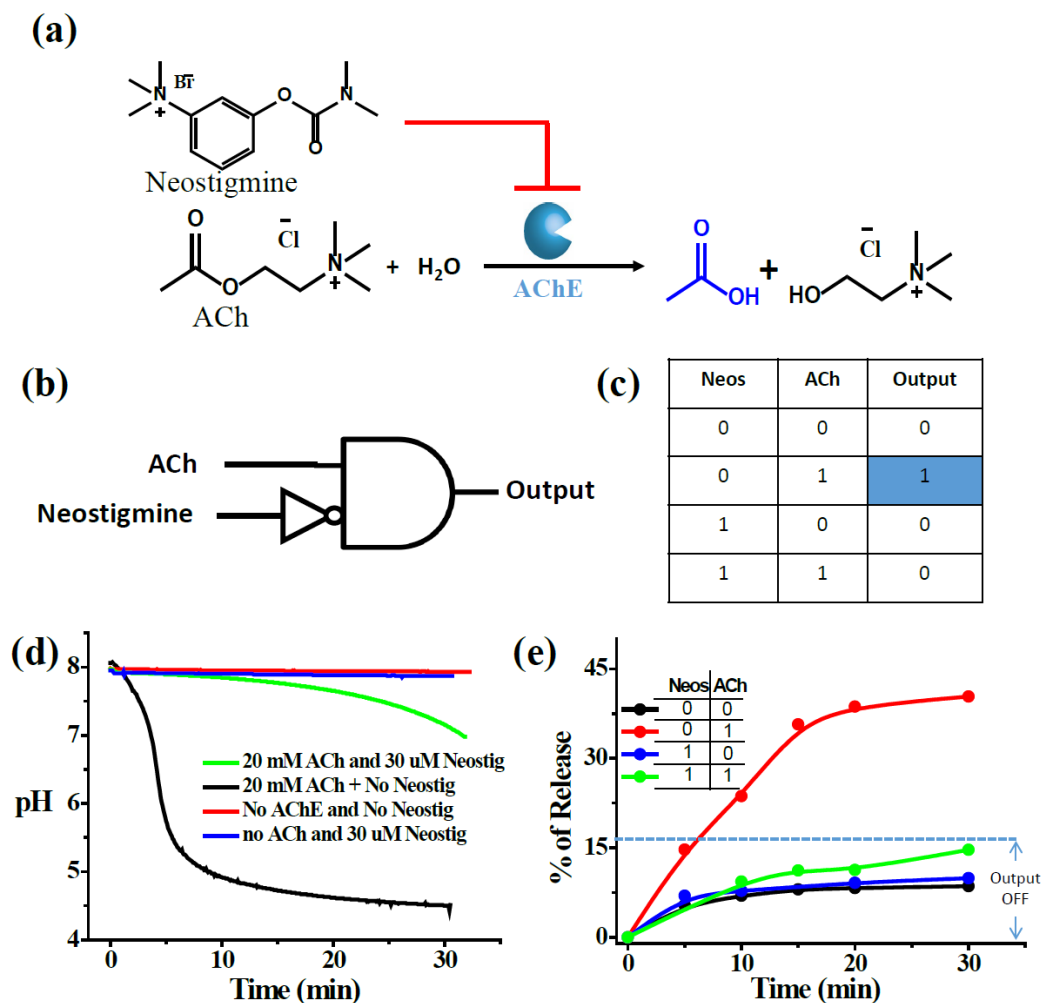


**Figure 12. INH Logic gate controlled release of  $CV^+$  from MCM-Z:** (a-b) Construction of INHIBIT gate using acetylcholine esterase. Presence of acetylcholine substrate produces acetic acid and therefore trigger the release of  $CV^+$  from MCM-Z. Neostigmine inhibit the activity of the acetylcholine esterase, and hence no acetic acid formation so no release of  $CV^+$  will be observed. (c) The truth table corresponding to INHIBIT logic gate. (d) The pH profiles of the solution consisting of acetylcholine esterase and different combinations of substrates (neostigmine and acetylcholine). (e) Release profiles of  $CV^+$  from MCM-Z in presences of different combinations of substrates showing a INHIBIT gated release.

### 1.3.6. Conclusions

In conclusion, we have successfully demonstrated a generic strategy to utilize the mesoporous silica in combination with certain enzymes as a logic gate information processing unit. The release of cargo from mesoporous silica was interpreted as the output read out. The strategy involves a pH dependent charge reversal silica and pH



switchable medium consisting of selected combination of enzymes. In this proof-of-concept design, release of cargo from the mesoporous silica was achieved via an OR gated and INH gated manner in response to substrates such as ethylacetate, acetylcholine and neostigmine. The generic strategy presented in this chapter could further extended to achieve number of other logic gates as well and therefore expected to widen the scope of mesoporous silica based information processing and security systems.

### 1.3.7. References

- (1) de Silva, P. A.; Gunaratne, N. H. Q.; McCoy, C. P. A molecular photoionic AND gate based on fluorescent signalling. *Nature* **1993**, *364* (6432), 42-44.
- (2) de Silva, A. P.; Uchiyama, S. Molecular logic and computing. *Nat. Nanotechnol* **2007**, *2*, 399.
- (3) de Silva, A. P. A layer of logic. *Nature* **2008**, *454*, 417.
- (4) De Silva, A. P. Molecular logic gets loaded. *Nat. Mater.* **2005**, *4* (1), 15-16.
- (5) Silva, A. P. d. *Molecular Logic-based Computation* Royal Society of Chemistry; 1 edition (November 29, 2012): 2012.
- (6) de Silva, A. P.; Dixon, I. M.; Gunaratne, H. Q. N.; Gunnlaugsson, T.; Maxwell, P. R. S.; Rice, T. E. Integration of Logic Functions and Sequential Operation of Gates at the Molecular-Scale. *J. Am. Chem. Soc.* **1999**, *121* (6), 1393-1394.
- (7) de Silva, A. P.; McClenaghan, N. D. Molecular-Scale Logic Gates. *Chem.: Eur. J.* **2004**, *10* (3), 574-586.
- (8) de Silva, A. P.; Gunaratne, H. Q. N.; McCoy, C. P. Molecular Photoionic AND Logic Gates with Bright Fluorescence and “Off-On” Digital Action. *J. Am. Chem. Soc.* **1997**, *119* (33), 7891-7892.
- (9) Uchiyama, S.; Kawai, N.; de Silva, A. P.; Iwai, K. Fluorescent Polymeric AND Logic Gate with Temperature and pH as Inputs. *J. Am. Chem. Soc.* **2004**, *126* (10), 3032-3033.
- (10) Magri, D. C.; Brown, G. J.; McClean, G. D.; de Silva, A. P. Communicating Chemical Congregation: A Molecular AND Logic Gate with Three Chemical Inputs as a “Lab-on-a-Molecule” Prototype. *J. Am. Chem. Soc.* **2006**, *128* (15), 4950-4951.
- (11) Prasanna de Silva, A. Molecular Logic Gate Arrays. *Chem.: Asian J.* **2011**, *6* (3), 750-766.

- 
- 
- (12) de Silva, A. P.; Uchiyama, S.; Vance, T. P.; Wannalarse, B. A supramolecular chemistry basis for molecular logic and computation. *Coord. Chem. Rev.* **2007**, *251* (13), 1623-1632.
- (13) de Silva, A. P.; Vance, T. P.; West, M. E. S.; Wright, G. D. Bright molecules with sense, logic, numeracy and utility. *Org. Biomol. Chem* **2008**, *6* (14), 2468-2480.
- (14) de Silva, A. P.; Gunaratne, H. Q. N.; Maguire, G. E. M. 'Off-on' fluorescent sensors for physiological levels of magnesium ions based on photoinduced electron transfer (PET), which also behave as photoionic OR logic gates. *J. Chem. Soc., Chem. Commun.* **1994**, (10), 1213-1214.
- (15) de Silva, A. P.; Dobbin, C. M.; Vance, T. P.; Wannalarse, B. Multiply reconfigurable 'plug and play' molecular logic via self-assembly. *Chem. Commun.* **2009**, (11), 1386-1388.
- (16) Callan, J. F.; de Silva, A. P.; McClenaghan, N. D. Switching between molecular switch types by module rearrangement: Ca<sup>2+</sup>-enabled, H<sup>+</sup>-driven 'Off-On-Off', H<sup>+</sup>-driven YES and PASS 0 as well as H<sup>+</sup>, Ca<sup>2+</sup>-driven AND logic operations. *Chem. Commun.* **2004**, (18), 2048-2049.
- (17) de Silva, A. P.; McClenaghan, N. D. Simultaneously Multiply-Configurable or Superposed Molecular Logic Systems Composed of ICT (Internal Charge Transfer) Chromophores and Fluorophores Integrated with One- or Two-Ion Receptors. *Chem.: Eur. J.* **2002**, *8* (21), 4935-4945.
- (18) Magri, D. C.; Vance, T. P.; de Silva, A. P. From complexation to computation: Recent progress in molecular logic. *Inorg. Chim. Acta* **2007**, *360* (3), 751-764.
- (19) de Silva, A. P. Luminescent Photoinduced Electron Transfer (PET) Molecules for Sensing and Logic Operations. *J. Phys. Chem. Lett* **2011**, *2* (22), 2865-2871.
- (20) Ling, J.; Daly, B.; Silversen, V. A. D.; de Silva, A. P. Taking baby steps in molecular logic-based computation. *Chem. Commun.* **2015**, *51* (40), 8403-8409.
- (21) Magri, D. C.; de Silva, A. P. From PASS 1 to YES to AND logic: building parallel processing into molecular logic gates by sequential addition of receptors. *New J. Chem.* **2010**, *34* (3), 476-481.
- (22) Douglas, S. M.; Bachelet, I.; Church, G. M. A Logic-Gated Nanorobot for Targeted Transport of Molecular Payloads. *Science* **2012**, *335* (6070), 831-834.
- (23) Raymo, F. M. Digital Processing and Communication with Molecular Switches. *Adv. Mater.* **2002**, *14* (6), 401-414.

- (24) Margulies, D.; Felder, C. E.; Melman, G.; Shanzer, A. A Molecular Keypad Lock: A Photochemical Device Capable of Authorizing Password Entries. *J. Am. Chem. Soc.* **2007**, *129* (2), 347-354.
- (25) Collier, C. P.; Wong, E. W.; Belohradský, M.; Raymo, F. M.; Stoddart, J. F.; Kuekes, P. J.; Williams, R. S.; Heath, J. R. Electronically Configurable Molecular-Based Logic Gates. *Science* **1999**, *285* (5426), 391-394.
- (26) Akkaya, E. U.; Katz, E.; Pischel, U. Molecular Logic: From Single Logic Gates to Sophisticated Logic Circuits, from Fundamental Science to Practical Applications. *ChemPhysChem* **2017**, *18* (13), 1665-1666.
- (27) Erbas-Cakmak, S.; Kolemen, S.; Sedgwick, A. C.; Gunnlaugsson, T.; James, T. D.; Yoon, J.; Akkaya, E. U. Molecular logic gates: the past, present and future. *Chem. Soc. Rev.* **2018**, *47* (7), 2228-2248.
- (28) Ikeda, M.; Tanida, T.; Yoshii, T.; Kurotani, K.; Onogi, S.; Urayama, K.; Hamachi, I. Installing logic-gate responses to a variety of biological substances in supramolecular hydrogel–enzyme hybrids. *Nat. Chem.* **2014**, *6*, 511.
- (29) Bi, S.; Yan, Y.; Hao, S.; Zhang, S. Colorimetric Logic Gates Based on Supramolecular DNzyme Structures. *Angew. Chem. Int. Ed.* **2010**, *49* (26), 4438-4442.
- (30) Komatsu, H.; Matsumoto, S.; Tamaru, S.-i.; Kaneko, K.; Ikeda, M.; Hamachi, I. Supramolecular Hydrogel Exhibiting Four Basic Logic Gate Functions To Fine-Tune Substance Release. *J. Am. Chem. Soc.* **2009**, *131* (15), 5580-5585.
- (31) Maligaspe, E.; D'Souza, F. NOR and AND Logic Gates Based on Supramolecular Porphyrin–Fullerene Conjugates. *Org. Lett.* **2010**, *12* (3), 624-627.
- (32) Lin, G.; Lin, Y.; Cui, R.; Huang, H.; Guo, X.; Li, C.; Dong, J.; Guo, X.; Sun, B. An organic–inorganic hybrid perovskite logic gate for better computing. *J. Mater. Chem. C* **2015**, *3* (41), 10793-10798.
- (33) Du, J.; Yin, S.; Jiang, L.; Ma, B.; Chen, X. A colorimetric logic gate based on free gold nanoparticles and the coordination strategy between melamine and mercury ions. *Chem. Commun.* **2013**, *49* (39), 4196-4198.
- (34) Liu, D.; Chen, W.; Sun, K.; Deng, K.; Zhang, W.; Wang, Z.; Jiang, X. Resettable, Multi-Readout Logic Gates Based on Controllably Reversible Aggregation of Gold Nanoparticles. *Angew. Chem. Int. Ed.* **2011**, *50* (18), 4103-4107.

- (35) Xu, X.; Zhang, J.; Yang, F.; Yang, X. Colorimetric logic gates for small molecules using split/integrated aptamers and unmodified gold nanoparticles. *Chem. Commun.* **2011**, 47 (33), 9435-9437.
- (36) de la Rosa, V. R.; Zhang, Z.; De Geest, B. G.; Hoogenboom, R. Colorimetric Logic Gates Based on Poly(2-alkyl-2-oxazoline)-Coated Gold Nanoparticles. *Adv. Funct. Mater* **2015**, 25 (17), 2511-2519.
- (37) Oliveira-Silva, R.; Pereira, R. A.; Silva, F. M.; Gaspar, V. M.; Ibarra, A.; Millán, Á.; Sousa, F. L.; Mano, J. F.; Silva, N. J. O. Temperature-responsive nanomagnetic logic gates for cellular hyperthermia. *Mater. Horizons* **2019**, 6 (3), 524-530.
- (38) Hu, Y.; Wu, Y.; Mukherjee, M.; Cao, B. A near-infrared light responsive c-di-GMP module-based AND logic gate in *Shewanella oneidensis*. *Chem. Commun.* **2017**, 53 (10), 1646-1648.
- (39) Jochum, F. D.; Forst, F. R.; Theato, P. PNIPAM Copolymers Containing Light-Responsive Chromophores: A Method Toward Molecular Logic Gates. *Macromol. Rapid Commun* **2010**, 31 (16), 1456-1461.
- (40) Suresh, M.; Ghosh, A.; Das, A. Half-subtractor operation in pH responsive N-heterocyclic amines. *Tetrahedron Lett.* **2007**, 48 (46), 8205-8208.
- (41) Qi, H.; Yue, S.; Bi, S.; Ding, C.; Song, W. DNA logic assembly powered by a triplex-helix molecular switch for extracellular pH imaging. *Chem. Commun.* **2018**, 54 (61), 8498-8501.
- (42) Wang, M.; Zhang, G.; Zhang, D. Enzyme-driven i-motif DNA folding for logic operations and fluorescent biosensing. *Chem. Commun.* **2015**, 51 (18), 3812-3815.
- (43) Gupta, T.; van der Boom, M. E. Redox-Active Monolayers as a Versatile Platform for Integrating Boolean Logic Gates. *Angew. Chem. Int. Ed.* **2008**, 47 (29), 5322-5326.
- (44) Freeman, R.; Finder, T.; Willner, I. Multiplexed Analysis of Hg<sup>2+</sup> and Ag<sup>+</sup> Ions by Nucleic Acid Functionalized CdSe/ZnS Quantum Dots and Their Use for Logic Gate Operations. *Angew. Chem. Int. Ed.* **2009**, 48 (42), 7818-7821.
- (45) Lien, C.-W.; Chen, Y.-C.; Chang, H.-T.; Huang, C.-C. Logical regulation of the enzyme-like activity of gold nanoparticles by using heavy metal ions. *Nanoscale* **2013**, 5 (17), 8227-8234.

- (46) Zhao, L.; Wang, S.; Wu, Y.; Hou, Q.; Wang, Y.; Jiang, S. Salicylidene Schiff Base Assembled with Mesoporous Silica SBA-15 as Hybrid Materials for Molecular Logic Function. *J. Phys. Chem. C* **2007**, *111* (49), 18387-18391.
- (47) Lin, X.; Liu, Y.; Deng, J.; Lyu, Y.; Qian, P.; Li, Y.; Wang, S. Multiple advanced logic gates made of DNA-Ag nanocluster and the application for intelligent detection of pathogenic bacterial genes. *Chem. Sci.* **2018**, *9* (7), 1774-1781.
- (48) Xiao, S. J.; Hu, P. P.; Chen, L. Q.; Zhen, S. J.; Peng, L.; Li, Y. F.; Huang, C. Z. A Visual Dual-Aptamer Logic Gate for Sensitive Discrimination of Prion Diseases-Associated Isoform with Reusable Magnetic Microparticles and Fluorescence Quantum Dots. *PLOS ONE* **2013**, *8* (2), e53935.
- (49) Gust, D.; Andréasson, J.; Pischel, U.; Moore, T. A.; Moore, A. L. Data and signal processing using photochromic molecules. *Chem. Commun.* **2012**, *48* (14), 1947-1957.
- (50) Andréasson, J.; Pischel, U.; Straight, S. D.; Moore, T. A.; Moore, A. L.; Gust, D. All-Photonic Multifunctional Molecular Logic Device. *J. Am. Chem. Soc.* **2011**, *133* (30), 11641-11648.
- (51) Aznar, E.; Casasús, R.; García-Acosta, B.; Marcos, M. D.; Martínez-Máñez, R.; Sancenón, F.; Soto, J.; Amorós, P. Photochemical and Chemical Two-Channel Control of Functional Nanogated Hybrid Architectures. *Adv. Mater.* **2007**, *19* (17), 2228-2231.
- (52) Wen, Y.; Xu, L.; Li, C.; Du, H.; Chen, L.; Su, B.; Zhang, Z.; Zhang, X.; Song, Y. DNA-based intelligent logic controlled release systems. *Chem. Commun.* **2012**, *48* (67), 8410-8412.
- (53) Angelos, S.; Yang, Y.-W.; Khashab, N. M.; Stoddart, J. F.; Zink, J. I. Dual-Controlled Nanoparticles Exhibiting AND Logic. *J. Am. Chem. Soc.* **2009**, *131* (32), 11344-11346.
- (54) Zhao, J.; He, Z.; Li, B.; Cheng, T.; Liu, G. AND logic-like pH- and light-dual controlled drug delivery by surface modified mesoporous silica nanoparticles. *Mater. Sci. Eng. C* **2017**, *73*, 1-7.
- (55) Díez, P.; Sánchez, A.; Gamella, M.; Martínez-Ruíz, P.; Aznar, E.; de la Torre, C.; Murguía, J. R.; Martínez-Máñez, R.; Villalonga, R.; Pingarrón, J. M. Toward the Design of Smart Delivery Systems Controlled by Integrated Enzyme-Based Biocomputing Ensembles. *J. Am. Chem. Soc.* **2014**, *136* (25), 9116-9123.

- 
- 
- (56) Zhou, S.; Du, X.; Cui, F.; Zhang, X. Multi-Responsive and Logic Controlled Release of DNA-Gated Mesoporous Silica Vehicles Functionalized with Intercalators for Multiple Delivery. *Small* **2014**, *10* (5), 980-988.
- (57) Chen, X., Soeriyadi, A. H., Lu, X., Sagnella, S. M., Kavallaris, M. and Gooding, J. J. . Dual Bioresponsive Mesoporous Silica Nanocarrier as an “AND” Logic Gate for Targeted Drug Delivery Cancer Cells. *Adv. Funct. Mater* **2014**, *24* (44), 6999-7006.
- (58) Tregubov, A. A.; Nikitin, P. I.; Nikitin, M. P. Advanced Smart Nanomaterials with Integrated Logic-Gating and Biocomputing: Dawn of Theranostic Nanorobots. *Chem. Rev.* **2018**, *118* (20), 10294-10348.
- (59) Huh, S.; Wiench, J. W.; Yoo, J.-C.; Pruski, M.; Lin, V. S. Y. Organic Functionalization and Morphology Control of Mesoporous Silicas via a Co-Condensation Synthesis Method. *Chem. Mater.* **2003**, *15* (22), 4247-4256.
- (60) Sparreboom, W.; van den Berg, A.; Eijkel, J. C. T. Principles and applications of nanofluidic transport. *Nat. Nanotechnol* **2009**, *4*, 713.
- (61) Fisk, J. D.; Batten, R.; Jones, G.; O'Reill, J. P.; Shaw, A. M. pH Dependence of the Crystal Violet Adsorption Isotherm at the Silica–Water Interface. *J. Phys. Chem. B* **2005**, *109* (30), 14475-14480.
- (62) Manzo, V.; Navarro, O.; Honda, L.; Sánchez, K.; Inés Toral, M.; Richter, P. Determination of crystal violet in water by direct solid phase spectrophotometry after rotating disk sorptive extraction. *Talanta* **2013**, *106*, 305-308.
- (63) B. V. V. S. Pavan; Salikolimi, K.; Eswaramoorthy, M. Glucose- and pH-Responsive Charge-Reversal Surfaces. *Langmuir* **2014**, *30* (16), 4540-4544.
- (64) Hasselmo, M. E. Neuromodulation: acetylcholine and memory consolidation. *Trends Cogn. Sci.* **1999**, *3* (9), 351-359.
- (65) Trevisani, G. T.; Hyman, N. H.; Church, J. M. Neostigmine. *Dis. Colon Rectum* **2000**, *43* (5), 599-603.

## **PART - 2**

**Chapter 2.1: Introduction to Bio-inspired Temporally Regulated Functional Materials**

**Chapter 2.2: Bio-inspired Temporal Regulation of Ion-Transport in Nanochannels**

**Chapter 2.3: Bio-inspired Temporal Control of Catalytic Activity of a Nanozyme**

**Chapter 2.4: Bio-inspired Temporally Programmed Switching in Dual Functional Polymer Film**



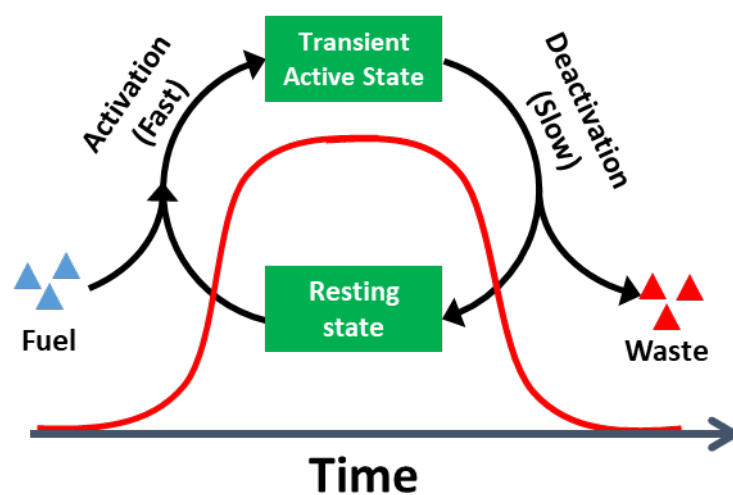


## Chapter 2.1

### *Introduction to Bio-inspired Temporally Regulated Functional Materials*

#### **Summary:**

*Living systems are distinctly different from man-made systems in terms of their features such as metabolism, energy consumption, temporal regulation, adaptation, self-replication and transience. These features often result from the spatiotemporal control of structures and functions. The spatiotemporal regulations occur via signalling, enzymatic regulatory networks, feedback loops, energy dissipation etc. Recently, efforts have been made to mimic these machineries for fabricating intelligent, autonomous, transient functional systems. This chapter aims to provide an overview of temporally regulated transient functional systems with an emphasis on various design principles.*





### 2.1.1. Temporal Control in Stimuli-Responsive Switchable Systems.

Smart materials with stimuli-responsive features are getting increasing attention in recent years for their on-demand performance in controlled release<sup>1-2</sup>, actuation<sup>3-4</sup>, photonics<sup>5-6</sup> etc. These materials switch between states, functionally active and inactive states in response to stimuli such as light<sup>7-8</sup>, temperature<sup>9-10</sup>, pH<sup>11-13</sup>, redox conditions<sup>14-15</sup> etc., and such switchability often relies on the responsiveness of constituent molecular motifs. On a conceptual level, such transitions are passive (*classical responsive systems*), where they always need an outside trigger to induce one-way transformation between two or more thermodynamically stable states.<sup>16-17</sup> When moved from one stable state to another, they remain stable unless otherwise an external trigger is used to revert the system to the initial state. Clearly, this type of stimuli-responsive systems does not show the self-regulation or autonomous temporal control over their functional states (passive in the time domain). On the contrary, biological systems show autonomous, temporally-

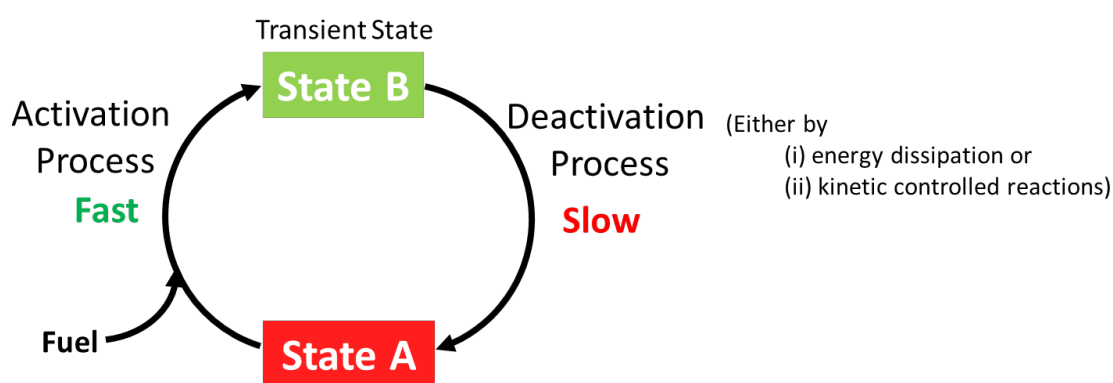


**Figure 1.** Self-regulated systems temporally regulated state B (transient) by employing the appropriate activation and deactivation pathways. The activation of switching from state A (initial state) is faster compared to the deactivation step ( $k_{\text{activation}} \gg k_{\text{deactivation}}$ ). By carefully tuning the rates of these pathways, the lifetime of the transient B state can be regulated.

-controlled switching between the active and inactive states orchestrated through energy dissipative and kinetically controlled processes (*self-regulated, temporally controlled systems*).<sup>18-20</sup> The term ‘temporal control’ is used in this context to collectively describe the processes of activation and deactivation, which leads to transient (temporary) active state with pre-programmed lifetime (Figure 1). Such transient states can be achieved by employing appropriate activation and deactivation pathways.<sup>21</sup> Further, these pathways

need to be precisely regulated in the time co-ordinate. The system can adopt either temporally regulated activation pathway (with unregulated deactivation)<sup>22</sup> or temporally regulated deactivation pathways (with unregulated activation).<sup>18</sup> In addition, systems can also have temporal control over both activation and deactivation pathways.<sup>23</sup> However, the principal condition is that activation pathway (or process) should be significantly faster than the deactivation.<sup>18</sup> In the deactivation process the system (which is in the high energy state) reaches the original state by energy dissipative mechanism or else it (deactivation) can be induced through kinetically controlled catalytic processes.<sup>18, 24-25</sup> In this chapter, we will discuss energy dissipative mechanism and kinetically controlled approaches for achieving temporally controlled transient state in switchable systems.

**2.1.1.1 Systems with Energy Dissipative Deactivation Route.** In case of energy dissipation, the active state is maintained far from equilibrium with a constant supply of energy. They have inherent structural urge to return to their low energy state (i.e. the initial state) by dissipating energy to the surrounding.<sup>26</sup> The energy dissipative system can be identified depending upon the energy source: i.e., chemical fuel molecules<sup>27-28</sup> or external energy sources such as light<sup>22, 29-30</sup>, magnetic field<sup>31</sup> etc.

Chemically fuelled dissipative systems offer a higher level of temporal regulation (or autonomous behaviour) as the activation and deactivation processes occur through direct chemical modification of building blocks (Figure 2a).<sup>27-28</sup> These activation and deactivation processes can be fine-tuned to precisely control the time domain of the active state. A well-studied example for temporally controlled energy dissipative system is microtubule (an important component for cellular functions such as mobility and cell division).<sup>32-34</sup> The microtubules are formed through the self-assembly of the building block (the tubulin proteins). The tubulin is a dimer consisting of two closely related polypeptides, namely  $\alpha$ -tubulin and  $\beta$ -tubulin (Figure 2b). The microtubules are consisting of tubulin dimer arranged in a head-to-tail manner. Therefore, the microtubules can be seen as polar structures with two distinct ends ( $\beta$ -tubulin monomer pointing towards the faster-growing end (plus end) and their  $\alpha$ -tubulin monomer exposed at the slower-growing end (minus end)) (Figure 2b). The polymerization of tubulin dimer to microtubule occurs only if the monomers are activated by a chemical fuel molecule, GTP (Guanosine triphosphate) binding (the activation route). The self-assembled activated building blocks are at the high energy state and therefore, the GTP bound to

the  $\beta$ -tubulin is prone to hydrolysis (to result in GDP-tubulin) which deactivation route. Once the hydrolysis does occur, the microtubules become highly unstable as the stored energy in the lattice is released, and this results in a rapid shrinking of the microtubule (Figure 2c).

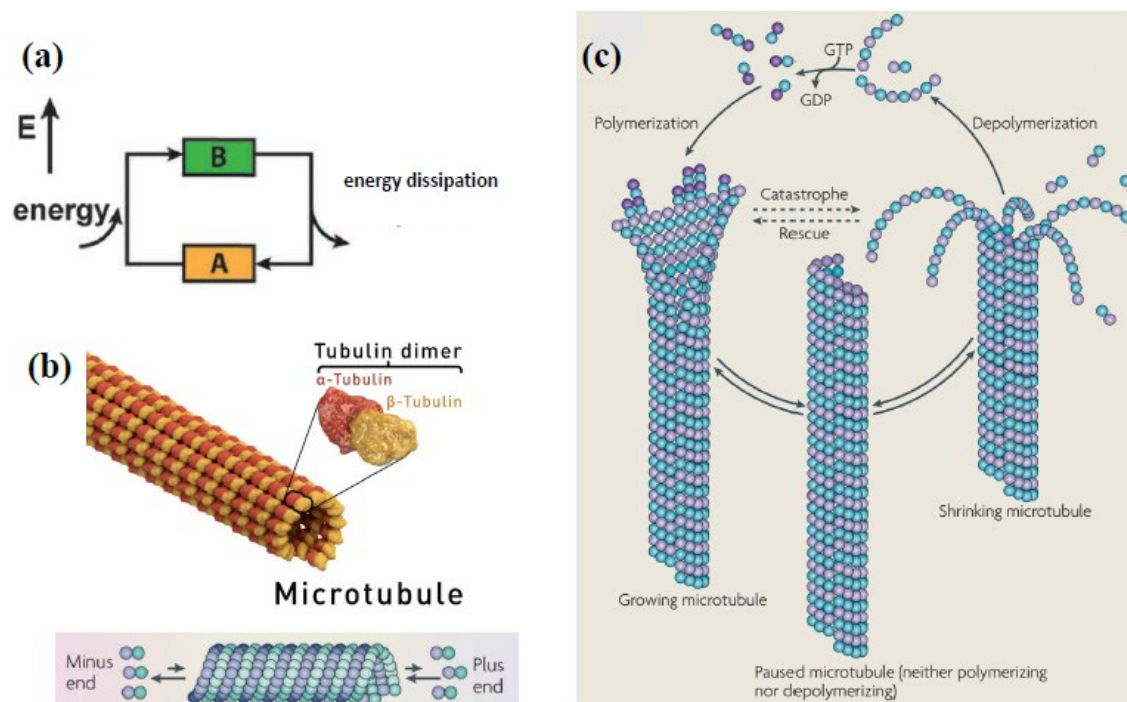


**Figure 2.** (a) Energy driven activation and dissipative deactivation in temporally regulated switchable systems. (b) Structure of microtubules.  $\alpha$ - and  $\beta$ -tubulin dimer polymerizes to form microtubules (linearly assembled  $\alpha$ - and  $\beta$ -tubulin dimer) assembled around a hollow core. The  $\beta$ -tubulin monomer pointing towards the faster-growing end (plus end) and their  $\alpha$ -tubulin monomer exposed at the slower-growing end (minus end). (c) Temporally regulated assembly and disassembly of microtubules. Dynamic instability of microtubules arose from the energy-driven polymerization and delayed depolymerization processes. Reproduced with permission from reference 18 (Copyright 2015, Royal Society of Chemistry) and from reference 33. (Copyright 2009, Nature Publishing Group).

Inspired by energy dissipative self-assembly of tubulin proteins in biological systems, van Esch and co-workers developed the first synthetic strategy towards chemically fuelled dissipative self-assembly (SA) (Figure 3).<sup>35</sup> They have used a simple hydrogelator, dibenzoyl-L-cystine (DBC) which could be activated through double alkylation using methyl iodide (MeI) as chemical fuel (Figure 3a). The alkylation

transforms the non-gelating diacid to gelating diester. The competing dissipative reaction is slow hydrolysis of diester back to diacid. Initially, the esterification process outruns the hydrolysis and by this means the fibers are formed about 100 hours after the addition of fuel. Later, the formed fibers started disappearing after 120 hours due to the hydrolysis of the activated building blocks (Figure 3b).

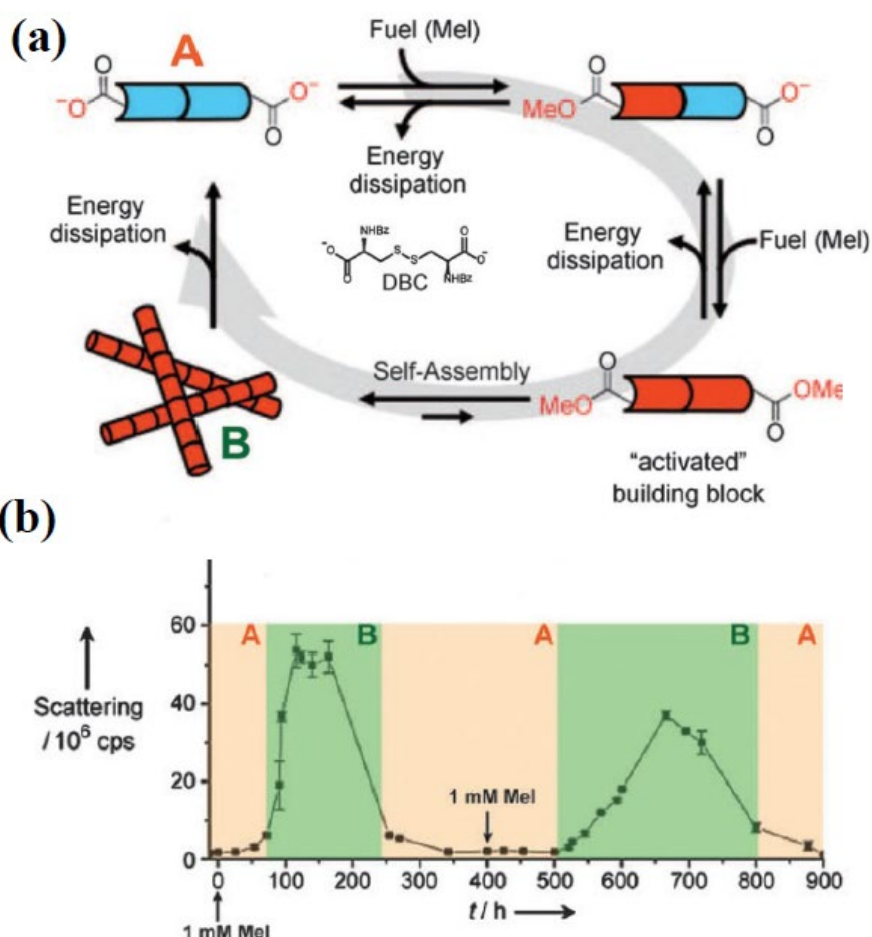


**Figure 3. Temporal control of assembly-disassembly of DBC by energy dissipation mechanism.** (a) Chemically fuelled transient fiber formation in a closed system. DBC (state A) is activated by the fuel molecule (methyl iodide) MeI through double alkylation. The activated DBC (DBC diester) self-assemble to form fibers. The energy is dissipated through the hydrolysis of ester groups and the system return back to state A. (b) The time-dependent fiber formation monitored through light scattering experiments. The refuelling has been done by adding 1 mM MeI after 400 hours. Reproduced with permission from reference 35. Copyright 2010, Wiley-VCH (Germany).

Similar systems can also be fabricated using external energy sources such as UV-light, magnetic field etc. for activation step. For instance, Grzybowski, Klajn, and co-worker demonstrated light (*as an external energy source*) induced transient self-assembly of noble metal nanoparticles (capped with azobenzene ligands) (Figure 4).<sup>22</sup> The UV irradiation triggers the photoisomerization of azobenzene motifs from *trans* to *cis* form (with larger dipole moment) which leads attractive dipole-dipole interactions between the particles and cause AuNPs assembly. Once the energy supply (i.e. light) is stopped, the metastability of the *cis* isomer determines the life-time of the assembly. The efficiency of the initial isomerization is decided by the wavelength, intensity and the duration of light supply and hence these parameters can be utilized to fine-tune the life-time of the assembly.

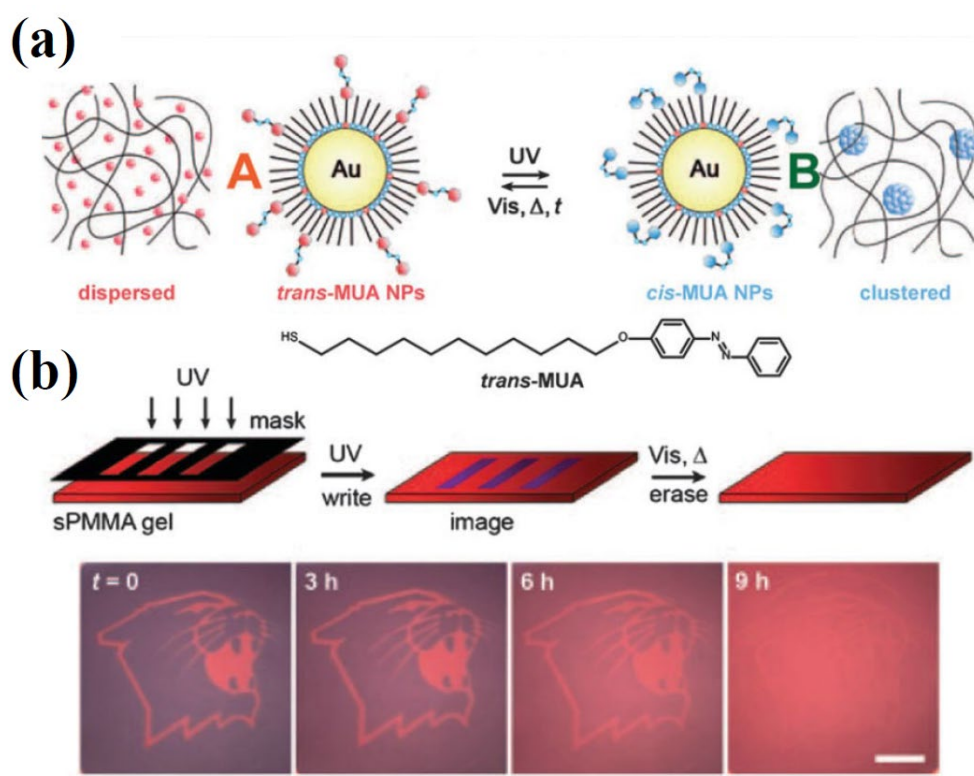


**Figure 4.** (a) Light-activated transient assembly (**State B**) of azo-MUA capped AuNPs via *cis*- to *trans*- isomerization of azobenzene groups. The disassembly back to **state A** is occurs through spontaneous transformation of *cis*-azobenzene to *trans*-azobenzene. (b) The transient assembly of nanoparticles utilised for self-erasing writings. After irradiating UV light through a lithography mask. AuNPs assembled state is seen in blue colour. Reproduced with permission from reference 22. Copyright 2009, Wiley-VCH (Germany).

**2.1.1.2 Systems with Kinetically Controlled Deactivation Route.** In this case, both initial and active states of the system are at equilibrium; a transient active state (with programmable lifetime) can be realised by employing kinetically controlled deactivation pathway which revert the system to the initial state. For example, Ulijn and co-workers employed the kinetic control of activation and deactivation by using enzymes to-

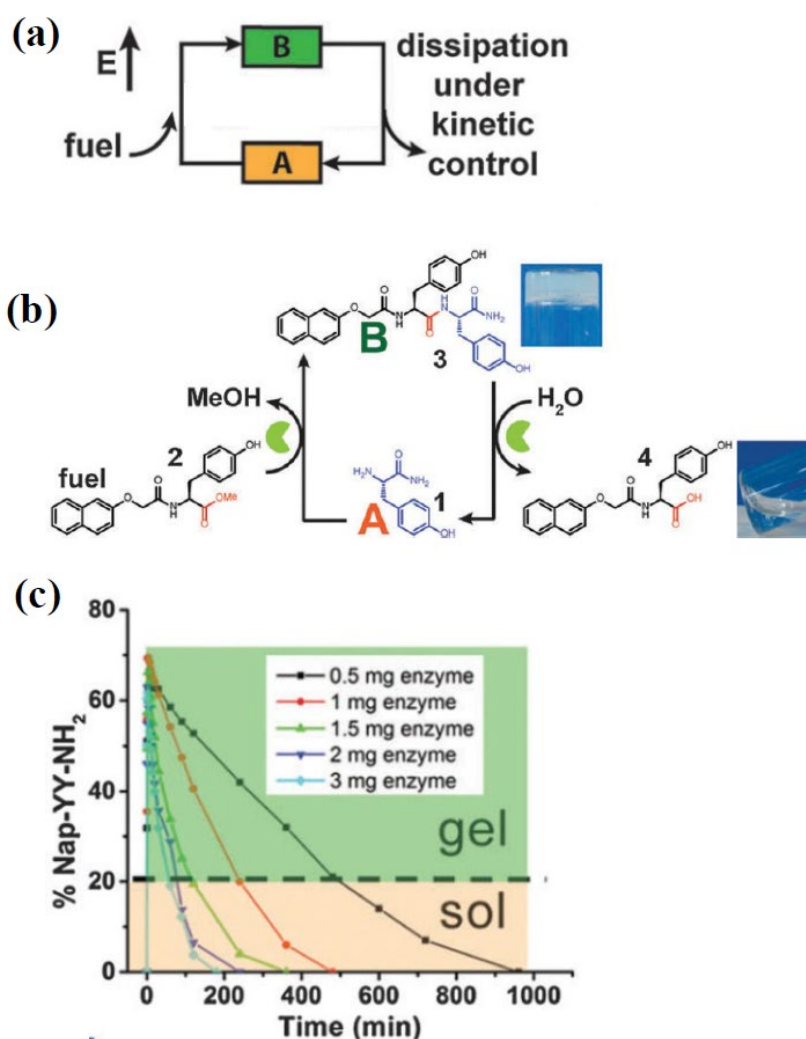


**Figure 5.** (a) Temporally regulated self-assembly via kinetic control. Biochemically regulated transient peptide self-assembly to form nanofibers. A-chymotrypsin catalyzed the activation of NH<sub>2</sub>-Phenyl-CONH<sub>2</sub> (state A) to a dissipative gelator (Nap-Phenyl-Phenyl-CONH<sub>2</sub>) by consuming the fuel molecule Nap-Phenyl-Ome. The subsequent hydrolysis of gelator to non-gelating mono-peptide acid (Nap-Phenyl-OH) along with the recovery of NH<sub>2</sub>-Phenyl-CONH<sub>2</sub> deactivates the system and return to the initial state B. (b) The lifetime of transient gel can be tuned by varying the enzyme concentration. Reproduced with permission from reference. 18 (Copyright 2015, Royal Society of



*Chemistry) and reference 36 (Copyright 2013, American Chemical Society (United States)).*

-temporally control the time domain of self-assembly (SA).<sup>36</sup> They used the enzyme-  $\alpha$ -chymotrypsin – to transiently form the peptide-based hydrogelator which self-assembles to nanofibers (Figure 5a). In the initial **state A**, the system contained an amino acid amide ( $\text{NH}_2\text{-Y-CONH}_2$ , Y = tyrosine, **[1]**) that is converted to an activated hydrogelator dipeptide amide (Nap-YY-NH<sub>2</sub>, **[3]**), by reaction with a naphthalene mono-peptide ester (Nap-Y-OMe, **[2]**) (fuel) enzymatically. This transacylation quickly yields a self-standing gel (**state B**). The kinetically controlled deactivation occurs through the enzymatic hydrolysis of hydrogelator dipeptide amide (Nap-YY-NH<sub>2</sub>, **[3]**) yielding naphthalene mono-peptide acid (Nap-Y-OH) and the amino acid amide ( $\text{NH}_2\text{-Y-CONH}_2$ , **[1]**) which leads to back to the initial sol state (A). The life-time of the SA was programmed in this system through of hydrolysis rate which could be modulated via enzyme concentration (Figure 5b-c).

Another interesting example of kinetically controlled transient self-assembly system was reported by Prins and co-workers based on  $\text{C}_{16}\text{TACN}\cdot\text{Zn}^{2+}$  surfactant (Figure 6).<sup>37</sup> This surfactant formed a vesicular structure in presence of adenosine 5'-triphosphate (ATP) owing to its ability to interact simultaneously with multiple surfactant molecules (activation step). To demonstrate self-regulated, temporally controlled self-assembly, they installed additional deactivation step using enzyme potato apyrase which hydrolyses ATP into adenosine 5' monophosphate (AMP) and two molecules of orthophosphate. Evidently, the hydrolysis products do not stabilize the vesicles and therefore it breaks into monomeric units. Further, the lifetime of this transient vesicle could be controlled by regulating the hydrolysis rate of ATP via varying the enzyme concentrations (Figure 6).

A facile and generic kinetic strategy to manage the time domain of self-assembly (SA) was introduced by Walther and co-workers for which they employed an internal feedback loop system (IFS) that generates a transient pH profile to which the building blocks of SA could respond to.<sup>23, 38-40</sup> The IFS comprises of a fast activator and a dormant deactivator (DD). For an IFS with acidic transient pH profile, activator could be an acid or acidic buffer, which instantaneously decrease the pH upon addition. On the other hand, dormant deactivator could be any molecule which slowly produces base upon chemical-

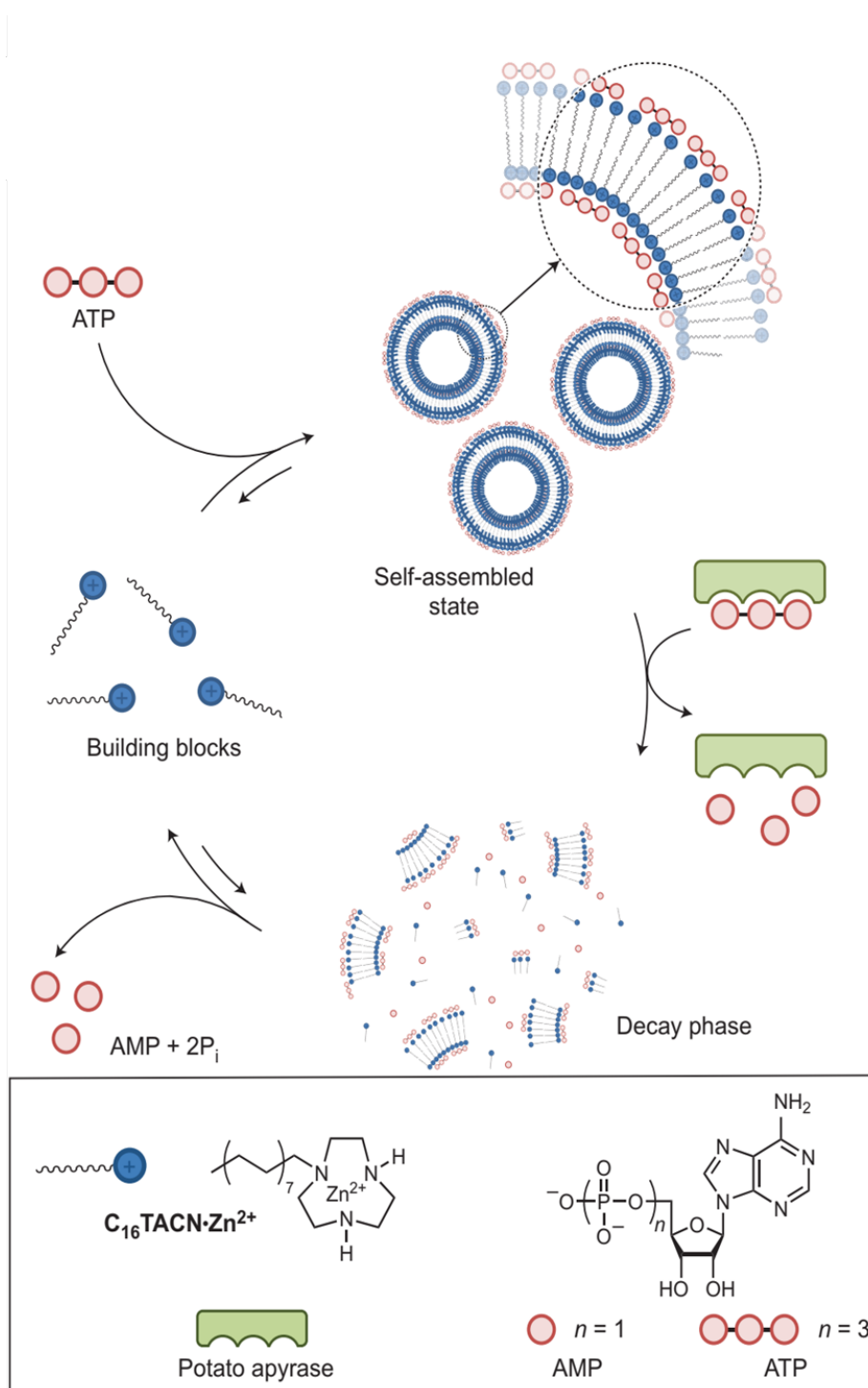


**Figure 6.** (a) Schematic representation of the transient self-assembly of vesicles through kinetically controlled hydrolysis of ATP (adenosine triphosphate). The ATP molecules stabilise the vesicles of surfactant,  $C_{16}TACN \cdot Zn^{2+}$ , through multi-valent interactions. In presence of potato apyrase, the stabilizing ATP molecules are slowly hydrolysed to AMP (adenosine monophosphate) and consequently the vesicles decayed into the initial monomeric states as AMP does not have the stabilising capabilities. Reproduced with permission from reference 37. Copyright 2016, Nature Publishing Group.

-reaction. The lifetime of the transient SA can be managed by modulating the base releasing chemical reaction. To this end, Walther and co-workers first reported such a SA by coupling IFS and pH-responsive building block (Figure 7).<sup>40</sup> The system consisted of a pH-responsive Fmoc-Leu-Gly-OH dipeptide, which self-assembles to nanofibers at pH below ca. 5.8 and urease enzyme. At the initial solution state (pH around 8), the gelator was unable to self-assemble, which upon addition of acidic buffer and dormant deactivator (urea), self-assembles due to protonation of acidic groups (state B). At lower pH urease enzyme slowly hydrolyses urea to produce ammonia, which gradually increases the pH back to the basic and the self-assembly breaks due to deprotonation of hydrogelator. The rate at which the urea hydrolysis occurs determine the lifetime of the assembly and this rate can be fine-tuned by enzyme concentration, urea concentration, and buffer capacity.

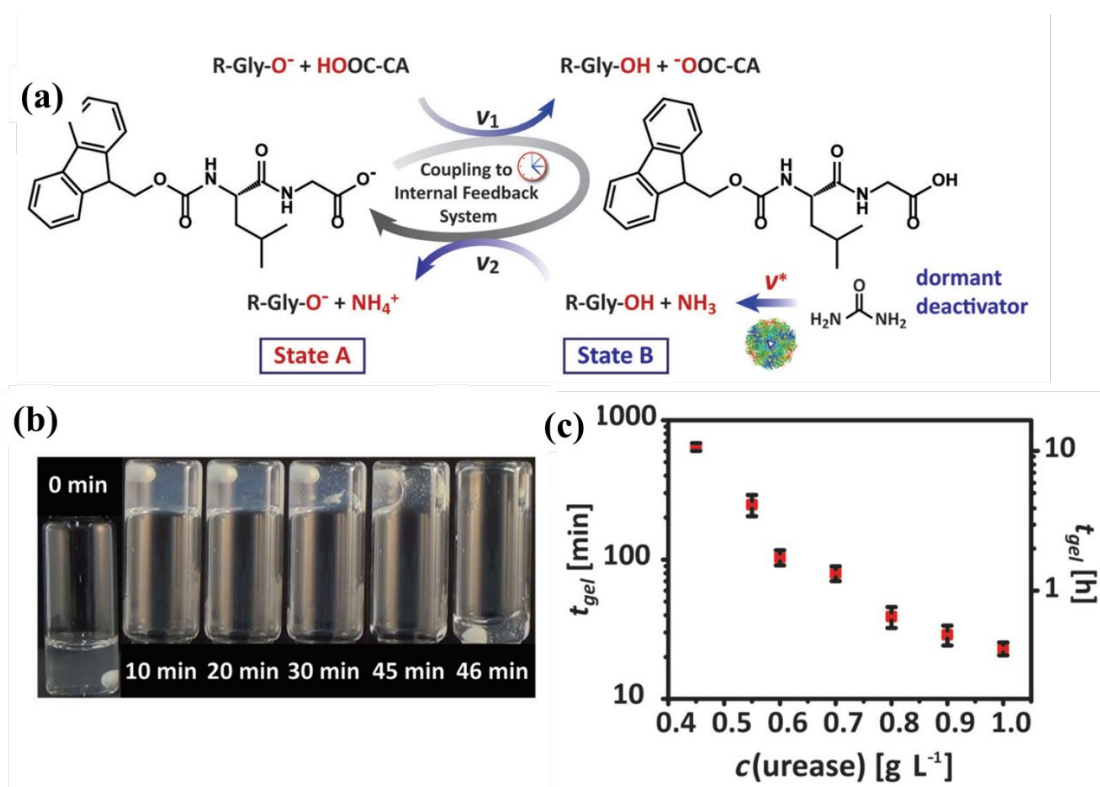


**Figure 7.** (a) Temporal regulation of pH-dependent Fmoc-Leu-Gly-OH dipeptide assembly through coupling it with an acidic IFS. (b) Series of photographs showing the temporally programmed dipeptide hydrogel formation. (c) The gel life-time can be modulated through urease enzyme concentration. Reproduced with permission from reference 40. Copyright 2015, Wiley-VCH (Germany).

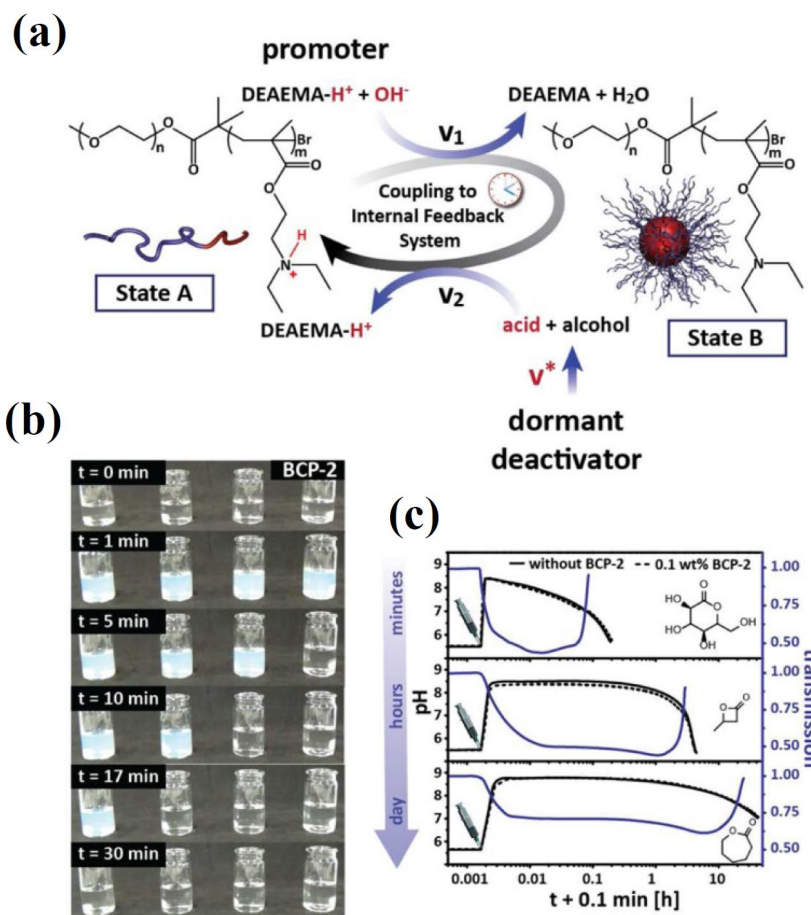


**Figure 8.** (a) Temporal regulation of pH-dependent DEAEMA block-co-polymer aggregation through coupling it with a basic IFS consisting of lactone. (b) Series of photographs showing the temporally programmed aggregation of DEAEMA block-co-polymer with life-time programmed via different concentration of  $\delta$ -GL. (c) The aggregated state lifetime can be modulated through lactones with different hydrolysis rate. Reproduced with permission from reference. 38. Copyright 2015, American Chemical Society (United States).

It is also possible to achieve a basic transient pH profile using a base or basic buffer as activator and lactone as dormant deactivator as demonstrated by Walther and co-workers. The system consisted of a pH-responsive block-copolymer, EO-co-DEAEMA and lactone as dormant deactivator (Figure 8).<sup>38</sup> The block-copolymer, EO-co-DEAEMA was having a ternary ammonium group in their repeating unit which undergoes protonation at pH below ca. 7, making the polymer soluble in aqueous medium. However, at the basic condition, the block-copolymer was insoluble due to the deprotonation of ternary ammonium group, leading the polymer to self-assemble to vesicular morphology. In the starting state, the pH of the solution was around 4.0, where

the polymer chains were soluble. Addition of base instantaneously increases the pH above ca. 8 where the polymer assembled to vesicle. Simultaneously, the lactone (dormant deactivator) (present in the system) started hydrolyzing to corresponding carboxylic acid which slowly reduced the pH back to initial state. Along with this pH change, the polymer vesicles also breakdown to the protonated building blocks and therefore the system reached back to the initial state. The lifetime of this basic transient state can be programmed via the amount of activator, buffer capacity and the type of lactone used. In this report, Walther *et al.* showed modulating the lifetime of transient basic state from minutes to hours to days by using gluconic acid  $\delta$ -lactone, methyl formate, and  $\epsilon$ -caprolactone, respectively.

In short, there are two important strategies to construct self-regulated, temporally controlled transient systems: the energy dissipation approach and the kinetic control approach. These strategies have been well-established for creating switchable self-assembly systems because the initial focus was to mimic the biological self-assembly.

Recently, the principles of managing the time domain of self-assembled systems have been applied in developing new types of functional systems (other than self-assembly) with temporally regulated transient functional states. These functional systems are expected to show new types of applications which demand higher operational freedom.<sup>37, 41-48</sup>

One of the early reported functional systems with the self-regulated functional state was by Walther and co-workers. They demonstrated a photonic device operating out of equilibrium with precise temporal control over its illumination properties.<sup>41</sup> They have used a pH-responsive photonic film based on PS<sub>528</sub>-*b*-P2VP<sub>533</sub> diblock copolymer (the numbers denote the degree of polymerization), along with the internal feedback loop system (IFS) which produces a transient acidic pH profile (Figure 9). The presence of pyridine groups gives rise to strong pH responsiveness leading to a hydrophilic and hydrophobic switching of the P2VP layer which provides subsequent swelling of the film. Below pH ca. 3.2, the pyridine groups get protonated and the electrostatic repulsion results in a volume expansion, leading to a photonic bandgap in visible region. At the initial state with basic surrounding pH, the film is transparent. Upon addition of acid, the pH immediately decreases and film shows green colour owing to the photonic bandgap in visible region. At lower pH, the IFS comprising urea (as dormant deactivator) and

urease slowly increase the pH due to the generation of ammonia. This brings the photonic film back to the transparent initial state. Walther and co-workers have further demonstrated how the temporal programmability helps in achieving memory, signal propagation and sensing in their system.

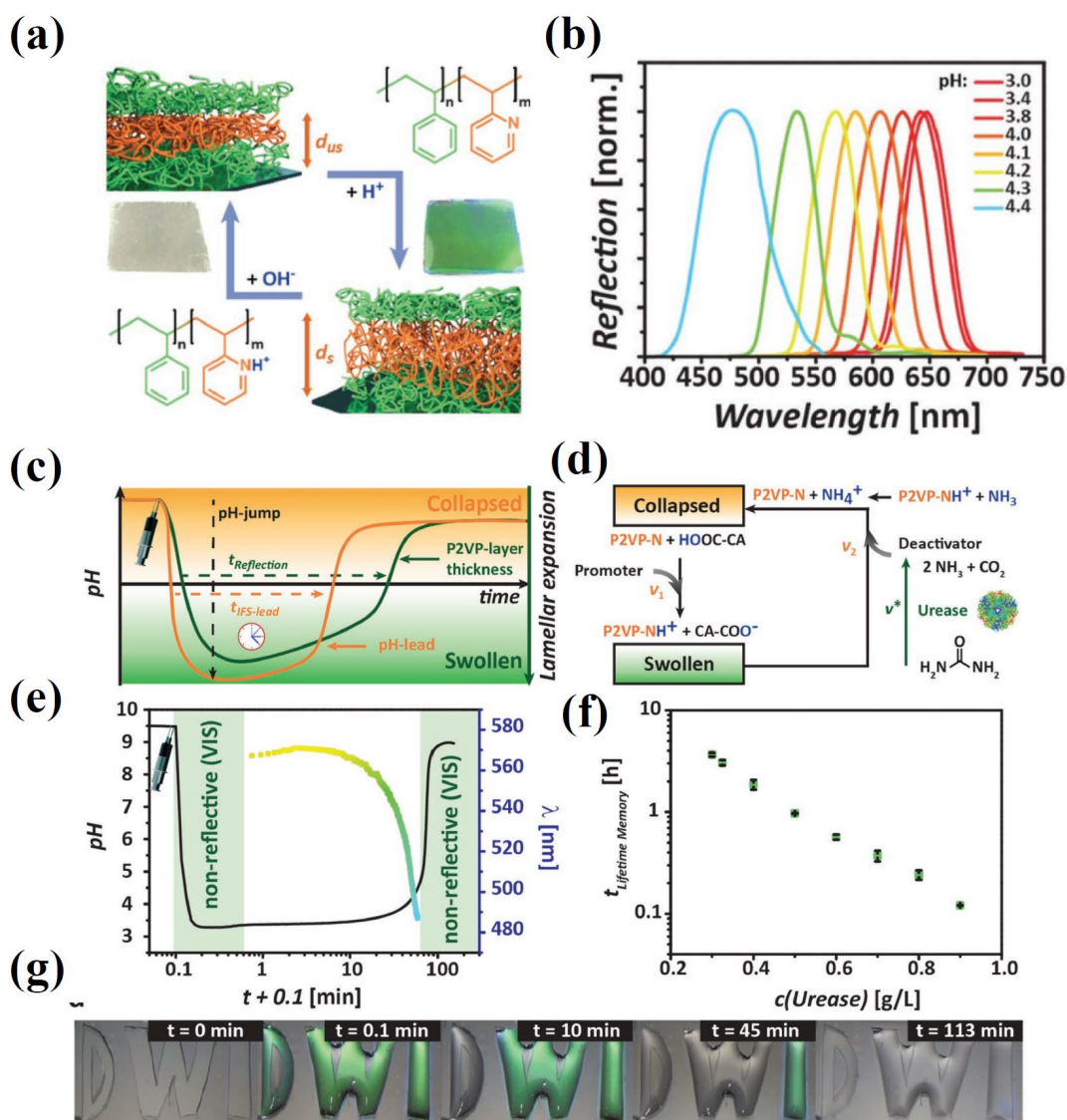


**Figure 9.** Temporal regulation of the reflective state of a polymer gel photonic crystal. (a) The protonation of the pyridine group in the PS-*b*-P2VP block-co-polymer (BCP) photonic film changes its thickness and therefore the wavelength of the refractive light. (b) pH dependent stop band position of the BCP film. (c-d) The pH dependent photonic film is coupled with an acidic IFS to temporally regulate the reflectance state of the film. The IFS consisted of urease enzyme and urea (dormant deactivator). Addition of promotor (acid) resulted in a transient pH profile (orange trace). The structural response of the film follow the pH change. (e-f) The life time of the transient state can be regulated

via urease enzyme concentration. (g) The snapshot showing the photonic films life time programmed with different enzyme concentration. Reproduced with permission from reference 41. Copyright 2017, Wiley-VCH (Germany).

Recently, Prins and co-workers elegantly designed a DNA-based receptor system showing transient loading and release of molecular cargo (Figure 10).<sup>42</sup> They employed a clamp-like DNA based receptor that can recognize a specific 9-base DNA cargo which forms a triplex structure (Figure 10b, resting-state or **state A**). They used an 18-base RNA strand that as fuel which binds to the loop portion of the DNA receptor and causes a conformational change that induces an opening of the triplex complex leading to the release of the DNA cargo (Figure 10b, transient state or **state B**). As the deactivation route, they employed the endoribonuclease enzyme (RNase H) which selectively hydrolyzes the RNA fuel strand. Therefore, once the fuel is consumed by the enzyme, the cargo DNA gets bound to the receptor and system reaches the resting state back. The life-time of the released state (**state B**) could be programmed via both fuel concentration and enzyme concentration (Figure 10c-d).

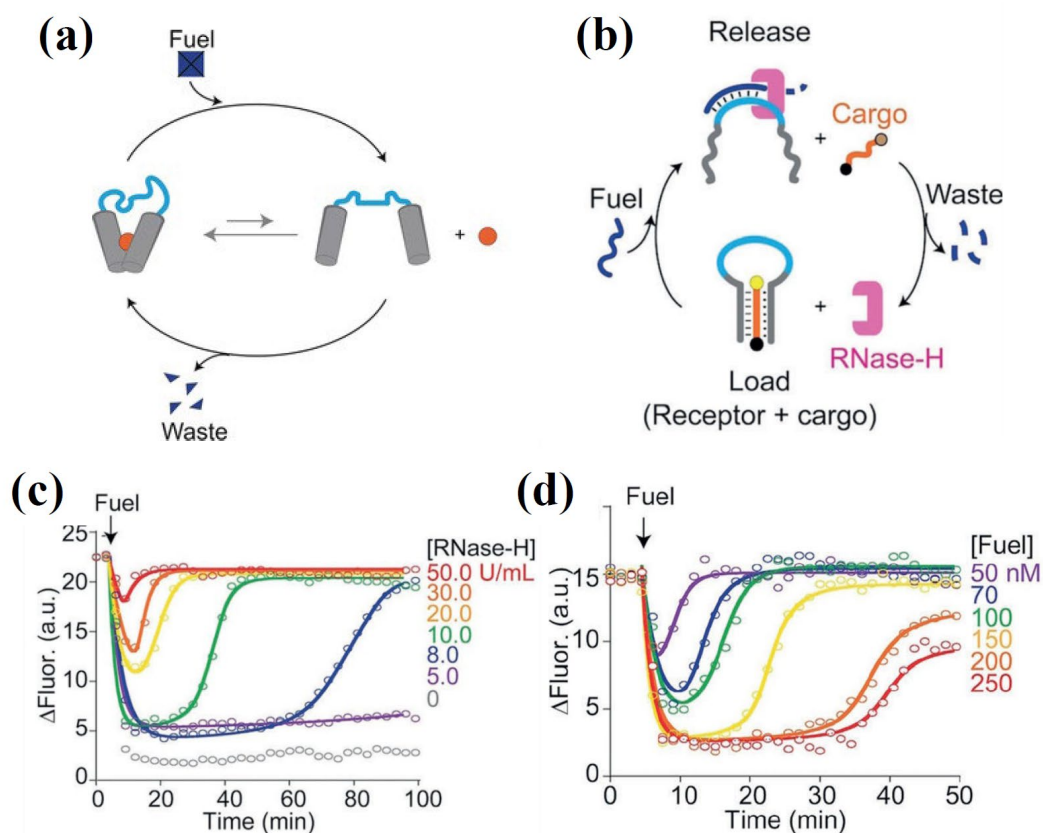


**Figure 10.** (a) Schematic representation of a self-regulated fuel-driven release system. (b) A DNA-based receptor (grey/blue strand) for the transient release of cargo (orange).

Kinetic traces showing the transient release of the cargo ( $3 \times 10^{-8} M$ ) from the receptor ( $3 \times 10^{-8} M$ ) after addition of the fuel strand ( $10^{-7} M$ ) and (c) at different concentrations of RNase H and (d) at different concentrations of fuel. Reproduced with permission from reference 42. Copyright 2018, Wiley-VCH (Germany).

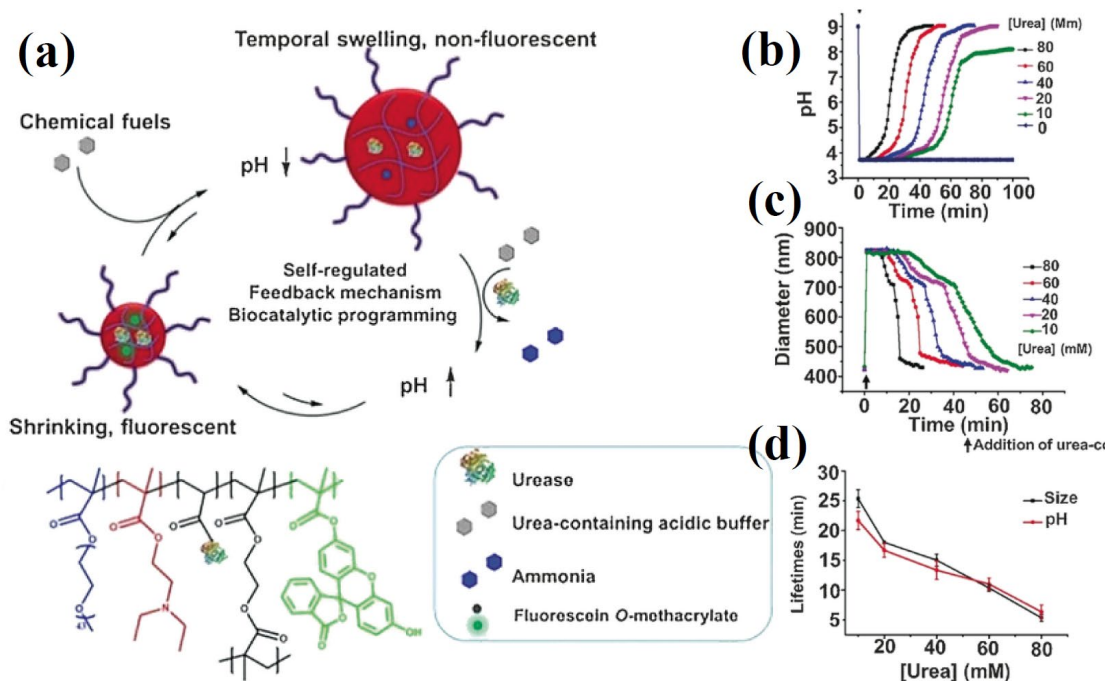


**Figure 11.** (a) The self-regulated swelling and shrinking of hybrid microgel with automatic fluorescence ON/OFF switching achieved through acidic IFS. The microgel consisted of crosslinked block-co-polymer of poly(ethyleneglycol), poly(*N,N*-dimethylaminoethylmethacrylate) and poly(fluorescein-*O*-methacrylate) along with covalently linked urease enzyme. (b) The transient acidic pH state can be fine-tuned through urea concentration. (c-d) The life-time of the swelled, non-fluorescent state can be regulated via urea concentration. Reproduced with permission from reference 45. Copyright 2017, Wiley-VCH (Germany).

Another representative example was reported by Jan C. M. van Hest and co-workers (Figure 11). They demonstrated a temporally controlled breathing of polymer microgel by coupling it with an internal feedback loop system (IFS).<sup>45</sup> The pH-responsive cross-linked polymer microgel was poly[(oligoethylene glycol methacrylate)-(POEGMA) - DEAEMA- ethylene glycol dimethacrylate (EGDMA)]. The microgel was fluorescein tagged to provide fluorescence feedback. The pH-responsive part of the microgel was DEAEMA which have a ternary ammonium group. At the basic condition



(pH above 8.0), the microgel was shrunken due to deprotonation of ammonium group and microgel showed fluorescence due to the ionized fluorescein molecules. Upon the addition of acidic activator (citric acid in this case), the microgel immediately goes to swollen state due to the protonation of DEAEMA groups and at this state the fluorescence gets quenched due to the protonation of fluorescein molecules. At the lower pH, the IFS comprising urease starts hydrolyzing the urea to produce ammonia which slowly increases pH back to initial pH. In response to this pH change, the microgel returns to its initial shrunken and fluorescent state. The life-time of the transient swollen state could be controlled by concentration of IFS components. This system represents temporally regulated breathing microgel, which may have application as autonomous delivery platforms.

### **2.1.2. Conclusions**

In summary, we have discussed the strategies to construct temporally regulated transient switchable systems. These approaches are well studied with respect to supramolecular self-assembly systems. Recently, the research in this area has been focusing towards the self-regulated temporally controlled functional materials/systems (for catalysis, controlled release, optical and electronic functionalities etc.). These systems and concepts are necessary to achieve next generation intelligent responsive materials. It is expected that these systems may bring out interesting applications that could never be achieved by currently existing switchable materials.

### **2.1.3. References**

- (1) Zhu, Y.; Shi, J.; Shen, W.; Dong, X.; Feng, J.; Ruan, M.; Li, Y. Stimuli-Responsive Controlled Drug Release from a Hollow Mesoporous Silica Sphere/Polyelectrolyte Multilayer Core–Shell Structure. *Angew. Chem. Int. Ed.* **2005**, *44* (32), 5083-5087.
- (2) Bae, Y.; Fukushima, S.; Harada, A.; Kataoka, K. Design of Environment-Sensitive Supramolecular Assemblies for Intracellular Drug Delivery: Polymeric Micelles that are Responsive to Intracellular pH Change. *Angew. Chem. Int. Ed.* **2003**, *42* (38), 4640-4643.

- (3) Moya, S.; Azzaroni, O.; Farhan, T.; Osborne, V. L.; Huck, W. T. S. Locking and Unlocking of Polyelectrolyte Brushes: Toward the Fabrication of Chemically Controlled Nanoactuators. *Angew. Chem. Int. Ed.* **2005**, *44* (29), 4578-4581.
- (4) Huck, W. T. S. Responsive polymers for nanoscale actuation. *Mater. Today* **2008**, *11* (7), 24-32.
- (5) Kang, Y.; Walish, J. J.; Gorishnyy, T.; Thomas, E. L. Broad-wavelength-range chemically tunable block-copolymer photonic gels. *Nat. Mater.* **2007**, *6*, 957.
- (6) Arsenault, A. C.; Puzzo, D. P.; Manners, I.; Ozin, G. A. Photonic-crystal full-colour displays. *Nat. Photonics* **2007**, *1*, 468.
- (7) Zhang, Q. M.; Li, X.; Islam, M. R.; Wei, M.; Serpe, M. J. Light switchable optical materials from azobenzene crosslinked poly(N-isopropylacrylamide)-based microgels. *J. Mater. Chem. C* **2014**, *2* (34), 6961-6965.
- (8) Becker, D.; Konnertz, N.; Böhning, M.; Schmidt, J.; Thomas, A. Light-Switchable Polymers of Intrinsic Microporosity. *Chem. Mater* **2016**, *28* (23), 8523-8529.
- (9) Li, Y.; Lokitz, B. S.; McCormick, C. L. Thermally Responsive Vesicles and Their Structural “Locking” through Polyelectrolyte Complex Formation. *Angew. Chem. Int. Ed.* **2006**, *45* (35), 5792-5795.
- (10) Lee, J.; Ku, K. H.; Park, C. H.; Lee, Y. J.; Yun, H.; Kim, B. J. Shape and Color Switchable Block Copolymer Particles by Temperature and pH Dual Responses. *ACS Nano* **2019**, *13* (4), 4230-4237.
- (11) Itano, K.; Choi, J.; Rubner, M. F. Mechanism of the pH-Induced Discontinuous Swelling/Deswelling Transitions of Poly(allylamine hydrochloride)-Containing Polyelectrolyte Multilayer Films. *Macromolecules* **2005**, *38* (8), 3450-3460.
- (12) Frisch, H.; Besenius, P. pH-Switchable Self-Assembled Materials. *Macromol. Rapid Commun.* **2015**, *36* (4), 346-363.
- (13) Zhang, Z.; Yu, H.; Guo, J.; Bai, Z.; Zhang, S.; Zhang, Y.; Wang, J. pH-Responsive smart non-woven fabrics (NWFs) with double switchable wettability between superhydrophilicity–superhydrophobicity–superhydrophilicity to oil/water separation. *New J. Chem.* **2019**, *43* (17), 6712-6720.
- (14) Fukino, T.; Yamagishi, H.; Aida, T. Redox-Responsive Molecular Systems and Materials. *Adv. Mater.* **2017**, *29* (25), 1603888.

- (15) Huo, M.; Yuan, J.; Tao, L.; Wei, Y. Redox-responsive polymers for drug delivery: from molecular design to applications. *Polym. Chem.* **2014**, *5* (5), 1519-1528.
- (16) Stuart, M. A. C.; Huck, W. T. S.; Genzer, J.; Müller, M.; Ober, C.; Stamm, M.; Sukhorukov, G. B.; Szleifer, I.; Tsukruk, V. V.; Urban, M.; Winnik, F.; Zauscher, S.; Luzinov, I.; Minko, S. Emerging applications of stimuli-responsive polymer materials. *Nat. Mater.* **2010**, *9*, 101.
- (17) Yan, X.; Wang, F.; Zheng, B.; Huang, F. Stimuli-responsive supramolecular polymeric materials. *Chem. Soc. Rev.* **2012**, *41* (18), 6042-6065.
- (18) Heinen, L.; Walther, A. Celebrating Soft Matter's 10th Anniversary: Approaches to program the time domain of self-assemblies. *Soft Matter* **2015**, *11* (40), 7857-7866.
- (19) Mann, S. Self-assembly and transformation of hybrid nano-objects and nanostructures under equilibrium and non-equilibrium conditions. *Nat. Mater.* **2009**, *8*, 781.
- (20) Yewdall, N. A.; Mason, A. F.; van Hest, J. C. M. The hallmarks of living systems: towards creating artificial cells. *Interface Focus* **2018**, *8* (5).
- (21) van Esch, J. H.; Klajn, R.; Otto, S. Chemical systems out of equilibrium. *Chem. Soc. Rev.* **2017**, *46* (18), 5474-5475.
- (22) Klajn, R.; Wesson, P. J.; Bishop, K. J. M.; Grzybowski, B. A. Writing Self-Erasing Images using Metastable Nanoparticle "Inks". *Angew. Chem. Int. Ed.* **2009**, *48* (38), 7035-7039.
- (23) Heinen, L.; Heuser, T.; Steinschulte, A.; Walther, A. Antagonistic Enzymes in a Biocatalytic pH Feedback System Program Autonomous DNA Hydrogel Life Cycles. *Nano Lett.* **2017**, *17* (8), 4989-4995.
- (24) Ashkenasy, G.; Hermans, T. M.; Otto, S.; Taylor, A. F. Systems chemistry. *Chem. Soc. Rev.* **2017**, *46* (9), 2543-2554.
- (25) Morris, E.; Chavez, M.; Tan, C. Dynamic biomaterials: toward engineering autonomous feedback. *Curr. Opin. Biotech.* **2016**, *39*, 97-104.
- (26) Tantakitti, F.; Boekhoven, J.; Wang, X.; Kazantsev, R. V.; Yu, T.; Li, J.; Zhuang, E.; Zandi, R.; Ortony, J. H.; Newcomb, C. J.; Palmer, L. C.; Shekhawat, G. S.; de la Cruz, M. O.; Schatz, G. C.; Stupp, S. I. Energy landscapes and functions of supramolecular systems. *Nat. Mater.* **2016**, *15*, 469.

- 
- 
- (27) De, S.; Klajn, R. Dissipative Self-Assembly Driven by the Consumption of Chemical Fuels. *Adv. Mater.* **2018**, *30* (41), 1706750.
- (28) Boekhoven, J.; Hendriksen, W. E.; Koper, G. J. M.; Eelkema, R.; van Esch, J. H. Transient assembly of active materials fueled by a chemical reaction. *Science* **2015**, *349* (6252), 1075-1079.
- (29) Kundu, P. K.; Samanta, D.; Leizrowice, R.; Margulis, B.; Zhao, H.; Börner, M.; Udayabhaskararao, T.; Manna, D.; Klajn, R. Light-controlled self-assembly of non-photoresponsive nanoparticles. *Nat. Chem.* **2015**, *7*, 646.
- (30) Samanta, D.; Klajn, R. Aqueous Light-Controlled Self-Assembly of Nanoparticles. *Adv. Opt. Mater.* **2016**, *4* (9), 1373-1377.
- (31) Timonen, J. V. I.; Latikka, M.; Leibler, L.; Ras, R. H. A.; Ikkala, O. Switchable Static and Dynamic Self-Assembly of Magnetic Droplets on Superhydrophobic Surfaces. *Science* **2013**, *341* (6143), 253-257.
- (32) Howard, J.; Hyman, A. A. Microtubule polymerases and depolymerases. *Curr. Opin. Cell Biol.* **2007**, *19* (1), 31-35.
- (33) Conde, C.; Cáceres, A. Microtubule assembly, organization and dynamics in axons and dendrites. *Nat. Rev. Neurosci.* **2009**, *10*, 319.
- (34) Nogales, E.; Wang, H.-W. Structural intermediates in microtubule assembly and disassembly: how and why? *Curr. Opin. Cell Biol.* **2006**, *18* (2), 179-184.
- (35) Boekhoven, J.; Brizard, A. M.; Kowligi, K. N. K.; Koper, G. J. M.; Eelkema, R.; van Esch, J. H. Dissipative Self-Assembly of a Molecular Gelator by Using a Chemical Fuel. *Angew. Chem. Int. Ed.* **2010**, *49* (28), 4825-4828.
- (36) Debnath, S.; Roy, S.; Ulijn, R. V. Peptide Nanofibers with Dynamic Instability through Nonequilibrium Biocatalytic Assembly. *J. Am. Chem. Soc.* **2013**, *135* (45), 16789-16792.
- (37) Maiti, S.; Fortunati, I.; Ferrante, C.; Scrimin, P.; Prins, L. J. Dissipative self-assembly of vesicular nanoreactors. *Nat. Chem.* **2016**, *8*, 725.
- (38) Heuser, T.; Steppert, A.-K.; Molano Lopez, C.; Zhu, B.; Walther, A. Generic Concept to Program the Time Domain of Self-Assemblies with a Self-Regulation Mechanism. *Nano Lett.* **2015**, *15* (4), 2213-2219.
- (39) Heinen, L.; Walther, A. Temporal control of i-motif switch lifetimes for autonomous operation of transient DNA nanostructures. *Chem. Sci.* **2017**, *8* (5), 4100-4107.

- (40) Heuser, T.; Weyandt, E.; Walther, A. Biocatalytic Feedback-Driven Temporal Programming of Self-Regulating Peptide Hydrogels. *Angew. Chem.* **2015**, *127* (45), 13456-13460.
- (41) Heuser, T.; Merindol, R.; Loescher, S.; Klaus, A.; Walther, A. Photonic Devices Out of Equilibrium: Transient Memory, Signal Propagation, and Sensing. *Adv. Mater.* **2017**, *29* (17), 1606842.
- (42) Del Grosso, E.; Amodio, A.; Ragazzon, G.; Prins, L. J.; Ricci, F. Dissipative Synthetic DNA-Based Receptors for the Transient Loading and Release of Molecular Cargo. *Angew. Chem. Int. Ed.* **2018**, *57* (33), 10489-10493.
- (43) della Sala, F.; Maiti, S.; Bonanni, A.; Scrimin, P.; Prins, L. J. Fuel-Selective Transient Activation of Nanosystems for Signal Generation. *Angew. Chem.* **2018**, *130* (6), 1627-1631.
- (44) Pezzato, C.; Prins, L. J. Transient signal generation in a self-assembled nanosystem fueled by ATP. *Nat. Commun.* **2015**, *6*, 7790.
- (45) Che, H.; Buddingh', B. C.; van Hest, J. C. M. Self-Regulated and Temporal Control of a "Breathing" Microgel Mediated by Enzymatic Reaction. *Angew. Chem.* **2017**, *129* (41), 12755-12759.
- (46) Che, H.; Cao, S.; van Hest, J. C. M. Feedback-Induced Temporal Control of "Breathing" Polymersomes To Create Self-Adaptive Nanoreactors. *J. Am. Chem. Soc.* **2018**, *140* (16), 5356-5359.
- (47) Nijemeisland, M.; Abdelmohsen, L. K. E. A.; Huck, W. T. S.; Wilson, D. A.; van Hest, J. C. M. A Compartmentalized Out-of-Equilibrium Enzymatic Reaction Network for Sustained Autonomous Movement. *ACS Cent. Sci.* **2016**, *2* (11), 843-849.
- (48) van Ravensteijn, B. G. P.; Hendriksen, W. E.; Eelkema, R.; van Esch, J. H.; Kegel, W. K. Fuel-Mediated Transient Clustering of Colloidal Building Blocks. *J. Am. Chem. Soc.* **2017**, *139* (29), 9763-9766.

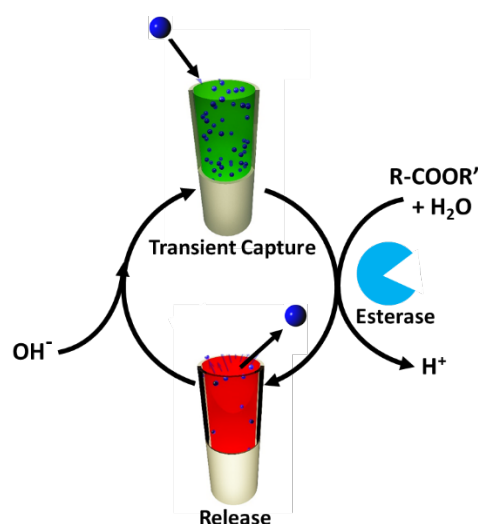


## Chapter- 2.2

### ***Bio-inspired Temporal Regulation of Ion-Transport in Nanochannels.***

#### **Summary:**

*Temporal regulation of mass transport across the membrane is a vital feature in biological systems. Such regulatory mechanisms relay on complex biochemical reaction networks, often operating far from equilibrium. Here in, we demonstrate a biochemical reaction driven temporal regulation of mass transport in silica mesochannels, a biomimetic compartment. A rationally designed silica compartment showing pH responsive electrostatic gating was fabricated through a hetero functionalization approach utilizing propylamine and carboxylic acid moieties. At a basic pH, cationic molecules can diffuse into the mesochannels (entrapped) which permeate back to the solution at an acidic pH. The 'entrapped' state was temporally controlled using base as a fuel along with esterase enzyme as the mediator. The slow enzymatic hydrolysis of a dormant deactivator (ethyl acetate) determines the transient life-time of 'entrapped' state, which is programmed by modulating the enzymatic activity of esterase.*



Publication based on this work has appeared in *Nanoscale Adv.*, **2019**, 1, 1847-1852





### **2.2.1. Introduction**

Biological systems have been a long standing inspiration for temporal control over self-assembled nanostructures and functions. From precise control over circadian rhythms to translocation of molecules across membranes, natural systems use complex chemical reaction networks facilitated by cascade of enzymes.<sup>1-2</sup> Inspired by this, scientists attempt to create adaptive materials with temporal control over structure and function. In this direction, many active self-assembled materials have been synthetically designed recently via fuel-driven, non-equilibrium structural/conformational changes.<sup>3-6</sup> However, autonomous, temporal control on biomimetic functions still remains a challenge and needs to be addressed to design life-like materials.

Recent attempts to achieve temporal regulation are, in general, concerned with transient assembly or conformational changes of supramolecular polymers and of colloidal systems.<sup>7-17</sup> However, temporally programmed functions similar to natural systems are very few.<sup>18-20</sup> Prins and co-workers designed systems showing transient signalling and transient catalysis.<sup>21-23</sup> Using a transient pH switch, Walther and co-workers have exemplified the applications in out-of-equilibrium photonics.<sup>24</sup> Very recently Ulijn and co-workers elegantly designed enzyme responsive chromophores for transient electronics.<sup>25</sup>

Amongst a plethora of autonomous functions, selective transport of molecules in and out of the cellular compartments is a vital feature of biological systems. In order to achieve this selective transport, cell employs various sophisticated membrane channel proteins.<sup>26</sup> There have been significant efforts to mimic such selective transport of molecules across the cell membrane in artificial nanochannels.<sup>27-38</sup> However, all such artificial systems that demonstrated selective transport of molecules often operate in a passive manner and lack autonomous behaviour, unlike their natural counterparts.<sup>34, 39-47</sup> Very recently, Lei Jiang and co-workers demonstrated an artificial nanochannel system that control the ion transport (across it) autonomously and periodically by integrating it with a chemical oscillator (Figure 1).<sup>48</sup> In this chapter, we attempt to fabricate a simpler system showing fuel-driven, temporally regulated ion-transport through its channels controlled via enzyme catalysed biochemical reactions.

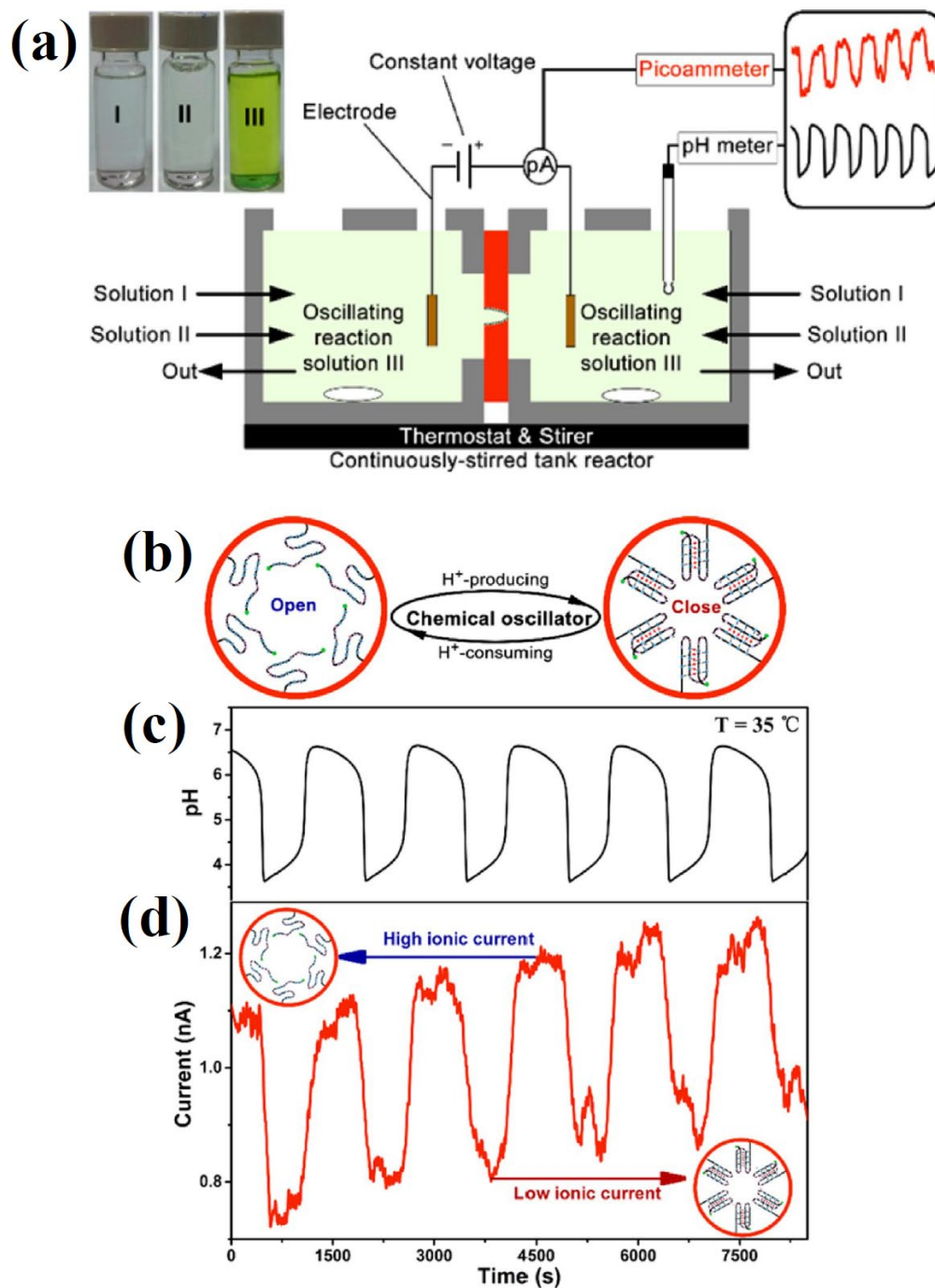
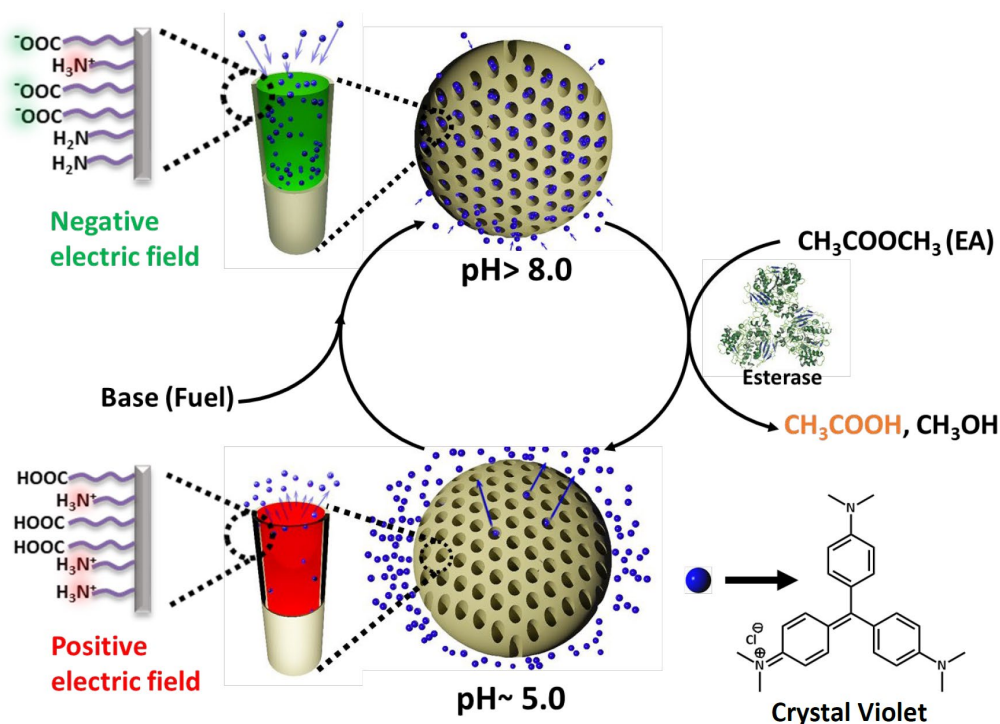


**Figure 1.** Autonomous oscillatory control of  $\text{K}^+$  ion transport across artificial conical nanochannels. (a) Experimental setup for the oscillatory nanochannel system. A  $\text{NaBrO}_3$  solution (I) and a mixed solution of  $\text{Na}_2\text{SO}_3$ ,  $\text{K}_4\text{Fe}(\text{CN})_6$ , and  $\text{H}_2\text{SO}_4$  (II) are pumped slowly and simultaneously from reservoirs into the continuously stirred two half-cells to form the oscillating reaction solution (III). Real-time pH variation of the oscillating reaction solution and real-time ionic current oscillation induced by the channel gating are recorded simultaneously by a pH meter and a picoammeter, respectively (b) Schematic illustration of the cyclic opening and closure of the

*nanochannel driven by the chemical oscillator. (c) Observed autonomous, and periodic pH oscillation of the reaction solution. (d) Ionic current oscillation of the nanochannel induced by the cyclic opening and closing of the nanochannel driven by the pH oscillation. Reproduced with permission from 48. Copyright 2017, American Chemical Society.*

### 2.2.2. Scope of the present investigation

In this chapter, we report a temporal regulation of ion transport in synthetic nanochannels using a bio-inspired, chemical fuel-driven strategy. We have used pH responsive, heterogeneously functionalized nanochannels of mesoporous silica particles as a model system (Scheme 1). Mesoporous silica functionalized with propylamine and carboxylic acid moieties on the surface shows pH responsive charge reversal with a  $pH_{iso}$  (isoelectric point) of 6. Owing to the mesochannels within the Debye length range, these-



**Scheme 1. Enzyme regulated temporal regulation of ion transport in nanochannels:** The pH responsive charge reversal of nanochannels in mesoporous silica are integrated with a non-linear pH modulating biochemical reaction of ethyl acetate (dormant deactivator, DD) hydrolysis by esterase. At the equilibrium state ( $pH \sim 5.0$ ), the transport of a cationic dye (crystal violet, CV<sup>+</sup>) to the nanochannels is blocked due to electrostatic

*repulsion. Injection of chemical fuel (base) along with dormant deactivator (ethyl acetate) reverses the surface charge of the nanochannels, leading to the uptake of  $CV^+$ . At basic pH, enhancement of enzymatic hydrolysis of ethyl acetate (DD) brings down the pH to acidic thereby releasing the dye from the mesopores.*

-compartments display electrostatic gating of ion transport. When the pH is lower than  $pH_{iso}$  ( $\sim 6.0$ ), the nanochannels block the cationic guest molecule from entering inside the pores due to electrostatic repulsion. Upon increasing the solution pH above  $pH_{iso}$  ( $> 6.0$ ), the nanochannels strongly attract the cationic molecules and entrap them inside. Importantly, further switching of the pH back to acidic condition induces the release of entrapped molecules to the surrounding medium. By integrating these pH responsive channels with a non-linear pH switching biochemical reaction (esterase catalysed hydrolysis of ethylacetate), temporal control of cations transport was achieved. Addition of base ( $OH^-$ ) to the resting state ( $pH < 5.0$ , where the cationic molecules are in the bulk solution), immediately raised the pH ( $pH > 8.0$ ) hence entrapped all cationic molecules inside the nanochannels. Simultaneously, the esterase started hydrolysing ethylacetate which changes the solution pH slowly back to the resting pH thereby cationic molecules are released from the nanochannels. The life-time of this release could be controlled by manipulating the biochemical reaction.

### 2.2.3. Experimental section

**Synthesis of MCM-41.** Mesoporous silica nanoparticles (MCM-41) were synthesized by following a previously reported procedure.<sup>49</sup> In a typical synthesis, 1.0 g (2.74 mmol) of hexadecyltrimethyl-ammonium bromide (CTAB) and 0.28 g of NaOH was dissolved in 480 mL of water under stirring and the temperature was raised to 80 °C. 5 ml (22.4 mmol) of tetraethyl orthosilicate (TEOS) was added drop wise and the reaction mixture was stirred for 2 h at 80 °C. The white solid product was centrifuged, washed thoroughly with water followed by ethanol, and dried in an oven overnight. The surfactant template (CTAB) was removed by refluxing the product for 6 h in acidic ethanol solution (50 mL EtOH containing 0.5 mL concentrated HCl (37 wt %)). The precipitate was thoroughly washed with water and ethanol.

**Synthesis of MCM-N.** 1.0 g of surfactant free MCM-41 (1.0 g) and 1.0 ml (5.67 mmol) of (3-aminopropyl)triethoxysilane (APTES) were added to 80 ml of anhydrous toluene and ultra-sonicated to get a homogenous dispersion. The mixture was refluxed with

stirring under N<sub>2</sub> atmosphere for 24 h. The reaction mixture was centrifuged and the precipitate was washed thoroughly with toluene, hexane followed by ethanol, finally dried under high vacuum at 353 K for 6 h.

**Synthesis of MCM-Z.** 0.5 g of MCM-N was dispersed in 25 mL 1,4-dioxane and ultrasonicated for 5 min. To this dispersion, a solution of 60 mg of succinic anhydride (0.6 mmol) in 12.5 mL of 1,4-dioxane was added under stirring. This mixture was heated at 80 °C for 1 h. The resultant product was centrifuged, and thoroughly washed with water followed by ethanol, and dried in oven overnight.

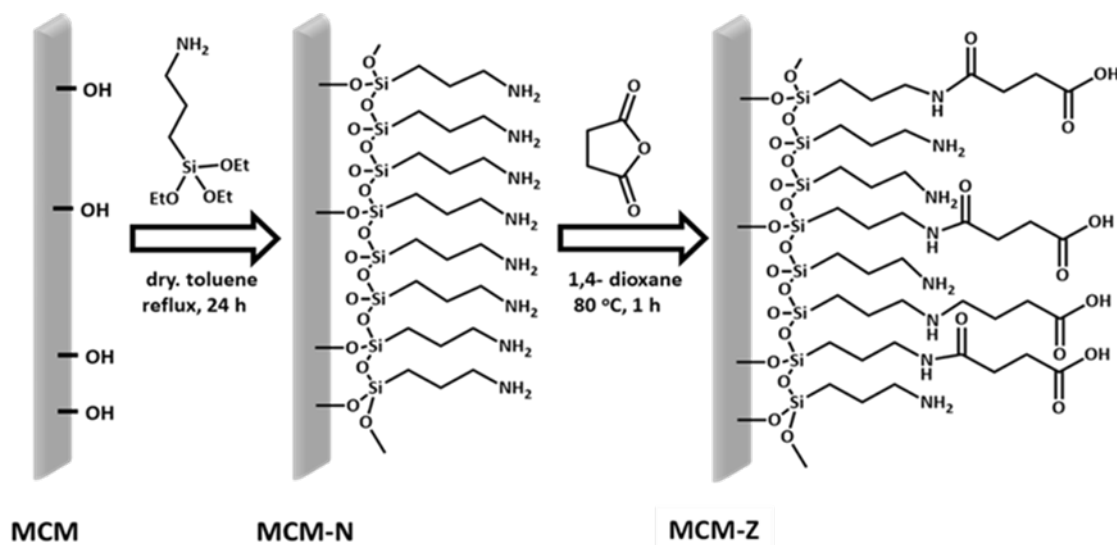


**Figure 2.** Schematic showing the synthetic strategy for functionalization of MCM nanochannels to create pH responsive hetero functionalized **MCM-Z** nanochannels.

**Zeta potential titration measurements.** A dispersion of MCM-N or **MCM-Z** in respective buffers (0.5 mg/mL) was used for the zeta potential measurements. The zeta titration was carried out by an Autotitrator (MPT 2 Titrator, Malvern Instruments). The pH was adjusted using 10 mM stock solutions of HCl or NaOH. The temperature was always kept at 25 °C with the help of inbuilt thermostat in Zetasizer Nano ZS.

**Passive CV<sup>+</sup> transport studies.** The loading of cationic dye (CV<sup>+</sup>) into the channels of **MCM-Z** at different pH buffers were studied as follows. 10 mg of **MCM-Z** was dispersed in 3 mL buffer solution (15 mM) of respective pH (3.0, 4.0, 5.0, 6.0, 7.0 and 8.0) containing 3.34 μM of CV<sup>+</sup>. The mixture was agitated in a vortex mixer for 10 min at room temperature. The dispersion was then centrifuged and the supernatants were subjected to absorption spectroscopic studies to determine the amount of CV<sup>+</sup> loaded into

the **MCM-Z** using Beer-Lambert law. The release of entrapped  $CV^+$  from **MCM-Z** was also estimated in the same method. 10 mg of  $CV^+$  loaded **MCM-Z** was dispersed in a 3.0 mL buffer solution (15 mM) of respective pH (3.0, 4.0, 5.0, 6.0, 7.0 and 8.0). The mixture was agitated in a vortex mixer for 10 min at room temperature. The dispersion was then centrifuged and the supernatants were subjected to UV-Vis absorption spectroscopy studies to determine the amount of  $CV^+$  released from the **MCM-Z**.

**$CV^+$  uptake cycling.** The recyclability of **MCM-Z** towards the  $CV^+$  transport was studied as follows. 10 mg of **MCM-Z** was dispersed in 3 mL of pH 3.0 buffer solution (15 mM) containing  $3.34 \mu\text{M}$  of  $CV^+$ . The mixture was agitated in a vortex mixer for 10 min at room temperature. The dispersion was then centrifuged and the supernatants were subjected to absorption spectroscopy to determine the amount of  $CV^+$  loaded. The precipitate was collected and re-dispersed in 3 mL pH 8.0 buffer solution (15 mM) containing  $3.34 \mu\text{M}$  of  $CV^+$ . The mixture was agitated in a vortex mixer for 10 min at room temperature. The supernatant was collected and the amount of  $CV^+$  loaded was quantified. Before the second cycle, the precipitate was washed with 3 mL pH 3.0 buffer solution (15 mM) to remove the loaded  $CV^+$  dye molecules. The precipitate was further subjected to second cycle of  $CV^+$  loading at pH 3.0 and 8.0 following same procedure.

**Temporal regulation of  $CV^+$  transport.** 10 mg of **MCM-Z** was dispersed into 2.5 mL 0.3 mM sodium citrate/citric acid buffer solution (pH 4.2) containing varying amount of esterase enzyme (0 – 3.6 U/mL), 0.3 mM sodium citrate/citric acid buffer solution (pH 4.2) and  $4.0 \mu\text{M}$   $CV^+$ . The mixture was agitated in a vortex mixer at room temperature. 0.5 mL of tris base solution (0.1 M) containing ethyl acetate (80 mM) was added to the above mixture to activate the system to “ $CV^+$  entrapped state”. The final concentration of the components in 3 mL mixture were: esterase enzyme (0 – 3 U/mL),  $CV^+$  dye ( $3.34 \mu\text{M}$ ), ethyl acetate (66 mM) and tris base (16 mM). The mixture was centrifuged and the supernatant was subjected to absorption spectroscopy at the predetermined time interval to determine the amount of  $CV^+$  entrapped in **MCM-Z**.

**Refuelling the system.** To demonstrate the refuelling capabilities of the system, 10 mg of **MCM-Z** was dispersed in 2.5 mL of 0.3 mM sodium citrate/citric acid buffer (pH 4.2) containing varying amount of esterase enzyme (0 – 3.6 U/mL), and  $4.0 \mu\text{M}$   $CV^+$ . The mixture was agitated in a vortex mixer at room temperature. 0.5 mL of tris base (0.1 M) containing ethyl acetate (80 mM) was added to the above mixture to attain a “ $CV^+$

entrapped state”. Once the equilibrium state was reached, another 0.5 mL of tris buffer (0.1 M) containing ethyl acetate (80 mM) was added to refuel the system and to activate again to the “CV<sup>+</sup> entrapped state”. Similarly, the refuelling process was carried one more cycle. The mixture was centrifuged and the supernatant was subjected absorption spectroscopy at the predetermined time interval to determine the amount of CV<sup>+</sup> entrapped to **MCM-Z**

#### **2.2.4. Characterization**

Please see the appendix for the details of the instrumentation of UV-Visible spectroscopy, X-ray diffraction, FT-IR spectroscopy, Transmission electron microscopy, Field emission scanning electron microscopy (FESEM), nitrogen sorption analysis, thermogravimetric analysis, zeta potential measurements and pH measurements.

#### **2.2.5. Results and discussion**

For a transient ion transport system based on electrostatic interactions, the first condition is to synthesize charge-switchable nanochannels that can undergo charge reversal (due to pH change) on addition of an external chemical fuel (activation). The second requirement is to have a chemical reagent that can revert the changes (bringing back the original pH and hence reverse the surface charge) in a temporal manner (deactivation). Accordingly, the charged cargo will be taken up from the solution when the channels are oppositely charged and will be released when they have the same charge as the cargo. Importantly, the steps (activation and deactivation) should work in tandem, with the rate of activation higher than the rate of deactivation. As the chemical fuel is consumed, the rate of deactivation becomes higher and the system comes to an equilibrium. To achieve this, we have heterogeneously functionalized the nanochannels of mesoporous silica particles with pH responsive amine and carboxylic acid functional groups (Scheme 1). Mesoporous silica spheres (MCM-41, hereafter referred as MCM) were synthesized following a well-known sol-gel procedure and the surface was covalently modified with (3-aminopropyl)triethoxysilane to obtain MCM-N with amine functionalized surface.<sup>49-50</sup> A portion of amine groups was then reacted with succinic anhydride to form **MCM-Z** (Figure 3a) with zwitterionic nature having carboxyl and amine groups on the nanochannel surface as described in Chapter 1.3. The thorough characterizations of **MCM-Z** were described in Chapter 1.3.

To monitor the surface charge of these biomimetic nanochannels, we employed zeta potential measurements. The variation of zeta potential with pH for both MCM-N and MCM-Z are shown in Figure 3b. As expected, propylamine functionalized MCM (MCM-N) showed a zeta potential of ca.  $+46 \pm 0.5$  mV at pH 3 that reduced to  $+24 \pm 2$  mV at pH 8.5. In the case of MCM-N, no charge reversal occurred on going from low pH to high pH (Figure 3b). On the other hand MCM-Z (that have both amine groups and carboxylic acid groups on the surface) showed a clear charge reversal with respect to pH. At a pH of ca. 3, MCM-Z was positively charged with a zeta potential of ca.  $+44 \pm 0.5$  mV associated with the protonation of free amines in MCM-Z. The surface charge became zero at around pH 6 (isoelectric point) and further increase in pH caused charge reversal from positive to negative with a zeta potential of ca.  $32 \pm 1$  mV at pH 8.5. This can be attributed to the generation of carboxylate groups along with the neutralization of amines. As a result, the functionalized nanochannels became anionic above the isoelectric point of pH 6.0 and cationic below pH 6.0.

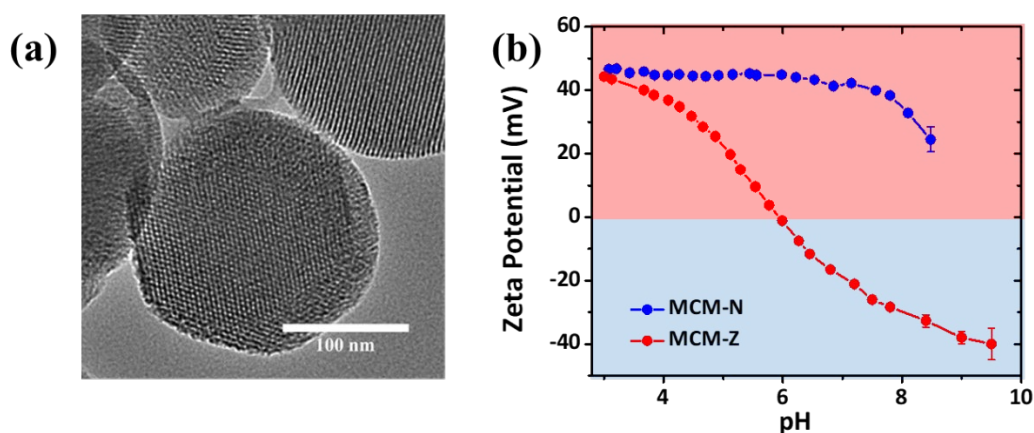


**Figure 3.** (a) TEM image of MCM-Z. (b) The pH dependent zeta potential variations for MCM-N, MCM-Z.

The pH dependent charge switchable property of nanochannels was explored to encapsulate and release cationic dye molecules. For this purpose, a cationic dye, crystal violet ( $CV^+$ ) was chosen which maintains the cationic nature in the pH range of 3 to 8.5.<sup>51-52</sup> The dye uptake and release were quantitatively probed via UV-Vis spectroscopy (Scheme 1, Figure 4). To investigate the amount of  $CV^+$  encapsulation, 10 mg MCM-Z was soaked in a  $3.34 \mu\text{M}$  aqueous solution of  $CV^+$  dye at pH 8 for 10 minutes. The absorption spectra of  $CV^+$  stock solution and supernatant solution after soaking with



**MCM-Z** was compared (Figure 5a). The disappearance of CV<sup>+</sup> absorption band for the supernatant solution suggested an efficient encapsulation of cationic dye into the negatively charged nanochannels at pH 8 via electrostatic attraction. The encapsulation is driven by electrostatic attraction between the CV<sup>+</sup> and silica surface. There are no physically entrapped dye molecules inside the pores as it is evident from ‘zero’ leak release of CV<sup>+</sup> from silica pores at pH > 8.0 (Figure 5c). The uptake of CV<sup>+</sup> calculated from the UV-vis spectra was found to be ca. 1 μmol g<sup>-1</sup> (Figure 5b). Similar encapsulation experiment done at pH 3 shows only a negligible uptake, confirming the strong electrostatic gating of **MCM-Z** nanochannels at pH 3 towards the cationic dye (Figure 5b).

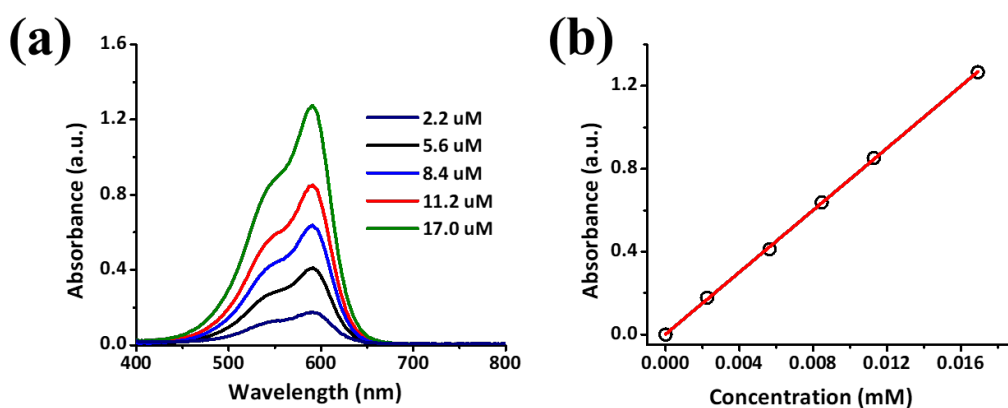


**Figure 4.** (a) UV Vis spectra (known concentrations) of crystal violet. (b) Calibration curve used for estimating crystal violet.

Next, we studied the CV<sup>+</sup> dye uptake in **MCM-Z** and its release as a function of pH (Figure 5c). The **MCM-Z** (10 mg) was incubated in a 3.34 μM CV<sup>+</sup> solution at different pHs (in the range of 3–8) for 10 minutes and the encapsulation was probed with absorption spectra. A gradual increase in the uptake of CV<sup>+</sup> was observed with an increasing pH and a maximum uptake was seen at pH 8 (ca. 1 μmol g<sup>-1</sup>) which can be explained based on the nature of surface charge developed at different pH as shown in Figure 3b. Release profile of CV<sup>+</sup> encapsulated in **MCM-Z** at pH 8.0 (high uptake due to electrostatic interactions) showed a maximum release at pH 3.0 due to charge repulsion between the positively charged nanochannels and the cationic dye (Figure 5c). We further investigated the recyclability of the charge reversal and dye encapsulation by sequentially changing the pH of the **MCM-Z** dispersion containing 1 μmol g<sup>-1</sup> CV<sup>+</sup> between 3 and 8. The encapsulation and release of CV<sup>+</sup> in and out of **MCM-Z** was

studied and a significant amount of dye uptake was observed up to three cycles (>80%) (Figure 5d). Thus, we obtained an efficient recycling, validating the adaptability and reversibility of these nanochannels to solution pH variations.

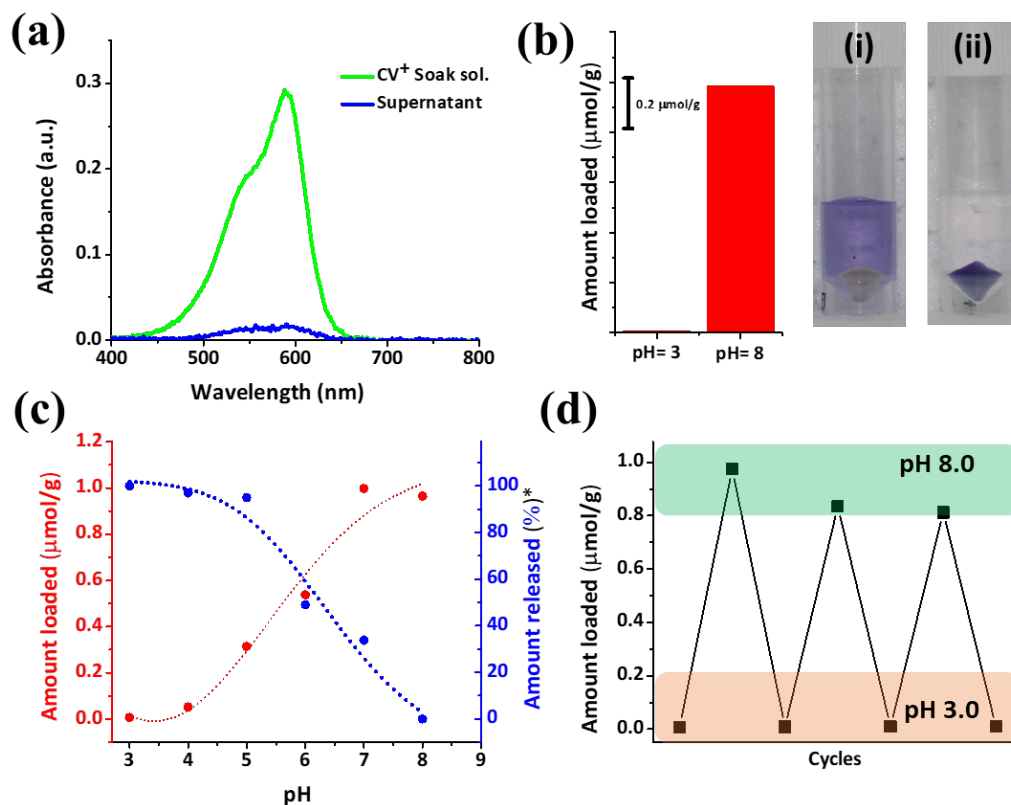


**Figure 5. Transportation of  $CV^+$  in MCM-Z nanochannels:** (a) absorption spectra of  $CV^+$  stock ( $3.34 \mu M$ ) solution and the supernatant after loading  $CV^+$  into MCM-Z at pH 8. (b) Amount of encapsulation of  $CV^+$  into MCM-Z at pH 3 and pH 8 ( $CV^+$  stock solution concentration was ca.  $3.34 \mu M$  and MCM-Z was ca. 10 mg). Photographs showing the supernatant solution after soaking  $CV^+$  with MCM-Z for 10 min in (i) pH 3 and (ii) pH 8. (c) Encapsulation and release of  $CV^+$  in MCM-Z at different pH. \*For release studies,  $CV^+$  was first encapsulated into MCM-Z at pH 8 and the released amount at different pH was normalized w.r.t. loading at pH 8. (d) Cycling of  $CV^+$  encapsulation into MCM-Z at pH 3 and 8.

Further, we investigated the structural stability of MCM-Z in basic aqueous solution (pH > 8.0) to evaluate the robustness of the nanochannels. The MCM-Z was dispersed in a tris buffer solution of pH 9.0 (10 mM) and the zeta potential was measured at regular time intervals up to 3 hours, which showed no change even after 2.5 hours

(Figure 6a). The XRD pattern (Figure 6b) and N<sub>2</sub> sorption analysis (Figure 6c) also confirmed the structural stability of **MCM-Z** nanochannels in basic conditions. This suggests that the functionalization of MCM with (3-aminopropyl)triethoxysilane gives protection to silica from OH<sup>-</sup> attack.

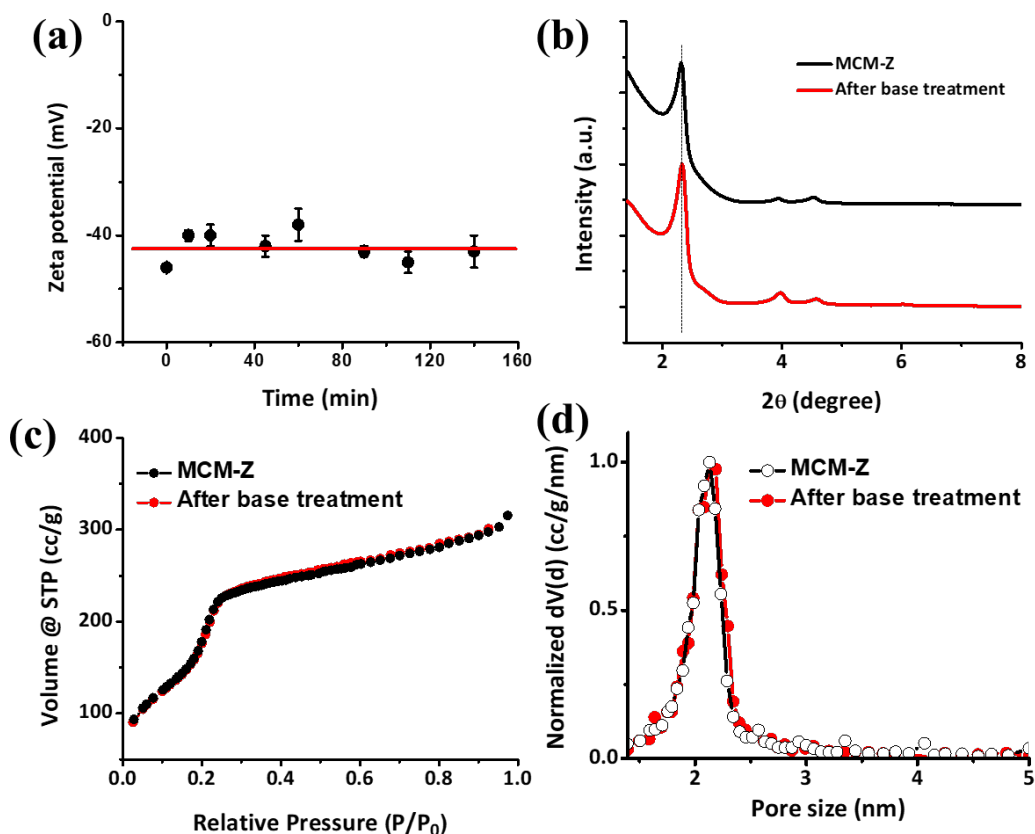


**Figure 6.** (a) Zeta potential measurement of **MCM-Z** dispersed in pH 9.0 buffer at different soaking time. (b) XRD pattern of **MCM-Z** before and after soaking in pH 9.0 buffer for 2 h. (c) Nitrogen adsorption isotherms and (d) Barrett-Joyner-Halenda pore size distribution curves of **MCM-Z** before and after soaking in pH 9.0 buffer for 2 h.

The encapsulation and release strategy of dye (CV<sup>+</sup>) molecules in **MCM-Z** channels in response to pH induced charge reversal (by on demand addition of base or acid), was then extended for the system showing a temporally controlled pH change to realise ‘transient ion transport’. For this purpose, we have designed a feedback-controlled chemical processes which temporally modulates the pH of the surrounding solution.<sup>53</sup> When we first inject a base to the acidic dispersion of **MCM-Z**, the increase in pH (*ca.* 9.0) deprotonates the carboxylic acid functional groups (and ammonium cations) resulting in the formation of anionic nanochannels (activation step). Furthermore, the

high pH initiates hydrolysis of ethyl acetate (by esterase enzyme) that gradually decreases the pH (due to the formation of acetic acid). As a result, amine and carboxylate functional groups get protonated and nanochannels become cationic (deactivation step). Since ethyl acetate decreases the pH of the system only through kinetically controlled hydrolysis (by esterase enzyme) it is referred to as dormant deactivator. The instantaneous activation (formation of anionic nanochannels) by the addition of base and the slow deactivation (leading to cationic nanochannels) due to ethyl acetate hydrolysis allow the nanochannels to exist in transient anionic state (Figure 7a).

We first investigated the efficiency to obtain temporal control on pH by varying the amount of esterase. The chemical fuel (tris(hydroxymethyl)aminomethane (base)) and ethyl acetate (DD) in appropriate concentrations were mixed and injected to a dispersion of **MCM-Z** containing  $\sim 1.0 \mu\text{mol g}^{-1} \text{CV}^+$  and esterase enzyme ( $0\text{--}3 \text{ U mL}^{-1}$ ) and a time dependent pH variation was monitored (Figure 7b). An initial increase in pH to  $\sim 9$  was observed which gradually decreased to pH 5.0, the equilibrium state, due to the formation of acetic acid (by the hydrolysis of ethyl acetate at high pH). The kinetics of ethyl acetate hydrolysis is dependent on the concentration of esterase. The increase in the concentration of enzyme (at constant concentration of ethyl acetate) resulted in higher rate of ethyl acetate hydrolysis and a corresponding decrease in the lifetime of transient alkaline pH state. For ca.  $0.7 \text{ U mL}^{-1}$  of esterase enzyme, it took more than  $180 \pm 3 \text{ min}$  to attain the pH back to ca. 5; however, it took only  $50 \pm 4 \text{ min}$  when the enzyme amount was increased to ca.  $2.8 \text{ U mL}^{-1}$  (Figure 7b, Figure 8b). On the other hand, the pH remained at 9.0 when no esterase enzyme was used. Interestingly, the temporal variation of solution pH showed three distinct slopes which were in agreement with the previously reported activity profile of esterase.<sup>53</sup>

The temporal control achieved on pH was then explored to autonomously control the permeation of ions in and out of the pH adaptive **MCM-Z** nanochannels using cationic dye ( $\text{CV}^+$ ) as a model system (Figure 5). To achieve a temporal control on ion transport, **MCM-Z**,  $\text{CV}^+$  and esterase enzyme at pH 4.2 were taken. The system stays at equilibrium and no significant encapsulation of  $\text{CV}^+$  by **MCM-Z** was observed even after 10 min of soaking (Figure 8a). However, addition of tris base (chemical fuel) and ethyl acetate (dormant deactivator), resulted in an instantaneous increase in pH that facilitated the spontaneous  $\text{CV}^+$  encapsulation in **MCM-Z** nanochannels. Subsequent, hydrolysis

of ethyl acetate (DD) by esterase gradually reduced the pH and a slow release of CV<sup>+</sup> back into the solution was observed.

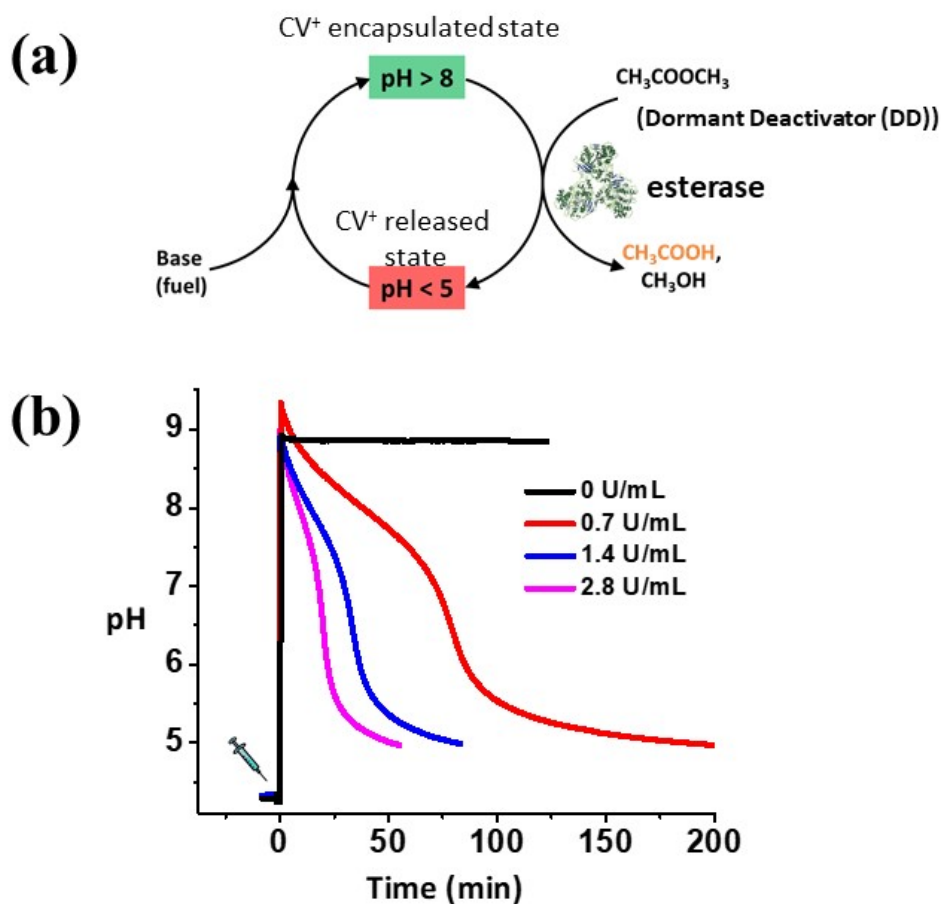


**Figure 7.** (a) Schematic showing transient ion transport with a base (tris base) driven activation and acid driven (ethyl acetate hydrolysis to acetic acid by esterase enzyme at high pH) deactivation steps. (b) The temporal change in pH of the system containing MCM-Z, esterase and ethyl acetate (DD). The equilibrium state pH is ca. 4.2 and addition of tris base (chemical fuel) increases the pH of the system to ca. 9.0. The transient basic pH state slowly comes back to equilibrium acidic state ca. (pH 5.0) as esterase catalyzed hydrolysis of ethyl acetate proceeds.

Further, the lifetime of the transient ‘CV<sup>+</sup> encapsulated state’ was programmed by modulating deactivation rate via enzyme concentration. In the case of 2.8 U mL<sup>-1</sup> esterase concentration, within 38 ± 6 min complete release of CV<sup>+</sup> was seen; on the other hand, when the esterase concentration was reduced to 0.7 U mL<sup>-1</sup>, it took longer time to reach complete release (>135 ± 5 min) (Figure 8). Interestingly, we noted that at any

esterase concentration, time taken for resetting pH back to the equilibrium pH (i.e. 5.0) ( $t_{\text{lead}}$ ) was higher than the time required for the complete release ( $t_{\text{response}}$ ) (Figure 8b).

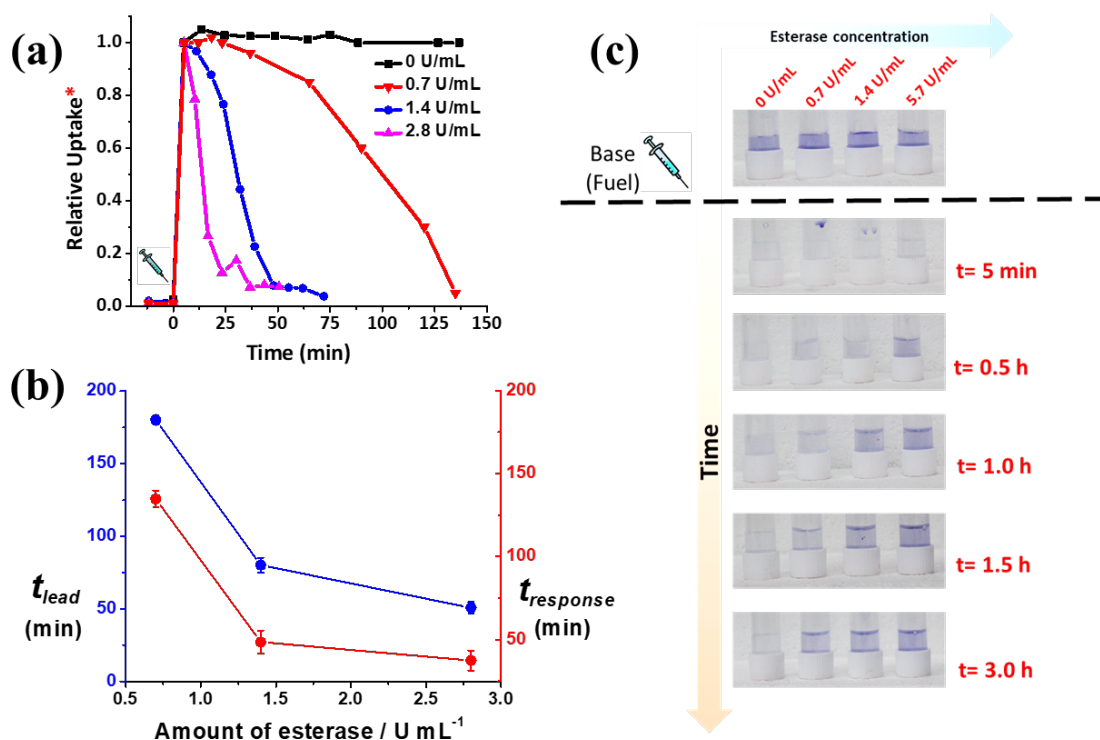


**Figure 8.** (a) Temporal regulation of CV uptake in **MCM-Z**. The lifetime of CV entrapped state is programmed by concentration of esterase. (b) Comparison between the lead time ( $t_{\text{lead}}$ , time taken for resetting pH to ca. 5.0) and response time ( $t_{\text{response}}$ , time taken for reaching 100 % CV release). (c) Photographs showing enzyme regulated temporal variation of the colour of supernatants. \*The CV<sup>+</sup> encapsulation is normalized w.r.t. amount of encapsulation at [esterase] = 0 U/mL.

The system was further tested for its ability to undergo multiple cycles on refueling chemical fuel (tris base) (Figure 9). For this purpose, a dispersion containing **MCM-Z**, CV<sup>+</sup> (~1.0  $\mu\text{mol g}^{-1}$ ) and 2.8 U mL<sup>-1</sup> esterase was taken at a pH of around 4.2 and the pH and CV<sup>+</sup> uptake was monitored (Figure 9). As expected no uptake was observed at this equilibrium state. However, an instantaneous entrapment of CV<sup>+</sup> was observed upon the addition of tris base (chemical fuel) (same amount used in the previous experiments). The entrapped CV<sup>+</sup> was then gradually released as ethyl acetate (DD) hydrolysis proceeds (ethyl acetate was added along with chemical fuel). On reaching the equilibrium state (pH ~5), system refuelling again (with the same amount of tris base)

showed a similar temporal profile. Refueling the system for the third time also resulted in a similar trend. Nevertheless, there was a dampening observed in the time required for complete release of  $CV^+$  as the cycles proceeded. This can be attributed to the accumulation of waste products in the closed system.

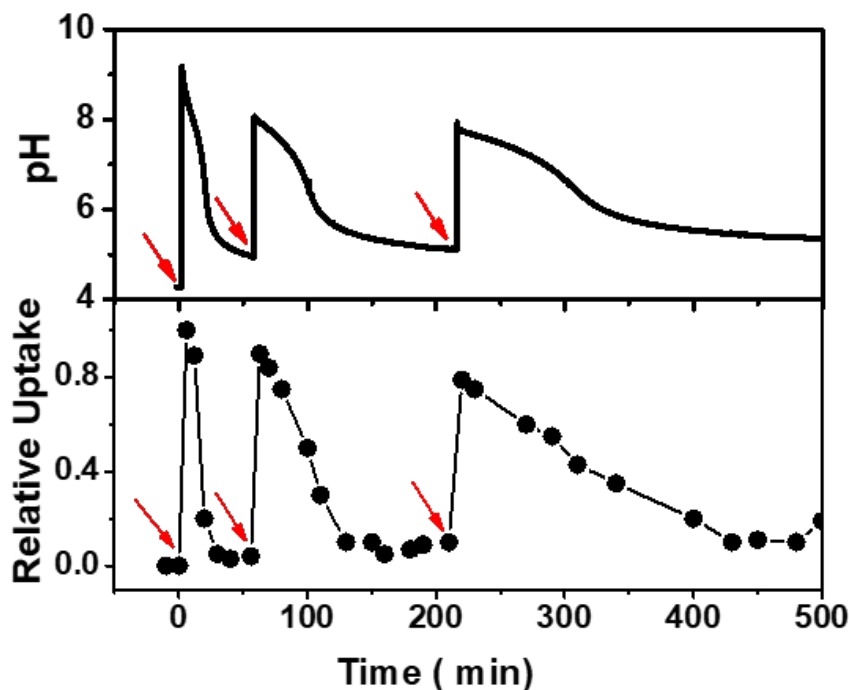


**Figure 9.** Refuelling the system showing the recyclable nature of  $CV^+$  encapsulation and release in *MCM-Z* along with corresponding pH trace. Red arrows indicate addition of fuel along with ethyl acetate (DD).

### 2.2.6. Conclusions

In summary, we demonstrated the construction of mesoporous silica based biomimetic nanochannels having enzyme mediated autonomous (temporal) regulation of ion transport. The fuel driven encapsulation of ions into the nanochannels and temporal control of their release have been shown for the first time in such nanochannels. The pre-programmable lifetime of transient ion transport was shown along with its refuelling capabilities. The nanochannels were also found to be very robust in terms of structural stability in basic medium. These temporally switchable and adaptive nanochannels shall pave the way for future on demand devices or delivery vehicles.

---

---

**2.2.7. References**

- (1) Korn, E. D. Actin polymerization and its regulation by proteins from nonmuscle cells. *Physiol. Rev.*, **1982**, *62* (2), 672-737.
- (2) Mitchison, T.; Kirschner, M. Dynamic instability of microtubule growth. *Nature* **1984**, *312* (5991), 237-242.
- (3) Ashkenasy, G.; Hermans, T. M.; Otto, S.; Taylor, A. F. Systems chemistry. *Chem. Soc. Rev.* **2017**, *46* (9), 2543-2554.
- (4) Heinen, L.; Walther, A. Celebrating Soft Matter's 10th Anniversary: Approaches to program the time domain of self-assemblies. *Soft Matter* **2015**, *11* (40), 7857-7866.
- (5) van Rossum, S. A. P.; Tena-Solsona, M.; van Esch, J. H.; Eelkema, R.; Boekhoven, J. Dissipative out-of-equilibrium assembly of man-made supramolecular materials. *Chem. Soc. Rev.* **2017**, *46* (18), 5519-5535.
- (6) Merindol, R.; Walther, A. Materials learning from life: concepts for active, adaptive and autonomous molecular systems. *Chem. Soc. Rev.* **2017**, *46* (18), 5588-5619.
- (7) Boekhoven, J.; Brizard, A. M.; Kowlgi, K. N. K.; Koper, G. J. M.; Eelkema, R.; van Esch, J. H. Dissipative Self-Assembly of a Molecular Gelator by Using a Chemical Fuel. *Angew. Chem. Int. Ed.* **2010**, *49* (28), 4825-4828.
- (8) Boekhoven, J.; Hendriksen, W. E.; Koper, G. J. M.; Eelkema, R.; van Esch, J. H. Transient assembly of active materials fueled by a chemical reaction. *Science* **2015**, *349* (6252), 1075-1079.
- (9) van Ravensteijn, B. G. P.; Hendriksen, W. E.; Eelkema, R.; van Esch, J. H.; Kegel, W. K. Fuel-Mediated Transient Clustering of Colloidal Building Blocks. *J. Am. Chem. Soc.* **2017**, *139* (29), 9763-9766.
- (10) Dhiman, S.; Jain, A.; George, S. J. Transient Helicity: Fuel-Driven Temporal Control over Conformational Switching in a Supramolecular Polymer. *Angew. Chem. Int. Ed.* **2017**, *56* (5), 1329-1333.
- (11) Jalani, K.; Dhiman, S.; Jain, A.; George, S. J. Temporal switching of an amphiphilic self-assembly by a chemical fuel-driven conformational response. *Chem. Sci.* **2017**, *8* (9), 6030-6036.



- (12) Wojciechowski, J. P.; Martin, A. D.; Thordarson, P. Kinetically Controlled Lifetimes in Redox-Responsive Transient Supramolecular Hydrogels. *J. Am. Chem. Soc.* **2018**, *140* (8), 2869-2874.
- (13) Kemper, B.; Zengerling, L.; Spitzer, D.; Otter, R.; Bauer, T.; Besenius, P. Kinetically Controlled Stepwise Self-Assembly of AuI-Metallopeptides in Water. *J. Am. Chem. Soc.* **2018**, *140* (2), 534-537.
- (14) Dong, B.; Liu, L.; Hu, C. ATP-Driven Temporal Control over Structure Switching of Polymeric Micelles. *Biomacromolecules* **2018**, *19* (9), 3659-3668.
- (15) Kariyawasam, L. S.; Hartley, C. S. Dissipative Assembly of Aqueous Carboxylic Acid Anhydrides Fueled by Carbodiimides. *J. Am. Chem. Soc.* **2017**, *139* (34), 11949-11955.
- (16) Pappas, C. G.; Sasselli, I. R.; Ulijn, R. V. Biocatalytic Pathway Selection in Transient Tripeptide Nanostructures. *Angew. Chem. Int. Ed.* **2015**, *54* (28), 8119-8123.
- (17) Sahoo, J. K.; Pappas, C. G.; Sasselli, I. R.; Abul-Haija, Y. M.; Ulijn, R. V. Biocatalytic Self-Assembly Cascades. *Angew. Chem. Int. Ed.* **2017**, *56* (24), 6828-6832.
- (18) Rangadurai, P.; Molla, M. R.; Prasad, P.; Caissy, M.; Thayumanavan, S. Temporal and Triggered Evolution of Host–Guest Characteristics in Amphiphilic Polymer Assemblies. *J. Am. Chem. Soc.* **2016**, *138* (24), 7508-7511.
- (19) Del Grosso, E.; Amodio, A.; Ragazzon, G.; Prins, L. J.; Ricci, F. Dissipative Synthetic DNA-Based Receptors for the Transient Loading and Release of Molecular Cargo. *Angew. Chem. Int. Ed.* **2018**, *57* (33), 10489-10493.
- (20) Che, H.; Buddingh', B. C.; van Hest, J. C. M. Self-Regulated and Temporal Control of a “Breathing” Microgel Mediated by Enzymatic Reaction. *Angew. Chem. Int. Ed.* **2017**, *56* (41), 12581-12585.
- (21) Pezzato, C.; Prins, L. J. Transient signal generation in a self-assembled nanosystem fueled by ATP. *Nat. Commun.* **2015**, *6*, 7790.
- (22) Maiti, S.; Fortunati, I.; Ferrante, C.; Scrimin, P.; Prins, L. J. Dissipative self-assembly of vesicular nanoreactors. *Nat. Chem.* **2016**, *8*, 725.
- (23) della Sala, F.; Maiti, S.; Bonanni, A.; Scrimin, P.; Prins, L. J. Fuel-Selective Transient Activation of Nanosystems for Signal Generation. *Angew. Chem. Int. Ed.* **2018**, *57* (6), 1611-1615.

- 
- 
- (24) Heuser, T.; Merindol, R.; Loescher, S.; Klaus, A.; Walther, A. Photonic Devices Out of Equilibrium: Transient Memory, Signal Propagation, and Sensing. *Adv. Mater.* **2017**, *29* (17), 1606842.
- (25) Kumar, M.; Ing, N. L.; Narang, V.; Wijerathne, N. K.; Hochbaum, A. I.; Ulijn, R. V. Amino-acid-encoded biocatalytic self-assembly enables the formation of transient conducting nanostructures. *Nat. Chem.* **2018**, *10* (7), 696-703.
- (26) Hille, B. *Ion Channels of Excitable Membranes*, 3 ed.; July 2001.
- (27) Liu, Q.; Xiao, K.; Wen, L.; Dong, Y.; Xie, G.; Zhang, Z.; Bo, Z.; Jiang, L. A Fluoride-Driven Ionic Gate Based on a 4-Aminophenylboronic Acid-Functionalized Asymmetric Single Nanochannel. *ACS Nano* **2014**, *8* (12), 12292-12299.
- (28) Brunsen, A.; Díaz, C.; Pietrasanta, L. I.; Yameen, B.; Ceolín, M.; Soler-Illia, G. J. A. A.; Azzaroni, O. Proton and Calcium-Gated Ionic Mesochannels: Phosphate-Bearing Polymer Brushes Hosted in Mesoporous Thin Films As Biomimetic Interfacial Architectures. *Langmuir* **2012**, *28* (7), 3583-3592.
- (29) Hou, X.; Yang, F.; Li, L.; Song, Y.; Jiang, L.; Zhu, D. A Biomimetic Asymmetric Responsive Single Nanochannel. *J. Am. Chem. Soc.* **2010**, *132* (33), 11736-11742.
- (30) Yameen, B.; Ali, M.; Neumann, R.; Ensinger, W.; Knoll, W.; Azzaroni, O. Single Conical Nanopores Displaying pH-Tunable Rectifying Characteristics. Manipulating Ionic Transport With Zwitterionic Polymer Brushes. *J. Am. Chem. Soc.* **2009**, *131* (6), 2070-2071.
- (31) Guo, W.; Tian, Y.; Jiang, L. Asymmetric Ion Transport through Ion-Channel-Mimetic Solid-State Nanopores. *Acc. Chem. Res.* **2013**, *46* (12), 2834-2846.
- (32) Peters, R. J. R. W.; Louzao, I.; van Hest, J. C. M. From polymeric nanoreactors to artificial organelles. *Chem. Sci.* **2012**, *3* (2), 335-342.
- (33) Peters, R. J. R. W.; Marguet, M.; Marais, S.; Fraaije, M. W.; van Hest, J. C. M.; Lecommandoux, S. Cascade Reactions in Multicompartmentalized Polymersomes. *Angew. Chem. Int. Ed.* **2014**, *53* (1), 146-150.
- (34) Dinsmore, A. D.; Hsu, M. F.; Nikolaidis, M. G.; Marquez, M.; Bausch, A. R.; Weitz, D. A. Colloidosomes: Selectively Permeable Capsules Composed of Colloidal Particles. *Science* **2002**, *298* (5595), 1006-1009.
- (35) Li, M.; Harbron, R. L.; Weaver, J. V. M.; Binks, B. P.; Mann, S. Electrostatically gated membrane permeability in inorganic protocells. *Nat Chem.* **2013**, *5*, 529.

- (36) Noireaux, V.; Libchaber, A. A vesicle bioreactor as a step toward an artificial cell assembly. *Proc. Natl. Acad. Sci. U.S.A* **2004**, *101* (51), 17669-17674.
- (37) Koga, S.; Williams, D. S.; Perriman, A. W.; Mann, S. Peptide–nucleotide microdroplets as a step towards a membrane-free protocell model. *Nat. Chem.* **2011**, *3*, 720.
- (38) Liu, W.; Liu, J.; Yang, X.; Wang, K.; Wang, Q.; Yang, M.; Li, L.; Song, C. Phosphate modulated permeability of mesoporous silica spheres: a biomimetic ion channel decorated compartment model. *J. Mater. Chem. B* **2015**, *3* (2), 323-329.
- (39) Dzieciol, A. J.; Mann, S. Designs for life: protocell models in the laboratory. *Chem. Soc. Rev.* **2012**, *41* (1), 79-85.
- (40) Gao, J.; Zhao, B.; Wang, M.; Serrano, M. A. C.; Zhuang, J.; Ray, M.; Rotello, V. M.; Vachet, R. W.; Thayumanavan, S. Supramolecular Assemblies for Transporting Proteins Across an Immiscible Solvent Interface. *J. Am. Chem. Soc.* **2018**, *140* (7), 2421-2425.
- (41) Fernando, I. R.; Ferris, D. P.; Frasconi, M.; Malin, D.; Strelakova, E.; Yilmaz, M. D.; Ambrogio, M. W.; Algaradah, M. M.; Hong, M. P.; Chen, X.; Nassar, M. S.; Botros, Y. Y.; Cryns, V. L.; Stoddart, J. F. Esterase- and pH-responsive poly( $\beta$ -amino ester)-capped mesoporous silica nanoparticles for drug delivery. *Nanoscale* **2015**, *7* (16), 7178-7183.
- (42) Liu, R.; Zhang, Y.; Zhao, X.; Agarwal, A.; Mueller, L. J.; Feng, P. pH-Responsive Nanogated Ensemble Based on Gold-Capped Mesoporous Silica through an Acid-Labile Acetal Linker. *J. Am. Chem. Soc.* **2010**, *132* (5), 1500-1501.
- (43) Wu, S.; Huang, X.; Du, X. Glucose- and pH-Responsive Controlled Release of Cargo from Protein-Gated Carbohydrate-Functionalized Mesoporous Silica Nanocontainers. *Angew. Chem. Int. Ed.* **2013**, *52* (21), 5580-5584.
- (44) Yao, X.; Chen, X.; He, C.; Chen, L.; Chen, X. Dual pH-responsive mesoporous silica nanoparticles for efficient combination of chemotherapy and photodynamic therapy. *J. Mater. Chem. B* **2015**, *3* (23), 4707-4714.
- (45) Yuan, L.; Tang, Q.; Yang, D.; Zhang, J. Z.; Zhang, F.; Hu, J. Preparation of pH-Responsive Mesoporous Silica Nanoparticles and Their Application in Controlled Drug Delivery. *J. Phys. Chem. C* **2011**, *115* (20), 9926-9932.

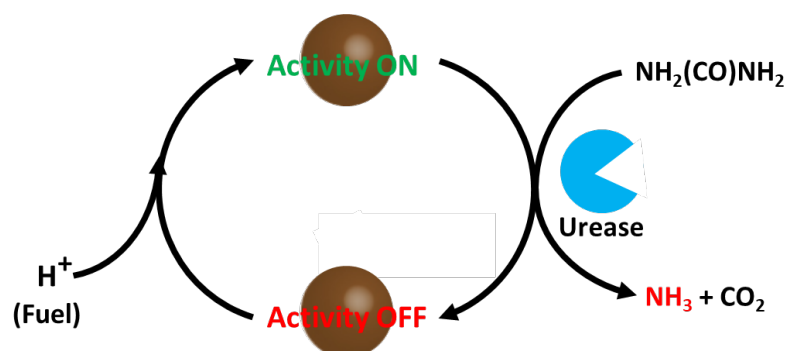
- 
- 
- (46) Lee, C.-H.; Cheng, S.-H.; Huang, I.-P.; Souris, J. S.; Yang, C.-S.; Mou, C.-Y.; Lo, L.-W. Intracellular pH-Responsive Mesoporous Silica Nanoparticles for the Controlled Release of Anticancer Chemotherapeutics. *Angew. Chem. Int. Ed.* **2010**, *49* (44), 8214-8219.
- (47) Xing, L.; Zheng, H.; Cao, Y.; Che, S. Coordination Polymer Coated Mesoporous Silica Nanoparticles for pH-Responsive Drug Release. *Adv. Mater.* **2012**, *24* (48), 6433-6437.
- (48) Wang, J.; Fang, R.; Hou, J.; Zhang, H.; Tian, Y.; Wang, H.; Jiang, L. Oscillatory Reaction Induced Periodic C-Quadruplex DNA Gating of Artificial Ion Channels. *ACS Nano* **2017**, *11* (3), 3022-3029.
- (49) Huh, S.; Wiench, J. W.; Yoo, J.-C.; Pruski, M.; Lin, V. S. Y. Organic Functionalization and Morphology Control of Mesoporous Silicas via a Co-Condensation Synthesis Method. *Chem. Mater.* **2003**, *15* (22), 4247-4256.
- (50) B. V. V. S. Pavan; Salikolimi, K.; Eswaramoorthy, M. Glucose- and pH-Responsive Charge-Reversal Surfaces. *Langmuir* **2014**, *30* (16), 4540-4544.
- (51) Fisk, J. D.; Batten, R.; Jones, G.; O'Reill, J. P.; Shaw, A. M. pH Dependence of the Crystal Violet Adsorption Isotherm at the Silica–Water Interface. *J. Phys. Chem. B* **2005**, *109* (30), 14475-14480.
- (52) Manzo, V.; Navarro, O.; Honda, L.; Sánchez, K.; Inés Toral, M.; Richter, P. Determination of crystal violet in water by direct solid phase spectrophotometry after rotating disk sorptive extraction. *Talanta* **2013**, *106*, 305-308.
- (53) Heinen, L.; Heuser, T.; Steinschulte, A.; Walther, A. Antagonistic Enzymes in a Biocatalytic pH Feedback System Program Autonomous DNA Hydrogel Life Cycles. *Nano Lett.* **2017**, *17* (8), 4989-4995.

## Chapter- 2.3

### *Bio-inspired Temporal Regulation of Catalytic Activity of a Nanozyme*

#### **Summary:**

*Biochemical reaction networks where one enzyme temporally regulates the activity of the other are hallmarks of biological systems. Often, such temporal regulation is achieved via dissipative machineries operating far-from-equilibrium. Inspired from this, there have been tremendous efforts to construct artificial enzyme networks operating either at equilibrium (without temporal regulations) or far-from-equilibrium (with temporal regulations). Recently, inorganic nanoparticles showing enzyme-like activity (nanozyme) have been emerged with several advantages compared to their natural counterparts. Subsequently, nanozymes have been utilized to construct artificial chemical networks for various sensing applications. However, in these networks (unlike their natural counterparts) temporal regulation was never demonstrated. In this chapter, we report a successful construction of simple artificial biochemical reaction network consisting of a nanozyme and an enzyme. The peroxidase mimicking activity of nanozyme is temporally regulated by the base producing urease activity (on urea) in a fuel-driven manner. The system represents a close mimic of the fuel-driven temporally regulated enzymes networks in biology.*



Manuscript based on this chapter is under preparation.



### 2.3.1. Introduction

The elegance with which nature constructed biochemical reaction networks consisting of multiple enzymes operate in tandem towards precise temporal occurrence of events have always inspired chemists to construct similar man-made counterparts.<sup>1-4</sup> In this direction, initial efforts have been mostly focused onto cascade enzyme systems where two or more enzymes were connected in a manner that the product of the first enzymatic reaction would be the substrate for second and so on.<sup>5-12</sup> Often these enzymes have been incorporated inside certain vessels like lipid vesicles<sup>7</sup>, proteinosomes<sup>13-14</sup>, polymersomes<sup>15-16</sup>, colloidosomes<sup>17</sup> etc. Such network systems have been well-established towards applications in the field of sensing and diagnostics.<sup>18-27</sup>

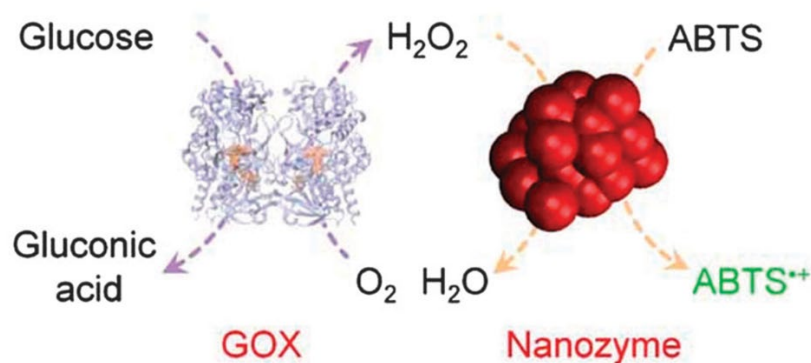


**Figure 1.** Nanozyme as peroxidase mimic for colorimetric sensing of H<sub>2</sub>O<sub>2</sub> and glucose when combined with glucose oxidase. In presence of glucose, the enzyme glucose oxidase convert it to gluconic acid and hydrogen peroxide (H<sub>2</sub>O<sub>2</sub>). In presence of H<sub>2</sub>O<sub>2</sub>, the nanozyme (peroxidase mimic) catalyses the oxidation of a chromogenic substrate (ABTS) to a coloured product (oxidized ABTS). The colour development is used as a visual response. Reproduced with permission from reference 28. Copyright 2013, Royal Society of Chemistry.

In the past decade, a new type of enzyme mimics (well-known as nanozyme) have been emerged.<sup>28-36</sup> These are inorganic nanoparticles intrinsically possessing the catalytic activities similar to their natural counter-parts such as superoxide dismutase (SOD)<sup>37</sup>, catalase<sup>38</sup>, peroxidase<sup>35</sup>, glucose oxidase<sup>39</sup>, RNase<sup>40</sup> etc. By virtue of their advantages such as high stability, wide operating conditions (pH and temperature), low cost etc. nanozymes find tremendous applications and often they are used in a network with another natural enzymes.<sup>32</sup> A cascade network consisting of glucose oxidase and

peroxidase-like nanozyme ( $\text{Fe}_3\text{O}_4$  nanoparticles, gold nanoparticles, graphene oxide,  $\text{V}_2\text{O}_5$  nanowires etc.) towards glucose sensing is a typical example (Figure 1).<sup>41-43</sup> Similar networks were also used for the sensing of a variety of analytes such as galactose<sup>44-45</sup>, choline<sup>46</sup>, cholesterol<sup>47</sup>, xanthine<sup>48</sup> etc. While these network systems (both enzyme-enzyme and nanozyme-enzyme) represent one aspect of natural reactions networks, the fuel-driven temporal regulation in these systems are largely unexplored.

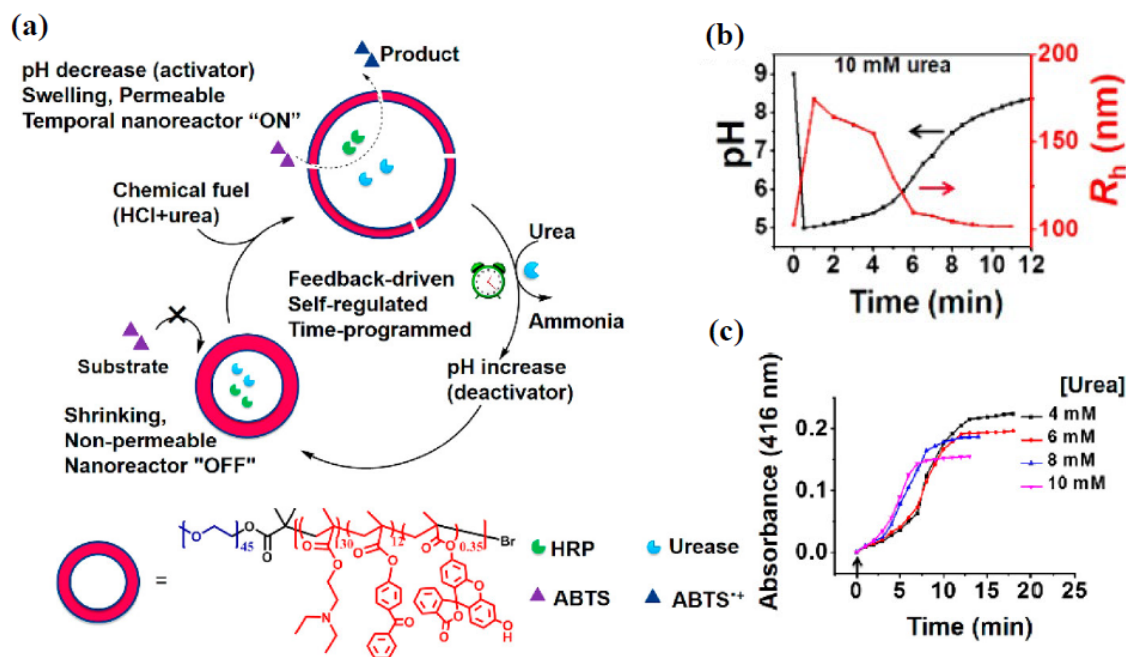


**Figure 2. Feedback-induced temporal control of “breathing” polymersomes to create self-adaptive nanoreactors** (a) Schematic overview of feedback-induced temporal control of polymersome nanoreactors. (b) Temporal variation of size changes of the polymersome nanoreactor along with variation of pH solution. (c) UV absorbance at 416 nm of the oxidation of ABTS by nanoreactors upon the addition of different concentrations of urea. Reproduced with permission from reference 51. Copyright 2018, American Chemical Society

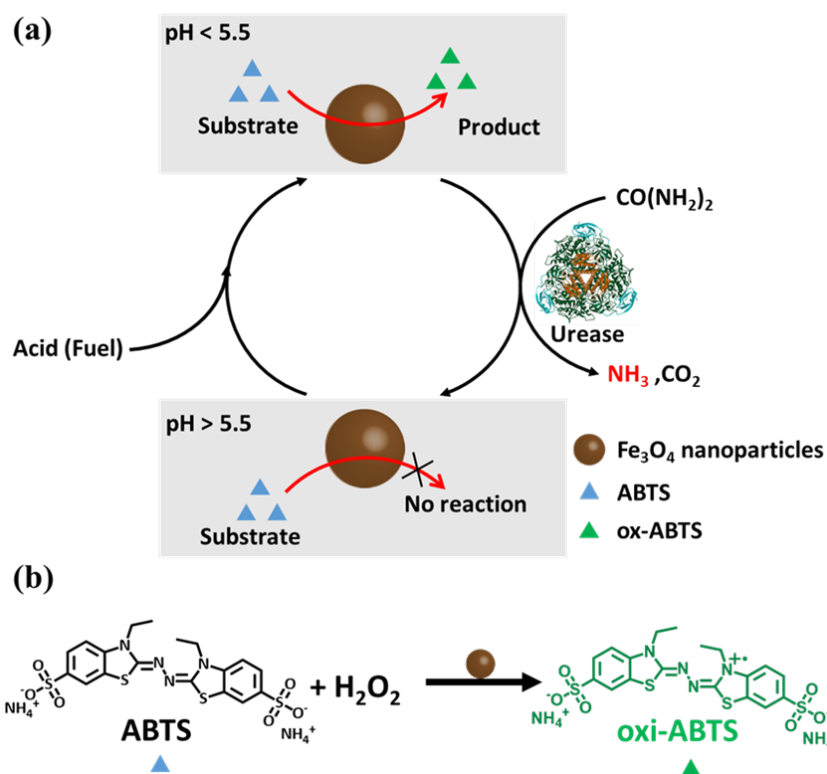
Inspired by recent developments in fuel-driven non-equilibrium self-assembly<sup>49-50</sup>, some efforts have been made to demonstrate enzyme networks operating far-from equilibrium with temporally regulated catalytic activity.<sup>51-55</sup> For instance, van Hest and co-workers elegantly designed a network of urease and horseradish peroxidase (HRP) enzymes encapsulated within a polymersome having pH dependent permeability (Figure 2).<sup>51</sup> At the resting state, the polymersome was impermeable, therefore, substrates of HRP (ABTS and  $\text{H}_2\text{O}_2$ ) were unable to reach at enzyme active site and hence no catalytic



reaction occurred. Addition of fuel (acid) decreased the pH and the polymersome became permeable and catalytic reaction started to occur (ON state). This ON state was temporally regulated by urease enzyme present in the polymersome. Thomas R. Ward and co-workers demonstrated a similar biochemical reaction network using an artificial metalloenzyme and urease towards temporal regulation of the catalytic activity of metalloenzyme.<sup>52</sup> However, such examples of fuel-driven temporally regulated enzymes (or artificial enzymes) networks are limited to these two reports. In order to expand the scope of such systems and therefore their functions, it is necessary to design many such fuel-driven temporally regulated self-adaptive biochemical reaction networks.

### 2.3.2. Scope of the present investigation

In this chapter, we demonstrated for the first time a self-adaptive nanozyme-natural enzyme network with temporally regulated catalytic activity. The envisioned network system with feedback-induced temporal controlled peroxidase-like catalytic-



**Scheme 1. Bio-catalytic fuel-driven temporal control of catalytic activity of nanozyme.**

(a) The peroxidase mimicking nanozyme (Fe<sub>3</sub>O<sub>4</sub> nanoparticles) convert chromogenic substrate (ABTS) in to a coloured product at a pH less than ca. 5.5. At the resting state (pH > 7), the nanozyme is inactive towards ABTS oxidation (OFF state). Upon addition

*of acid (fuel) the nanozyme becomes active and this ON state is temporally regulated by the pH re-setting urea hydrolysis reaction mediated by urease enzyme. (b) Fe<sub>3</sub>O<sub>4</sub> nanozyme catalyses the H<sub>2</sub>O<sub>2</sub> mediated oxidation of a chromogenic reactant (2,2'-azino-bis(3-ethylbenzothiazoline-6-sulphonic acid)). The oxidized product shows green colour with an absorption maximum at 416 nm.*

-activity is illustrated in scheme 1. The network consists of urea and urease feedback machinery and Fe<sub>3</sub>O<sub>4</sub> nanoparticles (the nanozyme with intrinsic peroxidase like activity). The catalytic activity of Fe<sub>3</sub>O<sub>4</sub> nanoparticles was designed to switch temporally in a fuel driven manner. The complete switching cycle (OFF to ON to OFF) consisted of fast activation and a slower deactivation processes. At the initial state or resting state (pH > 5.5), the catalytic activity of Fe<sub>3</sub>O<sub>4</sub> nanoparticle is switched OFF. The faster activation by the addition of acid (fuel) activate the nanozyme, thereby switching the activity ON. Over time, a gradual increase of the pH occur via catalytic hydrolysis of urea to ammonia. Therefore, the system comes back to the resting state and subsequently the activity gets switched OFF again. This system represents a unique, self-adaptive, nanozyme-natural enzyme network operating closely to the natural biochemical reaction networks (having features like cross regulation, self-adaptive and temporal regulation).

### 2.3.3. Experimental section

**Synthesis of Fe<sub>3</sub>O<sub>4</sub> nanoparticle.** The nanoparticles were prepared by co-precipitation of Fe<sup>2+</sup> and Fe<sup>3+</sup> in the molar ratio of 1:2. A 100 mmol of FeCl<sub>3</sub>.6H<sub>2</sub>O and 50 mmol of FeCl<sub>2</sub>.4H<sub>2</sub>O were dissolved in a 250 mL de-aerated water. The temperature of the solution was slowly increased to 80 °C under nitrogen atmosphere. Solution was vigorously stirred to prevent the formation of large polycrystalline particles. Turbulence was maintained by keeping the reaction flask under sonication. After 2 mins of mixing, 75 mL of NH<sub>4</sub>OH solution (25%) was added under vigorous mechanical stirring. The black precipitate formed indicating the formation nanoparticles. The mixture was further allowed to stir for another 30 min. After completing the reaction, the precipitate was thoroughly washed with water till the supernatant pH became neutral. The precipitate was then dried under vacuum.

**Catalytic activity of Fe<sub>3</sub>O<sub>4</sub> nanoparticle.** The peroxidase-like activity of Fe<sub>3</sub>O<sub>4</sub> nanoparticle was determined by using ABTS ((2,2'-Azinobis [3-ethylbenzothiazoline-6-sulfonic acid]-diammonium salt)) as substrate. The formation of oxidation product (ox-

ABTS) was monitored by UV–vis spectroscopy. The final concentrations of the components were following: ABTS (0.6 mM), Fe<sub>3</sub>O<sub>4</sub> nanoparticles (20 µg/mL) and H<sub>2</sub>O<sub>2</sub> (200 mM). The final volume of the reaction mixture was 2 mL and the pH of the buffer was 4.0. The UV-Vis spectra were recorded every 2 – 3 minutes. The kinetics of the reaction was determined by using time dependent absorption measurements at 414 nm. The absorbance values were converted to the amount of ox-ABTS by using previously reported molecular absorption coefficient of  $3.6 \times 10^4 \text{ M}^{-1} \text{ cm}^{-1}$ . The pH dependent activity of the Fe<sub>3</sub>O<sub>4</sub> nanoparticles were tested using the same procedure as above except for varying pH buffers in the range of 3 to 7.0.

**The kinetic analysis of Fe<sub>3</sub>O<sub>4</sub> nanoparticle (Michaelis Menten kinetics).** The kinetic measurements were carried out in ‘time drive’ mode (absorbance vs. time) by monitoring the absorbance change at 414 nm for every 5 seconds. In order to investigate the kinetic parameters, the initial rate of the reaction was determined for different concentrations of ABTS at a constant H<sub>2</sub>O<sub>2</sub> concentration (200 mM). The apparent kinetic parameters were calculated based on the Lineweaver–Burk plot (the double reciprocal plot of the Michaelis–Menten kinetics plot).

$$\frac{1}{v} = \left( \frac{K_m}{V_{max}} \right) \times \frac{1}{C} + \frac{1}{V_{max}}$$

where  $v$  is the initial velocity,  $K_m$  is the Michaelis-Menten constant,  $V_{max}$  is the maximal reaction velocity and  $C$  is the concentration of substrate, ABTS.

These measurements were carried out at room temperature in 10 mM buffer of pH 4.0 (3 mL).

**Temporal regulation of catalytic activity of Fe<sub>3</sub>O<sub>4</sub> nanoparticle.** A mixture consisting of ABTS (0.6 mM), Fe<sub>3</sub>O<sub>4</sub> nanoparticles (20 µg/mL) and H<sub>2</sub>O<sub>2</sub> (200 mM) were taken in a pH buffer of 7.0 (buffer concentration of 2.5 mM) along with urease enzyme of varying concentrations (0 to 15 U/mL). The total volume of the solution was 2.5 mL. To this mixture, 0.5 mL of citrate buffer (1 mL stock prepared by mixing 0.3 mL sodium citrate solution (0.1 M) and 0.7 mL citric acid solution (0.1 M)) with dissolved urea (18 mg, 0.37 mmol) was added to activate the system. The final concentration of urea in the solution was 100 mM. The rise of absorbance at 414 nm was monitored in ‘time drive’ mode (absorbance vs. time) to obtain the temporal changes of oxidation.

### 2.3.4. Characterization

Please see the appendix for the details of the instrumentation of UV-Visible spectroscopy, X-ray diffraction, Transmission electron microscopy, X-ray photoelectron spectroscopy and pH measurements.

### 2.3.5. Results and discussion

The  $\text{Fe}_3\text{O}_4$  nanoparticles (which is a peroxidase nanozyme) were synthesised via a typical co-precipitation method as previously described.<sup>56</sup> The transmission electron microscopy image (Figure 3a) shows nearly monodispersed nanoparticles with an average size around 15 nm. The Powder X-ray diffraction (PXRD) analysis shows crystalline feature of  $\text{Fe}_3\text{O}_4$  nanoparticles. The nanoparticle form of the  $\text{Fe}_3\text{O}_4$  was also evident-

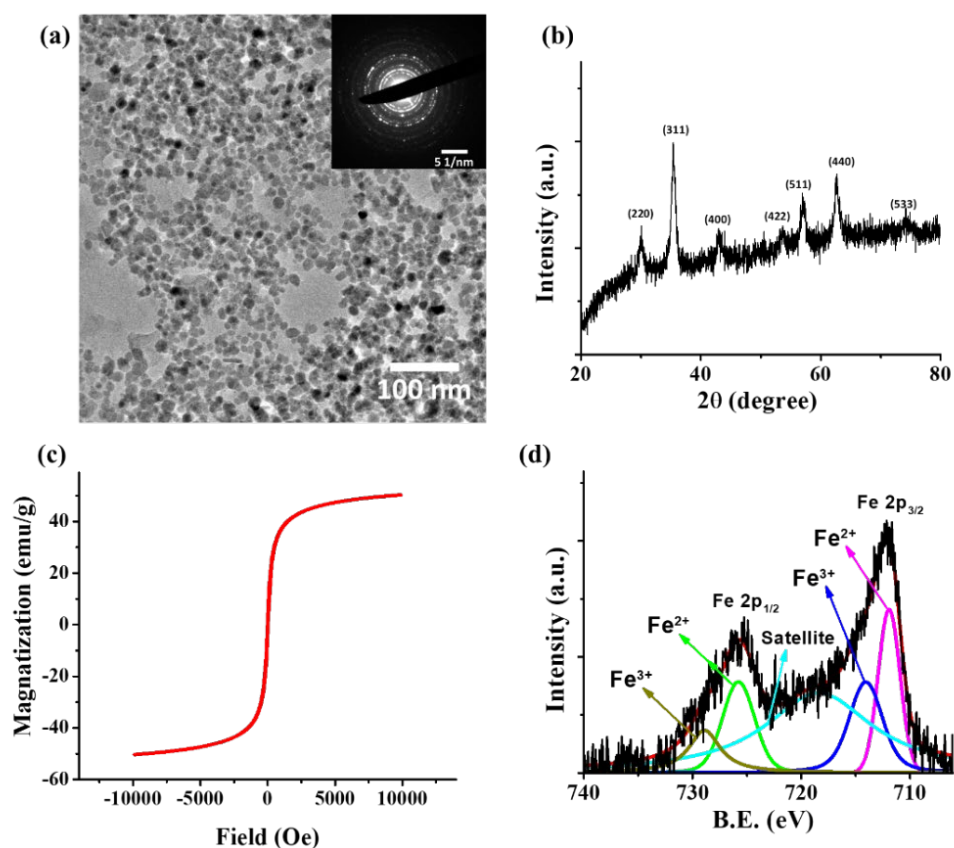


**Figure 3.** (a) Transmission Electron Microscopy image of  $\text{Fe}_3\text{O}_4$  nanoparticles. Inset showing the ED pattern of  $\text{Fe}_3\text{O}_4$  nanoparticles. (b) Powder X-ray diffraction pattern of  $\text{Fe}_3\text{O}_4$  nanoparticles. (c) Magnetization curve (B-H curve) of  $\text{Fe}_3\text{O}_4$  nanoparticles. (d) X-ray Photoelectron Spectra (Fe 2p) of  $\text{Fe}_3\text{O}_4$  nanoparticles.

-from the broad peaks in the XRD pattern. The Scherrer analysis shows that the crystalline domain size of  $\text{Fe}_3\text{O}_4$  nanoparticles was around 12 nm. The magnetization curve at room temperature suggest the superparamagnetic nature of the nanoparticles (Figure 3c). The X-ray photoelectron spectrum of the Fe 2p region (Figure 3d) revealed the presence of both  $\text{Fe}^{2+}$  and  $\text{Fe}^{3+}$  valence states which is essential for the peroxidase-like activity.<sup>57</sup> The satellite peak situated at about 718 eV is a characteristic peak of  $\text{Fe}^{3+}$  in  $\gamma\text{-Fe}_2\text{O}_3$ , suggesting that the nanoparticle was consisting of mixed phases of  $\text{Fe}_3\text{O}_4$  and  $\gamma\text{-Fe}_2\text{O}_3$  (nonstoichiometric  $\text{Fe}_3\text{O}_{4+\delta}$ ).<sup>58</sup>

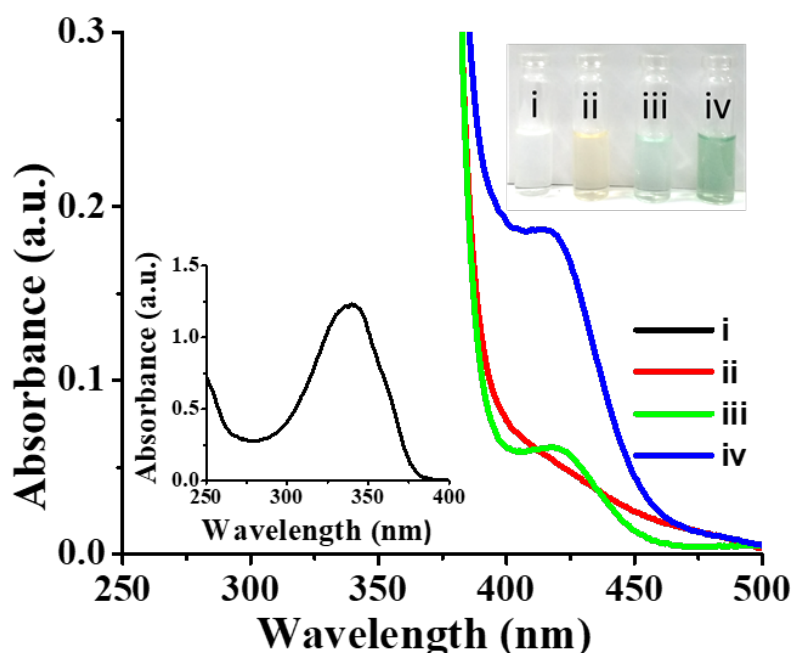


**Figure 4.** Peroxidase-like activity of  $\text{Fe}_3\text{O}_4$  NPs towards the oxidation of chromogenic substrate ABTS. UV-Vis spectra of (i) 0.03 mM ABTS, (ii) ABTS (0.6 mM) and  $\text{Fe}_3\text{O}_4$  nanoparticles (20  $\mu\text{g}/\text{mL}$ ), (iii) ABTS (0.6 mM) and  $\text{H}_2\text{O}_2$  (200 mM), (iv) ABTS (0.6 mM),  $\text{Fe}_3\text{O}_4$  nanoparticles (20  $\mu\text{g}/\text{mL}$ ) and  $\text{H}_2\text{O}_2$  (200 mM). Total volume of all the solutions was 2 mL.

The intrinsic peroxidase like activity of  $\text{Fe}_3\text{O}_4$  nanoparticles have been previously reported.<sup>35</sup> We tested this catalytic activity using 2,2'-Azino-bis(3-ethylbenzothiazoline-6-sulfonic acid) diammonium salt (ABTS) in presence of  $\text{H}_2\text{O}_2$  at pH around 4.0. As shown in the Figure 4, the  $\text{Fe}_3\text{O}_4$  nanoparticles were able to catalyse the oxidation of ABTS by  $\text{H}_2\text{O}_2$  to produce an intense green colour. The maximum absorption of the UV spectrum of the oxidized ABTS is around 414 nm. A set of control experiments were

conducted with ABTS in the absence of Fe<sub>3</sub>O<sub>4</sub> nanoparticles or H<sub>2</sub>O<sub>2</sub> and no oxidative reaction was found suggesting that both the components are necessary for the reaction as in the case of horseradish peroxidase (HRP) – a natural enzyme known to carry out ABTS oxidation in presence of H<sub>2</sub>O<sub>2</sub>. Further, we looked in to the temporal changes of the absorption spectra of oxidized ABTS as reaction proceeds (Figure 5a). Indeed, a conspicuous ascension of absorbance at 414 nm was observed in the case of Fe<sub>3</sub>O<sub>4</sub>-H<sub>2</sub>O<sub>2</sub> –ABTS system. The absorbance value at 414 nm was utilized to quantify the amount of oxidized ABTS using molecular absorption coefficient (ca.  $3.6 \times 10^4 \text{ M}^{-1} \text{ cm}^{-1}$ ). The given catalytic system could produce ox-ABTS as high as 5.3  $\mu\text{mol}$  within 20 min (Figure 5b).

The peroxidase-like catalytic activity of Fe<sub>3</sub>O<sub>4</sub> nanoparticle was further investigated at pH 4.0 using steady-state kinetics (Figure 6). The kinetic data were acquired by varying the concentration of ABTS while keeping the H<sub>2</sub>O<sub>2</sub> concentration constant. The initial reaction rates for each ABTS concentration were determined and applied to construct Michaelies-Menten kinetic plot for ABTS. The  $K_m$  (Michaelies-Menten constant) and  $V_{max}$  (maximal reaction velocity) were determined by Lineweaver–Burk plots (Figure 6b) and found to be around 0.38 mM and  $1.85 \times 10^{-8} \text{ Ms}^{-1}$  respectively which fall within the previously reported range.<sup>59</sup> The current  $K_m$  value of Fe<sub>3</sub>O<sub>4</sub> nanoparticle suggests its decent affinity towards ABTS.

Construction of nanozyme with self-regulated catalytic activity (by integrating Fe<sub>3</sub>O<sub>4</sub> nanoparticles with urease based pH resetting feedback system) requires Fe<sub>3</sub>O<sub>4</sub> nanoparticles to have pH switchable catalytic activity. This was tested in detail. Figure 7a shows the pH dependent catalytic activity of Fe<sub>3</sub>O<sub>4</sub> nanoparticles towards ABTS oxidation. Clearly, the maximum activity was observed for a pH around 3.5 and the activity got completely switched off for all pH higher than ca. 5.5. Interestingly, the catalytic activity could be switched on by adding an acid as a trigger (initially all the components were taken in a buffer of pH 7.0 where nanozyme was in OFF state) (Figure 7b). Further, the nanozyme in its ON state could be brought to the OFF state by adding a base as a trigger (Figure 7c-d). This ON-OFF switching was demonstrated for more than one cycle which clearly suggests the robustness of nanozyme for switching between ON and OFF states by the addition of antagonistic pH stimuli (Figure 7d).

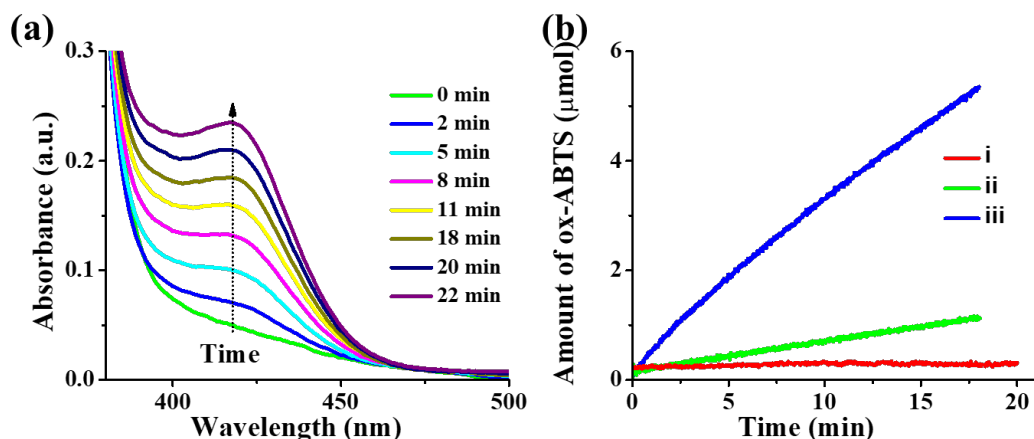


**Figure 5.** Peroxidase-like activity of  $Fe_3O_4$  NPs towards the oxidation of chromogenic substrate ABTS. (a) UV-Vis spectra showing the evolution of ox-ABTS in the reaction mixture as a function of time at pH 4.0 (b) The kinetics of oxidation of ABTS with (i) all components present, (ii) without  $Fe_3O_4$  nanoparticles and (iii) without  $H_2O_2$ . The pH of the reaction mixture is 4.0.

Temporal control of the catalytic activity of nanozyme was realized by integrating it with urease based chemistry. Firstly, the ability of urease based system to produce a temporal acidic pH profile by self-regulating the pH change upon addition of acid fuel was studied (Figure 8a). To this end, we have taken all the components of catalytic system ( $Fe_3O_4$  nanoparticles (20  $\mu\text{g}/\text{mL}$ ),  $H_2O_2$  (200 mM) and ABTS (0.6 mM)) along with urease (0-15 U/mL) at a pH of around 7.0 (total volume taken was 2.5 mL) and the time dependent pH variation was monitored (Figure 8b). The citric acid/ sodium citrate buffer (chemical fuel, 0.5 mL, 0.1 M) along with urea (dormant deactivator, 0.37 mmol) was added to the reaction mixture to activate the nanozyme. An initial decrease of pH to around 4.5 was observed that gradually increased to an equilibrium pH state of about 6.0 due to the formation of ammonia through the hydrolysis of urea by urease enzyme. The kinetics of urea hydrolysis was proportional to the amount of urease enzyme used. An increase of urease enzyme resulted in a higher rate of urea hydrolysis and subsequently resulted in a faster pH recovery. The pH remained around 4.5 if no urease enzyme was used signifying the importance of urease enzyme to construct the acidic pH temporal profile.

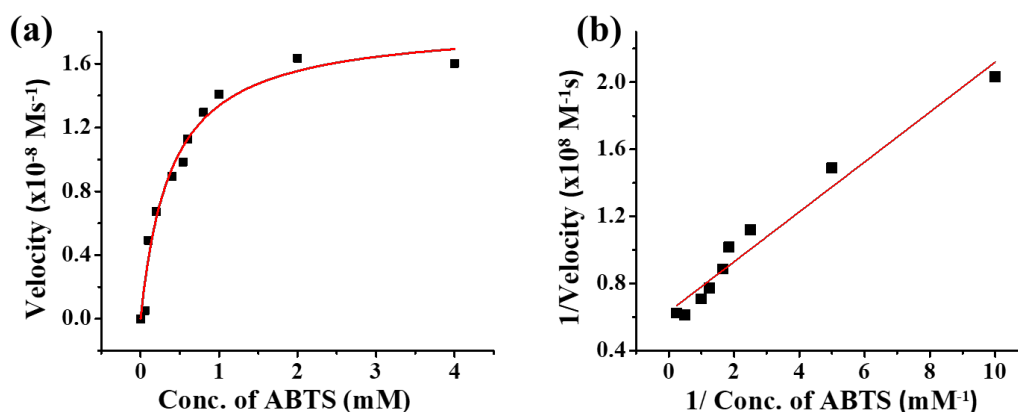


**Figure 6. Steady-state kinetic study of Fe<sub>3</sub>O<sub>4</sub> nanoparticles.** (a) The reaction velocity of ABTS oxidation by Fe<sub>3</sub>O<sub>4</sub> nanoparticles at varying concentration of ABTS. (b) Double reciprocal plot of reaction rates versus substrate concentrations for Fe<sub>3</sub>O<sub>4</sub> NP catalyzed oxidation of ABTS.

The pre-programmable temporal pH profile was then integrated to the peroxidase-like nanozyme to achieve a network of nanozyme - natural enzyme, working in tandem towards a temporally regulated activity. The above mentioned *in situ* pH modulation was expected to adjust, the activity of nanozyme autonomously (Figure 8c). At the initial equilibrium pH (around 7.0), no activity was observed. However, addition of citric acid/sodium citrate buffer (chemical fuel) along with urea (dormant deactivator) activated the nanozyme and the oxidized ABTS started to produce. In case of higher amounts (> 10 U/mL) of urease, the ABTS oxidation came to a stop as pH resettled to higher than 5.5. In the case of 8.2 U/mL urease amount, the catalytic switch OFF state was not observed within the time frame of the study which is in commensurate with the corresponding temporal pH profile (Figure 8b). The lifetime of the catalytic ON state could be modulated depending on the urease amount (Figure 8c-d). For example, in the case of 11.4 U/mL urease, the system took about  $14 \pm 3$  min to reset the activity, while for 14.7 U/mL urease, it took only about  $8 \pm 2$  min for the same. This clearly demonstrates the temporal programmability of nanozyme's catalytic activity. Further, it should be noted that the lead time (the time taken for resetting the pH back to ca. 5.5) and response time (the time taken for stopping the catalytic activity) showed reasonable agreements suggesting the quick response of the nanozyme (in terms of catalytic activity) to the change in pH of the surrounding solution.



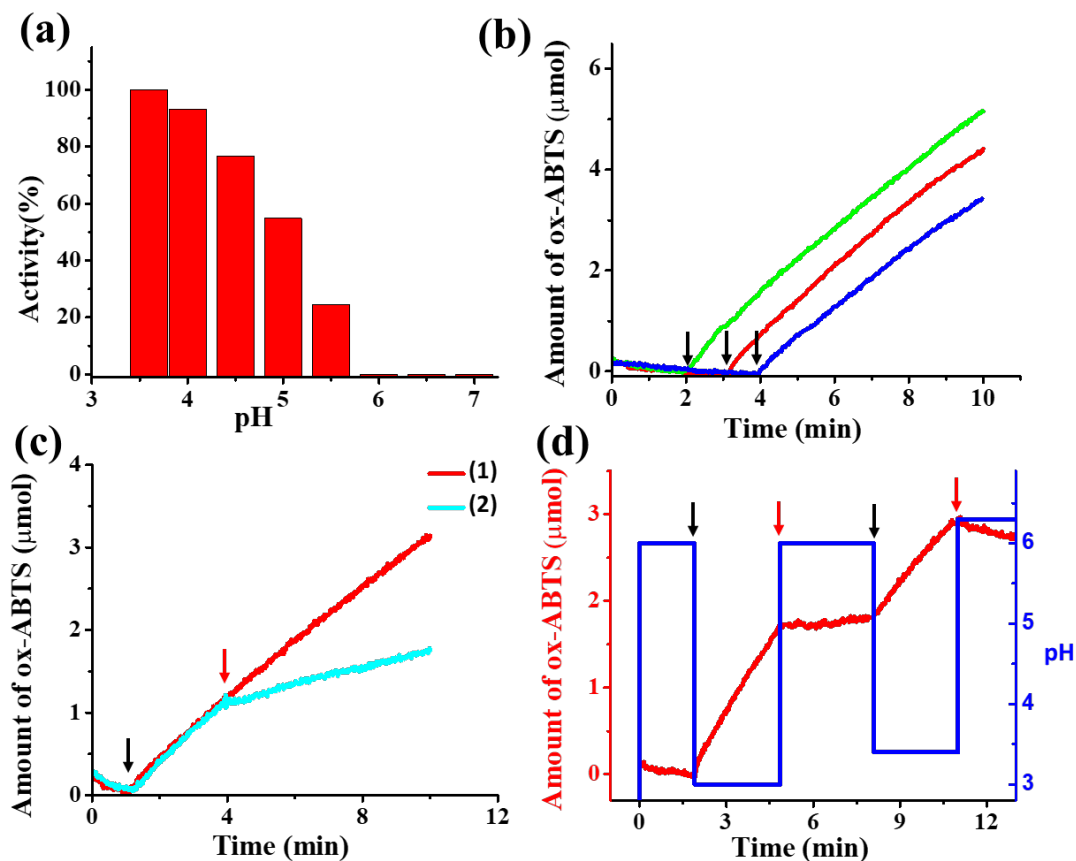


**Figure 7.** The pH dependent switching of catalytic activity of  $Fe_3O_4$  nanoparticles. (a) Relative activity of  $Fe_3O_4$  nanoparticles for oxidation of ABTS substrate at different pH. (b) Acid induced activation of  $Fe_3O_4$  nanoparticles towards oxidation of ABTS. At the beginning, pH of the solution was 7.0, which upon addition of CA/ $Na_3C$  buffer dropped to pH 3.1 thereby initiated the oxidation of ABTS. (c) Switching the catalytic activity ON at any point by decreasing the solution pH. Initial pH was around 7.0 (1) The kinetics of oxidation of ABTS without any interruption. (2) The base was added to the reaction mixture after 4 min which switched off the catalytic activity. (d) Manual addition of acid or base to switches on/off the reaction up to three cycles. ( $\downarrow$ ) and ( $\uparrow$ ) represent addition of acid and base respectively.

Interestingly, we observed that the initial rate of catalytic reaction was influenced by the urease enzyme (Figure 8c). This significant enhancement lead us to do few control studies (Figure 9). Firstly, we investigated the effect of urease enzyme alone (without the urea) at pH 4.0. Indeed, the activity of the nanozyme increased as a function of urease amount (Figure 9a). This increment could be due to the interaction of amino acid residues in the urease enzyme with  $Fe_3O_4$  nanoparticles as previously reported.<sup>60</sup> In a second set of experiments, the effect of urea on the catalytic activity of nanozyme was studied (Figure 9b). However, no significant change

in catalytic activity was observed for nanozyme in presence of different concentrations of the urea. Further, we also investigated if urease alone (without  $\text{Fe}_3\text{O}_4$  nanoparticles) has any role in catalysing the oxidation of ABTS by  $\text{H}_2\text{O}_2$  and found no influence (Figure 10).

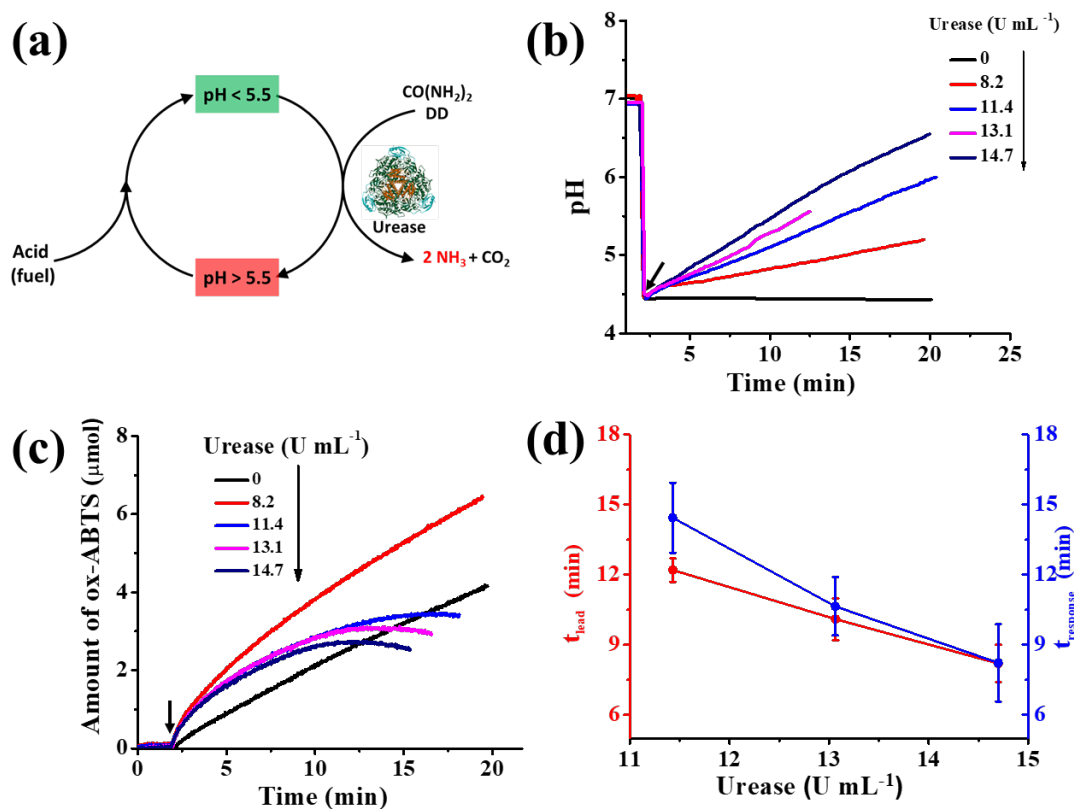


**Figure 8. Temporal regulation of catalytic activity of  $\text{Fe}_3\text{O}_4$  nanoparticles.** (a) Temporal regulation of catalytic activity of  $\text{Fe}_3\text{O}_4$  nanoparticles. (a) Bio-chemical reaction driven temporal regulation of pH of the system. The life-time of acid pH state can be regulated by urease catalyzed urea decomposition. (b) The temporal change in pH of the system containing  $\text{Fe}_3\text{O}_4$  nanoparticles, ABTS,  $\text{H}_2\text{O}_2$ , urease enzyme and urea. The amount of urease determine the life-time of acidic pH state. (c) The active state of  $\text{Fe}_3\text{O}_4$  nanoparticles towards oxidation of ABTS is temporally regulated using urease enzyme (0-15 U/mL), urea concentration (100 mM). (d) The time taken for resetting pH to 5.5 is in commensurate with life-time of the nanozyme's active state. (↓) represent the addition of acid fuel.

Finally, the robustness of this self-adaptive catalytic network system was scrutinized for the multiple fuelling cycles (Figure 11). The system with higher amount of urease (20 U/mL) was chosen for this purpose. The catalytic system was activated by adding acid fuel and the system switched from OFF state to ON state with concurrent

oxidation of ABTS. This oxidation reaction comes to a rest within 1 minute which marks the end of first cycle. The second addition of acid fuel activated the system again and oxidation reaction started to occur and a similar temporal profile was observed. This fuelling cycles were continued up to 4 cycles and each time a similar trend was observed which clearly demonstrates the robustness of this self-adaptive catalytic function.

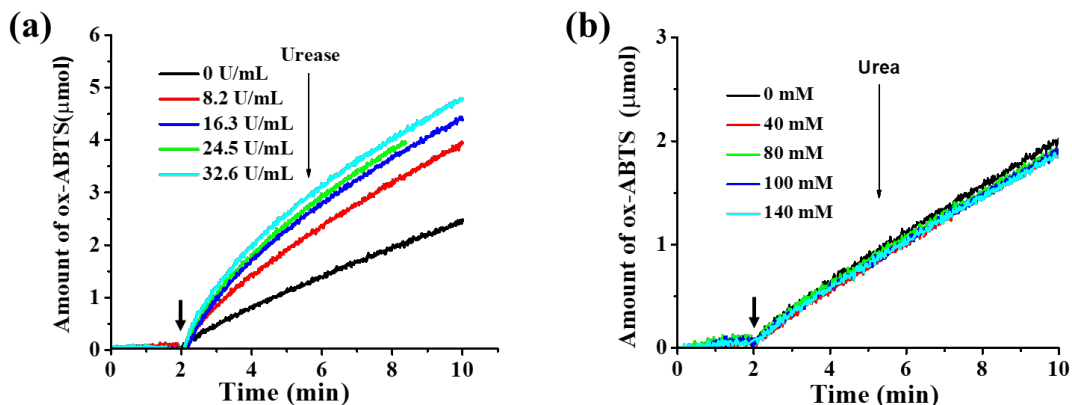


**Figure 9.** Influence of urease and urea on the activity of  $Fe_3O_4$  nanoparticles. (a) The activity towards oxidation of ABTS is modulated in presence of urease. (b) The activity was not influenced by urea. (All the measurements were carried out in pH 4.5).

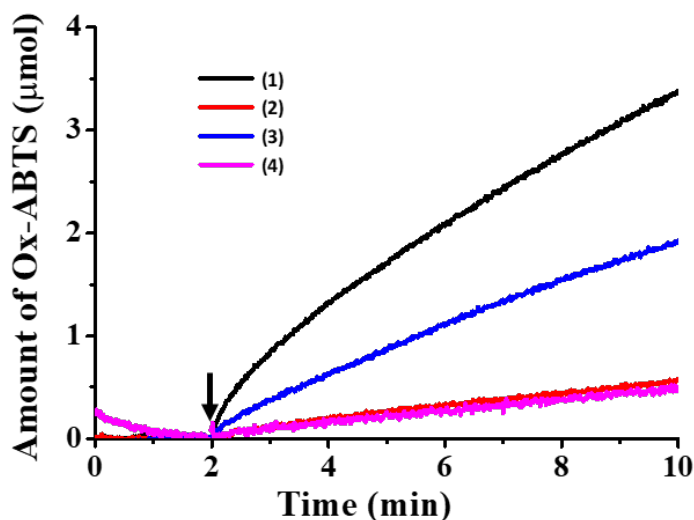


**Figure 10.** The activity towards oxidation of ABTS is modulated in presence of urease. However, urease alone didn't show any significant activity. (1)  $ABTS+Fe_3O_4+H_2O_2+Urease$  (8.2 U/mL), (2)  $ABTS+H_2O_2+Urease$  (8.2 U/mL), (3)  $ABTS+Fe_3O_4+H_2O_2$  and (4)  $ABTS+H_2O_2$ .

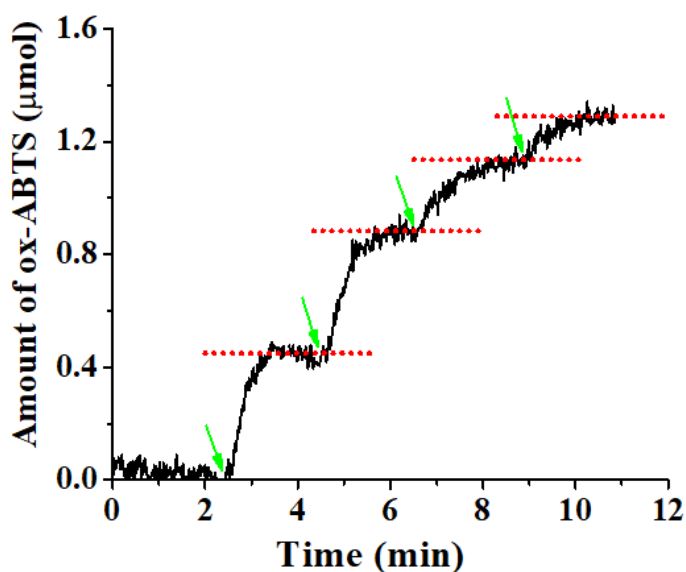


**Figure 11.** Re-fuelling the activity of  $Fe_3O_4$  nanoparticles. First addition of acid (fuel) initiate the oxidation of ABTS and eventually turn off once fuel is completely consumed. Off-state of nanozyme is re-initiated upon further addition of acid. (Amount of urease used is  $20 U mL^{-1}$ ).

### 2.3.6. Conclusions

In summary, we have successfully constructed a self-adaptive, temporally regulated nanozyme-natural enzyme network using  $Fe_3O_4$  nanoparticles and urease enzyme for the first time. The inherent pH dependent peroxidase-like activity of  $Fe_3O_4$  nanoparticle was utilised to integrate them into urease based autonomous feedback system (which cause temporal pH change) to achieve temporally regulated catalytic network. The pre-programmable lifetime of the catalytically active state was demonstrated along with the refuelability. This self-adaptive catalytic network and its design principles are expected to promote engineering of advanced intelligent chemical network systems.

### 2.3.7. References

- (1) Koshland, D.; Goldbeter, A.; Stock, J. Amplification and adaptation in regulatory and sensory systems. *Science* **1982**, *217* (4556), 220-225.
- (2) Bray, D. Protein molecules as computational elements in living cells. *Nature* **1995**, *376* (6538), 307-312.

- (3) Kholodenko, B. N. Cell-signalling dynamics in time and space. *Nat. Rev. Mol. Cell Biol* **2006**, *7* (3), 165-176.
- (4) Ferrell, James E.; Tsai, Tony Y.-C.; Yang, Q. Modeling the Cell Cycle: Why Do Certain Circuits Oscillate? *Cell* **2011**, *144* (6), 874-885.
- (5) Wang, H.; Zhao, Z.; Liu, Y.; Shao, C.; Bian, F.; Zhao, Y. Biomimetic enzyme cascade reaction system in microfluidic electrospray microcapsules. *Sci. Adv* **2018**, *4* (6), eaat2816.
- (6) van Dongen, S. F. M.; Nallani, M.; Cornelissen, J. J. L. M.; Nolte, R. J. M.; van Hest, J. C. M. A Three-Enzyme Cascade Reaction through Positional Assembly of Enzymes in a Polymersome Nanoreactor. *Chem.: Eur. J.* **2009**, *15* (5), 1107-1114.
- (7) Ishikawa, K.; Sato, K.; Shima, Y.; Urabe, I.; Yomo, T. Expression of a cascading genetic network within liposomes. *FEBS Letters* **2004**, *576* (3), 387-390.
- (8) Noireaux, V.; Libchaber, A. A vesicle bioreactor as a step toward an artificial cell assembly. *Proc. Natl. Acad. Sci. U.S.A* **2004**, *101* (51), 17669-17674.
- (9) Tanner, P.; Onaca, O.; Balasubramanian, V.; Meier, W.; Palivan, C. G. Enzymatic Cascade Reactions inside Polymeric Nanocontainers: A Means to Combat Oxidative Stress. *Chem.: Eur. J.* **2011**, *17* (16), 4552-4560.
- (10) Vriezema, D. M.; Garcia, P. M. L.; Sancho Oltra, N.; Hatzakis, N. S.; Kuiper, S. M.; Nolte, R. J. M.; Rowan, A. E.; van Hest, J. C. M. Positional Assembly of Enzymes in Polymersome Nanoreactors for Cascade Reactions. *Angew. Chem. Int. Ed.* **2007**, *46* (39), 7378-7382.
- (11) Tanner, P.; Balasubramanian, V.; Palivan, C. G. Aiding Nature's Organelles: Artificial Peroxisomes Play Their Role. *Nano Lett* **2013**, *13* (6), 2875-2883.
- (12) Kuchler, A.; Yoshimoto, M.; Luginbühl, S.; Mavelli, F.; Walde, P. Enzymatic reactions in confined environments. *Nat. Nanotechnol.* **2016**, *11*, 409.
- (13) Ugrinic, M.; Zambrano, A.; Berger, S.; Mann, S.; Tang, T. Y. D.; deMello, A. Microfluidic formation of proteinosomes. *Chem. Commun.* **2018**, *54* (3), 287-290.
- (14) Huang, X.; Li, M.; Mann, S. Membrane-mediated cascade reactions by enzyme-polymer proteinosomes. *Chem. Commun.* **2014**, *50* (47), 6278-6280.
- (15) Louzao, I.; van Hest, J. C. M. Permeability Effects on the Efficiency of Antioxidant Nanoreactors. *Biomacromolecules* **2013**, *14* (7), 2364-2372.

- 
- 
- (16) Klermund, L.; Poschenrieder, S. T.; Castiglione, K. Biocatalysis in Polymersomes: Improving Multienzyme Cascades with Incompatible Reaction Steps by Compartmentalization. *ACS Catal.* **2017**, *7* (6), 3900-3904.
- (17) Liu, Z.; Wang, B.; Jin, S.; Wang, Z.; Wang, L.; Liang, S. Bioinspired Dual-Enzyme Colloidosome Reactors for High-Performance Biphasic Catalysis. *ACS Appl. Mater. Interfaces* **2018**, *10* (48), 41504-41511.
- (18) Nishimura, T.; Akiyoshi, K. Biotransporting Biocatalytic Reactors toward Therapeutic Nanofactories. *Adv. Sci* **2018**, *5* (11), 1800801.
- (19) Tanner, P.; Egli, S.; Balasubramanian, V.; Onaca, O.; Palivan, C. G.; Meier, W. Can polymeric vesicles that confine enzymatic reactions act as simplified organelles? *FEBS Letters* **2011**, *585* (11), 1699-1706.
- (20) Cao, X.; Li, Y.; Zhang, Z.; Yu, J.; Qian, J.; Liu, S. Catalytic activity and stability of glucose oxidase/horseradish peroxidase co-confined in macroporous silica foam. *Analyst* **2012**, *137* (24), 5785-5791.
- (21) Zhu, L.; Yang, R.; Zhai, J.; Tian, C. Bienzymatic glucose biosensor based on co-immobilization of peroxidase and glucose oxidase on a carbon nanotubes electrode. *Biosens. Bioelectron* **2007**, *23* (4), 528-535.
- (22) Wei, Y.; Dong, H.; Xu, J.; Feng, Q. Simultaneous Immobilization of Horseradish Peroxidase and Glucose Oxidase in Mesoporous Sol–Gel Host Materials. *ChemPhysChem* **2002**, *3* (9), 802-808.
- (23) Crumbliss, A. L.; Stonehuerner, J. G.; Henkens, R. W.; Zhao, J.; O'Daly, J. P. A carrageenan hydrogel stabilized colloidal gold multi-enzyme biosensor electrode utilizing immobilized horseradish peroxidase and cholesterol oxidase/cholesterol esterase to detect cholesterol in serum and whole blood. *Biosens. Bioelectron* **1993**, *8* (6), 331-337.
- (24) Liu, H.; Ying, T.; Sun, K.; Li, H.; Qi, D. Reagentless amperometric biosensors highly sensitive to hydrogen peroxide, glucose and lactose based on N-methyl phenazine methosulfate incorporated in a Nafion film as an electron transfer mediator between horseradish peroxidase and an electrode. *Anal. Chim. Acta.* **1997**, *344* (3), 187-199.
- (25) Kumar, A.; Malhotra, R.; Malhotra, B. D.; Grover, S. K. Co-immobilization of cholesterol oxidase and horseradish peroxidase in a sol–gel film. *Anal. Chim. Acta.* **2000**, *414* (1), 43-50.

- (26) Eshkenazi, I.; Maltz, E.; Zion, B.; Rishpon, J. A Three-Cascaded-Enzymes Biosensor to Determine Lactose Concentration in Raw Milk<sup>1</sup>. *J. Dairy Sci.* **2000**, *83* (9), 1939-1945.
- (27) Jo, S.-M.; Wurm, F. R.; Landfester, K. Biomimetic Cascade Network between Interactive Multicompartmental Organized by Enzyme-Loaded Silica Nanoreactors. *ACS Appl. Mater. Interfaces* **2018**, *10* (40), 34230-34237.
- (28) Wei, H.; Wang, E. Nanomaterials with enzyme-like characteristics (nanozymes): next-generation artificial enzymes. *Chem. Soc. Rev.* **2013**, *42* (14), 6060-6093.
- (29) Wu, J.; Wang, X.; Wang, Q.; Lou, Z.; Li, S.; Zhu, Y.; Qin, L.; Wei, H. Nanomaterials with enzyme-like characteristics (nanozymes): next-generation artificial enzymes (II). *Chem. Soc. Rev.* **2019**, *48* (4), 1004-1076.
- (30) Lin, Y.; Ren, J.; Qu, X. Nano-Gold as Artificial Enzymes: Hidden Talents. *Adv. Mater.* **2014**, *26* (25), 4200-4217.
- (31) Huang, Y.; Ren, J.; Qu, X. Nanozymes: Classification, Catalytic Mechanisms, Activity Regulation, and Applications. *Chem. Rev.* **2019**, *119* (6), 4357-4412.
- (32) Wang, X.; Hu, Y.; Wei, H. Nanozymes in bionanotechnology: from sensing to therapeutics and beyond. *Inorg. Chem. Front* **2016**, *3* (1), 41-60.
- (33) Wu, J.; Li, S.; Wei, H. Multifunctional nanozymes: enzyme-like catalytic activity combined with magnetism and surface plasmon resonance. *Nanoscale Horiz.* **2018**, *3* (4), 367-382.
- (34) Pasquato, L.; Pengo, P.; Scrimin, P. Nanozymes: Functional Nanoparticle-based Catalysts. *Supramol. Chem.* **2005**, *17* (1-2), 163-171.
- (35) Gao, L.; Zhuang, J.; Nie, L.; Zhang, J.; Zhang, Y.; Gu, N.; Wang, T.; Feng, J.; Yang, D.; Perrett, S.; Yan, X. Intrinsic peroxidase-like activity of ferromagnetic nanoparticles. *Nat. Nanotechnol.* **2007**, *2*, 577.
- (36) Lin, Y.; Ren, J.; Qu, X. Catalytically Active Nanomaterials: A Promising Candidate for Artificial Enzymes. *Acc. Chem. Res.* **2014**, *47* (4), 1097-1105.
- (37) Zhang, L.; Laug, L.; Münchgesang, W.; Pippel, E.; Gösele, U.; Brandsch, M.; Knez, M. Reducing Stress on Cells with Apoferritin-Encapsulated Platinum Nanoparticles. *Nano Lett* **2010**, *10* (1), 219-223.
- (38) Mu, J.; Wang, Y.; Zhao, M.; Zhang, L. Intrinsic peroxidase-like activity and catalase-like activity of Co<sub>3</sub>O<sub>4</sub> nanoparticles. *Chem. Commun.* **2012**, *48* (19), 2540-2542.

- (39) Zhang, H.; Liang, X.; Han, L.; Li, F. "Non-Naked" Gold with Glucose Oxidase-Like Activity: A Nanozyme for Tandem Catalysis. *Small* **2018**, *14* (44), 1803256.
- (40) Manea, F.; Houillon, F. B.; Pasquato, L.; Scrimin, P. Nanozymes: Gold-Nanoparticle-Based Transphosphorylation Catalysts. *Angew. Chem. Int. Ed.* **2004**, *43* (45), 6165-6169.
- (41) Wei, H.; Wang, E. Fe<sub>3</sub>O<sub>4</sub> Magnetic Nanoparticles as Peroxidase Mimetics and Their Applications in H<sub>2</sub>O<sub>2</sub> and Glucose Detection. *Anal. Chem.* **2008**, *80* (6), 2250-2254.
- (42) Jv, Y.; Li, B.; Cao, R. Positively-charged gold nanoparticles as peroxidase mimic and their application in hydrogen peroxide and glucose detection. *Chem. Commun.* **2010**, *46* (42), 8017-8019.
- (43) Song, Y.; Qu, K.; Zhao, C.; Ren, J.; Qu, X. Graphene Oxide: Intrinsic Peroxidase Catalytic Activity and Its Application to Glucose Detection. *Adv. Mater.* **2010**, *22* (19), 2206-2210.
- (44) Kim, M. I.; Shim, J.; Li, T.; Woo, M.-A.; Cho, D.; Lee, J.; Park, H. G. Colorimetric quantification of galactose using a nanostructured multi-catalyst system entrapping galactose oxidase and magnetic nanoparticles as peroxidase mimetics. *Analyst* **2012**, *137* (5), 1137-1143.
- (45) Liu, S.; Tian, J.; Zhai, J.; Wang, L.; Lu, W.; Sun, X. Titanium silicalite-1 zeolite microparticles for enzymeless H<sub>2</sub>O<sub>2</sub> detection. *Analyst* **2011**, *136* (10), 2037-2039.
- (46) Zhang, Z.; Wang, X.; Yang, X. A sensitive choline biosensor using Fe<sub>3</sub>O<sub>4</sub> magnetic nanoparticles as peroxidase mimics. *Analyst* **2011**, *136* (23), 4960-4965.
- (47) Kim, M. I.; Shim, J.; Li, T.; Lee, J.; Park, H. G. Fabrication of Nanoporous Nanocomposites Entrapping Fe<sub>3</sub>O<sub>4</sub> Magnetic Nanoparticles and Oxidases for Colorimetric Biosensing. *Chem.: Eur. J.* **2011**, *17* (38), 10700-10707.
- (48) Wang, X.-X.; Wu, Q.; Shan, Z.; Huang, Q.-M. BSA-stabilized Au clusters as peroxidase mimetics for use in xanthine detection. *Biosens. Bioelectron* **2011**, *26* (8), 3614-3619.
- (49) Heinen, L.; Walther, A. Celebrating Soft Matter's 10th Anniversary: Approaches to program the time domain of self-assemblies. *Soft Matter* **2015**, *11* (40), 7857-7866.



- (50) Morris, E.; Chavez, M.; Tan, C. Dynamic biomaterials: toward engineering autonomous feedback. *Curr. Opin. Biotechnol.* **2016**, *39*, 97-104.
- (51) Che, H.; Cao, S.; van Hest, J. C. M. Feedback-Induced Temporal Control of “Breathing” Polymersomes To Create Self-Adaptive Nanoreactors. *J. Am. Chem. Soc.* **2018**, *140* (16), 5356-5359.
- (52) Okamoto, Y.; Ward, T. R. Cross-Regulation of an Artificial Metalloenzyme. *Angew. Chem. Int. Ed.* **2017**, *56* (34), 10156-10160.
- (53) van Rossum, S. A. P.; Tena-Solsona, M.; van Esch, J. H.; Eelkema, R.; Boekhoven, J. Dissipative out-of-equilibrium assembly of man-made supramolecular materials. *Chem. Soc. Rev.* **2017**, *46* (18), 5519-5535.
- (54) Ragazzon, G.; Prins, L. J. Energy consumption in chemical fuel-driven self-assembly. *Nat. Nanotechnol.* **2018**, *13* (10), 882-889.
- (55) Sorrenti, A.; Leira-Iglesias, J.; Markvoort, A. J.; de Greef, T. F. A.; Hermans, T. M. Non-equilibrium supramolecular polymerization. *Chem. Soc. Rev.* **2017**, *46* (18), 5476-5490.
- (56) Zhang, J.; Li, X.; Rosenholm, J. M.; Gu, H. C. Synthesis and characterization of pore size-tunable magnetic mesoporous silica nanoparticles. *J. Colloid Interface Sci.* **2011**, *361* (1), 16-24.
- (57) Wang, N.; Zhu, L.; Wang, D.; Wang, M.; Lin, Z.; Tang, H. Sono-assisted preparation of highly-efficient peroxidase-like Fe<sub>3</sub>O<sub>4</sub> magnetic nanoparticles for catalytic removal of organic pollutants with H<sub>2</sub>O<sub>2</sub>. *Ultrason. Sonochem.* **2010**, *17* (3), 526-533.
- (58) Wu, H.; Gao, G.; Zhou, X.; Zhang, Y.; Guo, S. Control on the formation of Fe<sub>3</sub>O<sub>4</sub> nanoparticles on chemically reduced graphene oxide surfaces. *CrystEngComm* **2012**, *14* (2), 499-504.
- (59) Yu, F.; Huang, Y.; Cole, A. J.; Yang, V. C. The artificial peroxidase activity of magnetic iron oxide nanoparticles and its application to glucose detection. *Biomaterials* **2009**, *30* (27), 4716-4722.
- (60) Fan, K.; Wang, H.; Xi, J.; Liu, Q.; Meng, X.; Duan, D.; Gao, L.; Yan, X. Optimization of Fe<sub>3</sub>O<sub>4</sub> nanozyme activity via single amino acid modification mimicking an enzyme active site. *Chem. Commun.* **2017**, *53* (2), 424-427.

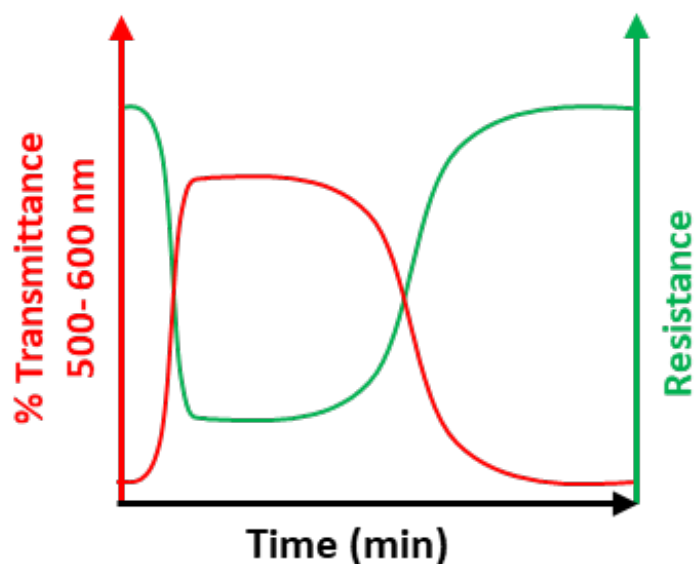


## Chapter- 2.4

### ***Bio-inspired Temporally Programmed Switching in Dual Functional Polymer Film***

#### **Summary:**

*The next generation of bio-inspired materials are expected to be active, adaptive, autonomous and intelligent by incorporating biological principles of non-equilibrium dynamics through complex chemical feedback loops. Recently, such efforts are being reported where classical switchable materials are re-engineered to operate in a temporal manner driven either by non-equilibrium dynamics or via kinetically controlled antagonistic chemical reactions. In this study, we have demonstrated a temporally regulated switching of light transmittance and electrical conductance in polyaniline films by employing enzyme-catalysed biochemical reaction. The enzymatic reaction produces feedback induced transient pH profile, whose life-time could be pre-programmed via enzyme concentration. This autonomous, temporally regulated polymer film represents an advancement to the existing switchable materials that operate at equilibrium.*



A manuscript based on this chapter is under preparation



### 2.4.1 Introduction

Living systems features unique characteristics such as self-regulation, adaptation, autonomy etc., owing to their precise spatiotemporal regulation of structures and functions through non-equilibrium dynamics and kinetic control mechanisms orchestrated via biochemical reaction networks.<sup>1-5</sup> Inspired by this, chemists tried to mimic life-like materials with autonomous temporal control over structures and functions.<sup>2,6-18</sup> Initially, the focus was mostly devoted to the out-of-equilibrium structural or conformational switching driven by chemical fuels.<sup>19-42</sup> A few transient functional systems have been reported recently whose active functional state is temporally regulated in an autonomous manner.<sup>43-46</sup> van Hest and co-workers reported self-adaptive nanoreactors that are capable of temporally regulating the permeation of the reactants into the nanoreactors and therefore autonomously regulating the catalytic function.<sup>47</sup> Walther and co-workers reported a photonic gel operating out-of-equilibrium showing the temporally modulated optical property which they further used for transient memory and signal propagation.<sup>48</sup> Recently, Ulijn and co-workers demonstrated supramolecular nanostructures with self-regulated electrical conductance.<sup>49</sup> These systems demonstrated single function modulated in a self-regulated temporal manner. Recently, Prins and co-workers designed functionalized gold nanoparticle system showing temporal control on dual functions; signal generation and catalysis (Figure 1).<sup>50</sup> However, system exhibiting temporal control for dual-functions are very few and several such systems need to be evolved to expand the scope of bio-inspired adaptive materials.

Polyaniline (PANi) has gathered significant interest owing to their switchable electrical conductivity and colour.<sup>51-52</sup> Its colour (transparent/ blue/ green) and electrical conductivity (insulating/ conducting) can be switched by electrical potential or pH.<sup>53-55</sup> By virtue of these switchable functionalities, PANi has been well-exploited to construct various devices such as sensors<sup>56-62</sup>, memory devices<sup>63-64</sup>, electrochromic devices<sup>52, 65-66</sup>, actuators<sup>67-69</sup>, optoelectronic applications<sup>70-72</sup> etc., and the next level of advances could be achieved by temporally switching these functional states with pre-programmable life time. Such functional devices would find interesting applications in signalling, sensing, logics and computation that are otherwise difficult to achieve with conventional, stimuli-responsive systems operating at equilibrium.<sup>6, 48</sup>

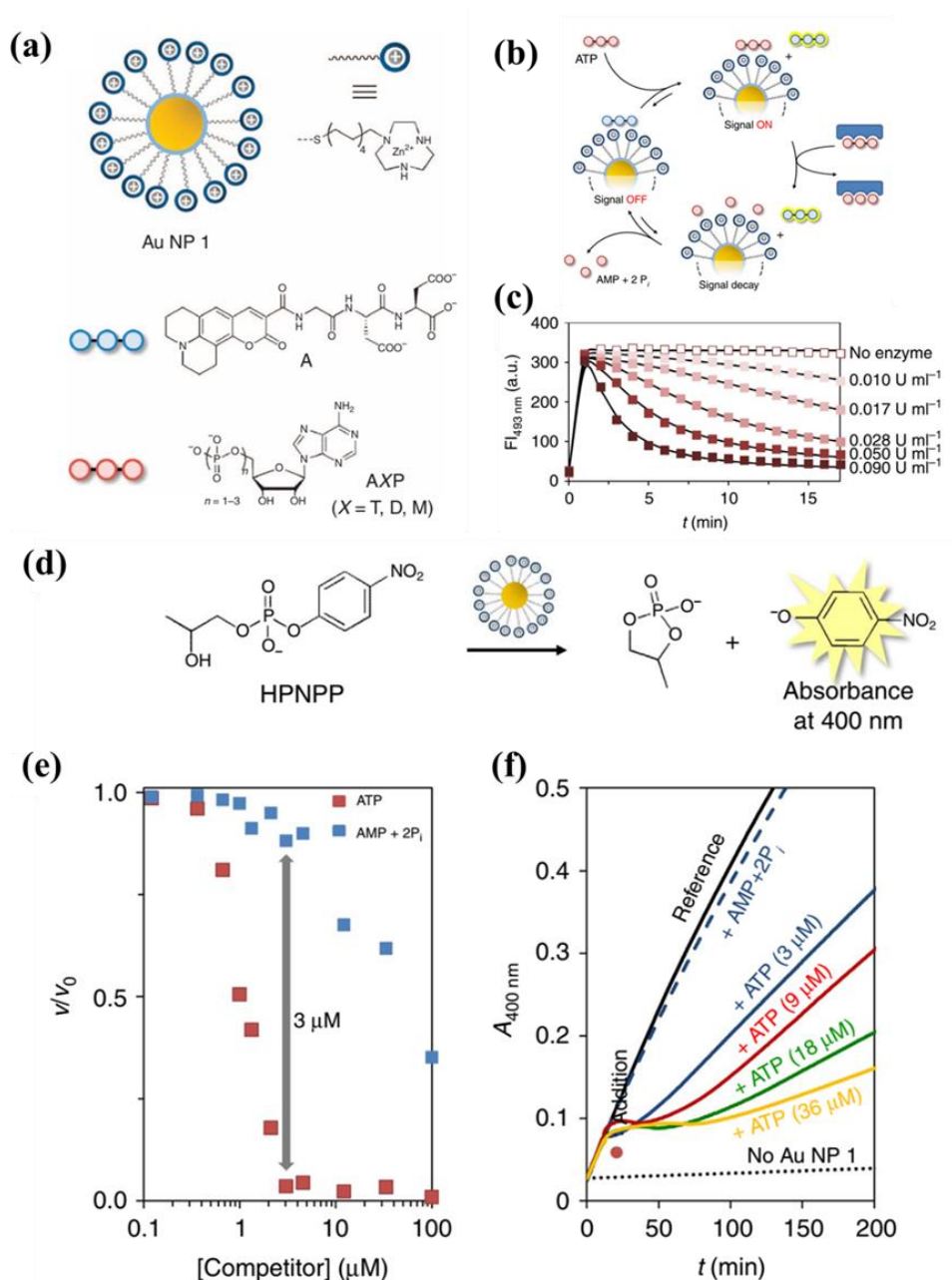
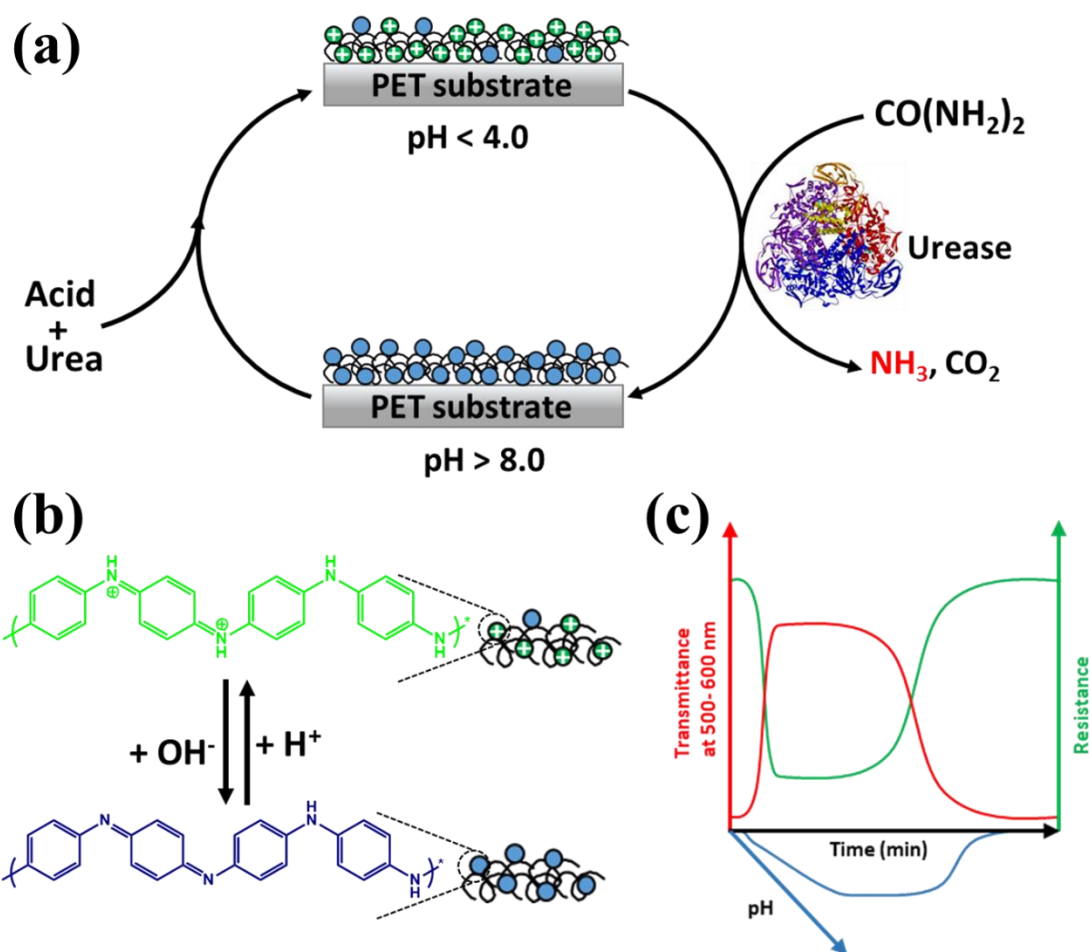


**Figure 1.** (a) Schematic representations of 1,4,7-triazacyclononane (TACN)•Zn<sup>2+</sup>-capped gold nanoparticles (AuNP-1) and chemical structures of fluorescence reporter and chemical fuel, adenosine triphosphate (ATP). (b) The activation and deactivation cycles in the current system. (c) The transient signal generation due to the transient displacement of fluorescence reporter molecules from AuNP surface. (d) Catalysis of the transphosphorylation of HPNPP by AuNP 1. (e) Relative reaction rates ( $v/v_0$ ) as a function of the concentration of either ATP or the mixture AMP and 2P<sub>i</sub>. Presence of ATP significantly inhibit the catalytic activity. (f) Transient down-regulation of catalytic activity of AuNP 1 through transient binding of ATP to AuNP 1. Reproduced with permission from reference 50. Copyright 2015, Nature Publishing Group.

### 2.4.2 Scope of the present investigation

In this chapter, we demonstrate the integration of flexible polyaniline film with an autonomous feedback system (AFS)<sup>41, 73</sup> to achieve self-regulated, temporally programmed switching of electrical and optical functional states. The AFS consists of urease enzyme as the acid-activated feedback unit (Scheme 1). The emeraldine oxidation state of polyaniline is utilized as the pH-responsive functional unit whose electrical conductivity and optical properties are switchable via acid ( $H^+$ ) doping and de-doping processes. At the equilibrium (resting) state (where pH is about 8.0), polyaniline exists-



**Scheme 1.** Bio-inspired enzyme controlled temporally regulated switching of functionally active state of polyaniline film. (a) Emeraldine form of polyaniline supported on transparent PET substrate. At resting pH (~ 8.0), the film adopts emeraldine base form. Injection of chemical fuel (citric acid and urea) switch the polymer to its functionally active emeraldine salt form and instantaneously kick start the urease enzymes to generate the ammonia. The slow generation of ammonia neutralizes the acid

---

---

*fuel added and slowly bring the polymer back to the resting emeraldine base form and therefore switching the functionally active state back to the inactive state. (b) The chemical structures of pH switchable emeraldine form of polyaniline. (c) The schematic representation of the temporal profiles of electrical resistance and optical transmittance of the polyaniline film.*

-in neutral emeraldine base (EB) form which is electrically insulating and characterized by its intense blue colour. Addition of chemical fuel (citric acid/sodium citrate buffer) along with urea results in an instantaneous decrease of pH which in turn converts the functionally inactive emeraldine base to optically transparent (for wavelengths in the range of 500 nm – 600 nm), electrically conducting emeraldine salt form (activation process). Once the system reaches low pH, urease enzyme starts generating ammonia (by hydrolysis of urea) which neutralizes the acid fuel added into the system and slowly increases the pH to its equilibrium (resting) state. This increase in the pH converts the polyaniline film back to the functionally inactive emeraldine base (de-activation process). The life-time of the active state of the system could be programmed via the urease concentration.

### 2.4.3 Experimental section

**Fabrication of PANi deposited PET films.** Firstly, PET films were cut into a size of 2 cm × 5 cm. These PET films were thoroughly cleaned with isopropanol and blow-dried under N<sub>2</sub> flow. The oxidative polymerization of aniline monomer<sup>74</sup> was carried out at room temperature in presence of cleaned PET films in order to fabricate PANi deposited PET (PANi@PET) films. In a typical synthesis procedure, a 50 mL aqueous solution containing 0.5 M H<sub>2</sub>SO<sub>4</sub> and 0.2 M aniline was taken. To this mixture, 1.14 g of ammonium persulfate (5 mmol) was quickly added and sonicated. To this mixture, five cleaned PET substrates were immersed and kept static for 1 hour (Figure 3 a-c). The polymer deposited films were taken out and thoroughly washed with a copious amount of 0.1 M H<sub>2</sub>SO<sub>4</sub> (Figure 3d). The films were blow-dried under the flow of N<sub>2</sub>.

**Electrochemical characterization of as synthesised PANi Films.** PANi was synthesized on an ITO coated glass slide (1 cm × 2 cm) by immersing it in the polymerization solution (50 mL) containing 0.5 M H<sub>2</sub>SO<sub>4</sub>, 0.2 M aniline and 1.14 g of ammonium persulfate (5 mmol). After polymerization is complete (1 h), the ITO slide was washed thoroughly with 0.1 M H<sub>2</sub>SO<sub>4</sub> solution. This slide was used as a working



electrode along with Ag/AgCl as a reference electrode and Pt wire as a counter electrode in a typical three-electrode configuration. The electrolyte used was 0.1 M H<sub>2</sub>SO<sub>4</sub>. The cyclic voltammograms were reordered within the window of -0.2 V to 0.8 V against Ag/AgCl at a scan rate of 50 mV/s.

**Autonomous Feedback System (AFS).** 3 mL tris- HCl buffer (pH 8.5 and 10 mM concentration) solution consisting of urease enzyme (varying amount between 0- 30 U/mL) was taken. To this solution, 0.05 mL of 1 M citric acid (fuel) and 36 mg of urea (0.6 mmol) (dormant deactivator) were added to activate the system.

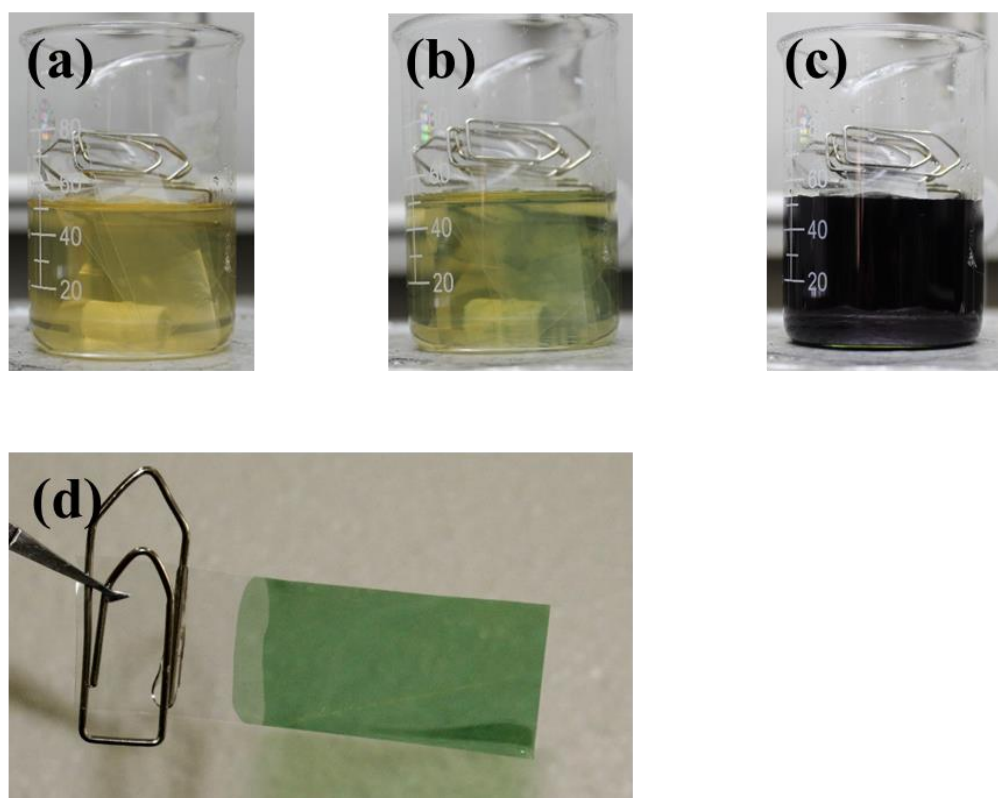


**Figure 2.** (a) Polymerization solutions with PET substrates dipped in it (before polymerisation started). (b) Green colouration indicates the starting of polymerisation. (c) After 1 h of polymerization (d) Photograph of as-synthesized PANi@PET film.

**Transient optical transmission measurements.** The PANi@PET film was cut into a size of 20 mm × 7 mm and placed inside an optical cuvette. The cuvette was placed in a UV-Vis spectroscopy in such a way that the light would pass through the film. The cuvette was then filled with AFS solution and the optical response of the film was recorded in ‘time drive’ mode (absorbance at single wavelength vs. time).

**Transient optical filter to control the excitation light.** The experiments were carried out (in a photoluminescence spectroscopy) by placing the PANi@PET film on one side of the inner wall of a 10 mm quartz cuvette which would face the excitation light source. The film was placed in such a way that the excitation light would fall into the rhodamine B solution only through the film (Figure 3). The concentration of rhodamine B was 0.01 mM in the AFS solution.

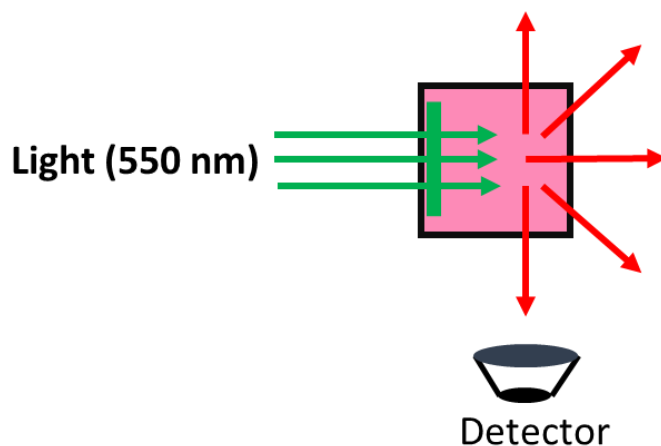


**Figure 3.** The top view schematic of the experimental setup. The excitation light and the detector are placed at right-angles to each other so that no direct light falls on to the detector. The PANi@PET film was placed on inner wall of the cuvette towards the light source.

**Resistance measurements.** The resistance measurements on PANi@PET film (that is in contact with AFS solution) were carried out using a custom-made cell. A cylindrical vial of 12 mm diameter having a slit (approximately 5 mm length) at the bottom was taken. The PANi deposited PET films were cut into a size of 5 mm  $\times$  30 mm and placed inside the vial with about 5 mm length protruding out through the slit. The film was then immobilized using the nail polish which would also seals the vial (Figure 4). After proper drying of the nail polish, the vial containing PANi@PET was placed upright and connections from the top and bottom ends of the films were made using alligator clips. A high precision resistance meter with real-time data logging was utilized to monitor and record the resistance of the film.

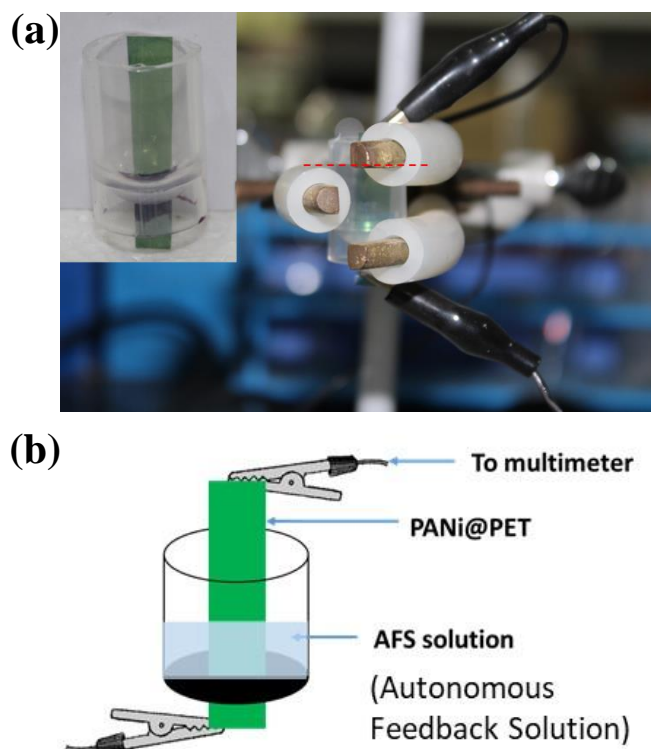


**Figure 4.** (a) Photographs showing the home-built set up to measure the resistance of the film while in contact with AFS solution. The AFS solution was added to the vial till the red-line mark. (b) A schematic showing the experimental setup.

#### 2.4.4. Characterization

Please see the appendix for the details of the instrumentation of UV-Visible spectroscopy, Photoluminescence spectroscopy, FT-IR spectroscopy, high accuracy multi-meter, electrochemical workstation, X-ray photoelectron spectroscopy and pH measurements.

#### 2.4.5. Results and discussion

The dual-functional film based on polyaniline was synthesized by *in situ* oxidative polymerisation of aniline monomer in presence of poly(ethylene terephthalate) (PET) substrate (Figure 2). The successful deposition of PANi on to the PET substrate was evident from the greenish appearance of the resultant films (Figure 5a). FT-IR spectra of the PANi@PET showed characteristic peaks for PANi at  $1578\text{ cm}^{-1}$  which corresponds to quinoid ring deformations of the aromatic ring. A peak at  $1501\text{ cm}^{-1}$  is due to the stretching vibrations of  $\text{C-N}^+$ . Absence of these two peaks in the blank PET -

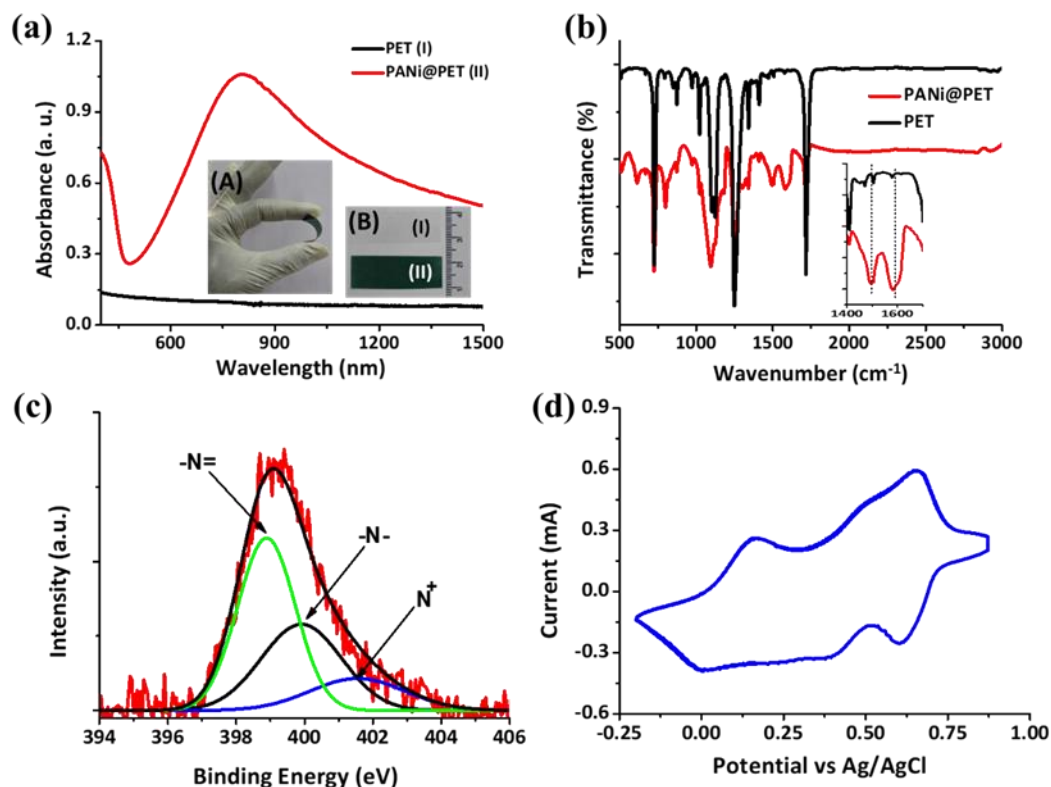


**Figure 5.** (a) UV-Vis spectra of blank PET substrate and PANi deposited as-synthesized film. Inset showing the photographs of the (A) PANi deposited PET film, (B-I) blank PET films and (B-II) PANi deposited PET film (PANi@PET). (b) The ATR-FTIR spectra of blank PET substrate and PANi deposited as-synthesized film. (c) XPS spectra in the N1s region of PANi@PET. (d) Cyclic voltammogram of PANi obtained using PANi deposited ITO as working electrode.

-indicated successful deposition of PANi on the PET film (Figure 5b). XPS spectrum of PANi film in N1s region (Figure 5c) is composed of three sub-peaks centred at about 399 eV ( $\text{-N=}$ , imine nitrogen), 400 eV ( $\text{-NH-}$ , amine nitrogen) and 401.6 eV ( $\text{N}^+$  positively charged nitrogen) which are consistent with previous reports.<sup>75-76</sup> To prove further the formation PANi during *in situ* polymerization, an ITO (indium tin oxide) coated glass slide was immersed in the polymerisation solution and got it deposited with PANi. This PANi@ITO was used as a working electrode in the three electrode configuration to record cyclic voltammogram (CV) (Figure 5d). The CV of the PANi films clearly shows two sets of redox peaks. The first set between 0 and 0.25 V vs. Ag/AgCl corresponding to the conversion of fully reduced leucoemeraldine base to the partially oxidized emeraldine. The second set of redox peak (0.6 to 0.8 V vs. Ag/AgCl) is associated with the conversion of emeraldine to the fully oxidized pernigraniline form.<sup>77</sup> This distinctive

electroactive nature of the polymer confirms the formation of PANi through oxidative polymerisation. The field emission scanning electron microscope (FESEM) image of PANi@PET shows that the PET film is covered with PANi particles of uniform size (Figure 6).

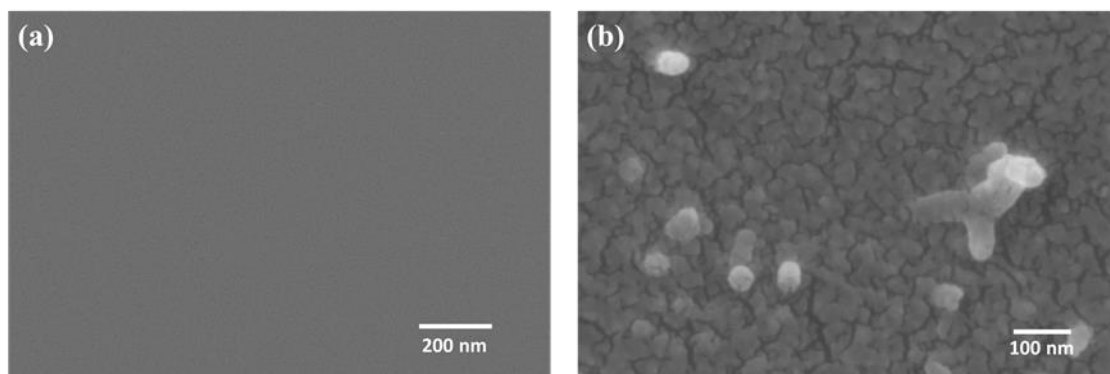


**Figure 6.** FESEM images of (a) blank PET substrate and (b) PANi deposited PET substrate.

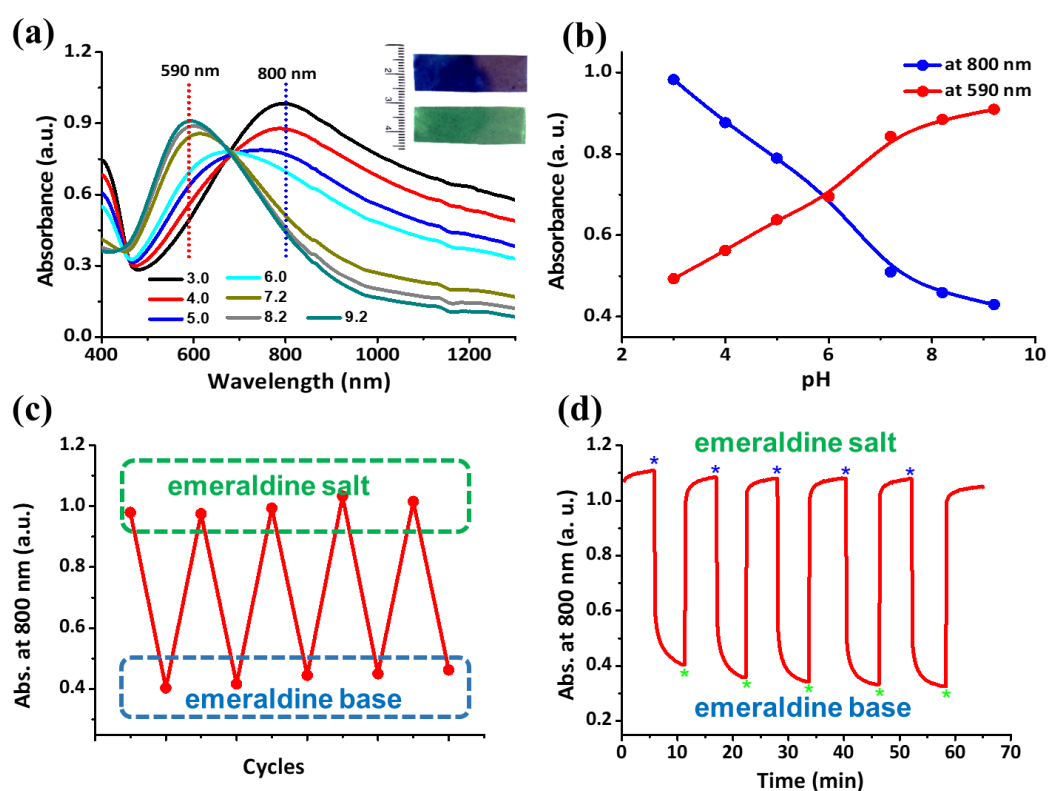


**Figure 7.** (a) UV-Vis absorption spectra of PANi@PET film in the pH range 3.0 to 9.2. Inset showing the photographs of the film immersed at pH 3.0 and pH 9.2. (b) Absorbance of the PANi@PET film at 590 nm and 800 nm as a function of pH. (c) Switching of emeraldine salt form of PANi@PET film to its base form by sequentially

---

---

*changing the pH between ca. 3.0 and ca. 9.0. (d) Variation of absorbance of PANi@PET film at 800 nm as a function of time upon changing the pH between ca. 3.0 and ca. 9.0 (the blue star indicate the addition of basic buffer and the green star indicate the addition of acid buffer).*

PANi deposited PET films (PANi@PET) were examined for their pH dependant optical properties. The greenish appearance of the as-synthesized film corresponds to the emeraldine salt form of PANi (Figure 5a). Absorption spectra of the film at pH ca. 3.0 shows peak around 800 nm corresponds to doping level and the formation of polaron in the emeraldine salt form (Figure 7a). Upon increasing the pH from ca. 3.0 to 9.2, the peak at 800 nm significantly decreased with emergence of a new peak at 590 nm which corresponds to the exciton absorption of the quinoid ring of emeraldine base form (Figure 7b). Owing to this strong absorption, the film immersed at pH 9.2 buffer showed intense blue colour (Figure 7a inset). The conversion between the emeraldine base form and salt form could be cycled up to 5 cycles by sequentially changing the pH between 3 and 9.0 (Figure 7 c-d).

Autonomous Feedback System (AFS) constitutes of two chemical processes working in tandem to produce a transient acidic pH profile. They are two antagonistic triggers one quickly decreases the pH whereas, the other slowly increase the pH in a feedback-driven manner (Figure 9a). The kinetics of these chemical reactions need to be subtly programmed in order to obtain a clear transient state. In addition, the response of PANi@PET to the pH changes in the surrounding solution should be reasonably faster for successful integration. We first investigated the kinetics of response of PANi@PET film to the pH of the surrounding solution. (Figure 8). The film in its emeraldine base state (by immersing the film in pH ca. 9.0 for 30 min) was immersed in pH 3.0 buffer and the absorbance at 800 nm was recorded as a function of time to understand the time taken for its transformation to emeraldine salt form. Similarly, the transformation kinetics of conversion of emeraldine salt to base form was also studied. It is evident from the studies that the conversion of emeraldine base to its salt form is relatively faster as compared to the switching of emeraldine salt (ES) to emeraldine base (EB). This would not cause any trouble to the measurement as the lower limit of the life-time of the AFS we are operating in this study is above 10 min (which is higher than the time scale of ES/EB and EB/ES conversions).

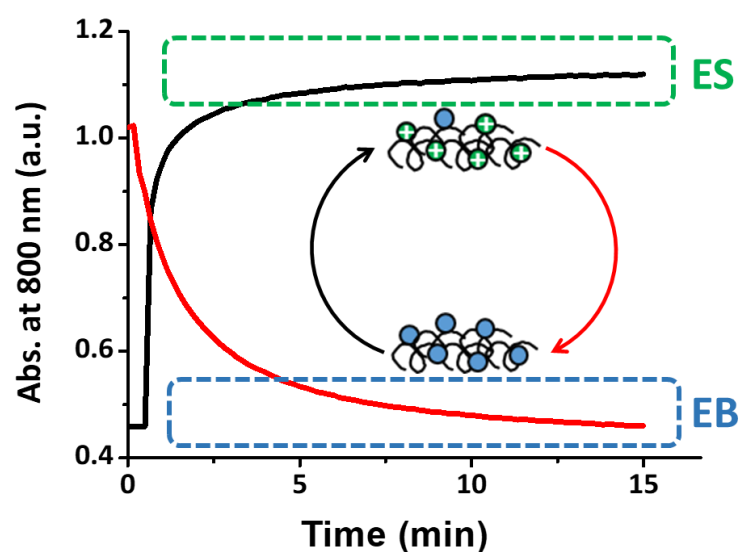


**Figure 8.** Variation of the absorbance of PANi@PET film at 800 nm upon converting emeraldine base form to salt form and visa- versa by immersing in the respective pH buffer. (Inset showing the schematics of the directions of conversions. Red curve for ES to EB and black curve for EB to ES).

The PANi@PET film was further integrated with AFS to obtain a transient emeraldine salt state with programmable life-time (Figure 9a). The AFS used in this study is based on urea-urease chemistry.<sup>41, 73</sup> We started with the initial (resting) alkaline pH of ca. 8.5 where the PANi@PET film displays intense blue colour and low absorbance at 800 nm owing to the emeraldine base form. The quick addition of acid (the fuel) to the system (the activation process) decreases the pH of the solution to about 3.4. At this pH, the urease enzyme is active enough to rise the pH (by acting on urea) back to 8.5 (the deactivation process) within definitive time period (determined by the enzyme concentration). The deactivation pH profile shown in Figure 9b consisted of three distinct slopes which are in agreement with the previously reported bell-shaped pH dependent activity profile of urease enzyme.<sup>41</sup> In the region of pH 3.0- 4.0 and also at pH above 8.0, the activity of enzyme is minimum and hence the rate of increase in pH is relatively low. However, in the intermediate pH range, the activity of enzyme (for urea hydrolysis) is high which is reflected in the sharp change in the slope in this region. The life time of the ASF could be programmed via the enzyme concentrations and the relation between the half-life of the AFS (the time taken for the pH to come back to 6, the half way between the initial and final pH) is found to be linear with urease concentration (Figure 9b, inset).

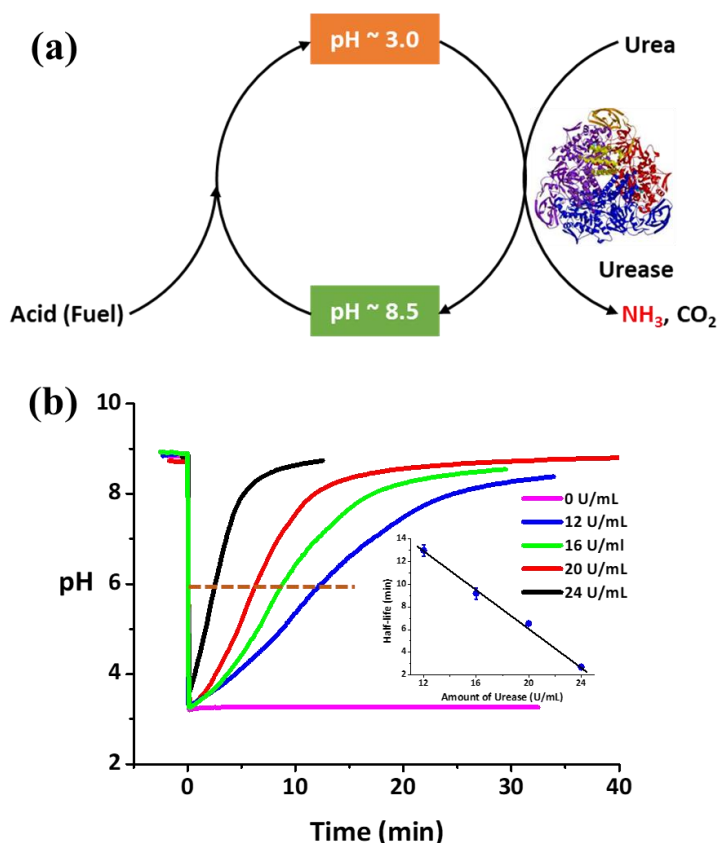


**Figure 9.** (a) Schematic representation of transient acidic pH state achieved using AFS driven by a biochemical reaction catalysed by urease enzyme. (b) The temporal change in pH of the AFS solution consisting of 200 mM urea and varying concentrations of urease enzyme. The points at which the dotted line is cutting the temporal profiles are taken as the half-life of the profile. Inset showing the programmability of the life time of AFS by varying the urease concentration.

We also looked into the corresponding optical changes in the PANi@PET films in response to the surrounding solution pH modulations. At the initial resting state, the PANi@PET exhibited an intense blue colour under visible light which blocks the light in the wavelength range of 500 – 600 nm (by absorbing the light) owing to the emeraldine base state (Figure 7a). A quick addition of acid (fuel) triggered the switching of film to its emeraldine salt form (activation) (Figure 10b). At this state, the film allowed the light in the wavelength range of 500 nm – 600 nm to pass through (Figure 10a). Simultaneously, the urea starts to hydrolyse by urease enzyme which eventually changes the pH back to the resting pH and therefore the film comes back to the emeraldine base form (we monitored this temporal changes via absorption changes at 800 nm). This cycle-



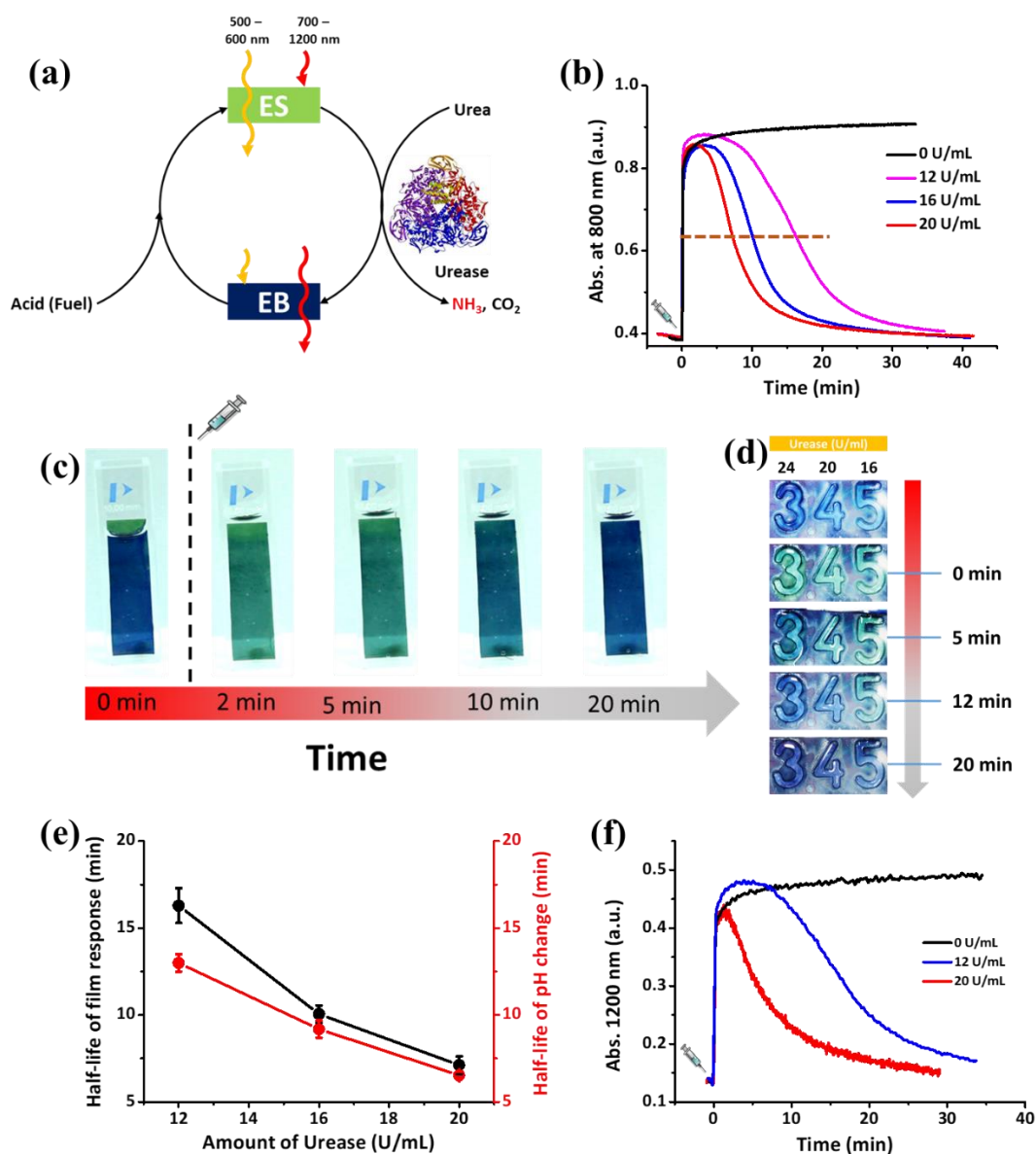


**Figure 10. Enzyme regulated temporal control of the optical states of the PANi film.**

(a) Schematics showing the transient optical switching with chemical fuel-driven step as activation and urea hydrolysis (catalysed by urease enzyme) step as deactivation (proving the successful integration of AFS with the film). (b) The temporal changes of the absorbance at 800 nm of the PANi film. The life-time of the transient emeraldine salt (ES) state could be programmed by enzyme concentrations (urea used was 200 mM). The horizontal dotted line represents point of half-life calculations. (c) The snapshots showing the temporal change in the colour of the PANi@PET films. (d) Snapshots of the PANi coated stencil showing transient writing with different life times as programmed by enzyme concentrations. (e) Comparison of half-life of AFS pH profiles (time taken for the pH to reset back to pH 6.0 (the half way between the initial and final pH) and the

response of the film (time taken for the film to come back to half of its total absorbance change at 800 nm). (f) The temporal changes of the absorbance at 1200 nm of the PANi film.

-of EB to ES to EB was also evident from the snapshots showing the temporal variation of film colour (Figure 10c). The life time of transient emeraldine salt state could be regulated using the enzyme concentration (Figure 10e). This programmable PANi was further used to create transient writings. For this purpose, a PET based stencil was used. The PANi polymer was deposited to the stencil using the same protocol used for the PET films. The number grooves on the stencil act as reservoir for AFS solution (Figure 10d). The addition of acid (fuel) to the grooves triggered the switching of emeraldine base (deep blue) to emeraldine salt (green) and subsequently each digit appeared green (remaining portion of the stencil maintained deep blue colour). The deactivation step slowly changed the colour back to the deep blue and therefore erased the green writing. By using different enzyme concentration in grooves, the life-time of the writing could be programmed.

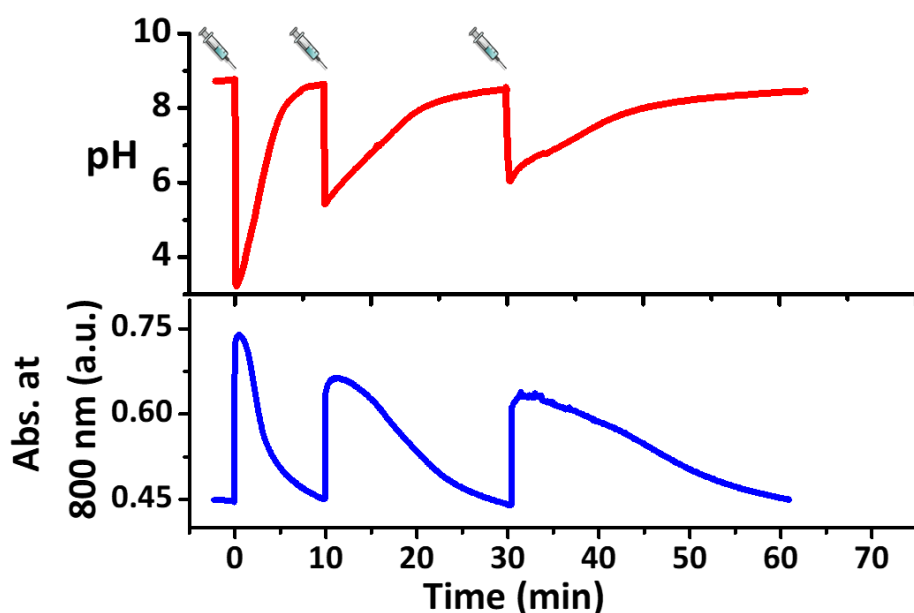


**Figure 11.** Refuelling the system for multiple cycles. Above panel shows temporal variations of pH upon successive fuelling events and the below panel shows the corresponding fuel-driven autonomous switching of PANi@PET between EB and ES forms (urease = 22 U/mL and urea = 200 mM). The syringe clipart marks the point of acid addition.

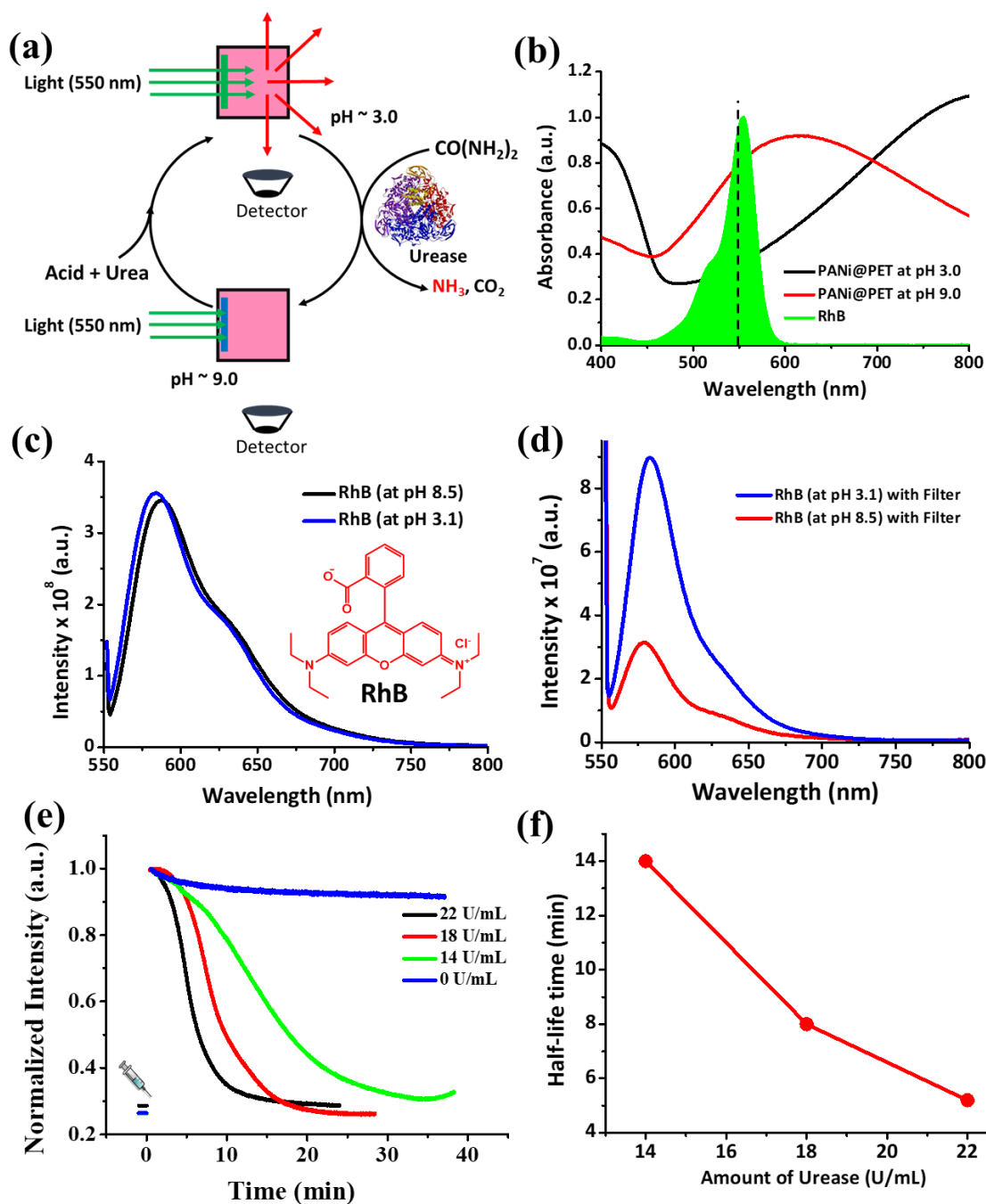


**Figure 12.** (a) Utilization of transient transmittance of PANi@PET film for the transient excitation of fluorophore. (b) UV spectra of PANi@PET and rhodamine B clearly showing the overlap region. (c) Emission spectra of rhodamine B at different pH (showing no pH dependency). (d) Emission spectra of rhodamine B at different pH with PANi@PET film at the path of excitation light. (e) The temporal variations of the emission intensity of rhodamine B (in presence of PANi@PET film) at different urease enzyme concentrations. The discontinuity in curves is due to the 30 sec we used for

---

---

*aligning the film properly after mixing fuel. (f) The life-time of the emissive state could be programmed via enzyme concentrations.*

The recyclability of the present system upon subsequent addition of fuel was tested. For this purpose, AFS consisting of 22 U/mL of urease was used. The first addition of fuel, resulted in complete cycle of activation and deactivation within 10 minutes. Second addition of fuel was done after the system came back to resting state. This fuelling event again resulted in activation-deactivation cycle but took more time than the previous cycle. The last cycle also resulted in a similar trend but with longer time period. The increase of the life time upon subsequent refuelling event could be attributed of the accumulation of waste products in the closed system.

One of the probable applications of this system could be in the field of adaptable smart windows showing rhythmic change in visible light transmittance. Furthermore, their ability to regulate the infra-red (IR) light transmittance helps in controlling the room temperature.<sup>78-79</sup> Thanks to the broad absorption spectrum of PANi@PET, it shows a significant cut-off of the infra-red (IR) light in its emeraldine salt state and therefore a transient state showing low IR transmittance could be achieved by coupling with AFS (Figure 10d).

Further, this emeraldine salt state was utilized for the transient excitation of a fluorophore which demonstrated its applicability in generating transient signalling.<sup>30, 50</sup> Rhodamine B was used as the fluorophore for its absorption in the range 500 to 600 nm (Figure 12b) and its pH independent emission at 590 nm (Figure 12 c). The film was placed inside the cuvette in the path of the excitation light and the emission detector was kept at 90° to the excitation light (Figure 12a). At a pH of ca. 9.0, the film absorbs most of the excitation light (wavelength ~ 550 nm) and therefore very minimum emission was observed from RhB solution (Figure 12d). At pH around 3.0, the film exists in the form of emeraldine salt, which allows the excitation light to pass through the film and therefore RhB gets excited. Consequently, a higher emission intensity was observed. This high emission state was transiently switched by coupling the entire system with AFS and the life time of the transient emission state was regulated via enzyme concentrations. (Figure 12 e-f).

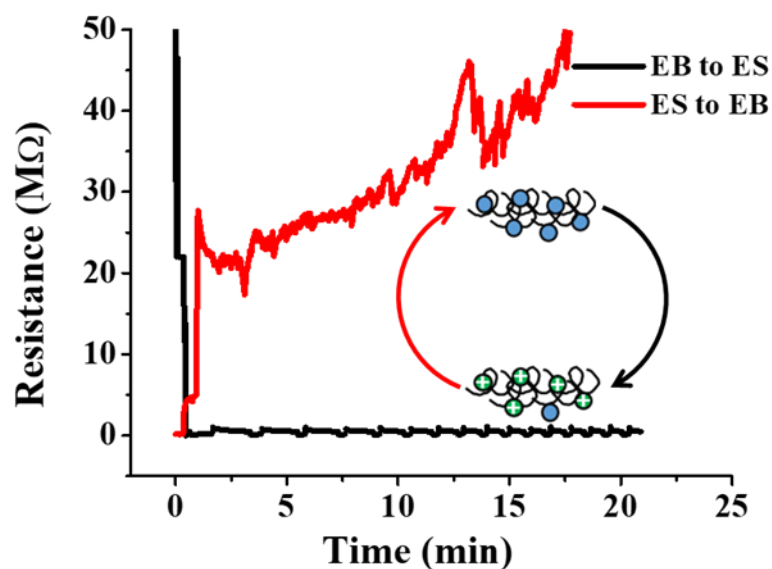


**Figure 13.** Kinetics of the pH dependent switching between the insulating emeraldine base state and the conducting emeraldine salt state.

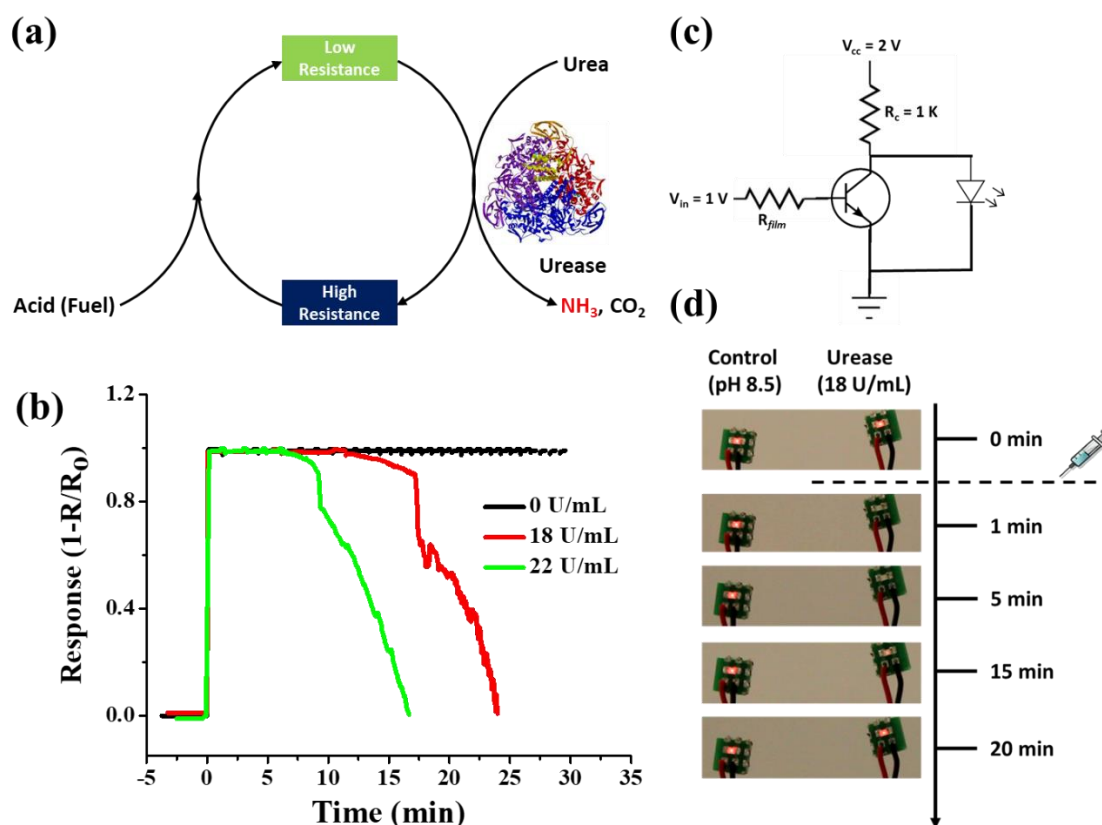


**Figure 14.** (a) Enzyme controlled temporal regulation of the electrical conducting properties of the film (switching between the insulating and conducting states). (b) The temporal variation of the resistance of the PANi@PET film. The life time of the

---

---

*conducting state could be programmed via urease concentrations. (c) A PNP transistor based switching circuit for switching the LED on and off depending on the resistance of the PANi@PET film. (d) Photographs showing the temporally regulated switching of a LED light. The temporal variation of the PANi@PET film driven by AFS is coupled with a switching circuit to switch the LED in a self-regulated manner. The control shows ON state of the LED when the PANi@PET film immersed in pH 8.5 buffer solution.*

After successful integration of PANi@PET film with AFS, we envisioned that the transient switching of PANi@PET film between the emeraldine base and emeraldine salt form could give rise to a transient electrical conducting nature in the film (Figure 14a). To study this, we have utilised a home-made setup where PANi@PET film was partially immersed in AFS solution yet both the ends were connected to a precision resistance meter with real-time data logging capabilities (Figure 4). The film in its emeraldine base state was electrically insulating with the resistance in the order of  $\sim 50$  M $\Omega$ . This film when exposed to the buffer solution of pH 3.0, the electrical resistance rapidly reduces to about 500 k $\Omega$  owing to the formation emeraldine salt (Figure 13). In a control study, a blank PET film without PANi was also studied for its electrical conductance in presence of pH 3.0 buffer. However, the blank PET film was electrically insulating suggesting that the electrical property is solely originated from the PANi polymer. The switching of the film from emeraldine salt to emeraldine base was studied and found to be slower than that of the reverse case (Figure 13) commensurating with the observations made on optical changes (Figure 8). Further, the PANi@PET film integrated with AFS to obtain the transient conducting state (Figure 14). The PANi@PET film at pH ca. 8.0 was taken where PANi existed as insulating emeraldine base which corresponds to zero electrical response as per the equation  $(1-R/R_0)$ . Addition of the fuel (acid) along with urea to the AFS solution immediately decreased the pH to acidic region and the film switched in to emeraldine salt form with low resistance of about 500 k $\Omega$  (maximum response). This state remained for certain period of time before returning to the resting emeraldine base form as the pH raised back to the resting pH. The life time of the transient electrically conductive state was programmed by modulating the enzyme concentration (Figure 14b).

Further, we utilised this transient resistance switching of the PANi@PET to switch a LED light on and off. For this purpose, a simple circuit consisting a PNP transistor was employed where the PANi@PET film was used between the  $V_{in}$  and base

terminal of the transistor. A low power LED was connected between the collector and emitter terminals of the transistor as shown in the circuit schematics (Figure 14c). In this configuration, the LED light would be switched on if the  $R_{\text{film}}$  is high and the same get switched off, if the  $R_{\text{film}}$  is smaller (less than 2 M $\Omega$ ). At the resting state, the PANi@PET film show insulating behaviour due to the emeraldine base form because of which the LED was switched on (Figure 14d). Addition of the acid to the system immediately switched off the LED light due to low resistance of the PANi@PET film at the acidic pH and as pH raised towards the resting state, the LED switched on again within ~ 10 min. As a control, another set of PANi@PET film was immersed in the pH 8.5 buffer during the entire time of this experiment and found to be resulted in a LED on state throughout the time, which clearly indicates that the switching of the LED occurred through successful integration of the fuel driven AFS with the PANi@PET films. This demonstration represents a significant step towards bio-mimetic life-like electronics which would open up arena of new types of applications and opportunities.

#### **2.4.6. Conclusions**

In summary, we have demonstrated fuel-driven temporally regulated switching of optical and electrical states of polyaniline film by integrating it with an autonomous feedback system (AFS) having a transient pH profile. The temporally regulated optical state of the polymer film was utilized for remote generation of fluorescent signals. On the other hand, the fuel-driven temporally regulated electrical conductivity was utilized for self-regulated switching in an electronic circuit. On a larger context, this proof-of-concept demonstration of integrating the enzyme chemistry with a functional system expands the scopes and opportunities of fuel-driven self-regulated autonomous systems.

#### **2.4.7. References**

- (1) Council, N. R. *Inspired by Biology: From Molecules to Materials to Machines*, The National Academies Press: Washington, DC, 2008; p 170.
- (2) Merindol, R.; Walther, A. Materials learning from life: concepts for active, adaptive and autonomous molecular systems. *Chem. Soc. Rev.* **2017**, *46* (18), 5588-5619.
- (3) Mitchison, T.; Kirschner, M. Dynamic instability of microtubule growth. *Nature* **1984**, *312* (5991), 237-242.

- (4) Korn, E. D. Actin polymerization and its regulation by proteins from nonmuscle cells. *Physiol. Rev.* **1982**, *62* (2), 672-737.
- (5) Whitesides, G. M.; Ismagilov, R. F. Complexity in Chemistry. *Science* **1999**, *284* (5411), 89-92.
- (6) Heinen, L.; Walther, A. Celebrating Soft Matter's 10th Anniversary: Approaches to program the time domain of self-assemblies. *Soft Matter* **2015**, *11* (40), 7857-7866.
- (7) Morris, E.; Chavez, M.; Tan, C. Dynamic biomaterials: toward engineering autonomous feedback. *Curr. Opin. Biotech.* **2016**, *39*, 97-104.
- (8) Bánsági Jr., T.; Taylor, A. F. Exploitation of Feedback in Enzyme-catalysed Reactions. *Isr. J. Chem.* **2018**, *58* (6-7), 706-713.
- (9) Ashkenasy, G.; Hermans, T. M.; Otto, S.; Taylor, A. F. Systems chemistry. *Chem. Soc. Rev.* **2017**, *46* (9), 2543-2554.
- (10) van Esch, J. H.; Klajn, R.; Otto, S. Chemical systems out of equilibrium. *Chem. Soc. Rev.* **2017**, *46* (18), 5474-5475.
- (11) Zwaag, D. v. d.; Meijer, E. W. Fueling connections between chemistry and biology. *Science* **2015**, *349* (6252), 1056-1057.
- (12) Tena-Solsona, M.; Boekhoven, J. Dissipative Self-Assembly of Peptides. *Isr. J. Chem.* **2019**, *59* (0), 1-9.
- (13) Boekhoven, J. Complexity from small molecules. *Nat. Nanotechnol.* **2018**, *13* (11), 979-980.
- (14) van Rossum, S. A. P.; Tena-Solsona, M.; van Esch, J. H.; Eelkema, R.; Boekhoven, J. Dissipative out-of-equilibrium assembly of man-made supramolecular materials. *Chem. Soc. Rev.* **2017**, *46* (18), 5519-5535.
- (15) Tantakitti, F.; Boekhoven, J.; Wang, X.; Kazantsev, R. V.; Yu, T.; Li, J.; Zhuang, E.; Zandi, R.; Ortony, J. H.; Newcomb, C. J.; Palmer, L. C.; Shekhawat, G. S.; de la Cruz, M. O.; Schatz, G. C.; Stupp, S. I. Energy landscapes and functions of supramolecular systems. *Nat. Mater.* **2016**, *15*, 469.
- (16) Rieß, B.; Boekhoven, J. Applications of Dissipative Supramolecular Materials with a Tunable Lifetime. *ChemNanoMat* **2018**, *4* (8), 710-719.
- (17) Panettieri, S.; Ulijn, R. V. Energy landscaping in supramolecular materials. *Curr. Opin. Struct. Biol.* **2018**, *51*, 9-18.
- (18) Dhiman, S.; Sarkar, A.; George, S. J. Bioinspired temporal supramolecular polymerization. *RSC Adv.* **2018**, *8* (34), 18913-18925.



- (19) Bisker, G.; England, J. L. Nonequilibrium associative retrieval of multiple stored self-assembly targets. *Proc. Natl. Acad. Sci. U.S.A* **2018**, *115* (45), E10531-E10538.
- (20) Boekhoven, J.; Hendriksen, W. E.; Koper, G. J. M.; Eelkema, R.; van Esch, J. H. Transient assembly of active materials fueled by a chemical reaction. *Science* **2015**, *349* (6252), 1075-1079.
- (21) Boekhoven, J.; Brizard, A. M.; Kowligi, K. N. K.; Koper, G. J. M.; Eelkema, R.; van Esch, J. H. Dissipative Self-Assembly of a Molecular Gelator by Using a Chemical Fuel. *Angew. Chem. Int. Ed. Engl.* **2010**, *49* (28), 4825-4828.
- (22) van Ravensteijn, B. G. P.; Hendriksen, W. E.; Eelkema, R.; van Esch, J. H.; Kegel, W. K. Fuel-Mediated Transient Clustering of Colloidal Building Blocks. *J. Am. Chem. Soc.* **2017**, *139* (29), 9763-9766.
- (23) Tena-Solsona, M.; Wanzke, C.; Riess, B.; Bausch, A. R.; Boekhoven, J. Self-selection of dissipative assemblies driven by primitive chemical reaction networks. *Nat. Commun.* **2018**, *9* (1), 2044.
- (24) Rieß, B.; Wanzke, C.; Tena-Solsona, M.; Grötsch, R. K.; Maity, C.; Boekhoven, J. Dissipative assemblies that inhibit their deactivation. *Soft Matter* **2018**, *14* (23), 4852-4859.
- (25) Grötsch, R. K.; Angı, A.; Mideksa, Y. G.; Wanzke, C.; Tena-Solsona, M.; Feige, M. J.; Rieger, B.; Boekhoven, J. Dissipative Self-Assembly of Photoluminescent Silicon Nanocrystals. *Angew. Chem. Int. Ed. Engl.* **2018**, *57* (44), 14608-14612.
- (26) Tena-Solsona, M.; Rieß, B.; Grötsch, R. K.; Löhner, F. C.; Wanzke, C.; Käs Dorf, B.; Bausch, A. R.; Müller-Buschbaum, P.; Lieleg, O.; Boekhoven, J. Non-equilibrium dissipative supramolecular materials with a tunable lifetime. *Nat. Commun.* **2017**, *8*, 15895.
- (27) Debnath, S.; Roy, S.; Ulijn, R. V. Peptide Nanofibers with Dynamic Instability through Nonequilibrium Biocatalytic Assembly. *J. Am. Chem. Soc.* **2013**, *135* (45), 16789-16792.
- (28) della Sala, F.; Neri, S.; Maiti, S.; Chen, J. L. Y.; Prins, L. J. Transient self-assembly of molecular nanostructures driven by chemical fuels. *Curr. Opin. Biotech.* **2017**, *46*, 27-33.
- (29) Chen, J. L.-Y.; Maiti, S.; Fortunati, I.; Ferrante, C.; Prins, L. J. Temporal Control over Transient Chemical Systems using Structurally Diverse Chemical Fuels. *Chem.: Eur. J.* **2017**, *23* (48), 11549-11559.

- 
- 
- (30) della Sala, F.; Maiti, S.; Bonanni, A.; Scrimin, P.; Prins, L. J. Fuel-Selective Transient Activation of Nanosystems for Signal Generation. *Angew. Chem. Int. Ed. Engl.* **2018**, *57* (6), 1611-1615.
- (31) Che, H.; Buddingh', B. C.; van Hest, J. C. M. Self-Regulated and Temporal Control of a "Breathing" Microgel Mediated by Enzymatic Reaction. *Angew. Chem.* **2017**, *129* (41), 12755-12759.
- (32) Cingil, H. E.; Meertens, N. C. H.; Voets, I. K. Temporally Programmed Disassembly and Reassembly of C3Ms. *Small* **2018**, *14* (46), 1802089.
- (33) Heuser, T.; Steppert, A.-K.; Molano Lopez, C.; Zhu, B.; Walther, A. Generic Concept to Program the Time Domain of Self-Assemblies with a Self-Regulation Mechanism. *Nano Lett.* **2015**, *15* (4), 2213-2219.
- (34) Dhiman, S.; Jain, A.; George, S. J. Transient Helicity: Fuel-Driven Temporal Control over Conformational Switching in a Supramolecular Polymer. *Angew. Chem.* **2017**, *129* (5), 1349-1353.
- (35) Jalani, K.; Dhiman, S.; Jain, A.; George, S. J. Temporal switching of an amphiphilic self-assembly by a chemical fuel-driven conformational response. *Chem. Sci.* **2017**, *8* (9), 6030-6036.
- (36) Dhiman, S.; Jain, A.; Kumar, M.; George, S. J. Adenosine-Phosphate-Fueled, Temporally Programmed Supramolecular Polymers with Multiple Transient States. *J. Am. Chem. Soc.* **2017**, *139* (46), 16568-16575.
- (37) Sawczyk, M.; Klajn, R. Out-of-Equilibrium Aggregates and Coatings during Seeded Growth of Metallic Nanoparticles. *J. Am. Chem. Soc.* **2017**, *139* (49), 17973-17978.
- (38) Bal, S.; Das, K.; Ahmed, S.; Das, D. Chemically Fueled Dissipative Self-Assembly that Exploits Cooperative Catalysis. *Angew. Chem. Int. Ed. Engl.* **2019**, *58* (1), 244-247.
- (39) Dong, B.; Liu, L.; Hu, C. ATP-Driven Temporal Control over Structure Switching of Polymeric Micelles. *Biomacromolecules* **2018**, *19* (9), 3659-3668.
- (40) Jain, A.; Dhiman, S.; Dhayani, A.; Vemula, P. K.; George, S. J. Chemical fuel-driven living and transient supramolecular polymerization. *Nat. Commun.* **2019**, *10* (1), 450.
- (41) Heuser, T.; Weyandt, E.; Walther, A. Biocatalytic Feedback-Driven Temporal Programming of Self-Regulating Peptide Hydrogels. *Angew. Chem. Int. Ed. Engl.* **2015**, *54* (45), 13258-13262.

- (42) Jee, E.; Bánsági Jr., T.; Taylor, A. F.; Pojman, J. A. Temporal Control of Gelation and Polymerization Fronts Driven by an Autocatalytic Enzyme Reaction. *Angew. Chem. Int. Ed. Engl.* **2016**, *55* (6), 2127-2131.
- (43) Maiti, S.; Fortunati, I.; Ferrante, C.; Scrimin, P.; Prins, L. J. Dissipative self-assembly of vesicular nanoreactors. *Nat. Chem.* **2016**, *8*, 725.
- (44) Trausel, F.; Maity, C.; Poolman, J. M.; Kouwenberg, D. S. J.; Versluis, F.; van Esch, J. H.; Eelkema, R. Chemical signal activation of an organocatalyst enables control over soft material formation. *Nat. Commun.* **2017**, *8* (1), 879.
- (45) Del Grosso, E.; Amodio, A.; Ragazzon, G.; Prins, L. J.; Ricci, F. Dissipative Synthetic DNA-Based Receptors for the Transient Loading and Release of Molecular Cargo. *Angew. Chem. Int. Ed.* **2018**, *57* (33), 10489-10493.
- (46) Okamoto, Y.; Ward, T. R. Cross-Regulation of an Artificial Metalloenzyme. *Angew. Chem. Int. Ed. Engl.* **2017**, *56* (34), 10156-10160.
- (47) Che, H.; Cao, S.; van Hest, J. C. M. Feedback-Induced Temporal Control of “Breathing” Polymersomes To Create Self-Adaptive Nanoreactors. *J. Am. Chem. Soc.* **2018**, *140* (16), 5356-5359.
- (48) Heuser, T.; Merindol, R.; Loescher, S.; Klaus, A.; Walther, A. Photonic Devices Out of Equilibrium: Transient Memory, Signal Propagation, and Sensing. *Adv. Mater.* **2017**, *29* (17), 1606842.
- (49) Kumar, M.; Ing, N. L.; Narang, V.; Wijerathne, N. K.; Hochbaum, A. I.; Ulijn, R. V. Amino-acid-encoded biocatalytic self-assembly enables the formation of transient conducting nanostructures. *Nat. Chem.* **2018**, *10* (7), 696-703.
- (50) Pezzato, C.; Prins, L. J. Transient signal generation in a self-assembled nanosystem fueled by ATP. *Nat. Commun.* **2015**, *6*, 7790.
- (51) Li, D.; Huang, J.; Kaner, R. B. Polyaniline Nanofibers: A Unique Polymer Nanostructure for Versatile Applications. *Acc. Chem. Res.* **2009**, *42* (1), 135-145.
- (52) Argun, A. A.; Aubert, P.-H.; Thompson, B. C.; Schwendeman, I.; Gaupp, C. L.; Hwang, J.; Pinto, N. J.; Tanner, D. B.; MacDiarmid, A. G.; Reynolds, J. R. Multicolored Electrochromism in Polymers: Structures and Devices. *Chem. Mater.* **2004**, *16* (23), 4401-4412.
- (53) Geniès, E. M.; Boyle, A.; Lapkowski, M.; Tsintavis, C. Polyaniline: A historical survey. *Synth. Met.* **1990**, *36* (2), 139-182.
- (54) Macdiarmid, A. G.; Chiang, J. C.; Richter, A. F.; Epstein, A. J. Polyaniline: a new concept in conducting polymers. *Synth. Met.* **1987**, *18* (1), 285-290.

- 
- 
- (55) Chandrasekhar, P. *Conducting Polymers, Fundamentals and Applications A Practical Approach*, Springer, Boston, MA: 1999.
- (56) Virji, S.; Huang, J.; Kaner, R. B.; Weiller, B. H. Polyaniline Nanofiber Gas Sensors: Examination of Response Mechanisms. *Nano Lett.* **2004**, *4* (3), 491-496.
- (57) Surwade, S. P.; Agnihotra, S. R.; Dua, V.; Manohar, N.; Jain, S.; Ammu, S.; Manohar, S. K. Catalyst-Free Synthesis of Oligoanilines and Polyaniline Nanofibers Using H<sub>2</sub>O<sub>2</sub>. *J. Am. Chem. Soc.* **2009**, *131* (35), 12528-12529.
- (58) Virji, S.; Kaner, R. B.; Weiller, B. H. Hydrazine Detection by Polyaniline Using Fluorinated Alcohol Additives. *Chem. Mater.* **2005**, *17* (5), 1256-1260.
- (59) Virji, S.; Kaner, R. B.; Weiller, B. H. Hydrogen Sensors Based on Conductivity Changes in Polyaniline Nanofibers. *J. Phys. Chem. B* **2006**, *110* (44), 22266-22270.
- (60) Virji, S.; Kojima, R.; Fowler, J. D.; Kaner, R. B.; Weiller, B. H. Polyaniline Nanofiber–Metal Salt Composite Materials for Arsine Detection. *Chem. Mater.* **2009**, *21* (14), 3056-3061.
- (61) Huang, J.; Virji, S.; Weiller, B. H.; Kaner, R. B. Polyaniline Nanofibers: Facile Synthesis and Chemical Sensors. *J. Am. Chem. Soc.* **2003**, *125* (2), 314-315.
- (62) Virji, S.; Fowler, J. D.; Baker, C. O.; Huang, J.; Kaner, R. B.; Weiller, B. H. Polyaniline Nanofiber Composites with Metal Salts: Chemical Sensors for Hydrogen Sulfide. *Small* **2005**, *1* (6), 624-627.
- (63) Tseng, R. J.; Huang, J.; Ouyang, J.; Kaner, R. B.; Yang. Polyaniline Nanofiber/Gold Nanoparticle Nonvolatile Memory. *Nano Lett.* **2005**, *5* (6), 1077-1080.
- (64) Wei, D.; Baral, J. K.; Österbacka, R.; Ivaska, A. Electrochemical fabrication of a nonvolatile memory device based on polyaniline and gold particles. *J. Mater. Chem.* **2008**, *18* (16), 1853-1857.
- (65) Shahabuddin, M.; McDowell, T.; Bonner, C. E.; Noginova, N. Enhancement of Electrochromic Polymer Switching in Plasmonic Nanostructured Environment. *ACS Appl. Nano Mater.* **2019**, *2* (3), 1713-1719.
- (66) Mortimer, R. J. Organic electrochromic materials. *Electrochim. Acta* **1999**, *44* (18), 2971-2981.
- (67) Wang, H.-L.; Gao, J.; Sansiñena, J.-M.; McCarthy, P. Fabrication and Characterization of Polyaniline Monolithic Actuators Based on a Novel

- Configuration: Integrally Skinned Asymmetric Membrane. *Chem. Mater.* **2002**, *14* (6), 2546-2552.
- (68) Baker, C. O.; Shedd, B.; Innis, P. C.; Whitten, P. G.; Spinks, G. M.; Wallace, G. G.; Kaner, R. B. Monolithic Actuators from Flash-Welded Polyaniline Nanofibers. *Adv. Mater.* **2008**, *20* (1), 155-158.
- (69) Smela, E.; Lu, W.; Mattes, B. R. Polyaniline actuators: Part 1. PANI(AMPS) in HCl. *Synth. Met.* **2005**, *151* (1), 25-42.
- (70) Kelly, F. M.; Meunier, L.; Cochrane, C.; Koncar, V. Polyaniline: Application as solid state electrochromic in a flexible textile display. *Displays* **2013**, *34* (1), 1-7.
- (71) Genies, E. M.; Lapkowski, M.; Santier, C.; Vieil, E. Polyaniline, spectroelectrochemistry, display and battery. *Synth. Met.* **1987**, *18* (1), 631-636.
- (72) Aleshin, A. N. Polymer Nanofibers and Nanotubes: Charge Transport and Device Applications. *Adv. Mater.* **2006**, *18* (1), 17-27.
- (73) Hu, G.; Pojman, J. A.; Scott, S. K.; Wrobel, M. M.; Taylor, A. F. Base-Catalyzed Feedback in the Urea-Urease Reaction. *J. Phys. Chem. B* **2010**, *114* (44), 14059-14063.
- (74) Bandgar, D. K.; Navale, S. T.; Nalage, S. R.; Mane, R. S.; Stadler, F. J.; Aswal, D. K.; Gupta, S. K.; Patil, V. B. Simple and low-temperature polyaniline-based flexible ammonia sensor: a step towards laboratory synthesis to economical device design. *J. Mater. Chem. C* **2015**, *3* (36), 9461-9468.
- (75) Wang, L.; Yao, Q.; Bi, H.; Huang, F.; Wang, Q.; Chen, L. PANI/graphene nanocomposite films with high thermoelectric properties by enhanced molecular ordering. *J. Mater. Chem. A* **2015**, *3* (13), 7086-7092.
- (76) Li, H.; Liang, Y.; Liu, S.; Qiao, F.; Li, P.; He, C. Modulating carrier transport for the enhanced thermoelectric performance of carbon nanotubes/polyaniline composites. *Org. Electron.* **2019**, *69*, 62-68.
- (77) Geniès, E. M.; Lapkowski, M.; Penneau, J. F. Cyclic voltammetry of polyaniline: interpretation of the middle peak. *J. Electroanal. Chem.* **1988**, *249* (1), 97-107.
- (78) Barile, C. J.; Slotcavage, D. J.; McGehee, M. D. Polymer-Nanoparticle Electrochromic Materials that Selectively Modulate Visible and Near-Infrared Light. *Chem. Mater.* **2016**, *28* (5), 1439-1445.
- (79) Khandelwal, H.; Schenning, A. P. H. J.; Debije, M. G. Infrared Regulating Smart Window Based on Organic Materials. *Adv. Energy Mater.* **2017**, *7* (14), 1602209.



## Conclusions and Outlook

This thesis mainly focuses on various synthetic strategies adopted for installing charge reversal in porous materials and for introducing temporally controlled functionalities in switchable porous and non-porous systems.

Chapter-1.1 briefly introduces mesoporous silica and present various surface modification approaches and their implications in regulating molecular transport in the mesochannels.

In chapter-1.2, a simple noncovalent strategy to create highly recyclable charge reversal mesoporous silica is introduced. The approach utilizes the hydrophobic interaction between alkyl functionalized mesoporous silica and ionic surfactant molecules. However, this approach is not limited to the ionic amphiphiles alone. It can be extended to reversibly immobilize other functional groups as well. In future, the generic nature of this strategy could be established.

In chapter-1.3, we demonstrate an approach to install the logic gate-controlled release of cargo from pH-dependent mesoporous silica by coupling it with pH switchable medium (consisting of multiple enzymes). To expand the scope of this generic approach, we attempted to demonstrate an AND gate control using glucose oxidase enzyme where glucose and molecular O<sub>2</sub> were used as the inputs. However, the hydrogen peroxide produced (during glucose oxidation reaction) decolourised CV<sup>+</sup> cargo molecules and hence the CV<sup>+</sup> release could not be studied. This issue should be addressed either by using cargo molecules that are resistant to oxidative decolorization or by replacing molecular O<sub>2</sub> with other electron acceptors.

Chapter-2.1 provides an overview of switchable materials having the self-regulated transient state. In this chapter, we illustrate various design principles through some of the representative examples.

In chapter 2.2, the temporal regulation of ion transport in mesoporous silica nanoparticles was studied by monitoring the adsorption and desorption of dye molecules. The concepts presented in this chapter can be readily translated to porous membrane models (such as conical nanochannels) where the ion transport can be monitored by

transmembrane current measurements. Development of such membrane systems where the ionic current is autonomously self-regulated will have tremendous applications in the field of sensing and biomedical engineering.

In chapter-2.3, a network of enzyme and nanozyme is presented. The network is constructed in such a way that the catalytic activity of the nanozyme is temporally regulated (autonomously) by the enzyme. It should inspire future research in the field of intelligent colorimetric sensing.

Chapter-2.4 describe a successful integration of dual-functional polymer film with an autonomous pH switching system for demonstrating self-regulated temporally controlled switching of functional states.

A major concern associated with the artificial, temporally controlled switchable materials is the lack of proper means to remove the waste products. Nature has evolved with sophisticated methods to remove the waste and therefore last for a longer time (a large number of cycles). However, almost all the artificial systems reported so far are having a limited number of cycles due to the waste accumulation. In the near future, significant emphasis should be given to solve this challenge to make use of these systems/materials for realistic applications.



# Appendix

---

## Instrumentation and Techniques for Characterization

**Transmission Electron Microscopy (TEM)** images were obtained using a JEOL JEM 3010 operating at an accelerating voltage of 300 kV. Samples for TEM analysis were prepared by dispersing the sample in either ethanol or water. A 10  $\mu$ l of dispersion was transferred on to holey carbon Cu grid and dried properly before loading to the TEM chamber.

**Field Emission Scanning Electron Microscopy (FESEM)** images were obtained using a NOVA NANOSEM 600 (FEI, Netherlands). A drop of ethanol or water dispersions of the sample was dried over aluminium stub for imaging.

**Nitrogen adsorption-desorption analysis** was performed on an Autosorb-1C (Quantachrome corp.). The samples were outgassed at 80 °C for 12 h under high vacuum before analysis. The specific surface areas and pore size distributions were calculated according to the BET method using the Quantachrome software (ASiQwin). Ultrahigh pure gases (99.9995%) were used for all experiments.

**Powder X-ray Diffraction (XRD)** patterns were recorded with a Bruker D8 Advanced diffractometer using Cu K $\alpha$  radiation. The average crystallite size was calculated by using the Debye-Scherrer formula

$$t = 0.9 \lambda / (\beta \cos \theta)$$

where  $t$  is the mean size of the ordered (crystalline) domains,  $\beta$  is the full width at half maxima in radians,  $\lambda$  is the wavelength of X-ray used and  $\theta$  is the Bragg angle.

**Thermogravimetric Analysis (TGA)** was carried out on a Mettler-Toledo-TG-850 instrument. 5-10 mg of sample was loaded into a small alumina boat for the analysis.

**UV-Vis absorption spectroscopy** – Spectra were recorded on Perkin-Elmer Lambda 750 UV/VIS/NIR spectrometer.

**Fluorescence spectroscopy** – Emission spectra were recorded on Horiba modular Nanolog Spectrofluorometer luminescence spectrometer. Emission spectra were recorded in right-angle geometry using a 10 mm cuvette.

**Infrared spectroscopy**- FT-IR spectra were recorded using Bruker IFS 66v/S spectrometer. 1-2 mg of sample was mixed with 100 mg of dry KBr and pelletized for recording spectra. Dry KBr pellets were used to correct for background.

**Dynamic light scattering and zeta potential measurements** were carried out using a NanoZS (Malvern, UK) employing a 532 nm laser at a backscattering angle of 173°. The temperature was always kept at 25 °C with the help of inbuilt thermostat in Zetasizer Nano ZS. The zeta titration was carried out by an Autotitrator (MPT 2 Titrator, Malvern Instruments). The pH was adjusted using 10 mM stock solutions of HCl or NaOH.

**pH measurements** were carried out using an Orion Star™ A211 pH Benchtop Meter equipped with a ROSS Sure-Flow glass-body pH electrode. The electrode was calibrated with ROSS pH buffer solutions of standard pH (4.00, 7.00 and 10.01) before the measurements. The temporal change in pH was recorded by interfacing the pH meter with a computer and recording the pH every 5 seconds.

**X-ray photoelectron spectroscopy (XPS)** analyses were performed using Omicron photoelectron spectrometer equipped with Al K $\alpha$  ( $h\nu = 1486.6$  eV) as the X-ray source.

**Electrochemical measurements** were performed on an electrochemical work station (CH instruments, USA) using polymer coated ITO slide as a working electrode, aqueous Ag/AgCl as a reference electrode and Pt wire as a counter electrode.

**Magnetization curve (B-H curve)** was obtained using a SQUID (Superconducting Quantum Interference Device) based MPMSXL-3-type magnetometer (Quantum Design, San Diego, USA).

**Electrical resistance measurements** were carried out using a Matrix+™ Digital Multimeter DM620. The temporal variations of resistance were recorded by interfacing the multimeter with a computer.

**Digital photographs** were taken using a Canon™ EOS 1300D digital camera.

## List of Publications

### From Thesis

1. **K. P. Sonu**, B. V. V. S. Pavan Kumar, Subi J. George and Muthusamy Eswaramoorthy, Simple and Facile Approach To Create Charge Reversible Pores via Hydrophobic Anchoring of Ionic Amphiphiles, *ACS Appl. Mater. Interfaces*, **2017**, 9, 9136-9142
2. **K. P. Sonu**, Sushmitha Vinikumar, Shikha Dhiman, Subi J. George and Muthusamy Eswaramoorthy, Bio-inspired temporal regulation of ion-transport in nanochannels, *Nanoscale Adv.*, **2019**, 1, 1847-1852
3. **K. P. Sonu**, Sushmitha Vinikumar, Shikha Dhiman, Subi J. George and Muthusamy Eswaramoorthy, Bio-inspired Temporal Regulation of Catalytic Activity of a Nanozyme, (Under Preparation)
4. **K. P. Sonu** and Muthusamy Eswaramoorthy, Molecular Logic Gate: Integrating Multi-Analyte Response in Mesoporous Silica for Logic Controlled Release, (Under Preparation)
5. **K. P. Sonu**, D. Selvakumar, Shikha Dhiman, Subi J. George and Muthusamy Eswaramoorthy, Bio-inspired Temporally Programmed Switching in Dual Functional Polymer Film, (Under Preparation)

### Other Publications

6. B. V. V. S. Pavan Kumar, **K. P. Sonu**, K. Venkata Rao, S. Sampath, Subi J. George and Muthusamy Eswaramoorthy, Supramolecular Switching of Ion-Transport in Nanochannels, *ACS Appl. Mater. Interfaces*, **2018**, 10, 23458-23465
7. Varma H. Rambaran, Shivani Boodram, Saumya S.M., Soumyabrata Roy, **K. P. Sonu**, Muthusamy Eswaramoorthy and Sebastian C. Peter, Design, Synthesis and Biological Evaluations of V(IV)O(pyridine diacetate)(H<sub>2</sub>O)<sub>2</sub>: Featuring Methods of Delivery and Administration, (Under Preparation)



## Curriculum Vitae



**K. P. Sonu** was born on November 30, 1990 in Ottapalam, Kerala (India). He completed his B.Sc. (Chemistry Hons.) from University of Calicut, Kozhikode in 2011. He obtained his MS in Materials Science from Jawaharlal Nehru Centre for Advanced Scientific Research (JNCASR) in 2014. He continued at JNCASR for his Ph.D. work under the supervision of Prof. M. Eswaramoorthy. His research work at Nanomaterials and Catalysis Laboratory is focused on design strategies for charge reversal and temporally regulated functionalities in porous and non-porous systems.

